Fluid driven processes in the crust – the formation of anorthositic dykes in the Troodos ophiolite (Cyprus)

Dissertation

zur

Erlangung des Doktorgrades (Dr. rer. nat.)

der

Mathematisch-Naturwissenschaftlichen Fakultät

der

Rheinischen Friedrich-Wilhelms-Universität Bonn

Vorgelegt von

Aurelia Lucretia Katharina Zirner

aus

Rosenheim, (BY) Deutschland

Bonn (July, 2017)

Angefertigt mit Genehmigung der Mathematisch-Naturwissenschaftlichen Fakultät der Rheinischen Friedrich-Wilhelms- Universität Bonn

1. Gutachter: Prof. Christian Gerhard Ballhaus

2. Gutachter: Privatdozent Dr. Raúl O. C. Fonseca

Tag der Promotion: 04.10.2017

Erscheinungsjahr: 2017

"...TO MANY PETROLOGISTS A VOLATILE COMPONENT IS EXACTLY LIKE A MAXWELL DEMON;

IT DOES JUST WHAT ONE MAY WISH IT TO DO."

(Bowen, 1928, p. 282 as cited in the blurb of Carroll and Holloway (1994))

TABLE OF CONTENTS

SECTION III: EXPERIMENTAL APPROACH

APPENDIX

ABSTRACT

Anorthositic dykes related with the Upper Cretaceous Troodos ophiolite are described for the first time. An entire anorthosite dyke swarm appears within the Limassol Forest Complex, crosscutting the supply channels of late Troodos extrusives. As inferred from crosscutting relations, the intrusion of dykes must be related to a very late magmatic stage of oceanic crust formation.

The appearance of anorthosites as dykes, imply that their composition had to be liquid at the time of intrusion. Melting experiments of such compositions show that even under H_2O saturated conditions, temperatures required for whole-sale melting are well above 1250 °C at 500 MPa, which is unrealistic for a derivative melt.

Pivotal aspect of the present work is the development of a genetic model, based on petrological, geochemical and experimental observations. Complex, multi-stage, open system phenomena are unrevealed, involving differentiation and unmixing of magmatic fluids and melts such as the enrolment of hydrothermal fluids.

Anorthositic dykes are interpreted to represent precipitates of a magmatic liquid that intruded the upper crust as a crystal mush. The anorthosite liquid is derived from unmixing of a highly evolved melt at depth. The fluid thereby is considered as a viscous gel, highly enriched in silicate solute, high field strength elements and rare earth elements. The solubility of the different species is granted by the saline, probably chloride rich composition of the liquid.

Normative bulk compositions of dykes range 80 - 100 wt.% plagioclase such that they are classified as anorthosites. Primary magmatic plagioclase approaches pure end member anorthite composition (X_{An} = 0.76 – 1.0). Anorthite, calcic pyroxene and accessory phases (titanite, rutile and zircon) are inferred as liquidus phases.

The observed mineral textures such as the trace element- and isotope composition confirms the intrusion of anorthosites to be related with a highly viscous magmatic fluid having a mutual source in boninites. A perfect correlation between lutetium content and the $^{176}Lu/^{177}Hf$ isotope ratio is observed in anorthosite rocks but does not appear in other Troodos extrusives emphasizing its unique generation history.

Liquidus experiments in the hydrous anorthosite system reveal melting temperatures of the bulk assembly exceeding 1150 °C; and anorthite (X_{An} = 1) as liquidus phase. Phase relation experiments in the H_2O saturated anorthite – diopside – forsterite system aim to duplicate and quantify the process responsible for the enrichment of the plagioclase component in the melt. It is demonstrated that the presence of a H_2O saturated melt coexisting with a H_2O-dominated fluid phase largely suppresses the crystallisation of anorthite from the fluid saturated melt. Simple system experiments further reveal the separation of a melt saturated fluid from the fluid saturated melt at conditions below the second critical point of water.

Decompression recrystallisation experiments with hydrous tholeiite compositions reconcile that fractionation of a mafic melt prior to unmixing of a fluid phase results in accumulation of the anorthite component and hence could represent the parental magma composition.

SECTION I: PREFACE

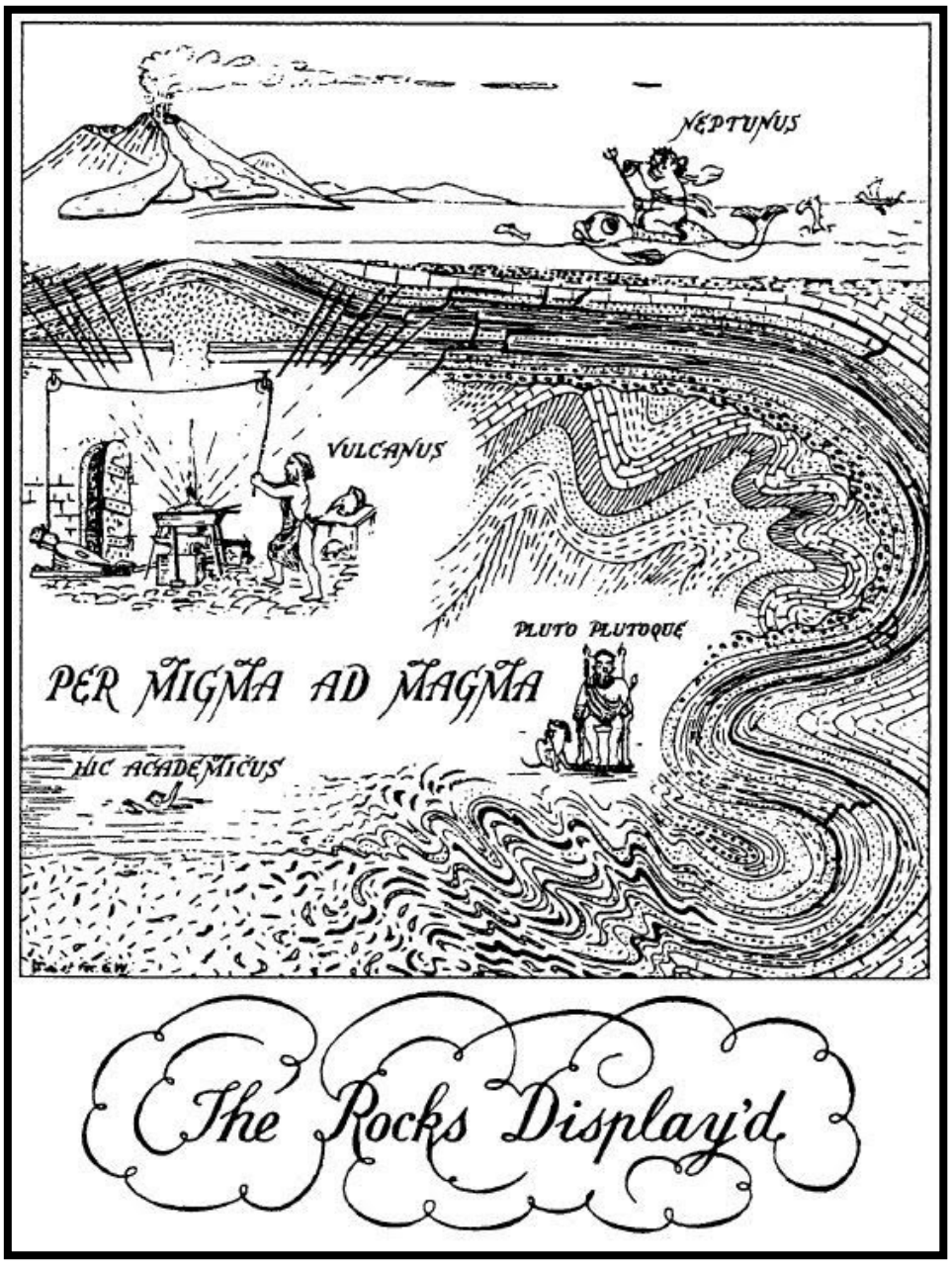

1 INTRODUCTORY WORDS

For the following introduction let us submerge into the mind pool of former and recent research on igneous processes and cast a light on various facts of crystal fractionation and fluid solubility in magmatic systems. As geologists trying to understand igneous rocks, we should first learn "TO THINK LIKE A (MOLTEN) SILICATE" (J. F. Schairer as cited in Yoder (1995)), so we should directly plunge into these fundamental issues of igneous petrology to be able to crystallize new ideas about how these systems might work.

The investigation of igneous rocks forms the basis of our knowledge on the composition, evolution, and internal processes of our home planet. Basically the Earth can be understood as an enormous igneous system - its interior is a high temperature assemblage of crystals and magmatic fluids, its crust is a layer of volcanic and intrusive rocks and the products of their weathering, erosion, and metamorphism.

Not much time has passed since it was still doubted that magmatism would play such a fundamental role in earth formation and rock generation. The controversy on the appraisal of magmatic phenomena and sedimentary as well as metamorphic processes mainly rose when scientists in the 18th and 19th century tried to explain rock genesis. Two contrasting theories opposed each other– the Neptunism vs. the Plutonism. Neptunists denominated after the Roman god of the sea Neptũnus were advocates of the theory that rocks originate from water. They assume rocks to have formed in a primordial ocean due to crystallisation and sedimentation. Picking up on Abraham Gottlob Werner's geological theories, Johann Wolfgang

Goethe, philosopher, poet and proponent of Neptunism, already expressed in 1784 in his essay on granite, his ideas on Granite formation:

> "GRANITE, WHICH IS THE MAIN COMPONENT OF THE WESTERN ALPS AS WELL AS OF THE HARZ, IS THE EMBLEM OF PRIMARY ROCKS, THE FIRST TO BE FORMED, SLOWLY, BY WATER CRYSTALLISATION, WHILE THE OTHER SEDIMENTARY OR CONGLOMERATE ROCKS ARE MUCH MORE RECENT."
>
> (GOETHE 1784 - ÜBER DEN GRANIT[1])

The theory of the Plutonists – named after the Roman god of the underworld Ploutōn however proposed "…PRIMORDIAL ROCKS…" to be the "…RESULTS OF MAGMATIC INTRUSIONS AND ERUPTIONS…" mainly represented by English naturalist James Hutton[2]. The controversy ended after all in favor for the Plutonists.

Magma is, so to speak, the basic module to think of. It can be defined as a completely or partly molten natural substance, which, upon cooling, solidifies as a crystalline or glassy igneous rock. Magmas can be understood as a suspension of liquids (melt and volatiles) and solids (crystals), the basic phases making up the magma. Melts are typically rich in silica, and even though volatiles constitute only a small weight fraction of the magma, their molecular weights are low, so that their mole fraction of the magma can be large. Moreover volatiles have disproportionately large effects on physical properties, such as viscosity, and on the composition, order of appearance, and form of crystallizing minerals (McBriney, 1993).

[1] Source of information: Gillespie, G., Engel, M., Dieterle, B., 2008. Romantic Prose Fiction A Comparative History of of Literatures in European Languages. John Benjamins Publishing Company, Amsterdam/Philadelphia.
[2] Source of information: Bressan, D., 2010. History of Geology The Granite Controversy: Neptunism vs. Plutonism.

Fig. 1: Front piece of "The Granite Controversy" by (Read, 1957), drawn by D. A. Walton. This cartoon is fitting to the 19th century controversy between Neptunism and Plutonism, however it was drawn to deal with the problem arose in the 20th century if granites are mainly of metamorphic origin.

Within the last century it has been shown that H_2O as the prominent volatile phase, plays a significant role for magmatic systems. Much effort was made to understand how H_2O enters the melt structure and how changes in external parameters influence its solution behaviour in a silicate melt. The present work focuses on the H_2O-melt pseudobinary system and implications for the generation of leucocratic rocks from basaltic melts.

2 DISCOURSE ON MELT DIFFERENTIATION

> "DIFFERENTIATION IS DEFINED AS ANY PROCESS BY WHICH MAGMAS EVOLVE AND BECOME MORE DIVERSIFIED"
>
> (MCBRINEY 1993 - IGNEOUS PETROLOGY)

Generally these processes are driven by changes in chemistry and physical conditions. A change in chemistry establishes a compositional difference in one or more phases, usually in response to changing physical conditions. Preservation of the differences is achieved by segregating or fractionating the phases. The term fractionation is thus applied to any process by which different phases are mechanically separated. It is not synonymous with differentiation. Fractionation is a mechanism; differentiation is its effect. (McBriney, 1993)

Superliquidus processes, such as the separation of two immiscible liquids, were accepted as a mechanism of igneous differentiation for silicates in the late 19th century, described with the term LIQUIDATION (Anfilogov, 1975 and references therin). Loewinson-Lessing (1884) was one of the first describing immiscibility within silicate melts. Unequivocal evidence for liquid immiscibility was first found in Fe-rich residual glasses of lunar rocks (Roedder and Weiblen, 1970) and a year later in some terrestrial basalts (Roedder and Weiblen, 1971). Differentiation due to silicate liquid immiscibility was extended to a much wider range of compositions by work of Philpotts (1976), emphasizing the relation between textural, experimental and compositional observations in the conjugate liquids. He described small spherical bodies of felsic material (ocelli) within fine grained basic rocks from the Monteregian alkaline province (Quebec, Canada) and concluded the ocelli had formed as droplets of immiscible liquid. Similar observations within the basaltic-H_2O system were described within the Troodos ophiolite by Ballhaus et al.

(2015). During superliquidus exsolution in silicate systems elements normally forming framework structures such as Si and Al are concentrated in the felsic liquid, whereas Fe, Mg and Ca, the less polymerizing ones, are strongly partitioned into the basic melt (Hess, 1971). Liquid-liquid equilibrium processes are as complex as, or even more complex, than processes in liquid-solid systems and will be introduced in the following Chapter.

2.1 LIQUID IMMISCIBILITY

The relevance of liquid immiscibility is now widely accepted and confirmed in many processes related to biology (lipid separation investigated in relation with membrane biology e.g.: McConnell and Vrljic, 2003; or Veatch and Keller, 2003) and metallurgy (Hume-Rothery and Anderson, 1960; Ziewiec et al., 2016). Especially progress in glass technology, even though mostly dealing with subsolidus -metastable immiscibility, made it increasingly apparent that immiscibility is an essential feature for silicate glasses.

Immiscibility under superliquidus conditions causes the separation of two stable liquids from a given melt. Phase separation occurs because the two separate liquids have a lower bulk free energy than the homogeneous system. The melt can arrive at this state of oversaturation by simple cooling, or by cooling and crystallisation and by decompression. The separation of liquids itself is a function of the melt composition but is completely independent of the presence, absence or the amount of crystals present. (Roedder, 1979)

The two conjugate liquids will develop sharp phase boundaries against each other. Depending on parameters such as surface tension and tensile strength, one liquid will develop minimal surface to volume ratios against its conjugate partner. The

formation of spheres allows to achieve the minimal energetic state in an isotropic medium such as a fluid or a melt (Ballhaus et al., 2015).

To approach a state of equilibrium at lowest energy level, the transfer of mass and energy is required, which is mainly achieved by diffusion. After phase separation and formation of one conjugate liquid sphere, all changes in composition of the two liquids require diffusion across the interface and through both liquids. The growth of a liquid sphere within the host liquid is comparable with the growth of a crystal of a solid solution from a melt with one significant difference. Diffusion rates in liquids will probably be many orders of magnitude faster than in crystals so equilibration is achieved much easier and faster in liquid-liquid systems than in solid-liquid systems (Hofmann, 1975).

A silicate melt that reaches saturation with a hydrous fluid behaves like any other system with liquid immiscibility (Roedder and Weiblen, 1970). To further discuss processes involving immiscibility between a hydrous fluid and silicate melts we first have to think about the relevance of H_2O in magmatic systems and the mechanisms how H_2O is incorporated in such melts to better understand what might happen when it then exsolves from its host.

2.2 H_2O IN SILICATE MELTS

H_2O is generally recognized as the most important magmatic volatile species. Both, for its abundance and for its effect on physical melt properties such as viscosity (Richet et al., 1996) and solid-liquid phase relations (Kushiro et al., 1968a; Kushiro et al., 1968b). Hence knowledge on the solubility behaviour of H_2O in silicate melts is essential for the understanding of many magmatic processes, such as melting processes, magma crystallisation, magma ascent, saturation, exsolution and

degassing of volatiles (Kent, 2008 and references therein). Together, volatiles and melts as mobile phases are the most important agents for mass and energy transport in the Earth. Supercritical (H_2O-dominated) fluids are thereby the most effective agents of mass transfer in high-pressure environments, and variations in the f_{H2O} in a system play a key role in controlling the extent of both crustal and mantle melting (Manning, 2004). Precise quantification of H_2O contents in glasses is still fraught with difficulty. Hardly surprising that the deep H_2O cycle is not fully understood and remains a fascinating enigma of earth sciences.

2.2.1 CHEMICAL SPECIATION AND SOLUBILITY OF H_2O IN MELTS

The first basic assumption argues that in order to dissolve, H_2O must chemically react with the silicate melt. Generally H_2O can be incorporated in the melt structure as molecular H_2O and as hydroxyl (-OH) anion (Stolper, 1982).

However, a first appropriate dissolution model for low H_2O concentrations is essentially based on the expectation of complete reaction of H_2O molecules to hydroxyl groups (Burnham, 1975). This dissolution model of H_2O in simple silicate melts involved association and dissociation reactions of hydrous species in the melt, and revealed a linear relationship between H_2O fugacity (f_{H2O}) as well as H_2O partial pressure (p_{H2O}) and the square of the mole fraction of dissolved H_2O (X_{H2O}^2) known as the "SQUARE ROOT RELATIONSHIP" (Moulson and Roberts, 1961). Infact, this was observed to be valid for X_{H2O} less than 0.5 but small positive deviations from this relation at higher H_2O contents were noticed. (Burnham, 1975; Burnham, 1981)

A more sophisticated model was proposed by Stolper (1982), also accounting for the solubility of molecular H_2O in the silicate melt. The model implies that H_2O is

not simply present as submicroscopic bubbles of trapped fluid, but must be considered as a true dissolving species in the melt. The two different H_2O species in the melt are described by the reaction:

$$H_2O_{molecular}\ (melt) + O^{2-}\ (melt) = 2\ OH^-\ (melt) \quad (1)$$

The derived equilibrium constant for the reaction inferred from the different activities of these melt species, implies ideal mixing of the melt species. The equilibrium between the two H_2O species is described as a homogeneous equilibrium as both species appear within the same phase, the melt. The heterogeneous equilibrium between vapor and melt describing the condition between the melt fraction and the coexisting H_2O dominated fluid is described by the reaction of Stolper (1982):

$$H_2O(vapor) = H_2O_{molecular}\ (melt) \quad (2)$$

The linear relationship between H_2O fugacity and the second power of the mole fraction of dissolved H_2O (e.g. Burnham, 1975) at low H_2O contents and its derivation of linearity at high total H_2O contents is attributed to different behaviour of homogeneous and heterogeneous equilibria of hydrous silicate melts. At a higher H_2O content in the melt the difference between the partial molar volumes of H_2O, compared to melts at low total H_2O contents, has a stronger effect such that the linear relationship is disturbed (e.g. Burnham, 1981).

One significant drawback of this model is that it relies on the assumption that observed concentrations of molecular H_2O and hydroxyl groups in hydrous silicate glasses reflect those of the melts from which they were quenched. Data obtained from quenched glasses rather reflect the melt structural environment near the

glass transition temperature than true temperature dependent solubility (Mysen, 2014).

Experimental data from temperature quenched hydrous glasses show that both, the amount and the proportions, of X_{OH} and X_{H2O} vary with bulk chemical composition of the melt and its total H_2O content (Dixon and Stolper, 1995; Stolper, 1982; Zotov and Keppler, 1998). The reaction of OH^- with Si^{4+}, Al^{3+} and the other metal cations, evoke changes in the melt configuration. In the simple SiO_2-H_2O system OH formation results in the breakage of bridging oxygen bonds (Wasserburg, 1957) and thus depolymerization of the melt. These observations are essential for the understanding of H_2O solubility in melts.

At pressures and temperatures relevant for natural magmatic conditions, the amount of volatiles such as H_2O that can be incorporated in silicate melts has been investigated in a wide range of melt compositions (Baker and Alletti, 2012; Behrens et al., 2009; Behrens et al., 2004; Blank and Brooker, 1994; Blank et al., 1993; Botcharnikov et al., 2005; Botcharnikov et al., 2006; Brooker et al., 2001; Di Matteo et al., 2004; Dixon, 1997; Dixon and Pan, 1995; Dixon et al., 1995; Holloway and Blank, 1994; Iacovino et al., 2013; Jakobsson, 1997; King and Holloway, 2002; King et al., 2002; Morizet et al., 2002; Morizet et al., 2010; Mysen et al., 2004; Shishkina et al., 2010; Tamic et al., 2001; Vetere et al., 2011) and has been subject of experimental studies since the work of Goranson (1931).

In general, it has been found that H_2O solubility decreases with increasing temperature at both high and low pressures whereas increasing pressure enhances H_2O solubility (Mysen, 1977). Compositional influences on H_2O solubilities can be summarized as an effect of the degree of polymerization of the

melt. The molar H_2O solubility increases with decreasing silica content for both binary and pseudobinary silicate systems. The H_2O solubility is additionally increased if associated with alkali systems compared to alkaline earth in silicate melts acting as network modifiers. In other words, the presence of Na_2O in a binary silicate melt has a larger effect on H_2O solubility than CaO or MgO. Also accounting for Al^{3+} as an additional network forming species, in a Na_2O-Al_2O_3-SiO_2 melt system, H_2O solubility increases with decreasing silica content (constant Na/Al), increases significantly with increasing Na_20 content (constant Si/Al), and decreases with increasing Al_2O_3 content (constant Na/Si). A detailed review of the influence of H_2O on the polymerization state of the melt and coexisting fluid, and thus its influence on numerous melt/fluid physicochemical properties, is given in Mysen (2014).

At high pressures, the phase relations in silicic magma-H_2O systems are complicated by the tendency of H_2O and silicate magma to mix completely (Boettcher and Wyllie, 1969; Hunt and Manning, 2012; Paillat et al., 1992; Shen and Keppler, 1997; Stalder et al., 2000). A decrease in H_2O solubility might be achieved by changing the melt composition, the temperature or the pressure and a system potentially reaches H_2O saturation. As a consequence the melt has to discharge (some of) its volatile content.

2.2.2 UNMIXING OF H_2O FROM A COEXISTING MELT

The thermodynamic reason for fluid exsolution is that at H_2O saturation, the two separate liquids have a lower bulk free energy than the homogeneous system. Written as a simplified reaction:

$$Fluid\ saturated\ melt_i \leftrightarrow melt\ saturated\ fluid + \ fluid\ saturated\ melt_{\ eq} \quad (3)$$

The reactant, the *fluid saturated melt*$_i$ (i refers to initial) exsolves a *melt saturated fluid* such that the initial fluid saturated melt composition changes towards compositions being less fluid rich. The melt composition at equilibrium denominated as *fluid saturated melt*$_{eq}$ in this equation (eq thereby refers to equilibrium).

The Gibbs free energies (G) of reaction (3) can be derived as:

$$\Delta G = G_{melt\ saturated\ fluid} + G_{fluid\ saturated\ melt_{\ eq}} - G_{fluid\ saturated\ melt_{\ i}} < 0 \quad (4)$$

Depending on parameters such as density contrasts between the two liquids, different textures will develop. Ballhaus et al. (2015) postulated that the two conjugate liquids will develop sharp interfaces against each other, and if enough space is available, one liquid phase will attain minimal surface to volume ratios against its conjugate partner. A sphere is the energetically most favourable shape in an isotropic medium such as a fluid or a melt.

By definition, the chemical potentials (μ_i) of all components in the coexisting liquids are identical under equilibrium conditions (Ghiorso and Sack, 1995). Ballhaus et al. (2015) concluded that at given P and T, both conjugate liquids are saturated with the same crystalline phases with fixed phase compositions, and both liquids have identical liquidus temperature (T_l). Nonetheless observation of various natural systems reveal that after cooling and solidification, the relative proportions of crystalline phases in former fluid and melt pools may differ greatly. This is attributed to: a) differences in the activity coefficients of components in the conjugate liquids, b) differences in the activation energies needed to crystallize

stable nuclei of crystalline phases in the two liquids, and c) differential wetting properties of melt and fluid toward the surfaces of crystalline phases.

All natural magmas contain dissolved H_2O or other volatile components that may be absorbed and exsolved in complex ways as magma rises from their source to cool and crystallize at shallower depth. Though much of the volatile content of volcanic rocks is lost before minerals crystallize at low pressure, plutonic rocks retain more of their volatiles and incorporate them into stable minerals. Nonetheless the major fraction of fluids, such as a magmatic fluid, is not solidified and rarely manifested within the geological record. Records of compositions of aqueous fluids in equilibrium with molten or crystalline silicates at depth relevant to magmatic processes are sparse as these fluids are not quenchable such as magmatic glasses. The closest approximation of naturally exsolved volatile-rich phases are fluid inclusions in phenocrysts where the immiscible magmatic liquids and vapour are trapped. Fresh, undisturbed melt-volatile inclusions do not appear in many magmatic systems, and as a consequence only little is known on magmatic hydrous fluids. Most, perhaps all, of the properties of such hydrous magmatic fluids (including the structure itself) cannot be determined by direct examination of the high-temperature/high-pressure fluid after quenching to ambient conditions.

Fluid immiscibility is likely to result in significant geochemical fractionation, Roedder (2003) noted that all chemical species present (elements, their isotopes, and the compounds they form) will become distributed between the two immiscible phases. The compositional divergence between the two can be extreme. In silicate systems, the partition coefficient for silica and the divalent oxides are very disparate, but those for alkalis and alumina are more nearly unity.

The present work aims to explain the generation of anorthositic melts, and assesses the question of the role of a fluid in this system. The presence of a fluid appears to be a realistic assumption, as Troodos in known to be related to an arc system, and arc magmas are known to be H_2O rich.

2.2.3 H_2O -RICH ARC SYSTEMS

Plank et al. (2013) reviewed literature data comprising H_2O contents of primitive to slightly evolved island arc basalts from seven well-studied volcanic arc settings (Cascades, Mexico, Kamchatka, Tonga, Marianas, Centam and Aleutians) and showed that the overall averaged H_2O content in most primitive melts of each arc system always ranges around 3.9 ± 0.4 wt.%. Maximum H_2O contents in melts reach in average 7 wt.% as observed in olivine hosted inclusions, from Klyuchevskoy Volcano, Kamchatka (Auer et al., 2009) and Augustine Volcano, Alaska (Zimmer et al., 2010), will reach saturation at crustal levels. A relevant pressure of ~ 400 MPa, corresponds to a depth of 15 – 16 km assuming an upper crustal density of $\rho = 2.6$ g/cm^3, and using the solution models of Newman and Lowenstern (2002) and Witham et al. (2012). Ballhaus et al. (2015) further concluded that melts containing ~ 4 wt.% H_2O will reach saturation in shallow crustal levels. Based on experimental data of Dixon et al. (1995), the corresponding pressure needed to dissolve 4 wt.% H_2O ranges 150 – 200 MPa, according to a depth of 6 km. The observation of similar H_2O contents (H_2O ~ 4 wt.%) throughout IABs was proposed to reflect coexistence of the melts with an exsolved H_2O rich fluid phase at depth of magma storage (Plank et al., 2013).

3 THE GEOLOGY OF CYPRUS - THE TROODOS COMPLEX

The island of Cyprus, the third largest Mediterranean island (surface area 9251 m^2) is situated in the north-eastern Mediterranean Sea and is part of a complex suture zone between the Eurasian and the African plate (Fig. 2). Its complex tectonic history might be illustrated by the fact that until about 20 Ma its core complex, Troodos, still made up Tethyan ocean floor sediments and underlying crust. Today, most of the island, geologically spoken exposes such former ocean floor rocks – referred to as Ophiolite. The term Ophiolite is understood as: "…SUITES OF TEMPORALLY AND SPATIALLY ASSOCIATED ULTRAMAFIC, MAFIC, AND FELSIC ROCKS THAT ARE INTERPRETED TO BE REMNANTS OF ANCIENT OCEANIC CRUST AND UPPER MANTLE" (Dilek and Furnes, 2014).

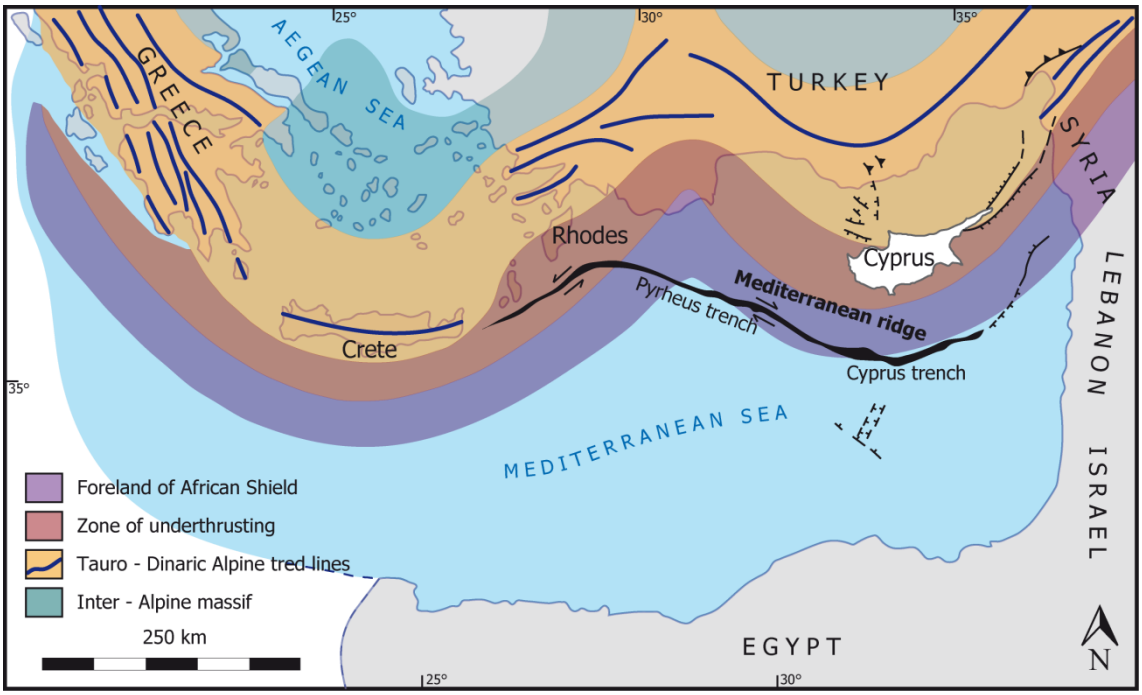

Figure 2: Overview map of the tectonic situation in the Aegean redrawn after Zitter et al. (2006) and Edwards et al. (2010). Note the present position of the island of Cyprus within the "zone of underthrusting".

The Troodos Ophiolite can be classified as supra subduction zone (SSZ) Ophiolite (Dilek and Furnes, 2014 and references therein). Based on age distribution of various ophiolites in the eastern Mediterranean region (e.g. Mirdita, Pindos, Kizildag, Oman) combined with geochemical data it has been proposed that the Tethyan oceanic crust is exposed not only at Troodos but rather represents one single slice of a huge system – of Cretaceous Tethyan SSZ ophiolites (Dilek and Furnes, 2009). These ophiolites probably developed as a consequence of the simultaneous initiation of a subduction zone within the southern Tethys along a more than 2000 km long belt (Coleman, 2014 and references therein).

3.1 GEOLOGICAL UNITS

In terms of its geological units the island is divided into four geological terranes: the Kyrenia range or Keryneia terrane, the Troodos terrane or Troodos Ophiolite complex (TOC), the Mamonia terrane and the Circum Troodos Sedimentary Succession of Upper Cretaceous to Pleistocene sediments (Fig. 3). The description of the different geological terranes is based on literature published on the webpage of the Geological Survey Department 1415 Nicosia (Republic of Cyprus et al., 2005-2016).

The heart piece of the island, the TOC, makes up the Troodos mountain range with the highest peak of the island – Mt. Olympus of almost 2000 m in height. Ophiolite components do not only appear in the central Troodos unit they crop out in the Limassol and Akapnou Forests south of the range having a characteristic elongated dome like structure, and minor outcrops appear in the Akamas peninsula and in the area of Troulloi village. The west trending Arakapas fault zone (Fig. 3) is interpreted as a fossil transform fault (Flower and Levine, 1987; Simonian and Gass, 1978).

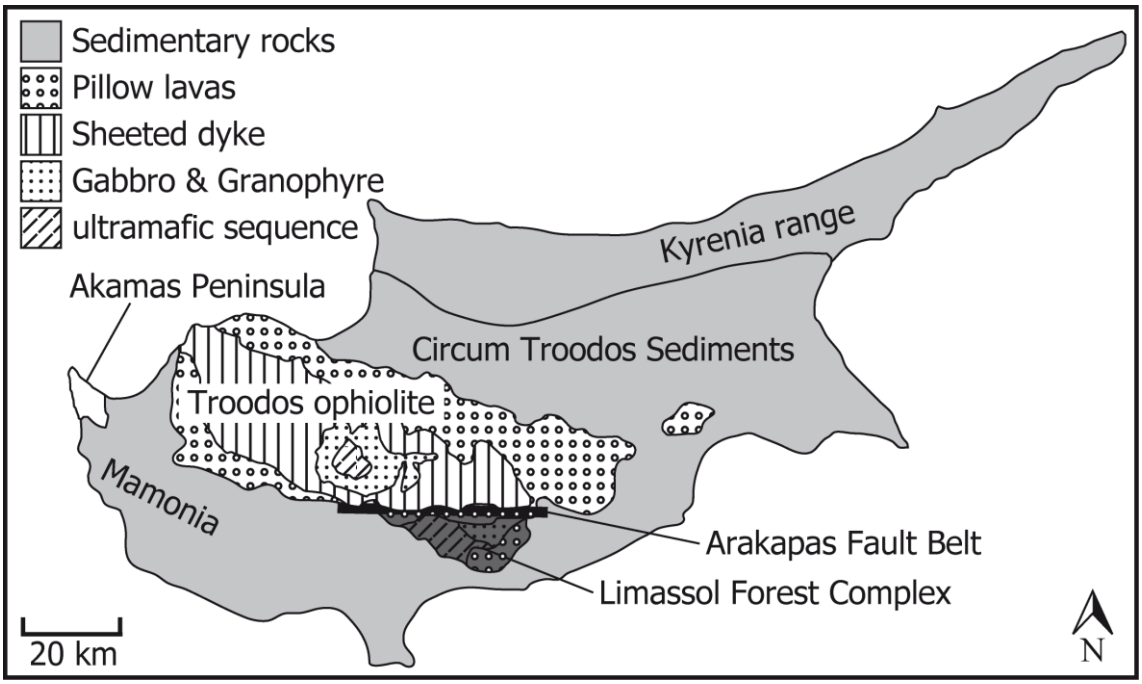

Figure 3: Simplified geological map of the island of Cyprus, displaying the different geological terranes and major tectonic features. Modified after Schmincke et al. (1983)

The Limassol Forest Complex (LFC), south of the Arakapas transform fault is interpreted as a deformed equivalent of the TOC. Deformation and alteration observed in LFC rocks is attributed to movement along the Arakapas fault zone.

3.2 OPHIOLITE EMPLACEMENT

The Ophiolite was emerged and placed in its present position through complicated tectonic processes related to the collision of the Eurasian plate to the north and the African plate to the south. The different terranes were thrusted onto the ophiolite related to microplate tectonics. The Kyrenia range thereby represents remnants of the southern-most portion of the Tauro-Dinaric Alpine Zone (Fig. 2). In contrast the Mamonian rocks are regarded as allochthonous with respect to Troodos oceanic crust. The ophiolite emplacement began with a 90° anticlockwise rotation between Upper Cretaceous and early Eocene time, and episodic abrupt uplift has

continued from the early Miocene to the present. (Moores et al., 1984; Robertson and Woodcock, 1979)

3.3 STRATIGRAPHY

The TOC is one famous example of an ophiolite in Europe. It gained attention as it displays a complete and intact stratigraphy through the Tethyan oceanic crust. It represents a fragment of a fully developed oceanic crust and upper mantle. From bottom to top of the former oceanic lithosphere it consists of the following stratigraphic units (numbers according to Fig. 4).

(1) Ultramafic metamorphic rocks are considered to represent restites after partial upper mantle melting responsible for the generation of basaltic magma. These mantle rocks are mainly represented by serpentinized harzburgites and dunites (Fig. 4).

(2) Intrusive rocks of the sheeted dyke complex (diabase) are basaltic to andesitic in composition (Fig. 4).

(3) The volcanic rock unit consists of two series of pillow lavas and lava flows. The two pillow series are namely the upper pillow lavas (UPL) and the lower pillow lavas (LPL) according to their stratigraphic position. LPLs display compositions of evolved tholeiitic arc andesites and dacites. Contrastingly the UPL are more primitive in composition and are represented by picrites and boninites (Cameron, 1985; Rautenschlein et al., 1985). Unlike the LPL, the UPL are not overprinted by hydrothermal alteration. The Basal Group between intrusives and pillow lavas is a transitional zone of both dykes and pillows (Fig. 4).

(4) As a result of hydrothermal activity (Fe and Mn rich solutions) due to the volcanic activity at the spreading center, the first sediments were deposited onto

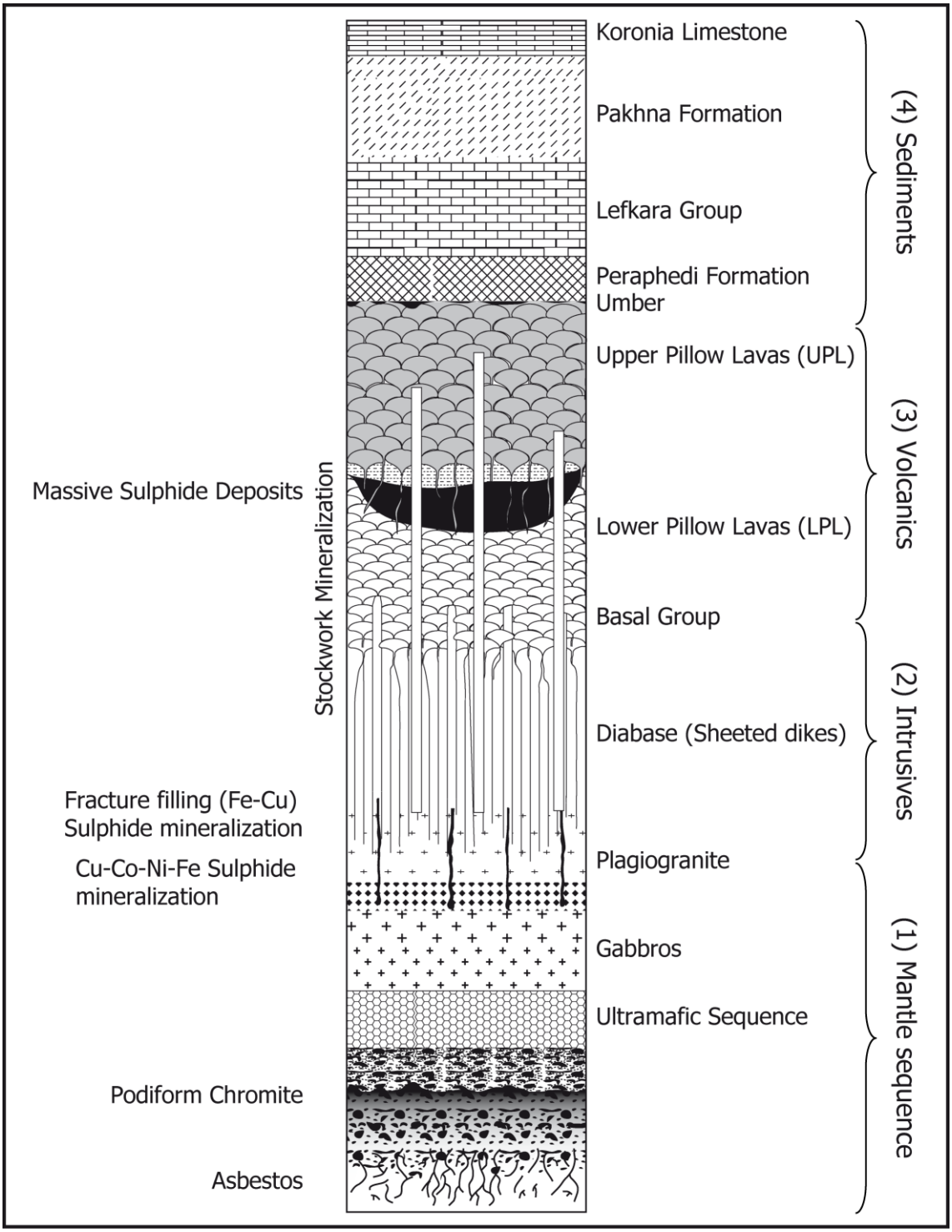

Figure 4: Simplified lithostratigraphic section of the Troodos ophiolite. After Constantinou (1980). The different units are briefly described in the text

the pillow lavas of the ophiolite. These sediments are comprised in the Perapedhi Formation which is composed of umber, radiolarites and radiolaritic shales (Fig. 4).

Massive sulphide and chromite deposits occur in several units of the TOC (Fig. 4).

Today the Troodos Ophiolite displays an inversion of the above described stratigraphic sequence with topography – a so called REVERSED STRATIGRAPHY (Ellis, 2000). Stratigraphically lower units (mantle sequence) outcropping at highest elevation, while the higher units (sediments) appear on the shallow periphery of the ophiolite. The inversion is due to the broad anticlinal structure of the Troodos Ophiolite which itself is related to its diapiric uplift and later erosion. (Edwards et al., 2010)

3.4 TECTONIC EVOLUTION

The genesis of the TOC has been a matter of debate especially in terms of the precise description of the geotectonic setting of oceanic crust formation. The Upper Cretaceous age of the ophiolite formation had been confirmed by U-Pb ages of zircons in plagiogranites giving ages of 91.4±1.4Ma (Mukasa and Ludden, 1987). Until the work of Miyashiro (1973) the Troodos ophiolite was widely accepted as the type example of a fragment of oceanic lithosphere generated at a constructive plate margin (Gass and Smewing, 1973; Moores and Vine, 1971).

Despite initial controversy on whether the Troodos Ophiolite was a classical MOR ophiolite (Moores, 1975) there is now a general consensus that Troodos is an SSZ ophiolite (Osozawa et al., 2012). The precise mechanism that induced extensional forces above the subduction zone to produce oceanic crust (in the upper Cretaceous) is still not fully understood.

The subdivision of the pillow lava sequence into LPL and UPL (Gass and Smewing, 1973) is confirmed by geochemical discrimination according to immobile trace elements (Pearce, 1975). The LPL and sheeted dykes display a geochemical fingerprint (e.g., high Ti) of both, Normal Mid Ocean Ridge Basalts (NMORB) and low K-tholeiites such as island arc basalts (IAB).

Observed low Ti, Zr, Y and Nb contents of the UPL are assigned to hydrous melting of a refractory mantle source. The mantle has previously been depleted in incompatible elements due to the extraction of melt for LPL generation (Pearce, 1975; Sun and Nesbitt, 1978).

3.5 THE H_2O-RICH MAGMATIC SYSTEMS OF CYPRUS

It has been previously demonstrated that the magmatic system related to Troodos extrusive rocks is H_2O rich (Cameron et al., 1979; Portnyagin et al., 1997; Robinson et al., 1983; Schmincke et al., 1983; Sobolev, 1996; Sobolev et al., 1993; to name some). The high H_2O content of the UPL ranging from 2 to 4 wt.% (e.g., Muenow et al., 1990) suggests that melts were H_2O saturated when generated from mantle melting (Dixon et al., 1995). Highest H_2O contents ($H_2O \sim 4$ wt.%) within the UPL were noted in glass-rich olivine tholeiites and high-Ca boninites (Cameron, 1985).

Textural evidence on an outcrop scale of the surplus of H_2O within the magmatic systems of Cyprus is given by the numerous occurrences of spheroidal textures as described by Ballhaus et al. (2015). According to Ballhaus et al. (2015) such spheroids are the result of the exsolution of fluid from a H_2O saturated melt, which in an attempt to minimize surface energy, result in spherical shapes. Spherules can be traced throughout the entire magmatic stratigraphic sequence of the Troodos ophiolite. Fluid exsolution textures together with observations of experimental

work, were interpreted such that H_2O saturation is assumed to have occurred at the base of the Moho (at 6 km depth) at pressures of around 150 - 200 MPa (Matveev and Ballhaus, 2002).

Ballhaus et al. (2015) described spheroidal textures within gabbros, the sheeted dyke complex and in extrusive rocks where they are more common compared to intrusive sequences. Within the UPL, spherules of glassy tholeiitic basalt are sitting in a glass-rich, micro-orbicular hyaloclastite matrix. In addition to spheroidal structures of basalts, more felsic spheroids were described and interpreted as fractionated melt pockets. The orbicules contain alumina enriched clinopyroxene micro-phenocrysts in a matrix of radially arranged skeletal calcic plagioclase, Alumina enrichment in pyroxene is referred to incorporation of the Calcium Tschermak molecule (CaTs). Ca-pyroxene, calcite, and small voids. Such textures were sampled for the present work (ZY92) and will be described in more detail.

The most impressive textural evidence on an outcrop scale for fluid exsolution within TOC is described as fluid escape structures in plagiogranite. Numerous sub-vertical epidosite channels and pods appear in the roof zone of a dioritic to plagiogranitic intrusion. Such textures indicate open system processes where an H_2O-rich fluid is exsolved within a solidifying hydrous magma body, accumulated in pods when the cumulates were already semi-solid respectively, to be channelled upwards along cracks towards the roof of the intrusion (Ballhaus et al., 2015).

The abundance of H_2O in all TOC related magmatic systems might be related to its SSZ position. As previously noted Plank et al. (2013) showed that parental magmas in arc settings are expected to be H2O saturated, and that arc magmas have average H2O contents around 4 wt.%.

SECTION II: PETROGRAPHIC AND GEOCHEMICAL CHARACTERISATION OF ANORTHOSITES AND RELATED LATE STAGE FLUID PRECIPITATES

1 OUTCROP AND SAMPLE DESCRIPTION

Sample material chosen to investigate for this study include samples from anorthositic dyke rocks and two allochthonous anorthosite samples. Furthermore one sample was investigated representing a spheroid probably precipitated from a late stage fluid.

1.1 ANORTHOSITIC DYKE SAMPLES

Nine anorthositic samples were taken from various dykes at an outcrop within the LFC at about 1.5 km N of Akrounta, Limassol (34°48.795'N; 33°05.106'E). The outcrop is located at a road cut on the way to Dierona. This sampling locality is referred to as ZY80. Accordingly, sample names collected at this locality are named ZY80X with X equivalent to different letters. The outcrop is about 4 x 12 m in size and comprises five approximately 0.5 m wide dykes and dozens of smaller (cm sized) ones. The dykes are roughly vertical (60° - 90°) but may crosscut each other, whereby it seems that larger dykes transect smaller ones (Fig. 5).

Figure 5: Field photograph of the sampling locality of the anorthositic dyke swarm transecting UPL supply channels within the LFC.

The anorthositic dykes appear in a bright greyish colour, and more altered parts turn up to be yellowish brownish. In parts the larger dykes fan out and reconsolidate again. The anorthositic dykes appear within a mafic dyke rock probably related to the UPL, referred as UPL supply channels. The host rock appears in a greyish to brownish colour and is strongly altered and brecciated in the interstices. In hand specimens the rock appears to be massive and unaltered. Acicular plagioclase crystals occasionally form radially arranged aggregates, reminiscent of spinifex textures (Fig. 6A). Spinifex textures would hint to very fast growth of anorthite due to rapid cooling. Some dykes display a dyke parallel zonation of darker and brighter areas (Fig. 6B).

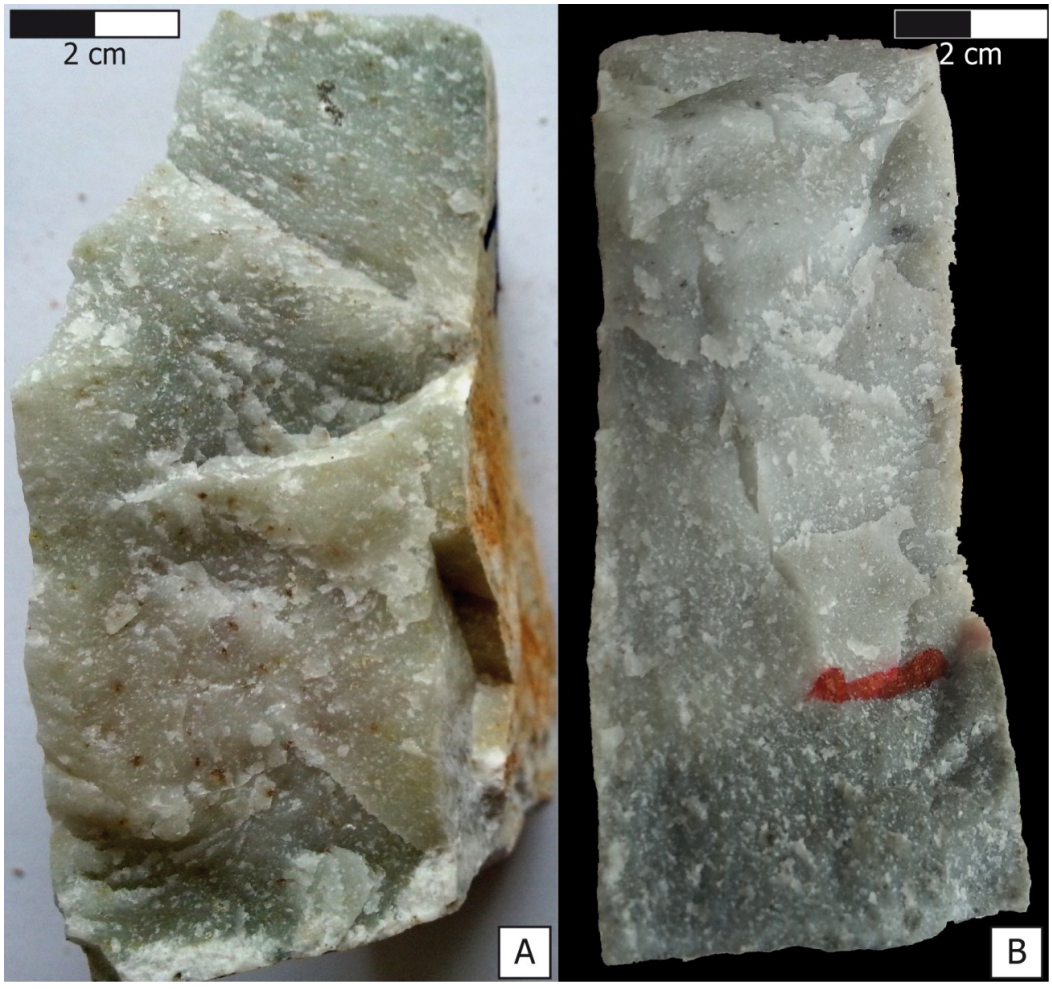

Figure 6: Photographs of anorthosite rock samples. A) Sample showing radially arranged acicular aggregates of Plagioclase reminiscent of spinifex textures and Rusty brown crystals of rutile. B) Sample showing the transition between anorthositic area (bright) and a Cpx enriched darker area.

Regarding the textures and minerals visible under the microscope, the rocks appear to be not as fresh anymore as in hand specimen. Major mineral constituents of all anorthosite dyke samples anorthite, albite, diopside and zeolite (thomsonite). Accessory minerals such as titanite, ilmenite, rutile, zircon and spinel (chromite) appear as early phases. Furthermore calcite and hydroxide minerals of the amphibole group (anthophyllite) and the chlorite group (clinochlore – chamosite) may be a component of the mineral assemblage.

Anorthite is the integral component of all these samples and appears as very fine to microcrystalline fragmented mineral "matrix" or as larger (1 mm) tabular crystals (Fig. 7A). Anorthite is replaced by albite along grain boundaries and fissures. The albite rim is commonly several µm wide and often retraces the former euhedral anorthite crystal boundaries especially in anorthite - zeolite textures. In contact with zeolite, the albite rims tend to be wider (tens of µm) (Fig. 7B and Fig. 8A/C). Textures indicate that anorthite is a primary magmatic mineral and albite a reaction product.

Diopside is another constituent of the primary magmatic assemblage and occurs as 50 – 250 µm large euhedral to xenomorphic grains or as acicular inclusions in zeolite (Fig. 7E and Fig. 8D/F). Crystals typically display chemical zonation visible in back scattered electron (BSE) mode. Commonly grains are concentrically zoned towards grain boundaries and patchily zoned in the core (Fig. 7B). Diopside crystals are often clustered in aggregates of euhedral concentrically zoned crystals together with zeolite (Fig. 7). Furthermore diopside is frequently associated with titanite (Fig. 9). In one anorthosite sample (ZY80A) diopside occurs as inclusions of µm sized acicular crystals in zeolite (Fig. 8/F).

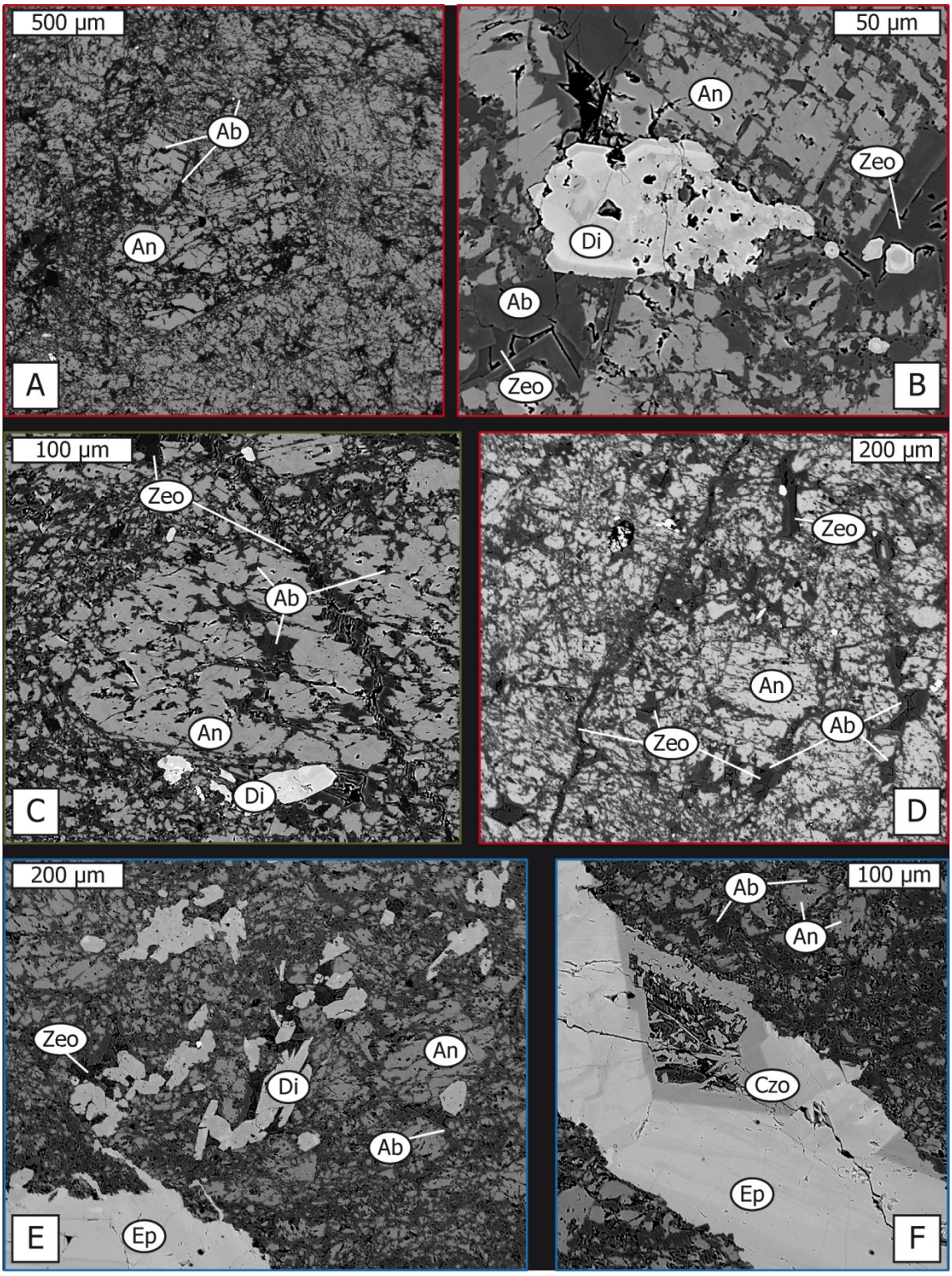

Figure 7: BSE images displaying Textures within the different anorthositic dyke samples, frame colours corresponds to anorthosite group as inferred from trace element composition (red=I, green=II and blue =III see subchapter 3.1 section II). (A) Overall anorthositic texture with fragmented anorthite crystals seamed with albite along fissures and grain boundaries (Sample ZY82A) (B) Chemically zoned interstitial diopside and thomsonite interstitial fillings (Sample ZY82A) (C) Fissured anorthite grain crosscut by a small thomsonite filled vein (Sample ZY80L) (D) Thomsonite filled vein and interstitial thomsonite fillings within the anorthite albite assembly (ZY82A) (E) Epidote vein (bottom left) and aggregate of subhedral to anhedral diopside within areas of increased thomsonite interstitial fillings (Sample ZY80B) (F) Chemically zoned epidote vein, partly digesting the magmatic assemblage (Sample ZY80B)

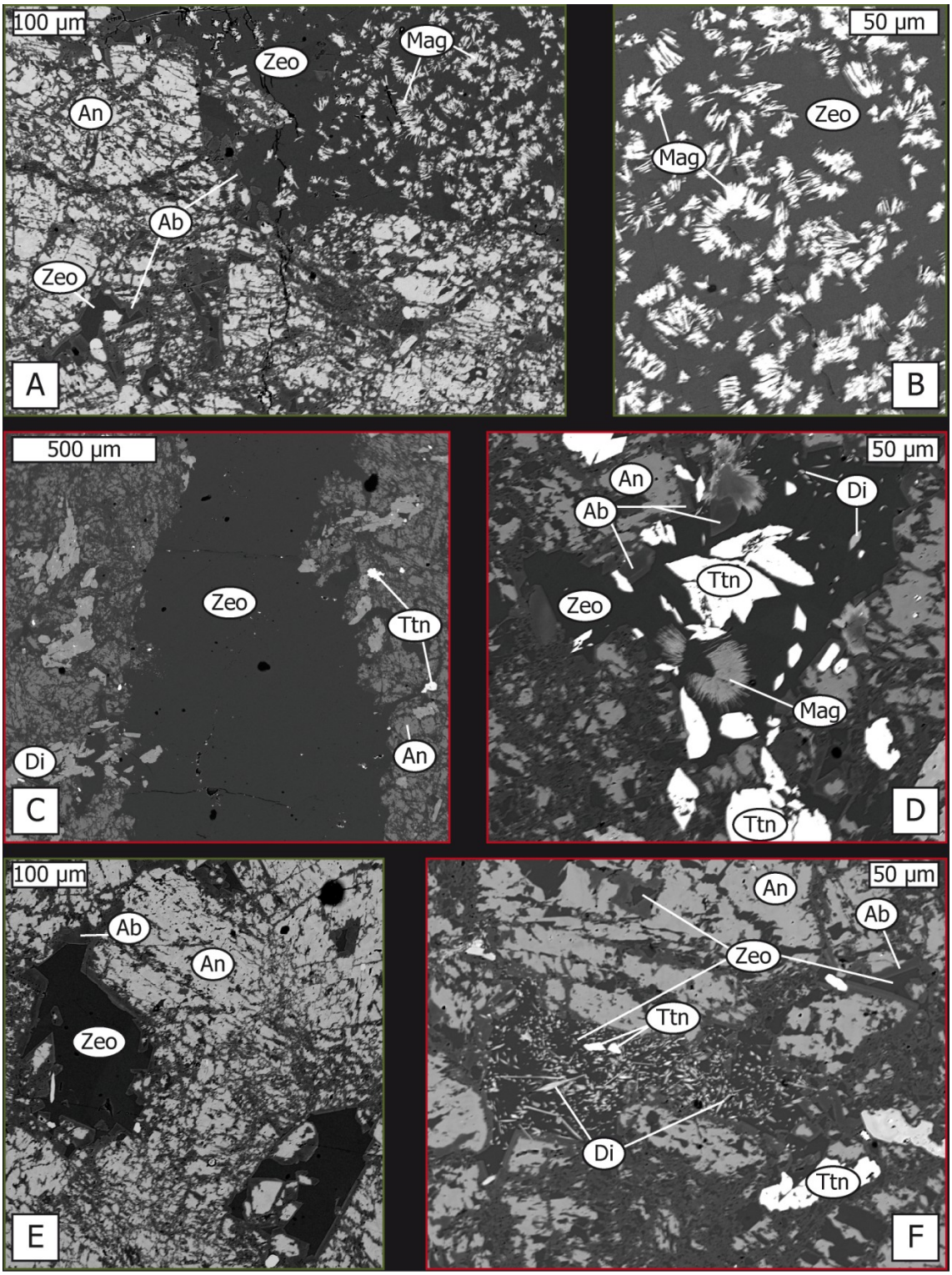

Figure 8: BSE Images displaying Textures within the different anorthositic dyke samples, frame colours corresponds to anorthosite group as inferred from trace element composition (red=I, green=II and blue =III see subchapter 3.1 section II). (A/B) Thomsonite texture revealing its origin from a magmatic glass as it displays chlorite quench crystals (enlarged in Figure 8B) (Sample ZY80L) (C) Large thomsonite "dyke" revealing its co genetic intrusion (as a melt) as fragments of the primary magmatic assemblage are enclosed (Sample ZY80A) (D) Interstitial thomsonite filling with titanite, diopside and magnetite inclusions. Magnetite and diopside reveal quench textures (Sample ZY80A) (E) Interstitial thomsonite filling revealing the primary euhedral shape of anorthite. Anorthite is replaced by albite along grain boundaries retracing initial anorthite crystal shape (Sample ZY80O) (F) Interstitial thomsonite filling with numerous diopside quench crystals and titanite inclusions (Sample ZY80A)

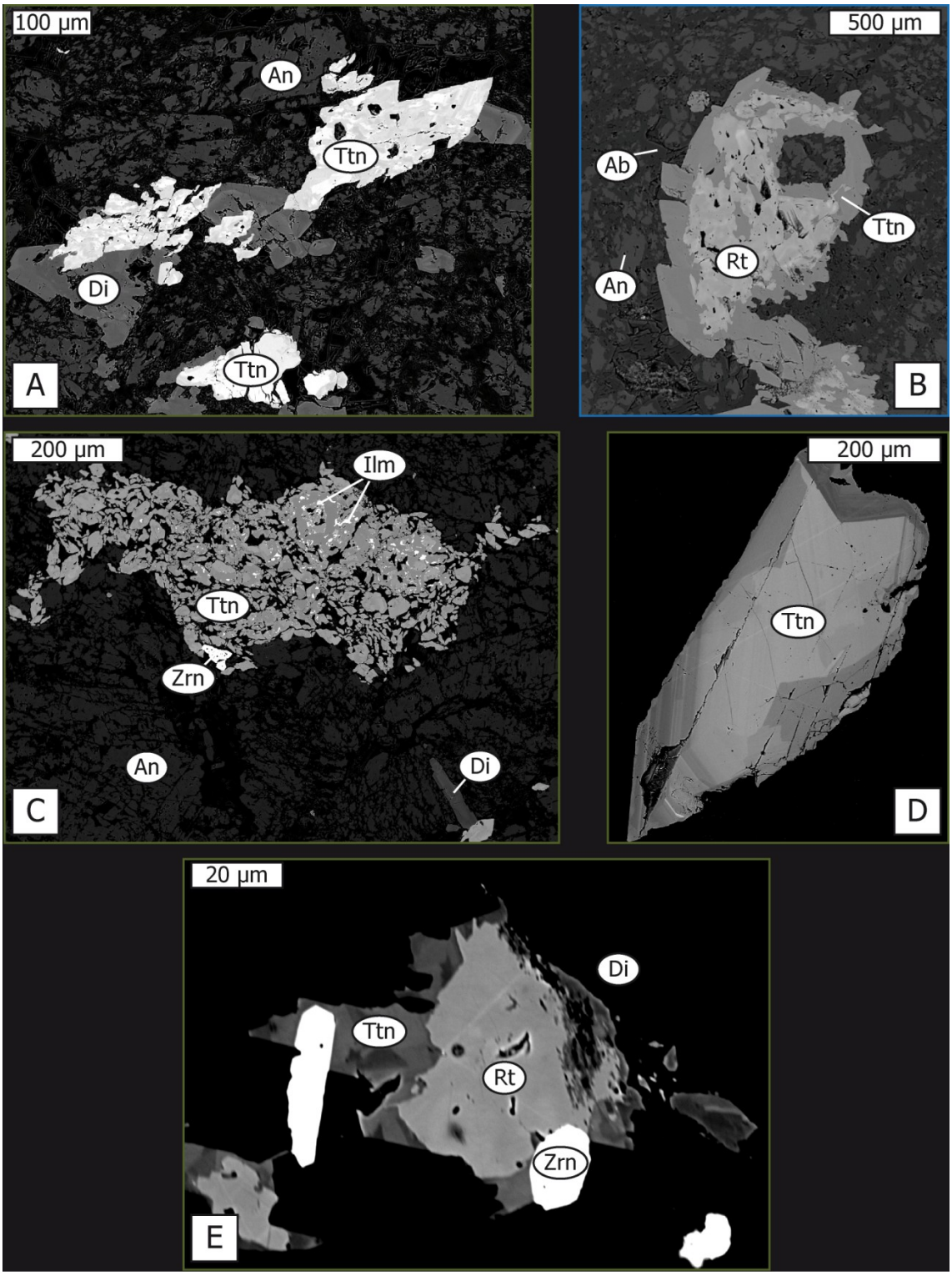

Figure 9: BSE Images displaying Textures within the different anorthositic dyke samples, frame colours corresponds to anorthosite group as inferred from trace element composition (red=I, green=II and blue =III see subchapter 3.1 section II). (A) Titanite associated/intergrown with diopside. Titanite appears to be patchily zoned and diopside rather concentrically zoned (Sample ZY80M) (B) Rutile inclusions in homogeneous titanite (Sample ZY80G) (C) Aggregate of titanite crystals with ilmenite inclusions and associated with zircon (Sample ZY80M) (D) Chemically zoned subhedral titanite crystal (Sample ZY80M) (E) Intergrowth of rutile titanite and zircon (Sample ZY80L)

Epidote/clinozoisite appears in one sample (ZY80H) as vein filling. Textural (Fig. 7F) evidence suggests that this 200 µm wide vein is late to post magmatic. The magmatic assemblage is digested in some parts by clinozoisite and epidote in some parts intersects primary magmatic anorthite crystals (Fig. 7E, Fig. 10).

Zeolite appears in all anorthosite samples along fissures (Fig. 8C) and veinlets (Fig. 7D and Fig. 8A/C) or as "interstitial matrix" (Fig. 7B/D/E and Fig. 8A/D/E/F). Texturally the zeolite is reminiscent of a glassy matrix suggesting pseudomorphic replacement of glass by thomsonite. Zeolithe hosts different mineral inclusions, which may be referred as phenocrysts assuming thomsonite to replace glass. Inclusions contained in thomsonite are diopside and chlorite quench crystals and euhedral titanite (Fig. 8A/B/D/F). In sample ZY80A a 500 – 700 µm wide fissure is filled with zeolite which has to be formed before or at the same time as the primary magmatic assemblage as it hosts diopside inclusions and does not form sharp boundaries towards the main anorthositic rock (Fig. 10).

Titanite appears as 100 – 600 µm large subhedral crystals (Fig. 9A/D), in aggregates of 20 – 50 µm large individual crystals (Fig. 9C), or as 5 -30 µm large euhedral inclusions in zeolite (Fig. 8D/F). Titanite is commonly associated with diopside and in some cases displays chemical zonation (oscillatory and/or patchily Fig. 9A/D). Titanite does not display any chemical zonation if associated with rutile (Fig. 9B/E). Anhedral rutile might be present in the core of titanite, textures are reminiscent of replacement reactions of rutile in favor of titanite (Fig. 9B/E). If titanite is associated with rutile commonly zircon also appears in the assembly. Further ilmenite might appear as microinclusions in titanite.

Textures of the Ti-phases (titanite, rutile and ilmenite) indicate either a long crystallisation interval or at least two distinct crystallisation events: titanite associated with rutile as an early stage and titanite inclusions in zeolite as a later one being younger than albite and zeolite (Fig. 10).

Textural observations indicate a sequence of crystallisation illustrated in Fig. 10. Zircon, rutile and titanite appear as early phases followed by anorthite and diopside. Chlorite might have formed short before or simultaneously with zeolite. Albite as a reaction product and vein fillings of epidote completes the sequence.

All samples of the anorthositic dyke swarm display about the same mineral paragenesis and textures, except variable relative mineral abundances of diopside and Ti-Phases relative to anorthite.

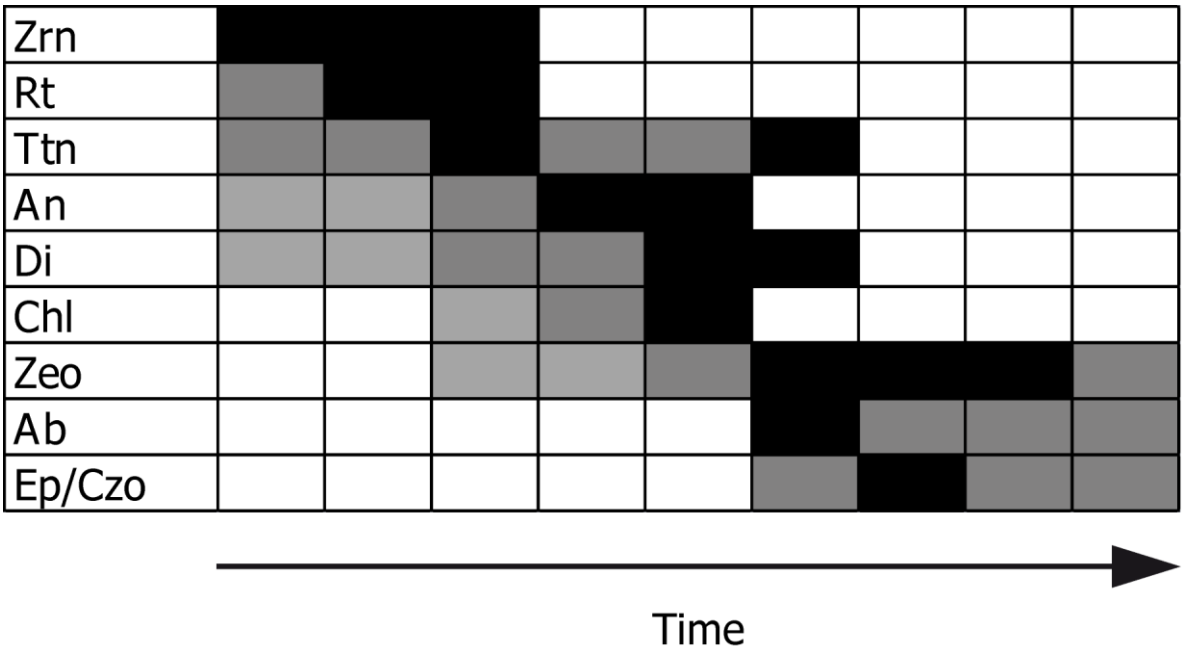

Figure 10: Schematic crystallisation sequence of accessory, primary magmatic and secondary minerals of the anorthosite samples deduced from interpretation of textures. X-axis corresponds to time (not to scale), the colours s light grey – black indicate the "probability" of appearance (black = definitely present).

1.2 ALLOCHTHONOUS ANORTHOSITE SAMPLES

In addition to the above described samples two anorthosite samples (ZY82A/B) of an allochthonous block (rubble stone) were investigated. The anorthosite block of a size about 2.5 x 3 m show up beside a coarse grained gabbro in a bend on the Atalanta trail about 1.3 km W beeline to the peak of Mt. Olympus within the ultramafic sequence (34°56.178'N; 32°51.141'E). The two samples from this locality are named ZY82A and ZY82B.

The allochthonous anorthosite samples appear greenish in hand specimen due to the occurrence of epidote and prehnite (Fig. 11). In terms of the primary magmatic assemblage, anorthite, diopside and titanite, they resemble the dyke rocks.

Figure 11: Photograph of an allochthonous anorthosite rock sample (ZY82B). The sample appears greenish due to higher epidote content.

Overall the samples seem to be much more altered (more albite and calcite), and diopside only appears as anhedral patchily zoned crystal and spinel appears to be more common.

1.3 SPHEROIDAL PRECIPITATE OF A LATE STAGE FLUID

For the investigation of the solute charge of an exsolved fluid equilibrated at depth with a fluid saturated melt, another sample type besides anorthosites is investigated for this study. The sampling locality of such spheroidal samples is referred as ZY92. The pockets of late stage fluid appear in association with orbicular tholeiite of the extrusive sequence within melt conduits of the UPL at an outcrop 250 m E of Kalavasos dam (34°48.181'N; 33°15.978'E).

The outcrop is cross-cut by calcite and the bright radial spheroids of about 0.5 mm in diameter are set in a slightly darker, pyroxene-enriched matrix (Fig. 12).

Figure 12: Photograph of the outcrop of spheroidal late stage melt pockets. The outcrop is cross-cut by several calcite veins an. For size comparison see one-cent piece (16.25 mm in diameter).

The overall image of these spheroids is comparable with scoops of ice-cream; if individual spheroids sit close together they are deformed such that they fill the empty spaces in between, or if more distant, the "matrix" consists of open space (Fig. 12). The mineral assemblage is made of phyllosilicates (phlogopite, vermiculite and of the chlorite group) acicular anorthite, calcite, and pyroxene phenocrysts (Fig. 13).

The spheroids are concentrically zoned. A chlorite rich rim hosting most of the pyroxene phenocrysts (Fig. 13C) and a core with acicular anorthite and orbicules of phlogopite and vermiculite. In the core vermiculite sometimes forms tube like structures (Fig. 13B/D). Calcite only appears at the interface between different spheroids.

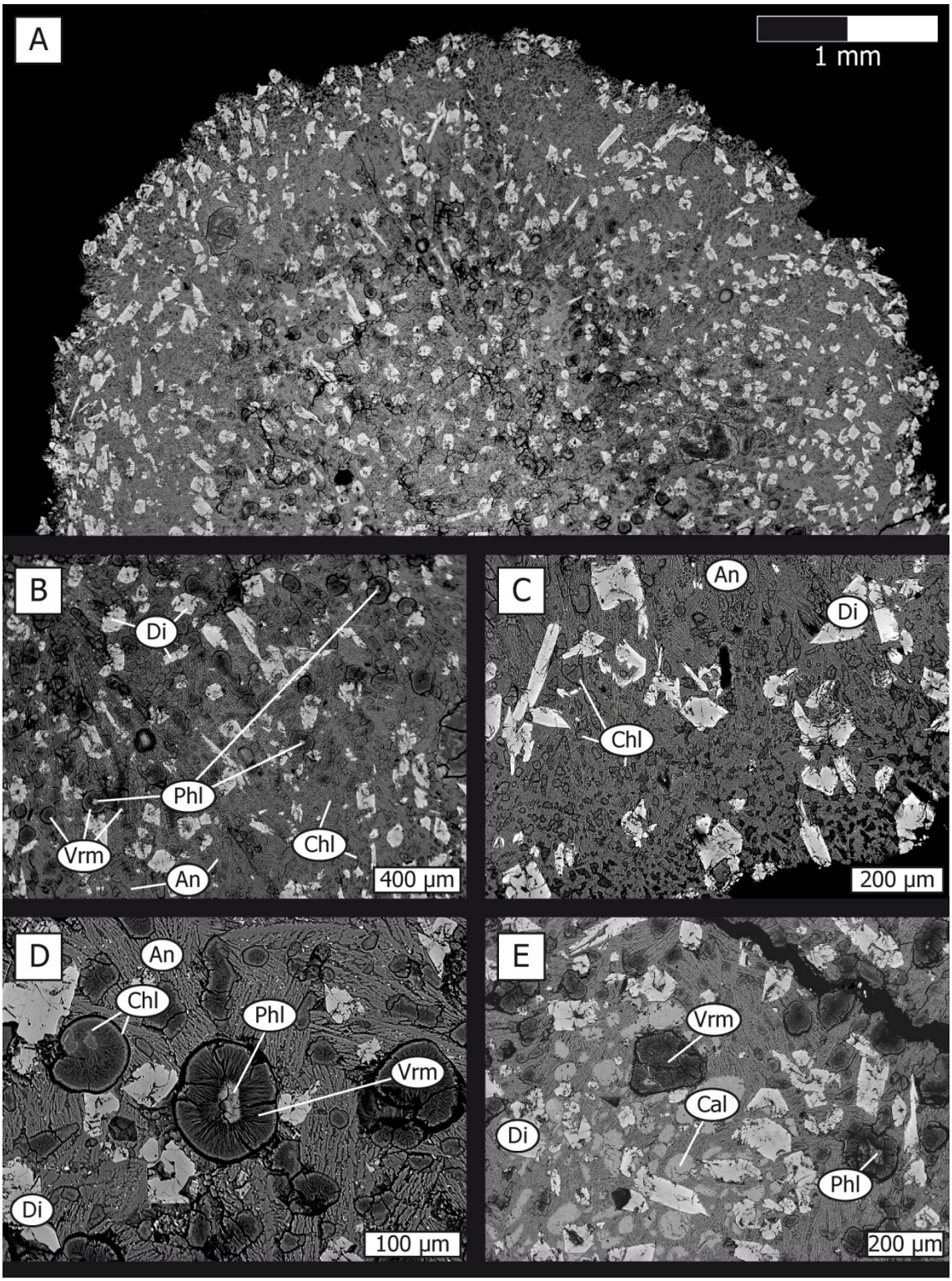

Figure 13: BSE images of one spheroid. (A) Overview image of the internal zonal structure of a spheroid. Texturally three zones can be distinguished; the core of the spheroid with subhedral Cpx crystals in a matrix of microcrystalline anorthite and chlorite, an intermediate zone (also see close up in Fig. B) and the outer area of the spheroid (also see Fig. C) (B) Close up of the intermediate zone of the sphere with radially arranged acicular anorthite and tubular vermiculite as well as vesicular phyllosilicates and subhedral diopside. (C) close up of the rim of the spheroid with small spherules of chlorite and subhedral diopside in a matrix of anorthite. (D) close up of dendrites of anorthite and vermiculite, phlogopite chlorite spheres. E) close up from the interface between two spheroids with calcite voids.

2 ANALYTICAL TECHNIQUES

Mineralogical and geochemical analyses of natural samples and experimental run products are analysed using various spectroscopic methods and methods based on mass spectrometry.

2.1 X-RAY FLUORESCENCE SPECTROSCOPY

The whole rock chemistry of two anorthositic dyke samples is investigated for major and some trace elements by Wavelength Dispersive X-ray Fluorescence Spectroscopy (WD-XRF). For XRF analyses about 100 g of freshly bright appearing areas of anorthosite dyke samples (ZY80A/B) are crushed and ground in an agate mill. Glass beads are fused from sample powder with lithium tetraborate (spectroflux) and lithium fluoride as flux added. The loss on ignition (L.O.I.) is determined by weight difference. Major elements and some trace elements are analysed with a PANALYTICAL AXIOS 3 KW Wavelength Dispersive XRF at the Steinmann-Institute Bonn. The PANALYTICAL AXIOS 3KW is equipped with a Rh-anode as a source of radiation using an energy of 3 kW to produce X-rays. The measuring file "Schmelze_081012" is used which is calibrated based on 45 MICROMATTER™ standard materials.

2.2 X-RAY DIFFRACTION SPECTROSCOPY

Crystalline components and the amorphous portion of 15 anorthositic samples and the late stage fluid precipitate are identified and quantified with X-ray Diffraction spectroscopy (XRD).

Anorthosite samples are crushed and ground in an agate mill and the powder is analysed within a measuring range of 4° - 70°, a step size of 0.02°, and one second acquisition time at 0.2 mm aperture of the detector and the variable- divergence

aperture V20. Data interpretation for qualitative identification of the mineral phases and quantitative estimation of their relative abundances is conducted with the BRUKER AXS software package DIFFRAC EVA 4.0, and DIFFRAC TOPAS 4.2 respectively.

Analyses are conducted at the Steinmann-Institute Bonn with a SIEMENS D5000 DIFFRACTOMETER equipped with a Theta-Theta-Goniometer, graphite single-crystal monochromator and a scintillation detector. X-rays are generated with a SIEMENS KRISTALLOFLEX 710D (40 kV and 40 mA).

2.3 ELECTRON PROBE MICRO-ANALYSER

Chemical compositions of all mineral phases occurring in the natural samples and experimental run products, as well as the bulk chemical compositions of natural samples, are investigated with a JEOL JXA 8900 electron probe micro-analyser (EPMA) equipped with a tungsten cathode at the Steinmann-Institute in Bonn. All measurements are performed at 15 kV acceleration voltage and a probe current of 15 nA. If it appears to be necessary to improve the resolution of back scattered electron (BSE) imaging, the beam energy is lowered. A focused beam is used for mineral analyses and a spot size of 3 – 10 µm for glasses respectively. Major elements are quantified on the Kα lines. Synthetic and natural materials are used as standard reference materials. Additionally as an external standard, a H_2O bearing- and a dry basaltic glass, is used if the H_2O content of a glass was quantified by difference to 100 wt.%. Matrix corrections are done online using the ZAF correction routine.

Quantification of the bulk composition of natural samples is achieved by analyzing homogeneous bubble free, crystal free glasses fused from 2 – 20 g sample powder.

Glasses are generated in platinum crucibles in two melting events, each 1 h at 1600 °C at a power of 8 kW, in a NABERTHERM RHT 08/16 batch furnace at the Georg-August-University of Göttingen. Elements with low condensation temperatures (such as sodium, potassium and manganese) might be lost during the melting process and are not considered for interpretation.

2.4 RAMAN SPECTROSCOPY

Natural samples of the anorthosite and the spheroidal late stage fluid precipitate are investigated for their mineral phase assemblage with a HORIBA SCIENTIFIC HR800 confocal Raman spectrometer equipped with an OLYMPUS BX41 optical microscope in 180° backscatter geometry and an EMCCD DETECTOR at the Steinmann-Institute Bonn. Thomsonite appearing in the anorthositic dyke samples is identified by its Raman spectrum, and textures including thomsonite are interpreted based on Raman-mapping. Furthermore, the phyllosilicates phlogopite, vermiculite and the chlorite group are identified. The Nd-YAG Laser (532.09 nm) is used as excitation source, set to 100 - 200 mW output power. The laser beam is focused using a x50 objective and is calibrated on a silicon standard (520.69 cm^{-1}). Spectra are accumulated with an exposure time of 30 – 60 s on each point in the frequency range of 30 – 1500 and 2700 - 3800 cm^{-1}. Slit and confocal hole correspond to default values of 100 and 1000 µm respectively. Identification of phases is achieved by comparison of the acquired Raman spectra with the RRUFF™ database (Lafuente et al., 2015).

Raman-maps are obtained with the ultra-fast mapping option (SWIFT), and the "least-squares" algorithm (CLS-Fitting) of the HORIBA LABSPEC 6 ANALYSIS MODULE is used to adjust different end member spectra to the observed spectra.

2.5 Inductively coupled Plasma Mass Spectrometry

Trace element chemistry of the individual mineral constituents of the anorthosite samples, as well as bulk trace element composition of glasses (Foley et al., 2000) from anorthosites and spheroidal late stage fluid precipitates is measured using a Resonetics M50-E 193 nm ArF Excimer laser ablation system of the facilities at the Steinmann-Institute Bonn. The laser ablation system is coupled to a Thermo Scientific X Series II quadrupole inductively coupled plasma mass spectrometer (Q-ICP-MS). The repetition rate of the laser is generally set to 15 Hz and a fluence of 8 J/cm^2. If possible, spot sizes of 100 µm are used and smaller diameters are chosen according to the available space and grain size (56 µm, 44 µm, 33 µm, 26 µm and 15 µm). The repletion rate for spot sizes ≤ 33 µm is decreased to 10 Hz. Count rates of following nuclides are monitored: ^{7}Li, ^{11}B, ^{29}Si, ^{43}Ca, ^{45}Sc, ^{47}Ti, ^{51}V, ^{52}Cr, ^{60}Ni, ^{65}Cu ,^{66}Zn, ^{85}Rb, ^{88}Sr, ^{89}Y, ^{90}Zr, ^{93}Nb, ^{95}Mo, ^{133}Cs, ^{137}Ba, ^{139}La, ^{140}Ce, ^{141}Pr, ^{146}Nd, ^{147}Sm, ^{153}Eu, ^{157}Gd, ^{159}Tb, ^{163}Dy, ^{165}Ho, ^{166}Er, ^{169}Tm, ^{172}Yb, ^{175}Lu, ^{178}Hf, ^{181}Ta, ^{182}W, ^{208}Pb, ^{232}Th and ^{238}U. As internal reference isotopes, ^{43}Ca and ^{29}Si are measured, and count rates are normalised using ^{43}Ca and ^{29}Si respectively. Count rates are converted to concentrations using the procedure outlined in Longerich et al. (1996). Oxide production rate is checked by monitoring the ThO/Th ratio during tuning, which is always kept below 1 %. The natural isotope abundances of elements with multiple isotopes are well reproduced showing that there are no significant isobaric or molecular interferences. As a check for external reproducibility, NIST SRM 610 is measured as a secondary standard. As an additional check for external reproducibility, a natural reference basaltic glass KL2-G is measured as a secondary standard. Using the method described above, trace element concentrations of these glasses are typically within 5 – 10 % of their

preferred value as given by Jochum et al. (2011). The method of trace element quantification in glasses is described in detail by Fonseca et al. (2017).

2.6 HIGH PRECISION ELEMENT AND ISOTOPE ANALYSIS

High precision element (Zr, Lu, Hf, Rb and Sr) and isotope ($^{176}Lu/^{177}Hf$, $^{176}Hf/^{177}Hf$, $^{87}Rb/^{86}Sr$ and $^{87}Sr/^{86}Sr$) composition analysis are performed on aliquots of digested whole rock (WR) powder. Both, isotope compositions and abundances are measured on the same aliquot, following the method of Weyer et al. (2002).

2.6.1 SAMPLE DIGESTION

About 100 mg sample powder of eleven anorthositic samples are each weighed into cleaned pre-bombed SAVILLEX® beakers. Samples are spiked with a mixed HFSE-spike (HFSE I: ^{94}Zr-^{176}Lu-^{180}Hf-^{180}Ta) and a ^{85}Rb-^{84}Sr tracer. The high pressure acid digestion procedure for felsic samples following the recipe of Hoffmann et al. (2010) is applied to the sample spike mix. As a first digestion step a 1:1 mixture of concentrated ultrapure hydrofluoric acid (24 M HF) and ultrapure nitric acid (14 M HNO_3) is added to the sample-spike mixture and placed on a hot plate for 24 h at 120 °C. The samples are dried down and treated in a second digestion step to ensure zircon and other accessory minerals being dissolved. For the second digestion step the SAVILLEX® beakers are refilled with 6 ml of the 1:1 HF-HNO_3 solution and inserted into a PARR® pressure vessel. Samples are pressurized at 180 °C for 3 days. After cooling, 1 ml reagent grade perchloric acid ($HClO_4$) is added and successively evaporated in two steps at 120 °C and 180°C respectively. To remove all residual organic matter, additional 2 ml 14 M HNO_3/0.01 M HF were added and subsequently evaporated. To achieve sample-spike equilibrium, a last digestion step is applied. The samples are taken up in 6 ml 6 M HCl/0.06 M HF and dried down after residing 6 h in acid.

Aliquots of sample material are prepared for trace element analyses. 20 % of the solution is transferred into 2 ml concentrated HNO_3, evaporated, and re-dissolved in 1 ml concentrated HNO_3. The solution is filled into 60 ml-PE wide neck bottles and diluted to 20 mg by adding MILLI-Q® (ultrapure water). The remaining 80 % of digested sample solution is used for chromatography and therefore evaporated and equilibrated in 5 ml 3N HCl.

2.6.2 ISOTOPE DILUTION

Mixing of the isotopic standard with the sample effectively dilutes the isotopic enrichment of the standard, the Isotope Dilution (ID). The dilution allows detecting the deviation of the standard ratio. Consequently this method is only applicable if at least two naturally occurring isotopes of the element of interest are available. If this is not the case a direct measurement is not possible. Mono-isotopic elements as Nb can be analysed either by using a radioactive spike, or in combination with another element (Zr/Nb). The concentration of the element of interest can be determined following the equation proposed by Stracke et al. (2014):

$$c_{Spl}\left[\frac{\mu g}{g}\right] = \left[\left(\frac{B}{A}\right)_{Spl+spike} - \left(\frac{B}{A}\right)_{spike}\right] \times \frac{wt._{spike}\ [g]\ c_{spike}\left[\frac{\mu g}{g}\right]\ ab(A_{spike})\ at.wt.(element_{Spl})}{wt._{Spl}\ [g]\ ab(B_{Spl})\ at.wt.(element_{spike})} \quad (5)$$

The ratio of $(B/A)_{Spl+spike}$ refers to the isotope ratio B/A of the sample diluted with the spike, which is directly measured. $(B/A)_{spike}$ accordingly refers to the known isotope ratio B/A of the spike. The initial weight of spike and sample in grams is abbreviated by $wt._{spike}$ and $wt._{Spl}$. The known elemental concentration (in ppm = µg/g) in the spike is referred to as c_{spike}. The known abundances of isotope A in the

spike and isotope B in the sample are abbreviated by ab(A_{spike}) and ab(B_{Spl}) respectively. The atomic weight of the element in spike and sample is abbreviated by at. wt. ($element_{spike}$) and at. wt. ($element_{Spl}$).

2.6.3 ION CHROMATOGRAPHY

Ion chromatography (IC) refers to the separation of ions from a mixture. To separate Lu, Zr, Hf, Nb, Rb, and Sr, three consecutive chromatography steps are performed with the sample solutions allowing to reduce interferences on atomic masses, and to assure a precise quantification.

2.6.3.1 HFSE and lutetium separation

A three stage ion exchange column chromatography as described by Münker et al. (2001) and Weyer et al. (2002) is applied to separate Lu, Hf, Zr-Nb, and Ta such as a matrix cut. Before charging the ion exchange columns, the digested sample is centrifuged and the column is cleaned and equilibrated. The stationary phase of the first and the third chromatographic step is filled with 1 ml EICHROM LN SPEC resin. This stationary phase with a 100 – 200 mesh corresponds to column I on Fig. 14. The second chromatographic step is performed with an anion resin illustrated by column II on Fig. 14. Column II is filled with 4 ml BIORAD-1-X8.

Four ml of the sample solutions are loaded to columns I, using each ~ 6 ml 3 M HCl. A matrix cut comprising the REE and alkaline (earth) elements is collected from the first 10 ml passing through the column for further separation steps (purple box in column I on Fig. 14). Subsequently 10 ml 6 M HCl is added to the columns I to elute Lu and 12 ml 2 M HF to elute the HFSE respectively. About 20 % of the obtained aliquot is directly used for Zr/Nb measurements (arrow *a* on Fig. 14). The remaining fraction of the aliquot is loaded to columns II (arrow *b* on Fig. 14) using

2 ml 2 M HF to wash in. The Ti-Zr-Hf fraction is subsequently eluted, using 12 ml 6 M HNO_3/0.2 M HF while Ta remains on the columns II. Repeated rinsing of the columns II with 6 M HNO_3/0.2 M HF allows complete separation of Hf and Ta. The clean Ta cut is collected using 10 ml 6 M HNO_3-0.2 M HF-1 wt.% H_2O_2 to elute.

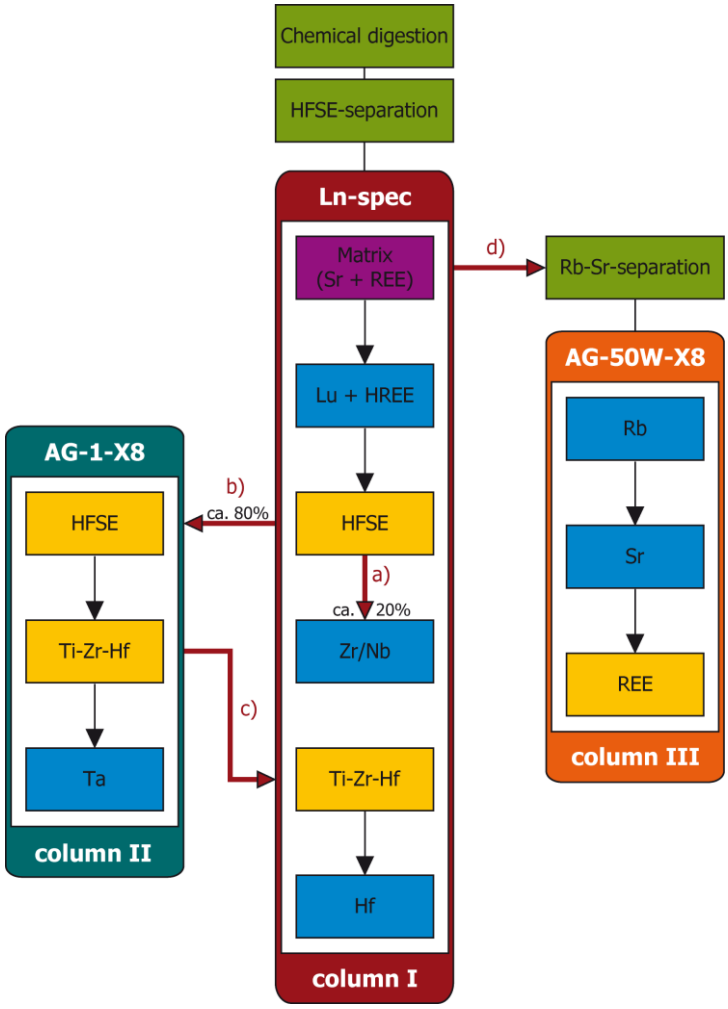

Figure 14: Diagram of performed separation steps modified after Marien (2015). Three different stationary phases (column I – III) are indicated in red petrol and orange. Blue boxes indicate the separated elements later analysed with ICP-MS whereas the yellow boxes display intermediate cuts. The purple box at the top of column I indicates the matrix cut which is used for further Rb, Sr and REE separation.

For Hf-separation, the Ti-Zr-Hf cut of columns II is evaporated, treated with 1 ml 6 N HNO_3-0.2 N HF-1 % H_2O_2 (to remove organics) and transferred into 3 M HCl and loaded on column I (arrow *c* on Fig. 14). The Ti-Zr-Hf cut is washed into the

columns using 10 ml 6 M HCl and 2+2 ml ultrapure H_2O. Titanium reacts to an orange peroxide complex by rinsing with 0.09 M HCit-0.45 M HNO_3- 1 % H_2O_2 it is washed from the column, such that after the elution of Zr using 10 ml 6M HCl/0.06 M HF a clean Hf cut is obtained in 12 ml 2 M HF.

2.6.3.2 Rubidium- strontium and REE separation

Rubidium, Sr, and the REE are separated from the matrix-cut that was obtained at the beginning of the HFSE separation procedure (arrow *d* on Fig. 14). The stationary phase is filled with 4 ml BIORAD AG-50W-X8 resin corresponding to a 200 - 400 mesh, illustrated as column III on Fig. 14. The matrix cuts are transferred into calibrated 2.5 M HCl. The columns are loaded with 1 ml of the sample solutions. To segregate the sample material down through the column the matrix cut is washed in using 15 – 17 ml 2.5 N HCl. Subsequently Rb and Sr are eluted with ongoing rinsing of 2.5 M HCl. The REE are washed out of the columns using calibrated 6 M HCl.

2.7 MULTI COLLECTOR INDUCTIVELY COUPLED PLASMA MASS SPECTROMETRY

The isotope composition- and isotope dilution concentration measurements of the different samples were performed using the THERMO-FINNIGAN TM NEPTUNE MC-ICP-MS at the Steinmann-Institute of Bonn University. Isotope composition and element concentration measurements were performed for Lu, Hf, Zr/Nb, Ta, Rb, and Sr. Isotope measurements for all elements were made in static mode using nine Faraday cups to obtain the highest precision on isotopic ratios. Isotope ratios were corrected for mass dependent fractionation by normalising measured values (Sr: $^{86}Sr/^{84}Sr = 0.1194$; Hf: $^{179}Hf/^{177}Hf = 0.7325$) and applying the exponential law. To monitor the quality of the isotope measurements, and to correct unknown

sample isotope ratios, standards with known isotopic composition were measured additionally to the sample material. The mass bias on MC-ICP-MS instruments is lower than 0.5 %/amu for heavy masses and not higher than 15 %/amu for light masses. Radiogenic $^{87}Sr/^{86}Sr$ and $^{176}Hf/^{177}Hf$ isotope ratios are corrected for an proposed age of ophiolite formation of 90 Ma according to U–Pb ages from zircon in plagiogranite (Mukasa and Ludden, 1987).

The relative 2σ external reproducibility for Hf is given as 40 ppm corresponding to ± 0.4 ε-units. External reproducibility for Sr is given as 50 ppm corresponding to 0.5 ε-units. The ε-units for Hf are calculated according the following equation and is analogue applicable $^{87}Sr/^{86}Sr$.

$$\varepsilon Hf = \left(\frac{\left(\frac{^{176}Hf}{^{177}Hf}\right)_{sample}}{\left(\frac{^{176}Hf}{^{177}Hf}\right)_{Chondrite}} - 1 \right) x\ 10^4 \qquad (6)$$

For measured concentrations of Zr, Lu, Hf, Rb and Sr the error is given as 2 σ = ± 1 % and for element ratios ± 0.2 % for Lu/Hf and for Zr/Hf ± 0.4 % respectively.

3 RESULTS

3.1 BULK COMPOSITION OF ANORTHOSITIC SAMPLES

Whole rock silica contents range from basic to intermediate (51 - 61 wt.% SiO_2) and compositions display a subalkaline character (3 – 6 wt.% Na_2O; 0 – 0.1 wt.% K_2O). However the bulk alkali and manganese content might be underestimated as they probably became vaporized during melting the rock powder. As inferred from whole rock glass analyses, the overall variability in composition is moderate and

does not reflect any systematic compositional changes among different anorthosite samples (Fig. 15). The moderate variability in bulk Al_2O_3, MgO, FeO* and CaO contents (disregarding sample ZY80E(2)) is attributed to differences in relative mineral proportions of anorthite and pyroxene. As a result of their high plagioclase content anorthosites display high concentrations in Al_2O_3 (23.6 – 31.4 wt.%) and CaO (11.5 – 18.1 wt.%). For comparison, fresh basalts of the UPL contain about 16 wt.% Al_2O_3 and 19 wt.% CaO as reported by Fonseca et al. (2017). In terms of their bulk TiO_2 (0.13 – 0.52 wt.%) anorthosites overlap with fresh basaltic compositions of the UPL ranging 0.25 to 0.89 wt.% (Fonseca et al., 2017).

Sample ZY80A(2) is an outlier regarding high silica concentrations. It contains about 60 wt.% SiO_2 compared to ~ 53 wt.% SiO_2 in the rest of the anorthosite samples. High silica content in sample ZY80A(2) coincides with an increased quartz content as identified by XRD (20 % Qz in ZY80A(2) relative to ~ 0.8 % Qz in the others). The high quartz content might be explained by a present quartz vein in this sample. Quartz does not belong to the primary anorthosite mineral assemblage and the quartz content is therefore overestimated. Another outlier in respect of Al_2O_3, CaO, FeO and MgO concentrations, as well concerning its mineralogical composition, is sample ZY80E(2). The relative proportion of diopside is significantly higher (^{CIPW}Di ~ 48 wt.%) compared to other anorthosite samples (^{CIPW}Di ~ 6.5 wt.%). In the hand specimen sample ZY80E(2) appears slightly darker due to higher diopside proportions, compared to the adjacent anorthositic composition (Fig. 6B).

Anorthite and other minerals of the primary assemblage, such as titanite, in this sample are indistinguishable from those in the other samples. The transition

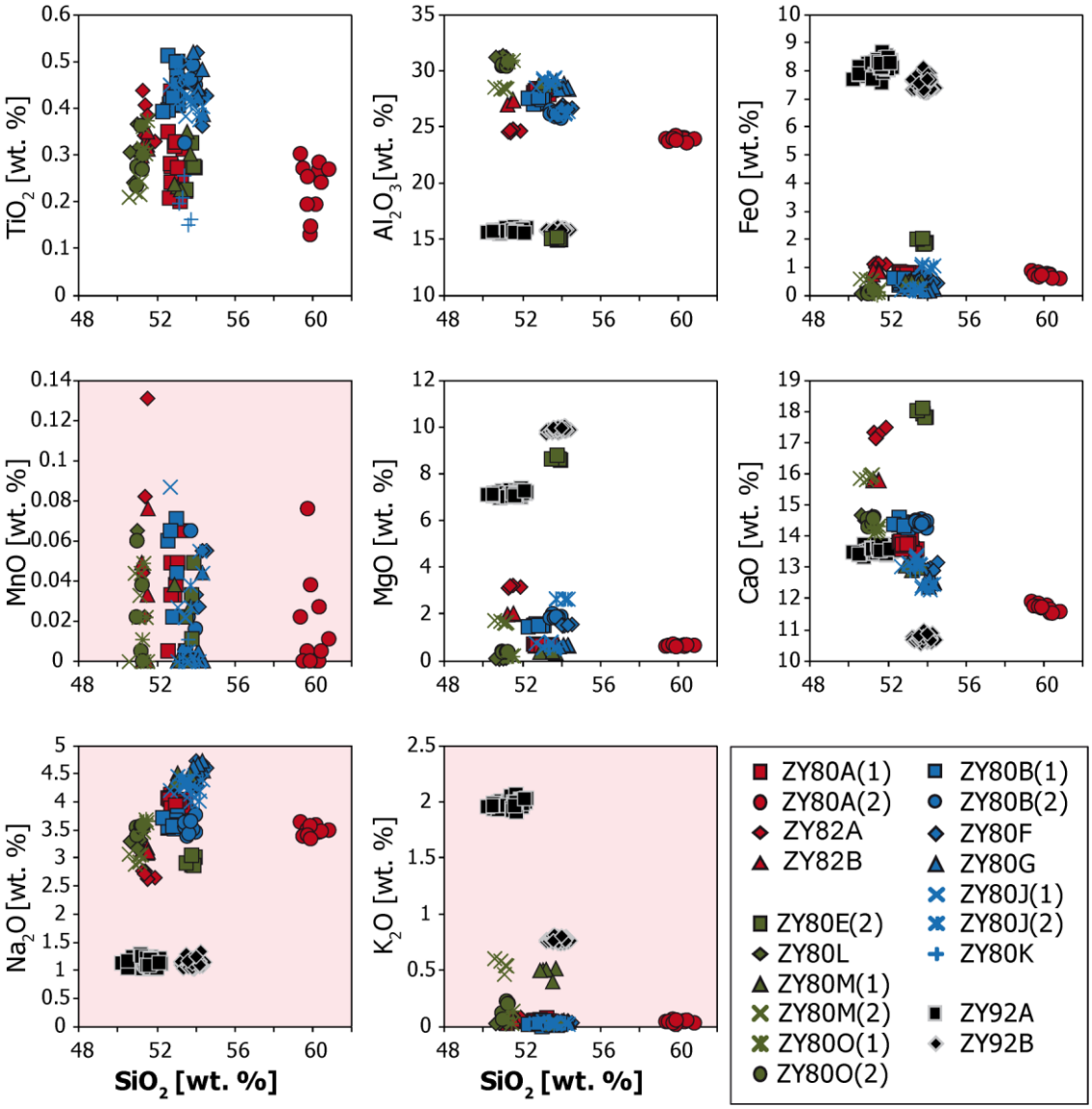

Figure 15: Harker diagrams displaying the bulk composition of all anorthosite samples as well as the spheroidal late stage precipitate (black symbols). Chemical compositions are analysed on glasses fused from whole rock sample powder by EPMA. Data of MnO, Na_2O and K_2O (pale red background) might be underestimated due to a loss during the melting event. Colour coding refers to different groups (red=I, green=II and blue=III) of anorthosite samples distinguished based on trace element composition.

towards the diopside enriched area appears to be gradually with the relative proportions of anorthite and diopside progressively changing.

Estimation of modal mineral abundances from visual impressions as well as from XRD data (Fig. 16 and Fig. 17) reveals plagioclase as major mineral constituent. According to QAPF-classification of plutonic rocks the investigated samples might be classified as anorthosites. As reported by IUGS anorthosites are intrusive

plutonic rocks composed of calcic plagioclase with less than 10 % ferro-magnesian minerals and less than 5 % quartz.

Data of EPMA analyses of bulk compositions measured on glasses such as XRF and XRD results are listed in table I of the appendix.

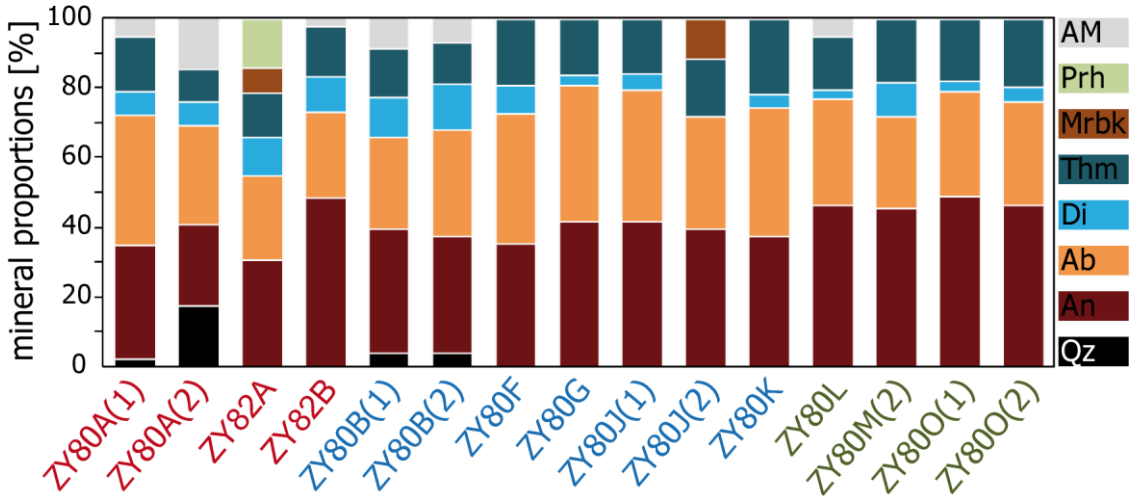

Figure 16: Histogram showing the relative abundances of mineral phases in anorthosite samples based on XRD data.

The trace element composition of anorthosite samples is determined by Q-ICP-MS. As for bulk major element composition, the bulk trace element chemistry is analysed from glass samples fused from whole rock powder. Concentrations of moderately volatile and volatile elements determined in glasses should be treated with caution as they might be vaporised during melting. The high field strength elements (HFSE) and the heavy REY (HREY) exceed the bulk silicate earth (BSE) value defined by Palme et al. (2014) (Fig. 18).

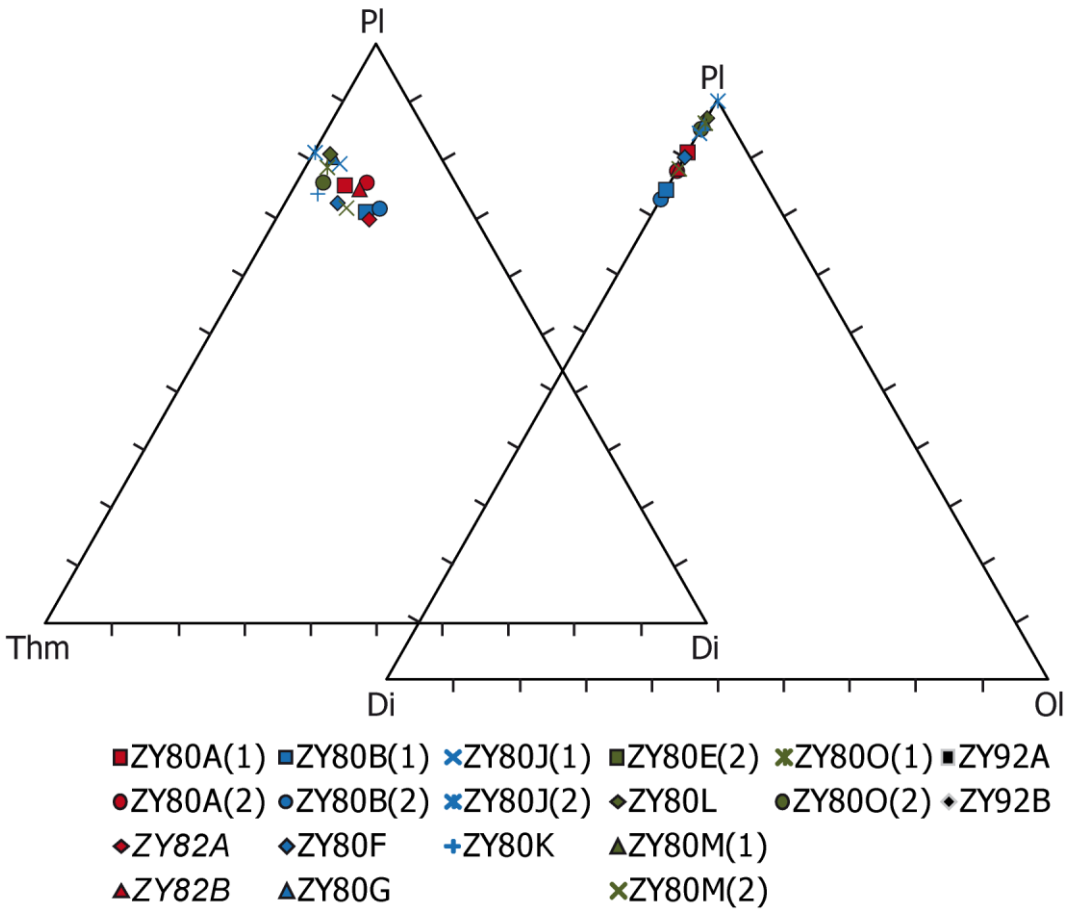

Figure 17: Ternary plot of relative mineral proportions based on XRD-data. Colour coding refers to groups (I=red, II=green and III=blue) defined by trace element chemistry.

All samples display W enrichment of two to four orders in magnitude relative the BSE value, and furthermore enrichment (one – two orders in magnitude) in Th, U, Nb and Ta. Lead content is highly variable and Zr and Hf display slight enrichment whereas Ti is fixed at the BSE value. Concerning the LILE only Sr is relatively enriched (one order of magnitude), Ba, Rb and Cs are slightly below BSE values. Concentrations of Rb and Cs might be underestimated in the glass (Fig. 18A).

The overall BSE normalised REY patterns are rather flat, displaying a negative Eu-anomaly. The LREE of group I are slightly depleted compared to BSE. Scattering of the REY concentrations of all the different anorthosite samples is not evenly distributed but rather reveals three populations of concentrations (Fig. 18B).

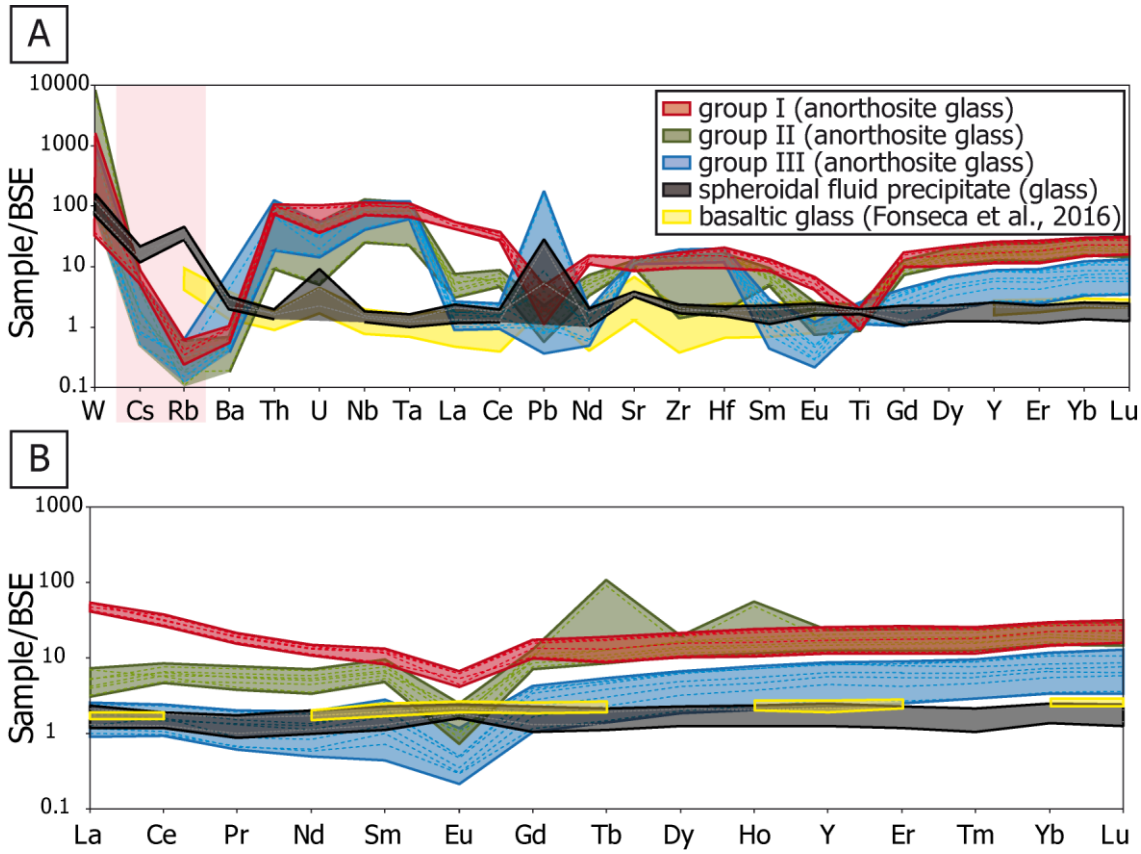

Figure 18: (A) Spider diagram displaying Q-IAP-MS data of WR glasses of different anorthosite samples and the spheroidal precipitate. The concentrations of Cs and Rb might be underestimated in the glass. (B) Corresponding REY pattern. Data is plotted relative to bulk silicate earth (BSE) values (Palme et al., 2014). Dotted lines represent averaged compositions of 10 – 30 Q-ICP-MS analyses of each investigated glass (three in group I: ZY80A(1/2) and ZY82A; six in group II: ZY80E(2), ZY80L, ZY80M(1/2) and ZY80O(1/2) and seven in group III: ZY80B(1/2), ZY80F, ZY80G, ZY80J(1/2) and ZY80K). Transparent coloured areas refer to the result pane whereas solid lines represent minimum and maximum values of each series of measurements. The yellow area refers to analyses of fresh basaltic UPL glass from Troodos, Cyprus (Fonseca et al., 2017).

Indications of major differences in REY distribution, responsible for the subdivision in three groups are listed in Table 1.

Group I includes both, the allochthonous anorthosite samples and dyke rocks. Group II comprises six anorthosite dyke samples. The HREY of group II overlap with group I, whereas LREE have distinctively lower concentrations. One sample of group II, ZY80O(1) namely, is enriched in Tb and Ho. Concentrations of Tb and Ho are consistent throughout the ten analyses of the glass and thus represent a true

signal. Sample ZY00(1) is cut from the same hand specimen as sample ZY80O(2), whereas the latter appeared slightly darker. Neither mineralogical- nor differences in major element composition were detected for ZY80O(1) compared to the rest of group II. Group III comprises seven samples.

Table 1: Major differences in bulk REY among different groups of anorthosite compositions

Whole rock	**Group I**	**Group II**	**Group III**
Samples	ZY80A(1), ZY80A(2), ZY82A and ZY82B	ZY80M(1), ZY80M(2), ZY80O(1), ZY80O(2) ZY80E(2), and ZY80L	ZY80B(1), ZY80B(2), ZY80F, ZY80G, ZY80K, ZY80J(1) and ZY80J(2),
Eu/Eu*	0.45	0.19	0.23
Lu/Dy	1.4	1.4	1.6
Sm/La	0.2	1.2	1.0
Pattern shape	V-shape	Stepwise pattern	valley for Pr and Nd
Note	Max REY	LREE<HREY	Min REY

3.2 MINERAL CHEMISTRY OF ANORTHOSITES

The major element composition of mineral phases in the different anorthosite samples is investigated with EPMA (Table II – V in the appendix). Trace element composition of mineral phases is investigated with Q-ICP-MS respectively (included in Table III and V in the appendix).

Magmatic plagioclase displays no chemical zonation and is rich in the calcic component (X_{An} = 0.76 - 1) approaching anorthite composition (Fig. 19A).

Anorthite is replaced by sodium rich plagioclase, predominantly oligoclase along grain boundaries and fissures. Both, calcic and sodium rich plagioclase compositions are similar throughout all samples (Fig. 19A and Fig. 20A).

Trace element concentrations in albite and anorthite of the different anorthosite samples are well below the detection limit of the method used and thus data is not reported.

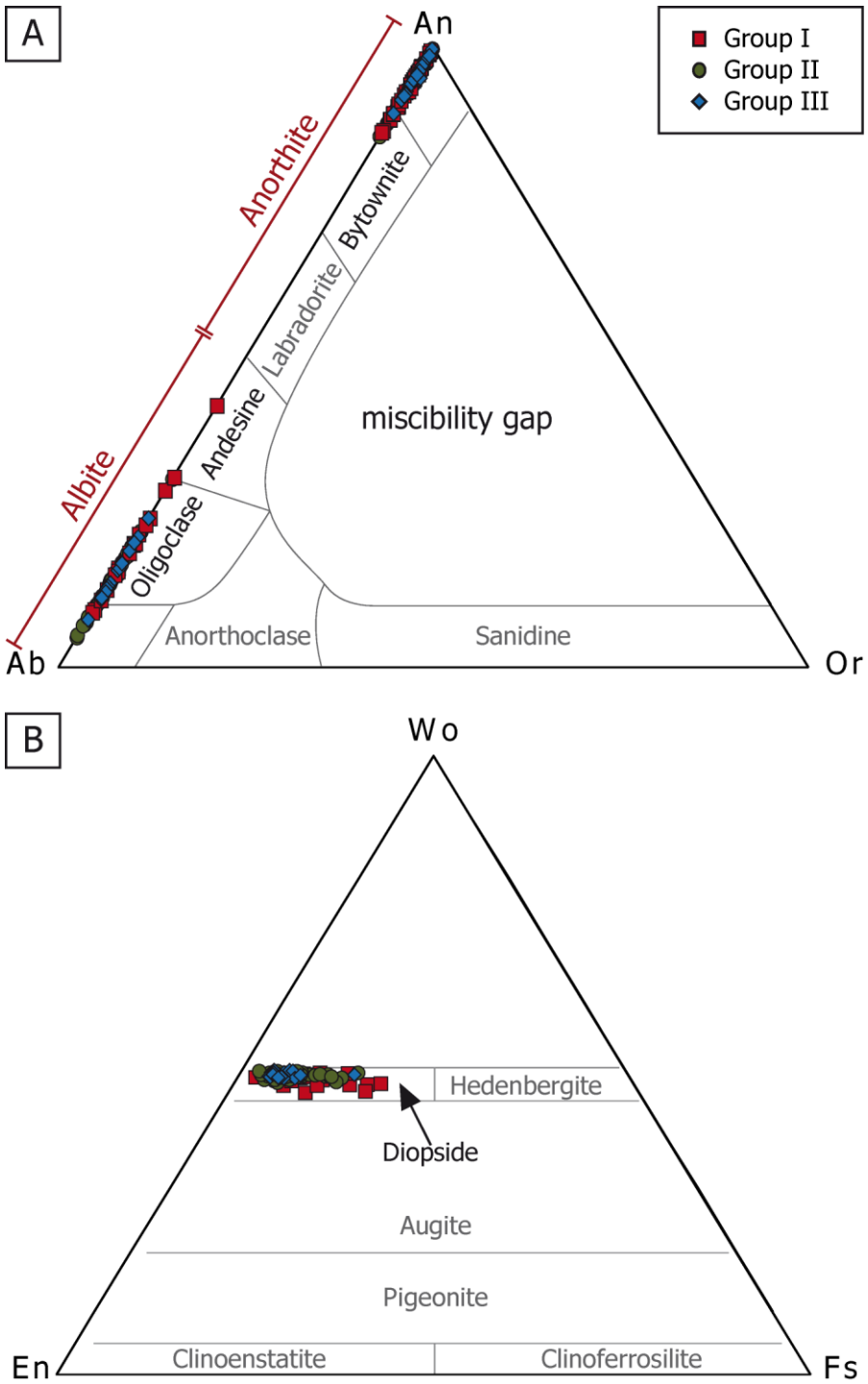

Figure 19: (A) Compositional plot of unordered monoclinic feldspar in anorthosite samples (after Schreyer, 1976). All analyses reveal plagioclase compositions as the orthoclase component equals zero. Two end member groups, of albite and anorthite compositions can be distinguished. (B) Compositional plot of pyroxene (after Morimoto, 1988) in anorthosite samples. The CaTs component is subtracted from wollastonite. All analyses reveal diopside compositions. An increased hedenbergite component (up to $X_{Hed} = 0.35$) was observed for some analyses. Colour coding is based on trace element chemistry indicating the three different groups (group I = red, group II = green and group III = blue).

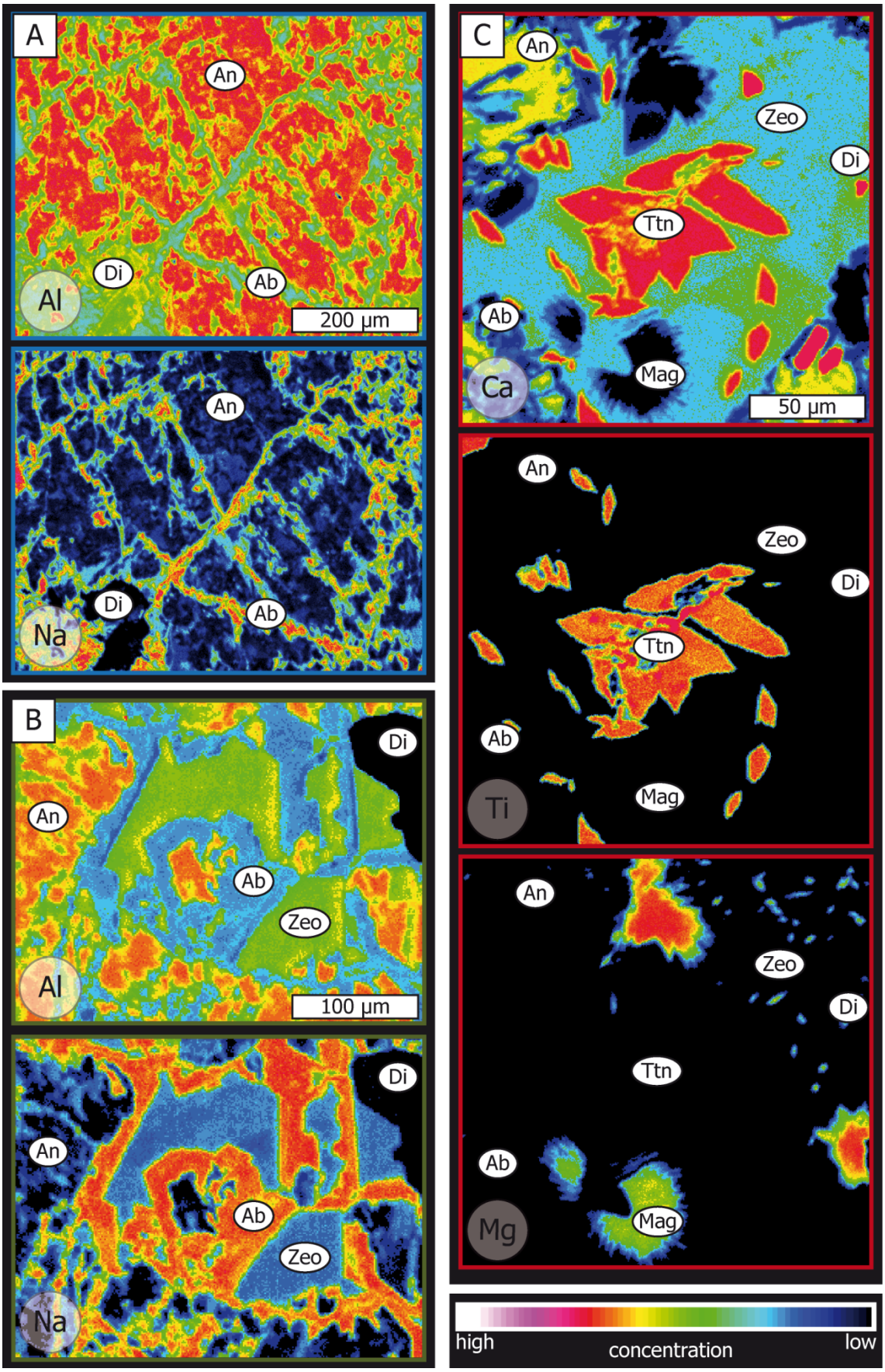

Figure 20: Element maps of mineral assemblages within anorthosite samples. (A) Texture displaying albitisation of homogeneous anorthite along grain boundaries and fissures. (B) Interstitial thomsonite (Zeo) with titanite and diopside inclusions and magnetite quench textures. (C) Albitisation of anorthite and interstitial thomsonite. Frame colour corresponds to group (red=I, green =II and blue=III).

Primary magmatic pyroxene is rich in the calcic component and is considered as diopside (Fig. 19B). Diopside is chemically zoned regarding the REY (Fig. 7B). Diopside is mostly patchily zoned and displays in some grains concentrically zonation towards the crystal boundaries. No systematic behaviour in zonation or correlation of Fe and Mg content in diopside and the REY is detected. Trace element data is illustrated as spider diagrams and REY diagrams in Fig. 21A and Fig. 21B respectively. Diopside is moderately enriched in HFSE not displaying significant differences among the different anorthosite groups. Regarding the REY diopside increasingly incorporates HREY reflected in a positive slope (Sm/La ~ 2.6 and Lu/Dy ~ 2.8). Moreover all samples display a moderate negative Eu-anomaly (Eu/Eu* ~ 0.1).

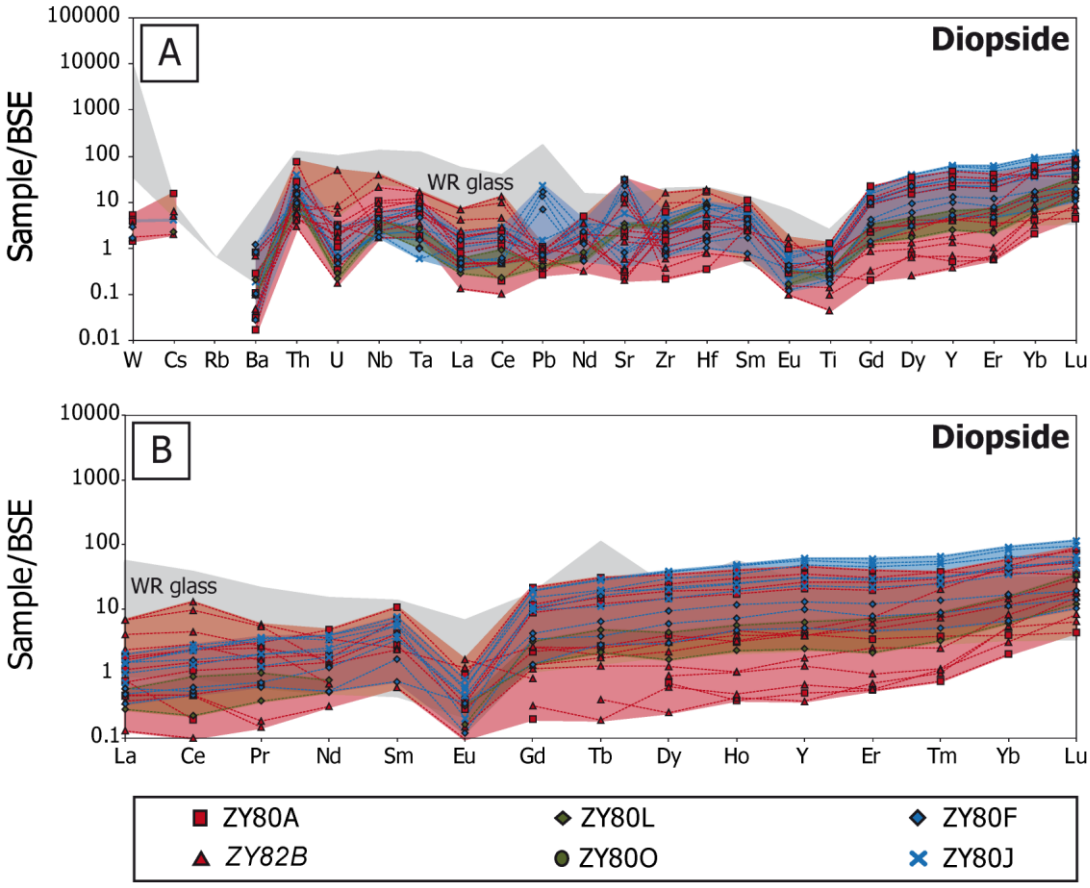

Figure 21: (A) Spider diagram and (B) REY diagram displaying Q-IAP-MS data of individual diopside crystals in different anorthosite samples. Data is plotted relative to bulk silicate earth values (Palme et al., 2014). Each line corresponds to one laser spot in different grains. Grey shaded area highlights WR glass composition of anorthosite samples (total range of group I-III).

Thomsonite, a mineral of the zeolite group, appears in all anorthosite samples as extensive interstitial phase or as vein filling (Fig. 8). The thomsonite composition is variable in terms of occupancy of tetrahedral sites, whereas silica predominates (~21 a.p.f.u.) over Al (19 a.p.f.u.). The cations sites occupied by Ca are negatively correlated with silica of T-sites (Fig. 22A) whereas no correlation is observed with tetrahedral alumina, nor between sodium and silica (Fig. 22B).

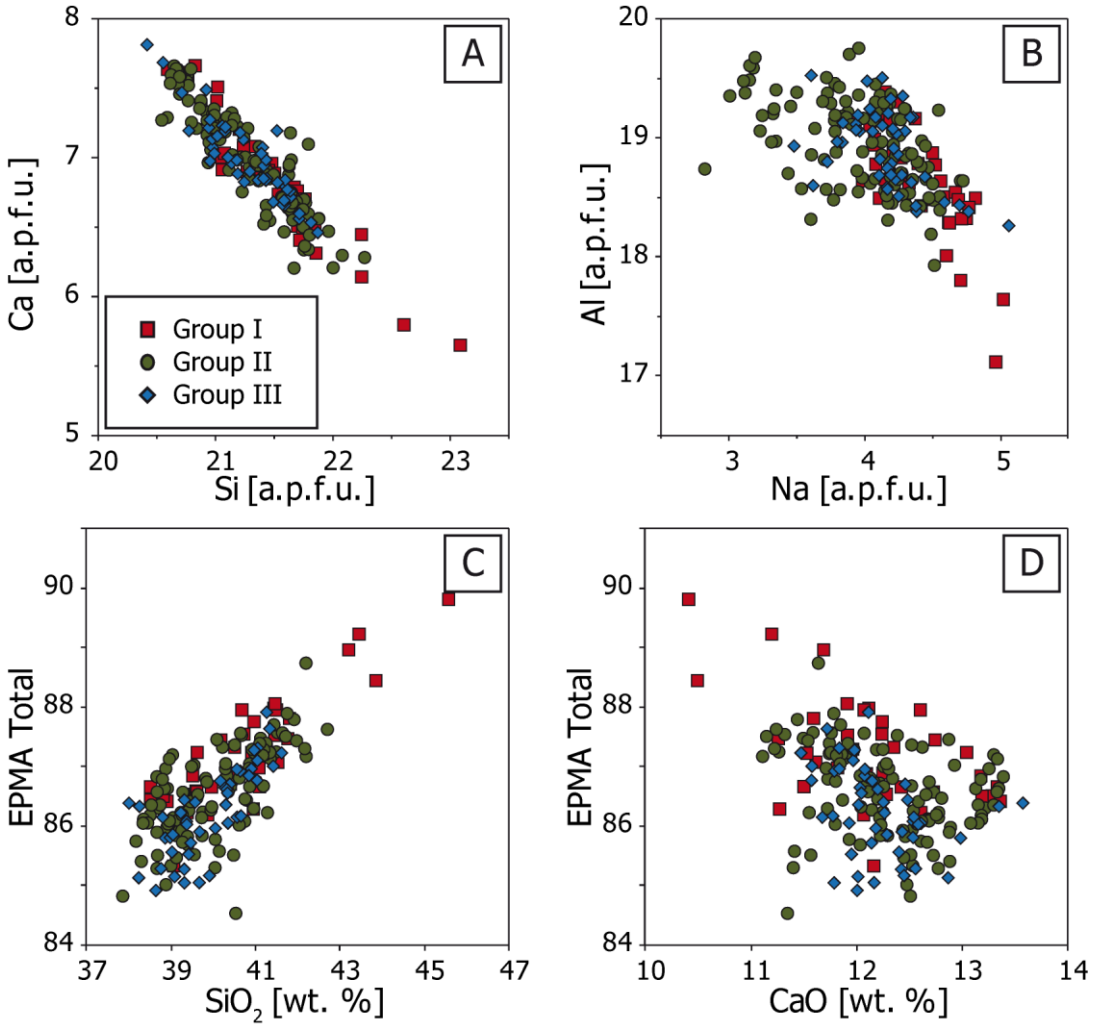

Figure 22: Variability in thomsonite composition. (A) Correlation of sites in thomsonite occupied by Ca and Si. (B) Binary plot of Na and Al sites in thomsonite. (C) Correlation of silica and the EPMA total. (D) Binary plot of CaO and the EPMA total.

Furthermore the silicon content is positively correlated with the total of oxides detected by EPMA (Fig. 22C), but no correlation of the total with oxides of Al, Ca and Na. The lack to the EPMA total is attributed to the molecular H_2O incorporated into the thomsonite mineral structure.

Compositional inhomogeneity of thomsonite in terms of Ca is displayed in element map in Fig. 20C revealing enhanced Ca concentrations in areas around titanite inclusions. Trace element composition of thomsonite is investigated with Q-ICP-MS, but due to ablation problems (high H_2O content) and concentrations close to the detection limit, no reliable data is acquired and data are not listed. Very low concentrations of HFSE and LILE can be assumed for thomsonite.

From mere interpretation of textural relationships, thomsonite might be interpreted as a pseudomorph replacement product of glass. Prior to solidification the liquid coexisted with anorthite, diopside and the accessory minerals of the primary magmatic assemblage such as titanite (Fig. 20). As a consequence, diopside and titanite inclusions would rather represent phenocrysts being trapped in the former glass. However, Raman spectroscopy reveals the crystallized nature of thomsonite (Fig. 23).

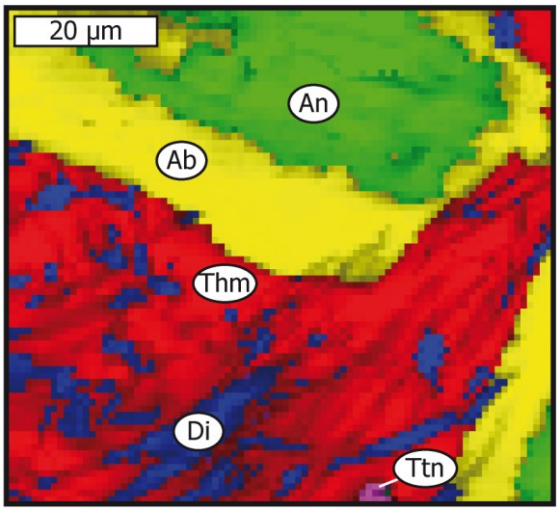

Figure 23: False colour Raman image displaying the phase distribution in sample ZY80A (group I). The map illustrates the albite rim (yellow) around anorthite (green) in a thomsonite matrix (red). Within thomsonite, inclusions of diopside (blue) and titanite (purple) appear.

Titanite is the most common accessory phase in all anorthosite samples and interpretation of textures reveals a long crystallisation sequence. The TiO_2 content of titanite and rutile, and the ZrO_2 content in zircon, is positively correlated with EPMA totals (Fig. 24A/B/C). The deficit in EPMA total is attributed to trace elements as Nb, Ta, Th, U and the REY being incorporated in the mineral structure of titanite, rutile and zircon not being considered in EPMA measurements. Except for iron in titanite, compositions of Ti and Zr phases are rather invariant in major element composition. Fe rich compositions are restricted to patchily zoned titanite crystals of anorthosite samples of the red group additionally characterized by low EPMA totals (Fig. 24D and E).

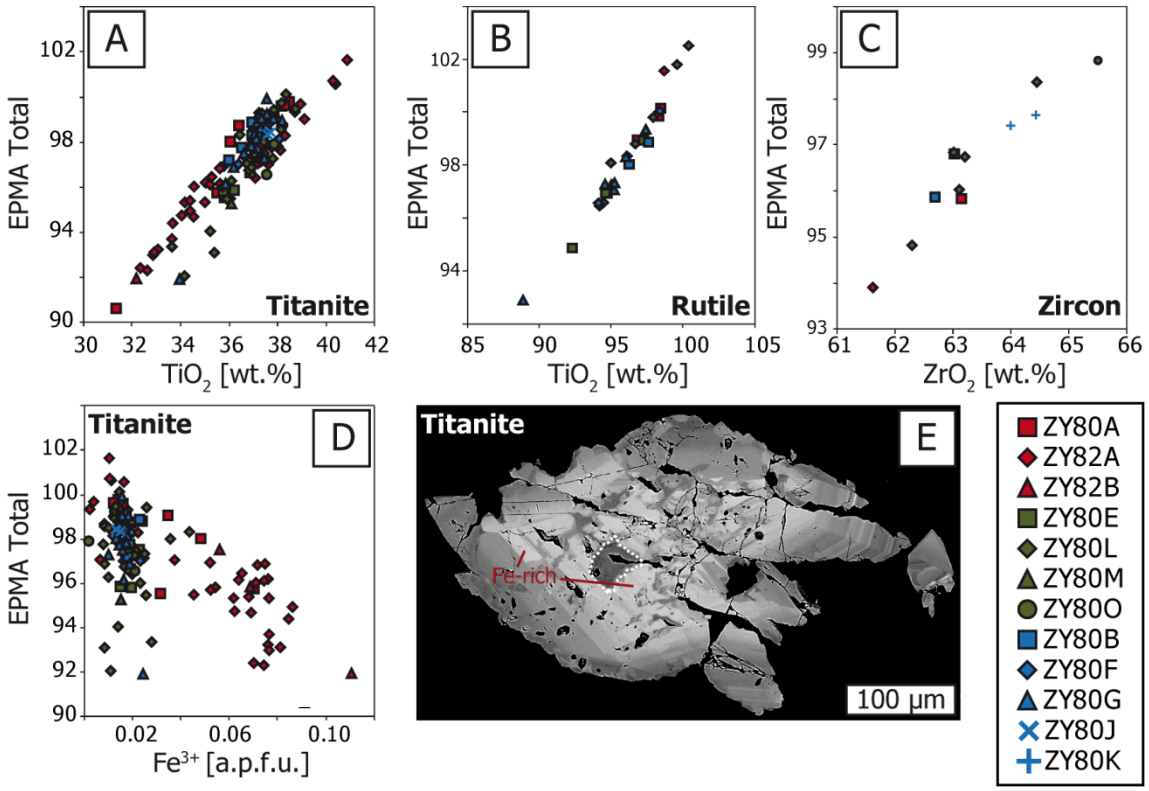

Figure 24: (A/B/C) Positive correlation of EPMA total with TiO_2 in titanite and rutile and with ZrO_2 in zircon respectively. The deficit to a total of 100 is attributed to oxides not being analysed by EPMA. (D) Iron in the titanite mineral structure (calculated based on 5 oxygen and thus 3 cations for $CaTiSiO_5$) versus EPMA total. Majority of data (entire group II and III) plots at low Fe^{3+} values ~0.02 a.p.f.u. only some compositions of the allochthonous sample displays higher contents of Fe^{3+} in the titanite structure and lower EPMA totals. (E) BSE image of titanite crystal in one of the allochthonous sample ZY82A with variable Fe content. The dark area in the center (highlighted by the dotted line) corresponds to low Fe values and high EPMA totals.

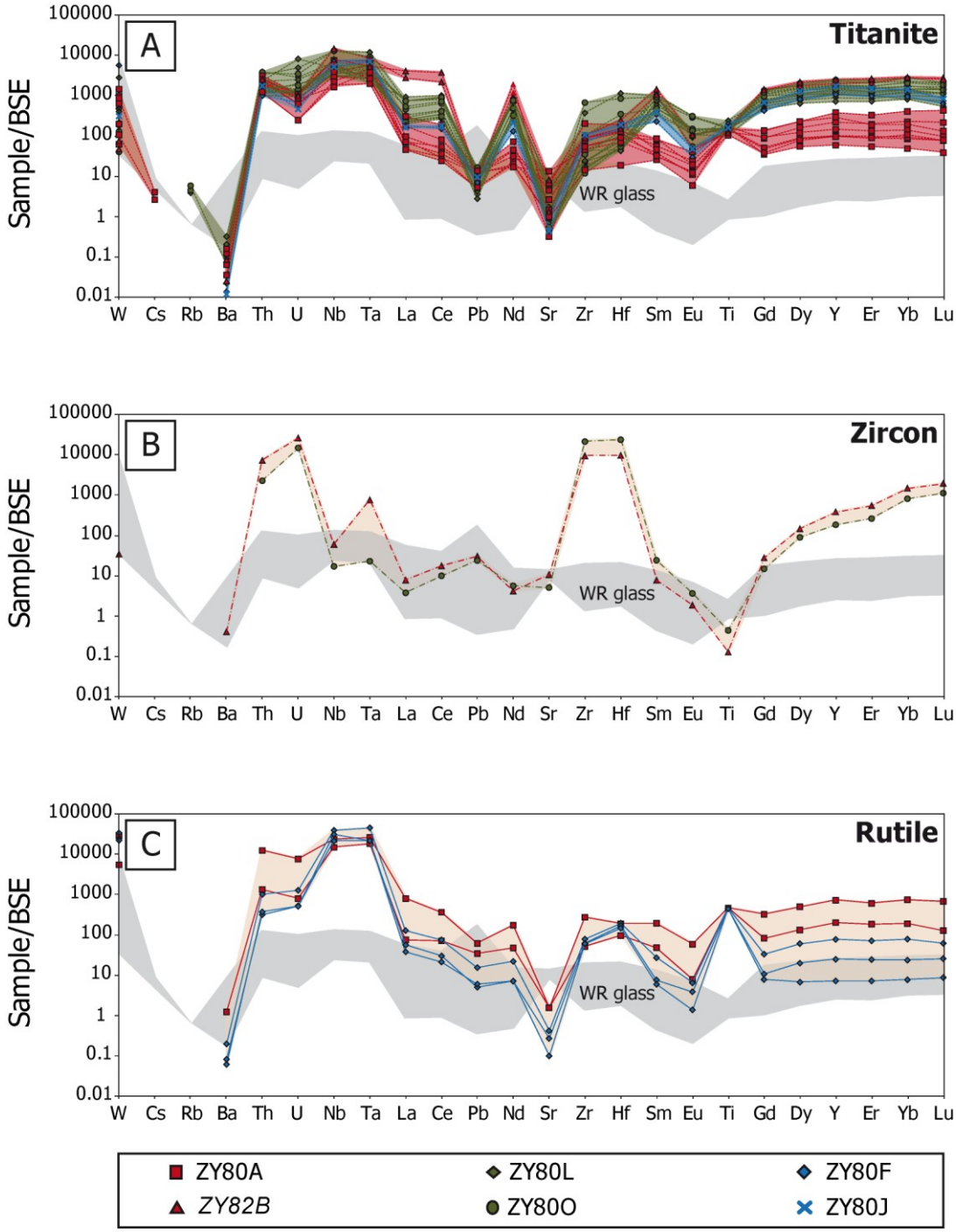

Figure 25: Spider diagram displaying Q-ICP-MS data of individual titanite, zircon and rutile crystals in different anorthosite samples. The elements are ordered according increasing compatibility towards the right. Data is plotted relative to bulk silicate earth values (Palme et al., 2014). Each line corresponds to one laser spot in different grains. The grey shaded area highlights WR glass composition of anorthosite samples (total range in groups I-III). Differences in trace element composition of titanite vary systematically in different groups. Red, green and blue shaded areas highlight their composition range. Transparent beige coloured areas refer to the result pane of different zircon and rutile compositions.

Titanium concentrations in titanite measured with EPMA (TiO_2~36.7 wt.%) and Q-ICP-MS (TiO_2~39.3 wt.%) are in good agreement.

Q-ICP-MS data confirms that areas in titanite, rutile and zircon displaying low EPMA totals, correspond to compositoins being enriched in elements such as the REY. The concentration of the sum of W, Th, U, Nb, Ta and REY detected by Q-ICP-MS converted to the weight fraction of oxides exceeds 8 wt.% in some areas of titanite. In fact HFSE concentrations other than Ti in titanite are very high, they are enriched two to four orders in magnitude relative to BSE values (Fig. 25A).

Similarly as shown for the whole rock glass compositions significant differences are visible for REY concentrations in the acessory phases (Fig. 26). Similarly as for bulk compositions, the REY patterns of titanite are indicative for the three different groups (Fig. 26A). The shape of REY patterns of titanite crystals in different samples within group III (ZY80F/J), group II (ZY80L/O) and group I (ZY82B) are consistent apart from minor variations in REY concentrations. HREY of group II and III overlap but LREE are less enriched in group III compared to group II and show a positive slope. Titanite in sample ZY82A displays highest LREY values with a moderate negative slope and HREY overlap with maximal values of group II. Furthermore ZY82A differs in a profound negative Eu-anomaly. Titanite from sample ZY80A displays overall the lowest REY contents and a minor pronounced negative Eu-anomaly, LREE are U-shaped with the depression at Pr and Nd. The HREY are parallel shifted to lower values compared to group II and III.

Table 2: Major characteristics of REY pattern of titanite from different groups

Titanite	**Group I**		**Group II**	**Group III**
Samples	ZY80A	ZY82B	ZY80L and ZY80O	ZY80F and ZY80J
Eu/Eu*	0.3	0.1	0.2	0.1
Lu/Dy	1.1	1.4	1.2	0.7
Sm/La	0.4	0.4	1.5	1.8

Only two zircons were large enough to be investigated with Q-ICP-MS, one in sample ZY82B (group I) and one in ZY80O (group II). Both are strongly enriched in Th, U and Hf (Th = 2289 – 7284 ppm, U = 14872 – 26302 ppm and Hf = 9672 – 23856 ppm) and are increasingly enriched HREY (Lu/Dy ~ 13), compared to BSE values (Fig. 26B).

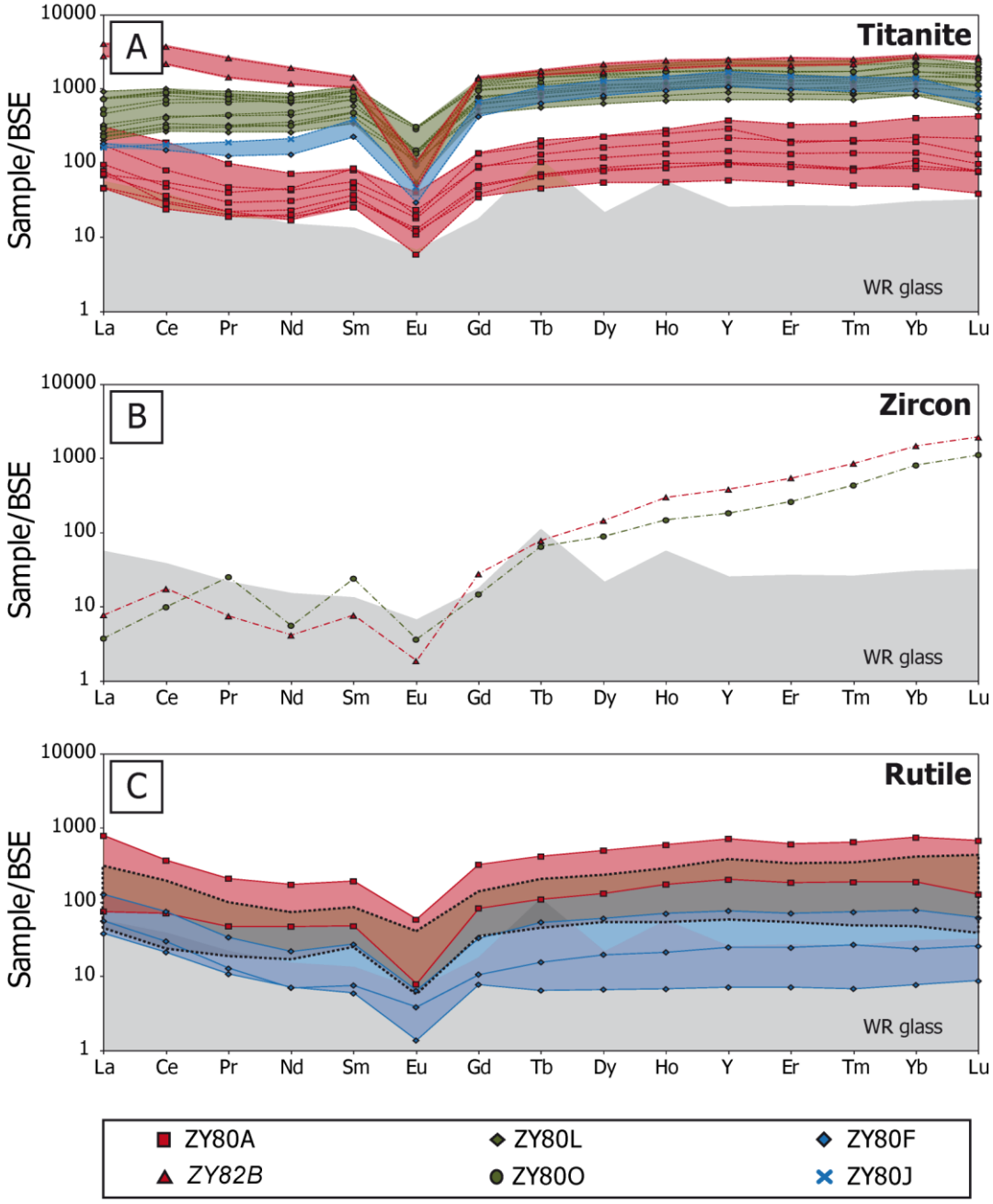

Figure 26: REY diagram displaying Q-ICP-MS data of individual titanite, zircon and rutile crystals in different anorthosite samples. Data is plotted relative to bulk silicate earth values (Palme et al., 2014). Each line corresponds to one laser spot in different grains. The grey shaded area highlights bulk glass composition of anorthosite samples (total range in group I-III).

Rutile grains were investigated for trace element composition in ZY80A (group I) and ZY80F (group III). Rutile is strongly enriched in W (66 - 410 ppm) and in other HFSE especially Nb (8880 - 23458 ppm) and Ta (791 – 1965 ppm) compared to BSE. REY pattern of rutile displays great similarities with titanite of sample ZY80A (Fig. 26C). LREE display a negative slope (Sm/La = 0.3 in group I and 0.2 in group III). The negative Eu-anomaly ranges from Eu/Eu* = 0.2 in ZY80 (group I) to 0.3 in ZY80F (group III).

3.3 HIGH PRECISION WET CHEMISTRY RESULTS OF ANORTHOSITES

Bulk concentrations of HFSE (Zr, Lu, Hf) and the LILE group (Rb, Sr) were analysed in solutions prepared from 11 different anorthositic samples. The determined HFSE concentrations are very high and display systematic variations among the different groups. The zirconium concentrations range from 152 to 218 ppm, Lu varies between 0.3 and 2.1 ppm and Hf from 5.2 to 7.3 ppm. Regarding the LILE, wet chemistry reveals concentrations of Sr between 222 and 282 ppm and for Rb variations between 0.14 and 2.7 ppm. Results of high precision HFSE and LILE investigation are listed in Table VI in the appendix.

Bulk concentrations of HFSE and LILE measured in solutions are not consistent with glass ICP-MS data (Fig. 27). Concerning the HFSE, if determined in solution, obtained concentrations are 10 – 25 % higher compared to glass ICP-MS data and HFSE in sample ZY82A are even 80 % increased compared to glass analyses. Concentrations for sample ZY82A were double checked. Strontium determined in solution is slightly (10 %) underestimated compared with glass data except for sample ZY82A. Results of wet chemistry Rb measurements do not reproduce values of EPMA glass data. The deviation to glass ICP-MS data is considered to be the result of differences in sample treatment. The digestion of accessory phases

hosting most of the HFSE and REY is more efficient in solution. Melting of rock powder probably does not allow complete digestion of accessories. As a result HFSE and REY are systematically underestimated if detected from glasses. Contrastingly Sr, commonly replacing Ca, appears to be overestimated in glasses. The Rb concentration determined in glasses is probably underestimated due to a loss during melting. The deviation in data of sample ZY82A might be additionally attributed to sampling effect. Rock powder of ZY82A digested for wet chemical investigation probably contained more accessory phases.

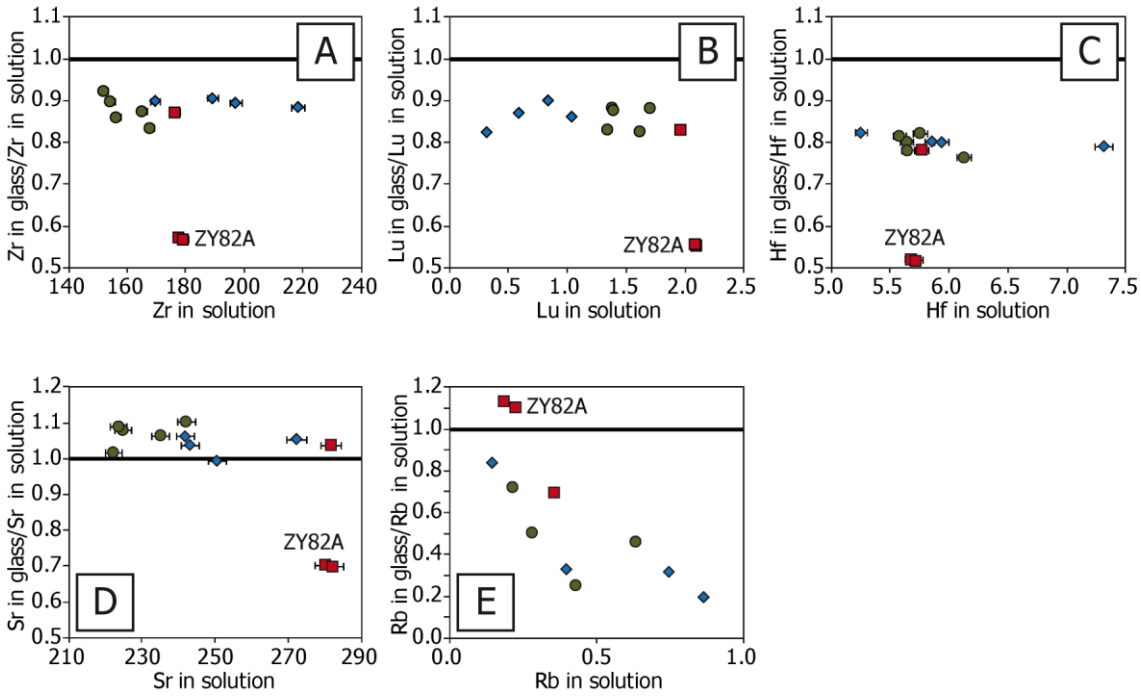

Figure 27: High precision wet chemistry data of Zr, Lu, Hf, Sr and Rb given in ppm of eleven different anorthositic samples. To display the deviation to glass ICP-MS data, wet chemistry data is plotted relative to ICP-MS values normalised to wet chemistry data. Error bars indicate the 2 σ error of 1 %.

Isotope ratios of $^{176}Lu/^{177}Hf$, $^{176}Hf/^{177}Hf$, $^{87}Rb/^{86}Sr$ and $^{87}Sr/^{86}Sr$ in anorthosite samples were investigated in solutions. Data are listed in Table VI in the appendix.

The Sr isotopic composition appears to be moderately variable. $^{87}Rb/^{86}Sr$ ranges from 0.0017 to 0.0326, $^{87}Sr/^{86}Sr$ from 0.7062 to 0.7069. Age corrected ratios of

$^{87}Sr/^{86}Sr$ do not display any systematic variation among different samples and are restricted to a narrow range between 0.7062 and 0.7068. Hf isotopic composition is more variable revealing differences among the different anorthosite groups. The $^{176}Lu/^{177}Hf$ ratio displays a large range from 0.0075 to 0.0524, whereas $^{176}Hf/^{177}Hf$ is restricted from 0.2830 to 0.2831. Age corrected Hf data varies from εHf_{90Ma} = 9.13 to 10.74.

3.4 BULK COMPOSITION OF SPHEROIDAL FLUID PRECIPITATE

Major element EPMA data as well as XRD data such as trace element composition is listed in table VII in the appendix. Compositional data of sample ZY92, the spheroidal fluid precipitate, is plotted together with anorthosite samples. Figurative description of its chemical composition is included in the Harker diagram (Fig. 15) and BSE normalised spider and REY diagrams (Fig. 18) shown for anorthosites.

To determine the bulk composition of this sample, two glasses namely ZY92A & B were fused at 1600 °C as described in chapter 2.3 section II. The interpretation of concentrations of moderately volatile and volatile elements measured in these glasses has to be considered with caution, as being probably underestimated. The silica content ranges from 50.2 to 54.2 wt.%. The alkali content, probably being underestimated ranges from 1.03 to 1.34 wt.% concerning sodium and 0.74 to 2.07 wt.% for potassium. The bulk composition of the glass fused from late stage fluid precipitate might be classified as basic to intermediate subalkaline rocks (basalt – basaltic andesite). Iron and Mg content in the precipitate is much higher than in anorthosite sample ranging 7.22 to 8.68 wt.% FeO and 6.97 to 10.05 wt.% MgO. Iron might be underestimated due to a loss to the Pt crucible during melting.

Trace element composition of the spheroidal fluid precipitate is comparable with BSE except for W, Cs, Rb, U and Pb which are enriched (Fig. 18A), compared to anorthosites Rb has significantly higher concentrations (Rb = 17 – 27 ppm). However, the Rb and Cs concentrations determined in the glass might be underestimated. The REY concentrations of sample ZY92 coincide with BSE values and no negative Eu-anomaly, as for the anorthosite samples is visible (Fig. 18B).

Major mineral constituents of the late stage fluid precipitate determined based on the CIPW norm calculated from glass compositions are anorthite (~ 34 %) and diopside (~ 22 %), which is confirmed by XRD data (Fig. 28).

Phases identified by XRD are diopside, sodium rich disordered anorthite, Ca-Al-silicon-oxide-hydroxides represented by montmorillonite, calcite, microcline and hornblende (Fig. 28). The term "sodian disordered anorthite" refers to the determined XRD reference of the BRUKER AXS software package #00-041-1481. Olivine, hypersthene, albite and quartz given by the CIPW norm are not considered as phases in this sample.

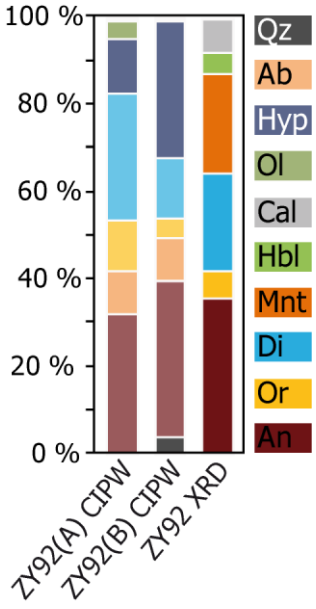

Figure 28: Histogram displaying relative mineral proportions in the spheroidal fluid precipitate. CIPW normative proportions (transparent bars) are based on EPMA analyses of WR glasses ZY92A & B. XRD data reveals similar mineral proportions.

3.5 MINERALOGY OF SPHEROIDAL FLUID PRECIPITATE

Mineralogical description of this sample is not straight forward as most phases display different stages of conversion and hydration reactions. Pyroxene displays grain sizes of about 100 µm and occurs as anhedral grains or as hexagonal crystals. Pyroxene is heterogeneous in its composition (Fig. 29) generally having Mg rich cores and Al and Fe enriched rims (Fig. 13 and Fig. 30A/B). Mineral compositions are listed in table III in the appendix.

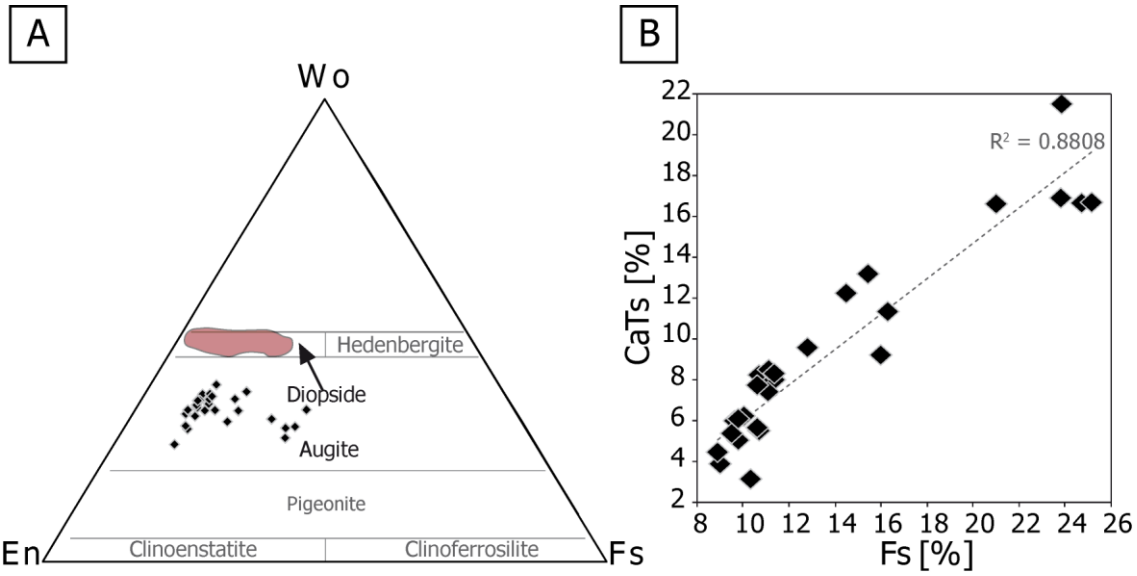

Figure 29: (A) Compositional plot of pyroxene (after Morimoto, 1988) displaying pyroxene composition in the spheroidal late stage sample ZY92, for comparison the red shaded area indicates the compositional range of diopside in anorthosites. The CaTs component is subtracted from wollastonite. (B) Pyroxene composition in the spheroidal late stage fluid precipitate displaying the Ca-Tschermak's component relative to ferrosilite component in pyroxene. The coefficient of determination R equals 0.88 for the linear relationship between increasing CaTs and increasing ferrosilite component.

Anorthite occurs as acicular quench crystals in the matrix. The existence of anorthite crystallised material (35.5 %) is supported by XRD data (Fig. 31) and further proofed by Raman spectra. The inner part of a spheroid preserve anorthite as radially arranged needles, reminiscent of spinifex textures, whereas anorthite needles are absent in the outer area (Fig. 30B)

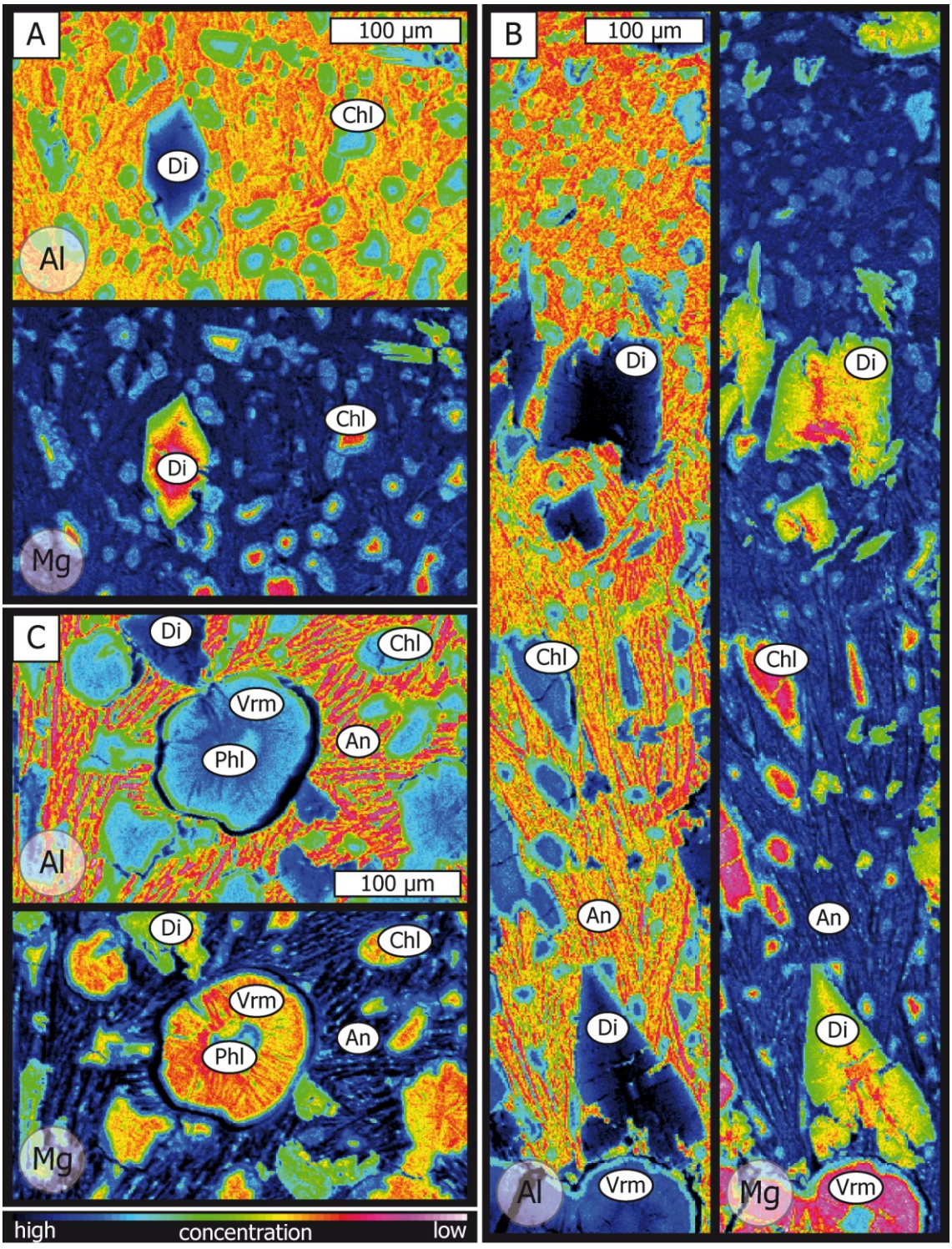

Figure 30: Element maps of different textures within the late stage fluid precipitate ZY92. Warm colours correspond to higher concentrations. (A) Map of the outer area of one spheroid displaying zoned augite phenocryst in a matrix of anorthite and chlorite also hosting small chlorite spheroids. (B) Profile through one spheroid with the center of the spheroid at the lower part and the outer area at the top. Note differences in matrix structure; anorthite needles only in the inner area, and tubular vermiculite-chlorite in the center (C) Map of the inner area of a spheroid displaying anorthite needles and an orbicule with phlogopite in the center surrounded by vermiculite. Furthermore tubular vermiculite-chlorite structures are visible.

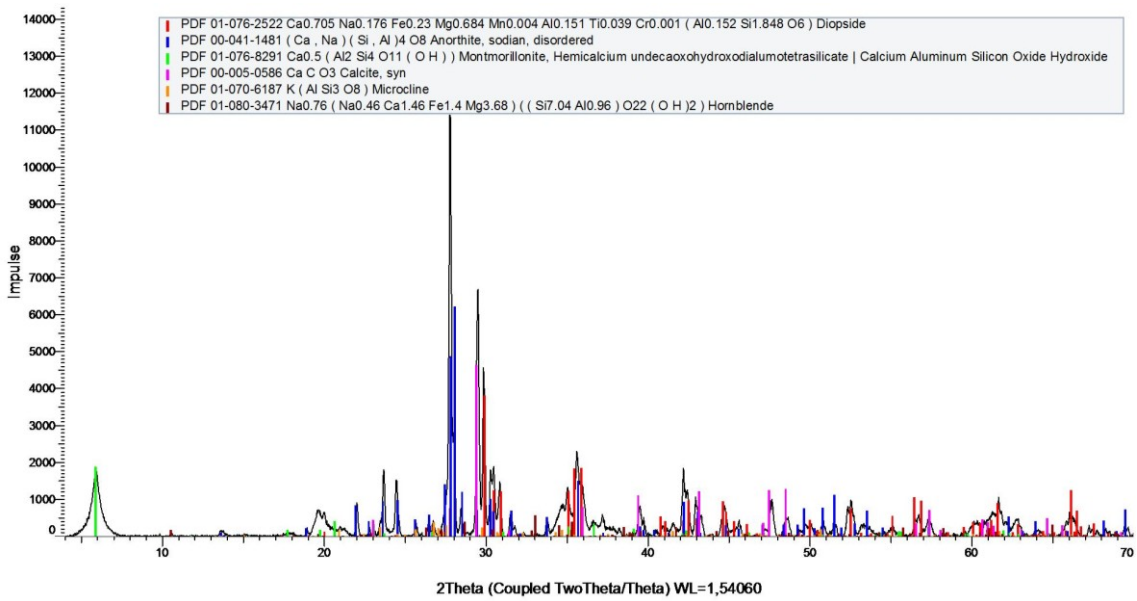

Figure 31: XRD spectra of the spheroidal late stage fluid precipitate sample ZY92 displaying the position of reflexes of occurring phases from EVA database.

Further phases identified by Raman spectroscopy are phlogopite, vermiculite and chlorite. Phlogopite occurs in the center of orbicules (~ 150 µm in diameter) surrounded by vermiculite and sometimes chlorite (Fig. 30C). Phlogopite bearing orbicules only occur in the inner zone of one spheroid.

4 DISCUSSION

The anorthosite samples and the late stage fluid precipitate were investigated in great detail for their chemical and mineralogical composition, offering numerous approaches for interpretation. Some of them will be discussed in the following subchapters.

4.1 ANORTHITE AS PRIMARY MINERAL

Calcic plagioclase (X_{An} = 0.76 – 1) is the major mineral component of the anorthositic rocks investigated for this study. It is homogeneous in composition

and no exsolution lamella or chemical zoning is observed. Anorthite is assumed to be a liquidus phase that is of magmatic origin. This assumption is predominantly based on textural observations. As anorthosites occur as dykes, it appears that material from which they precipitated had to be liquid at the stage of intrusion. The liquid from which they precipitated might be a silicate melt or a hydrothermal fluid sensu lato. It is reasonable to proceed on the assumption of a H_2O rich environment for the generation of this liquid, due to the subduction zone related setting. A reasonable emplacement depth of 1 - 3 km in the crust and a H_2O column of about 2 km imply a pressure range of 150 to 200 MPa. Liquidus temperatures of end member anorthite exceed 1200 °C even for H_2O saturated conditions (Fig. 32) which is very high for modern upper crustal conditions. The lower bound of the grey field in Fig. 32 demonstrates that the presence of quartz drastically reduces solidus temperatures of plagioclase, the melting temperature of anorthite T_m(An) is decreased to about 800 °C. The influence of quartz on solidus temperatures increases with increasing anorthite content. A temperature of ~800 °C seems to be a more realistic temperature for the precipitation of anorthite from the liquid. Such low temperatures at the same time limit the reaction kinetics.

Johannes (1978) could show by melting experiments in the (Qz-)Ab-An-H_20-system that reaction rates and attainment of equilibrium compositions is a process strongly affected by temperature. Assuming temperatures of about 800 °C and 500 MPa, it would take plagioclase several 100000 years to attain equilibrium with either the melt, quartz, or both. Furthermore it was observed that reaction rates are even slower for An ⟶ Ab reactions than vice versa. As a consequence, calcic plagioclase in the investigated samples represents liquidus compositions.

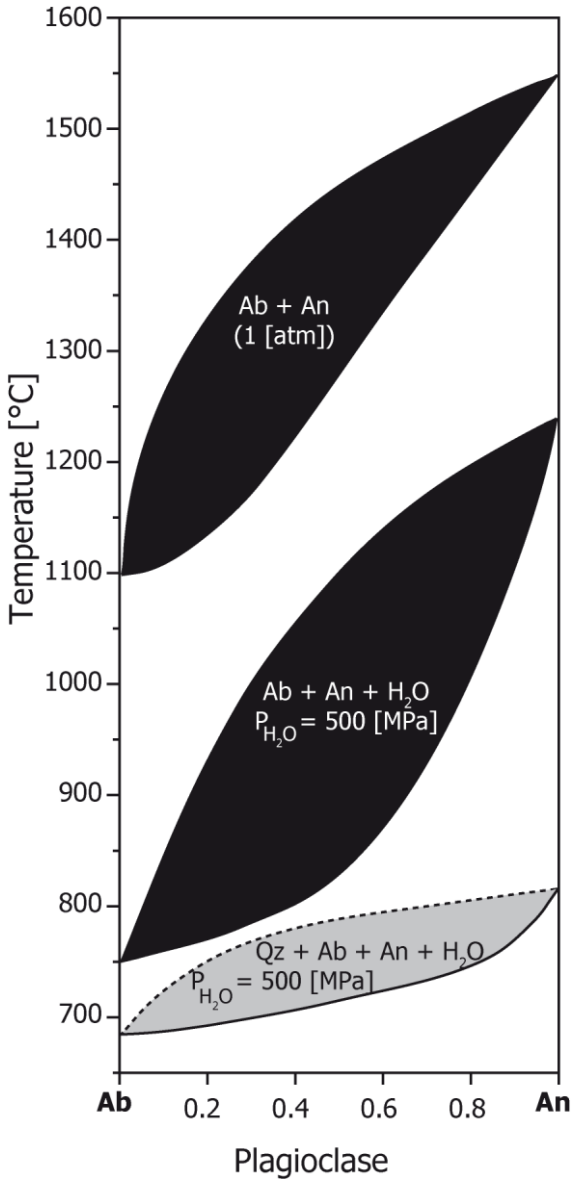

Figure 32: Compilation of projections of the solidus- and liquidus- relations, showing melting relations of plagioclase (Ab – An) in different experimentally investigated systems. Black fields correspond to binary fields of Qz free systems under nominally dry and H_2O saturated conditions, the grey area to systems containing Qz at P_{H2O} = 500 MPa. The dashed line corresponds to the liquidus and the solid line to the solidus of the Qz + Ab + An + H_2O system. Redrawn after (Johannes, 1978).

The Ca rich plagioclase composition did not change to more Ab-rich compositions upon cooling below 800 °C in the magmatic system. This assumption is further supported by perceptible initial euhedral crystal shapes of plagioclase. The homogeneous composition of anorthite might seem to be inconsequential at first glance as one would assume chemical gradients in such metastable minerals, but appears to be reasonable, considering the slow reaction rates in such systems (Johannes, 1978).

Plagioclase compositions with a high anorthite component (X_{An} = 0.98) have already been described in boninites and associated gabbros of the TOC (Duncan and Green, 1987; Thy et al., 1989). Proceeding on experimental work of Panjasawatwong et al. (1995), calcic plagioclase (X_{An} > 0.94), as those found in anorthosites, could only precipitate from extremely refractory liquids with CaO/Na_20 > 18 if precipitating at P > 500 MPa. However, at lower pressures (200 MPa), the high An content of plagioclase could be interpreted as a result of high H_2O contents at the time of crystallisation. At a given temperature X_{An} increases with H_2O content (Berndt et al., 2004 and references therein). Probably the calcic plagioclase of anorthosites precipitated from H_2O rich, extremely refractory liquids.

Generally the distribution of Ca and Na between plagioclase and the melt is used as a geothermometer (Kudo and Weill, 1970; Mathez, 1973). The distribution of the Ca-Tschermak's molecule between anorthite and pyroxene can be used as a geobarometer (McCarthy and Patiño Douce, 1998). The application of such methods is irrelevant for plagioclase in the investigated samples as it is not well calibrated for H_2O saturated conditions and, equilibrium between plagioclase and melt or plagioclase and pyroxene cannot be assumed. Disequilibrium between plagioclase and melt is well documented in plutonic and volcanic rocks (Pearce and Kolisnik, 1990) conspicuous in different types of zonation.

Further, homogeneous anorthite compositions might be a notion to assume hydrothermal annealing of initial plagioclase compositions. It has been shown experimentally by McConnell (1974) that plagioclase transforms to high albite solid solutions for sodic compositions and to anorthite for calcic compositions. It is

evident that anorthite reacted at some stage with a fluid as it is partly replaced by albite as described in the following subchapter.

4.2 ALBITISATION OF ANORTHITE

The formation of albite in anorthositic samples is considered to be a secondary process. The albitisation of anorthite is texturally recognizable (Fig. 7B and Fig. 8E) in anorthositic dyke rocks. Primary albite formation due to exsolution phenomena upon cooling is rather unlikely. It has been shown experimentally that the replacement product of plagioclase reacting under hydrothermal conditions (600 °C; 200 MPa) with an aqueous sodium silicate solution is rather enriched in the calcic component (Hövelmann et al., 2009). The process of albitisation is referred to as an interface-coupled dissolution–reprecipitation reaction (Putnis and Putnis, 2007) which is considered to be the dominant mechanism for mineral replacement reactions under hydrothermal conditions (Putnis, 2002). Albitisation of anorthite in anorthositic samples results in pseudomorphic replacement of anorthite by albite, as indicated by a sharp chemical interface and the preservation of the initial crystal shape and crystallographic orientation of anorthite (Fig. 7B, Fig. 8E and Fig. 23). Pseudomorphic replacement was also observed for hydrothermal experiments of Hövelmann et al. (2009).

The shape and crystallographic orientation of anorthite is preserved by sub sequential epitaxial precipitation of albite to its surface. The preceding reaction of anorthite with fluid led to congruent dissolution on crystal surfaces of anorthite and resulted in a thin albite supersaturated fluid film (Putnis, 2002).

However anorthite needs to be dissolved by a solvent supersaturated in albite. This solvent is assumed to be a hydrothermal fluid responsible for the removal of

Ca and addition of Na and Si. Hövelmann et al. (2009) expressed the process of albitisation in a simplified model exchange reaction where anorthite reacts with a fluid to form albite.

$$CaAl_2Si_2O_8 + Na^+ + Si^{4+} \leftrightarrow NaAlSi_3O_8 + Al^{3+} + Ca^{2+} \quad (7)$$

It is known that albite can be dissolved in aqueous fluids at high pressure (Shen and Keppler, 1997) but the nature of the metasomatizing fluid responsible for anorthite dissolution is difficult to trace back.

4.3 THOMSONITE - HYDROTHERMAL REPLACEMENT OF GLASS

Thomsonite (thomsonite-Ca sensu stricto: $NaCa_2Al_5Si_5O_{20}$ x 6 H_2O), a mineral of the zeolite group appears in all anorthositic samples. Variability in thomsonite composition in anorthosite samples is rather restricted. Texturally it resembles a volcanic glass as it appears as interstitial filling and sometimes contains metal bearing inclusions (Fig. 8). Especially textures including magnetite (Fig. 8A and B) suggest that thomsonite is the reaction product of a glass. Acicular radially arranged magnetite has previously been described as typical quench phase in pillow lavas (Bryan, 1972). Direct precipitation of thomsonite from a liquid appears to be unlikely however it might be the replacement product of pre-existing silicates. A Raman map of thomsonite was generated to display its extensive homogenous crystallographic orientation (Fig. 33), an observation which also supports the assumption of its secondary hydrothermal generation from a glass. The iron bearing inclusions (hematite and goethite) might be also interpreted as quench phases from a melt that rejects the incorporation of iron due to low solubilities prior to solidification.

Zeolite is widely used in the chemical industry (e.g. as ion-exchange material) and its hydrothermal synthesis has been investigated since quite a while (Cundy and Cox, 2003). It is well known that minerals of the zeolite group can be readily synthesized within few hours under hydrothermal conditions. Relating the results of zeolite synthesis at high temperatures and pressures to natural zeolite formation, opposes problems in terms of the kinetic description of such processes (Sand, 1980). Hydrothermal zeolite synthesis from natural reactants at low temperature and pressure, relevant to geological processes, have been matter of numerous investigations (Barth-Wirsching and Holler, 1989; Berger et al., 1988; De'Gennaro et al., 1999; Hawkins, 1981).

Hydrothermal alteration of natural glasses and zeolite formation is often described in relation to mid-ocean ridge hydrothermal systems and the alteration of oceanic crust. Similarly as described for the process of albitisation the formation of zeolite from a glass requires previous dissolution of the glass by reaction with a solvent and subsequent reprecipitation of zeolite (Hawkins, 1981). The reaction of glass with seawater in hydrothermal systems at mid ocean ridges renders these preconditions (Berger et al., 1988). Seawater containing alkaline elements could also be a suitable solvent for the process of albitisation.

The formation of different zeolite species in nature is observed to be determined by differences in: source material, chemical composition, concentration and pH of the solution, chemical gradient, temperature and temperature gradient, age of occurrence, and open vs. closed system processes (Boles, 1982; Hay, 1986).

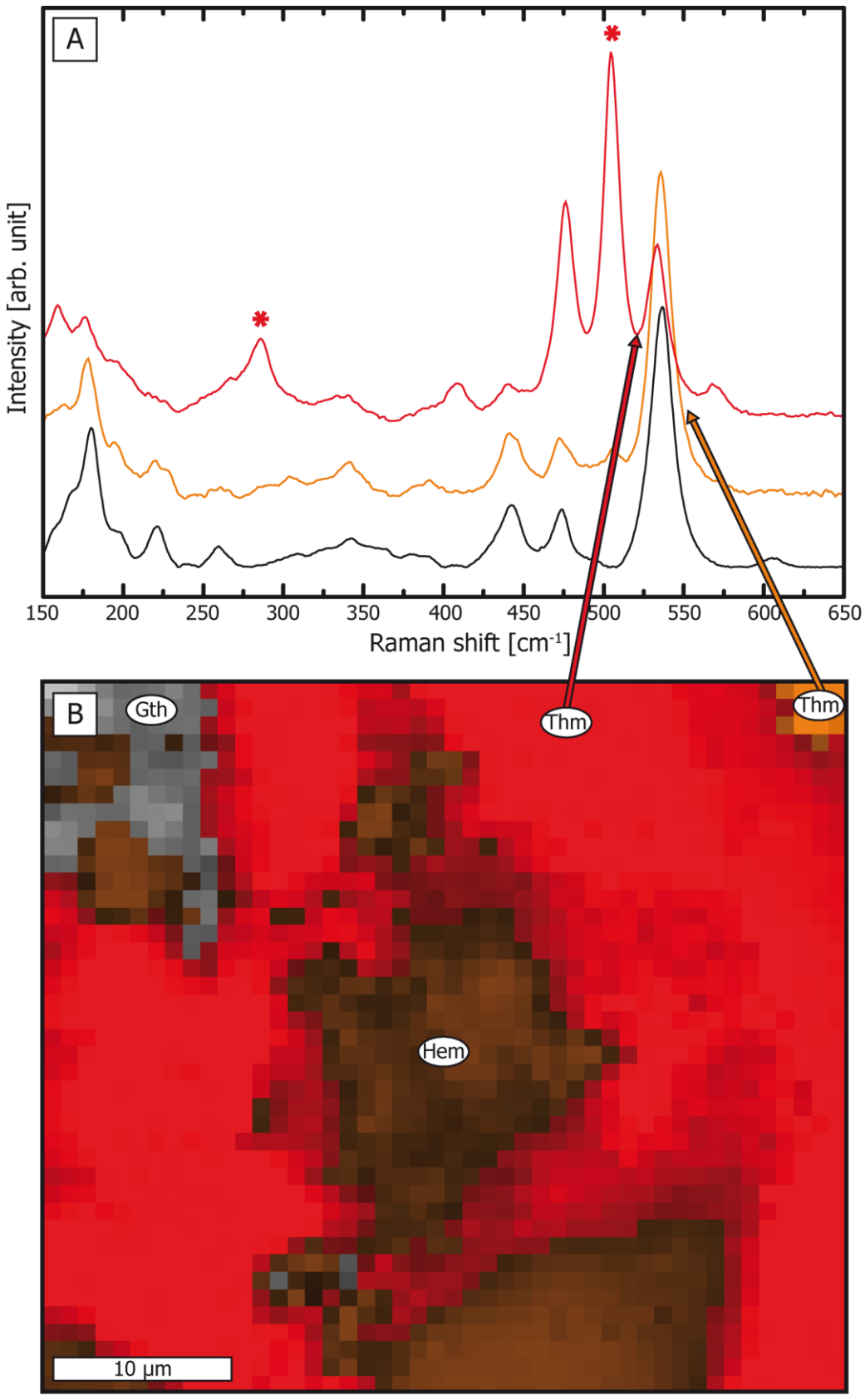

Figure 33: (A) Raman spectra of two thomsonite grains with different crystallographic orientation (red and orange) as indicated by differences in intensities of thomsonite bands. Black line corresponds to the thomsonite reference spectra (RRuff: # R050103). Red stars indicate the position of anorthite bands. (B) False colour Raman image corresponding to spectra in figure A, displaying two differently orientated thomsonite grains with hematite and goethite inclusions within the anorthosite sample ZY80L (group II).

Hydrothermal experiments by Barth-Wirsching and Holler (1989) show that the concentration and distribution of alkali and alkaline earth cations in the newly formed zeolite is determined by their amounts and concentrations both in the starting material and in the initial solution (solvent). Further, the Si/Al ratio of zeolite is controlled by the pH of the solvent. In an open system the pH is profoundly affected by Si-removal or by Si-addition through the migrating solution. Zeolite H_2O content appears to be affected by temperature as well as reaction time. Applying the observations of Barth-Wirsching and Holler (1989) to the observed zeolite composition in anorthosite rocks it allows to draw conclusions as to the composition of the solvent and the glass. However it is necessary to assume an externally controlled open system for thomsonite formation in anorthosites. This profoundly complicates the interpretation of thomsonite compositions as mass transfer is possible from the reacting solution. Thomsonite formation was only observed for the alteration of nepheline with 0.1 – 0.01 N $CaCl_2$ at elevated temperatures (>150 °C; P = 100 MPa) in open systems as nepheline could supply sufficient Na. Above 250 °C thomsonite becomes unstable and instead anorthite stabilizes (Barth-Wirsching and Holler, 1989). However crystals with thomsonite-like structures have been also observed to form from Na-free gels containing only Ca, Al and Si, in a temperature range between 225 °C and 245 °C (Barrer and Denny, 1961). Further thomsonite was also formed by hydrothermal treatment of glasses of different Ab-An compositions between 200 °C and 275 °C (Juan and Lo, 1968) which seems to be a more realistic initial glass composition. Sodium has thus to be supplied by the hydrothermal solution.

The pre-existing glass has to be dissolved by an alkaline hydrothermal solution before thomsonite reprecipitates. A strong correlation between the alkalinity of

the solution and zeolite composition in the low temperature regime at saline, alkaline lakes has been described by Mariner and Surdam (1970). Mariner and Surdam (1970) observed increasing solubility of silica rich glasses with increasing alkalinity of the solution. The Si/Al ratio of thomsonite precipitating from the solution, in turn, decreases with increasing alkalinity of the solution. The relationship between pH and the Si/Al ratio of the precipitating thomsonite has also been described by Barth-Wirsching and Holler (1989). The Si/Al ratio of thomsonite in anorthosite samples ranges from 1.2 for less silicic thomsonite compositions in sample ZY80L of group II, to 1.6 for maximal silica contents of thomsonite in sample ZY82A of group I. The thomsonite composition in anorthosites is rather silicic; this in turn requires a higher alkalinity of the former hydrothermal solution.

4.4 Systematics in trace element chemistry of Anorthosites

Trace element composition of anorthositic samples and the spheroidal late stage fluid precipitate are investigated for bulk compositions, for diopside and Ti-Zr accessory phases. Further, wet chemistry data is acquired for Zr, Lu, Hf and Rb and isotope ratios of $^{176}Lu/^{177}Hf$, $^{176}Hf/^{177}Hf$, $^{87}Rb/^{86}Sr$ and $^{87}Sr/^{86}Sr$ are determined. Trace element chemistry of anorthositic dyke rocks is remarkable in terms of extraordinary enrichment of HFSE and REY.

The generation of anorthositic liquids is assumed to be related to the Troodos extrusive sequence. The dykes transect the supply channels of the UPL lavas and are thus referred to as a late- to post magmatic event. The source of anorthositic liquids should be somehow related with the H_2O saturated melts of the UPL sequence (boninite, picrites, OIB). UPL melts were produced from melting of subarc mantle in a subduction related setting (SSZ). Other leucocratic rocks such as

plagiogranites from the TOC are proposed to be the product of high degree fractional crystallisation of mafic precursor melts, either of a tholeiitic or boninitic composition (Freund et al., 2014; Marien, 2015). However it is not evident that today's trace element bulk compositions of anorthosite dykes correspond to the composition of the intruding "anorthosite" liquid. Processes such as albitisation and thomsonite formation have been shown to be related to interactions with a hydrothermal fluid. As a consequence, the bulk compositions do not display the initial composition of the intruding liquid.

4.4.1 BULK TRACE ELEMENT COMPOSITION OF ANORTHOSITES IN COMPARISON WITH OTHER EXTRUSIVES OF TOC

Anorthosites appear to have extraordinary high HFSE contents compared to other extrusive rocks from Cyprus and compared to the BSE values (Table 3).

Table 3: Averaged bulk HFSE (extended) composition of anorthosites (Ø of 18 Q-ICP-MS analyses of glasses) in comparison with TOC extrusives (Ø of 45 analysed) and BSE values.

	Anorthosites	**UPL/LPL**	**BSE**
[ppm]	This study	(Regelous et al., 2014)	(Palme et al., 2014)
Nb	54.3	1.00	0.60
Ta	3.97	0.07	0.04
Zr	145	50.2	10.3
Hf	4.42	1.62	0.30
Ti	2108	272	1265
W	7.96	0.08	0.01
Th	7.08	0.25	0.08
U	0.96	0.12	0.02

The Zr, Hf, Nb and Ta content of the anorthosites appear to be extremely enriched relative to BSE values (Fig. 34A/B), whereas in anorthosites, Nb and Ta are even stronger enriched (factor ~120) than Zr and Hf (factor ~ 20). Enrichment of Zr, Hf, Nb and Ta has previously been described for mafic extrusives of the TOC (Fonseca et al., 2017; König et al., 2008; Regelous et al., 2014) and Cyprus' plagiogranites

(Marien, 2015). Both element pairs, Zr-Hf and Nb-Ta are positively correlated (Fig. 34A/B). Compositions of the extrusive sequence and plagiogranites display a good correlation between Zr and Hf (R^2 = 0.99), whereas the correlation for anorthosites appears to be less significant (R^2 = 0.58). Concerning Nb-Ta, the correlation is very strong for the extrusive basaltic sequence (R^2 = 0.93) but less coherent for boninites and some plagiogranites. Concerning boninites and derived plagiogranites the deviation in correlation of Nb-Ta is attributed to a depleted and subduction related mantle source (König et al., 2008; Marien, 2015). The Zr/Hf ratios of all investigated anorthosite samples are significantly lower than the ratios from BSE values, the most depleted samples have Zr/Hf ratios as low as 26.9, whereas the more enriched group I reaches values of 33.2 (Fig. 34C). The ratio of Nb/Ta is less variable scattering around BSE value, ranging from 8.96 to 16.64 covering about the same compositional range as plagiogranites (Fig. 34C). The Zr/Hf ratio of different anorthosite groups is not correlated with the Ti-content, which is comparable low in respect to the Ti-content in the tholeiitic extrusive sequence (Table 3) and plagiogranites but matches the Ti-content of boninites (Fig. 34D).

Following the assumption that the anorthositic liquid is somehow related to the extrusive sequence of TOC, an additional process is required to enrich Zr-Hf and Nb-Ta to such an extent. Supposing high concentrations of Zr-Hf and Nb-Ta to be the result of fractional crystallisation this would be reflected in correlations with components indicative for fractional crystallisation processes such as SiO_2, CaO, Al_2O_3, $^{87}Sr/^{86}Sr$ and REY. Fractionation processes will result in a gradual increase of incompatible elements. Within the extrusive sequence of TOC such phenomena have been shown to be relevant (e.g. Regelous et al., 2014) which is apparent by

decreasing Lu/Hf ratios with increasing silica (Fig. 34E). Furthermore the Eu/Eu* ratio in TOC extrusives decreases (corresponding to an increase in negative anomaly) with increasing silica (Fig. 34F) probably attributed to increasing plagioclase fractionation. No such correlation between REY systematics and silica or other fractionation indexes is observed in bulk anorthosite compositions. The ratio of Lu/Hf in all anorthositic samples varies at constant silica (Fig. 34E). Following up previous observations on HFSE behaviour during fractionation it is concluded that the different HFSE distribution in the different anorthosite groups cannot be assigned only to different degrees of fractionation, and that anorthositic melts could not be generated by fractionation of mafic melts.

The age corrected εHf data obtained for anorthosite samples ($\varepsilon Hf_{(90Ma)} \sim 9.8$) appears to be much lower in comparison with other TOC extrusives (Fig. 34G/H). However, in terms of the age corrected Sr-isotopic composition (Fig. 34H) anorthositic samples display similar values ($^{87}Sr/^{86}Sr_{(90\ Ma)} = 0.7062 - 0.7068$) as described for boninites ($^{87}Sr/^{86}Sr_{(91\ Ma)} = 0.7059 - 0.7066$ according to König et al. (2010)). This observation probably mirrors the strong influence of cretaceous seawater (cretaceous seawater $^{87}Sr/^{86}Sr \sim 0.7070 – 0.7075$ according to Burke et al. (1982) on the Sr-isotope ratio.

One striking observation concerning anorthositic trace element and isotopic composition is the correlation ($R^2 = 0.99$) of the Lu-content with the isotopic ratio of $^{176}Lu/^{176}Hf$ (Fig. 34I). This reveals that the variability in $^{176}Lu/^{176}Hf$ is exclusively controlled by the HREE distribution. No such correlation is apparent for other rock suites that have been described on Cyprus, strengthening the fact that a different process is responsible for the generation of the anorthosite liquid. Explanation of their HFSE signature requires different and maybe more complex

processes as variations in source composition or fractionation processes. It is noteworthy that a correlation between age corrected εHf data with $^{176}Lu/^{176}Hf$ is only apparent for group I-II but not for group III (Fig. 34G). Such differences have to be attributed to differences in the apportionment of REY on Zr-bearing phases and other REY hosting accessory minerals.

4.4.2 MINERALS HOSTING HFSE AND REY

In principal, Ti-oxide, clinopyroxene and amphibole are capable of controlling the budget of HFSE (Foley et al., 2000; Green and Pearson, 1987; Münker et al., 2004). The slightly different behaviour of Nb and Ta during melting and crystallisation processes is explained by the minute difference in ionic radii of 0.015 Å between Nb to the smaller Ta (Foley et al., 2002) affecting their distribution coefficients (Green and Pearson, 1987).

Generally clinopyroxene is the major host for Zr-Hf and prefers Hf over Zr (Blundy et al., 1998; McDade et al., 2003). Diopside is the volumetrically dominant Zr and Hf host in anorthosites, but however, it cannot be the only Zr and Hf sequestering phase. The anorthositic bulk content of Zr and Hf exceeds concentrations in diopside (Fig. 36A). The volumetrically negligible accessory phases, titanite, rutile and zircon appear to be the major HFSE hosts.

Texturally, no significant differences in the distribution of accessory minerals are apparent comparing the different anorthosite groups. Rutile only appears in association with titanite, whereas textures suggest rutile replacement by titanite. Zircon is very sparse; if present it is associated with titanite, commonly in clusters of accessories (Fig. 9C).

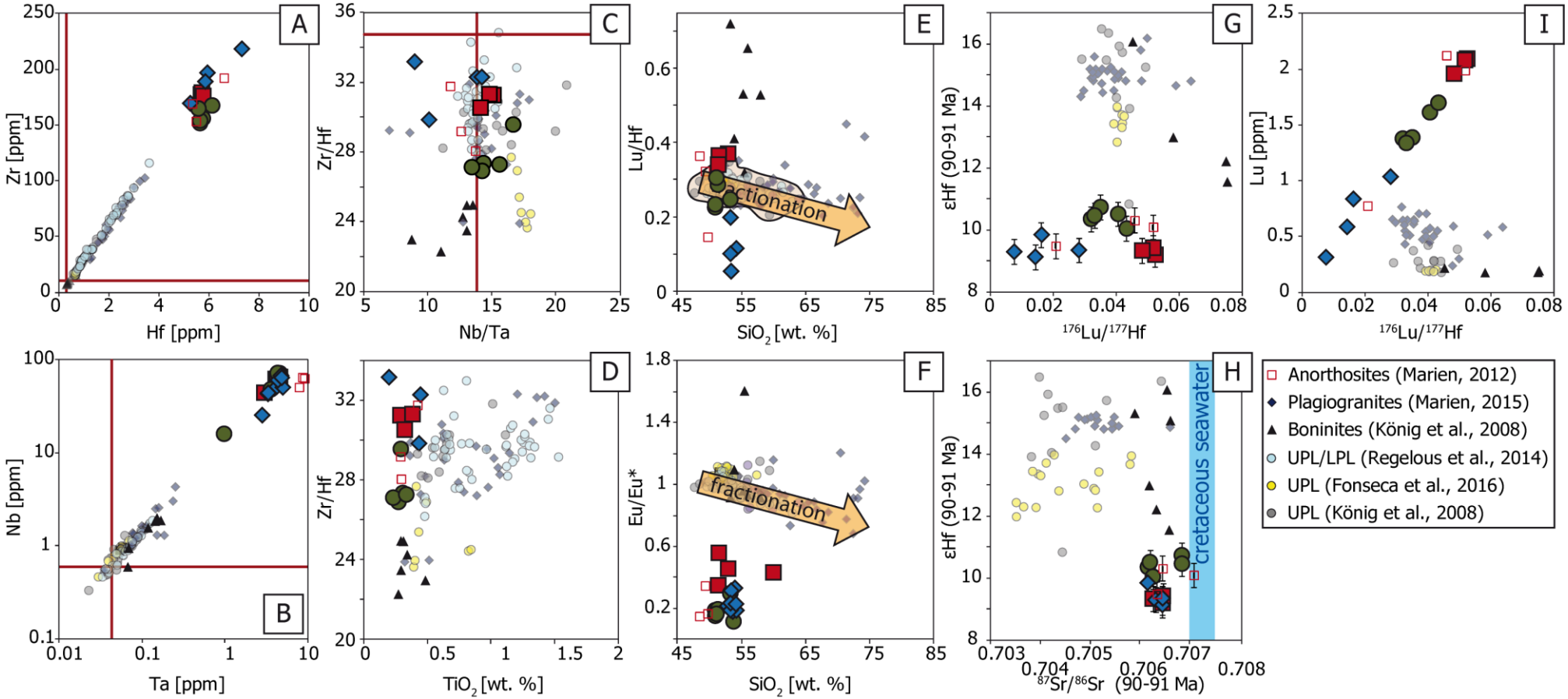
A
Zr [ppm]
Hf [ppm]
B
Nb [ppm]
Ta [ppm]
C
Zr/Hf
Nb/Ta
D
Zr/Hf
TiO2 [wt. %]
E
Lu/Hf
SiO2 [wt. %]
fractionation
F
Eu/Eu*
SiO2 [wt. %]
fractionation
G
εHf (90-91 Ma)
176Lu/177Hf
H
εHf (90-91 Ma)
87Sr/86Sr (90-91 Ma)
Cretaceous seawater
I
Lu [ppm]
176Lu/177Hf
Anorthosites (Marien, 2012)
Plagiogranites (Marien, 2015)
Boninites (König et al., 2008)
UPL/LPL (Regelous et al., 2014)
UPL (Fonseca et al., 2016)
UPL (König et al., 2008)

Figure 34: Bold red lines correspond to bulk silicate earth values (Palme et al., 2014). Pale circles correspond to previous analyses of basaltic lavas from Cyprus (blue: fresh volcanic glasses from a 3.5 km long section of the Akaki Canyon on the NE flank of the TOC comprising UPL and LPL and Low-Ti and High-Ti lavas (Regelous et al., 2014), yellow: fresh basaltic glass samples from UPL localities at Kalavasos, Klirou bridge along the Akaki river canyon, and Kapilio (Fonseca et al., 2017), grey: unaltered mafic glasses (UPL) and lavas of the Arakapas Fault Belt of the TOC, grey triangles correspond to boninites investigated in the same study by (König et al., 2008). Pale dark blue diamonds correspond to plagiogranites investigated by (Marien, 2015). Red rectangles correspond to previously investigated anorthosites (Marien, 2012). Green, red and blue large symbols refer to investigated anorthosite groups of this study. (A) Binary plot of the element pair Zr-Hf displaying strong correlation and the enormous enrichment in anorthosite samples. Further it is apparent that the group I-II displays less variation in Hf compared to group III; (B) Binary plot of the element pair Nb-Ta displaying strong correlation and the enormous enrichment in anorthosite samples (C) Zr/Hf-Nb/Ta plot displaying the overlap of ratios with analyses of the extrusive TOC sequence; (D) Binary plot displaying Zr/Hf vs. Ti-content: Note the low Ti-concentration of anorthosites compared to tholeiitic TOC rocks and the overlap in Ti-content with Boninites. (E) Binary plot of Lu/Hf vs. silica. Note the negative correlation for the tholeiitic Troodos extrusive sequence and the deviating trend for Boninites and anorthosites. (F) Eu/Eu* vs. silica. Note the significant negative Eu-anomaly in anorthosite samples compared to extrusive TOC rocks and plagiogranites. Further note the negative trend for pale blue circles of Regelous et al. (2014) data indicating an increasing Eu-anomaly with fractionation. (G) Age corrected εHf data vs. the $^{176}Lu/^{177}Hf$ ratio. Glasses of the TOC sequence are age corrected for 91 Ma (Fonseca et al., 2017; König et al., 2008) whereas anorthosites and plagiogranites are corrected for 90 Ma. Note the generally low εHf values compared to other TOC rocks and the elevated εHf values of the green group compared to red and blue group of the anorthosites. (H) Age corrected εHf values vs. the ratio of $^{87}Sr/^{86}Sr$ including the $^{87}Sr/^{86}Sr$ compositional range of Cretaceous seawater ($^{87}Sr/^{86}Sr$ = 0.7070 – 0.7075) (Burke et al., 1982). Note the high $^{87}Sr/^{86}Sr$ values for anorthositic samples overlapping with boninitic Sr-isotopic signature trending towards cretaceous seawater composition. (I) Binary plot displaying the Lu-content vs. the $^{176}Lu/^{177}Hf$ ratio. Note the positive correlation (R^2 = 0.99) for anorthositic samples.

4.4.2.1 Ti-bearing accessories

Titanite, rutile and ilmenite appear as Ti-bearing accessory phases whereas titanite is the volumetrically dominant one. The HFSE concentrations in titanite and rutile in anorthosites are high (Fig. 36). It is well known that Ti in titanite (Cempírek et al., 2008) and rutile (Klemme et al., 2005) can be substituted by HFSE.

Titanite and rutile appear as major hosts of Nb and Ta in anorthosites (Fig. 36B). Their appearance is responsible for the stronger enrichment of Nb and Ta (factor ~120) in anorthosites compared to Zr- and Hf enrichment (factor ~ 20) relative to BSE. The substitution mechanism by which Nb and Ta are incorporated into the rutile structure has control over partition coefficients (Horng and Hess, 2000).

Rutile precipitating from liquids with high aluminium activity is expected to incorporate higher contents of Nb and Ta according the coupled substitution:

$$Nb^{5+} + Al^{3+} = 2Ti^{4+} \text{ or accordingly } Ta^{5+} + Al^{3+} = 2Ti^{4+} \quad (8)$$

The incorporation of the isovalent Zr^{4+} and Hf^{4+} for Ti^{4+} appears to be less affected by the liquid composition (Klemme et al., 2005). The substitution mechanism relevant for the incorporation of Nb and Ta into the titanite structure is described according to equation 8, identical as for rutile (Prowatke and Klemme, 2005 and references therein).

Moreover titanite and rutile appear to accommodate most of the W anorthosites (Fig. 36C/D). Tungsten concentrations in rutile are higher (66.1 – 410 ppm) than in titanite (0.49 – 326 ppm). Basalts and boninites of Cyprus are known to be enriched in W (0.0243 – 0.177 ppm) which has been related to an enriched melt reservoir (König et al., 2008). Enrichment of the Cyprus mantle reservoir is explained by fluids originating from subducted pelagic sediment (König et al., 2008). However, W rich titanite and rutile compositions have to be attributed to a different W reservoir. An enrichment of W in titanite (1.9 – 570 ppm) in a similar extent as observed for titanite in anorthosites has been described in W deposits in Yukon and British Columbia, Canada (Che et al., 2013). Great similarities appear in textures and composition of titanite in anorthosites to W rich titanite from Yukon and British Columbia. Similar degree of REY enrichment in titanite is observed. Che et al. (2013) described increasing substitution of Ti^{4+} and Ca^{2+} by Al^{3+}, $Fe^{3+}$and REE^{3+} in W rich titanite for hydrothermal titanite relative to magmatic titanite. The adequate substitution mechanism is described by Shannon (1976).

$$Ca^{2+} + Ti^{4+} = REY^{3+} + (Al, Fe)^{3+} \quad (9)$$

Compositions of titanite in anorthosites appear to be similarly influenced by this substitution. This is confirmed by the 1:1 correlation between Ti sites and the sum of Al and Fe sites in the titanite structure (Fig. 35).

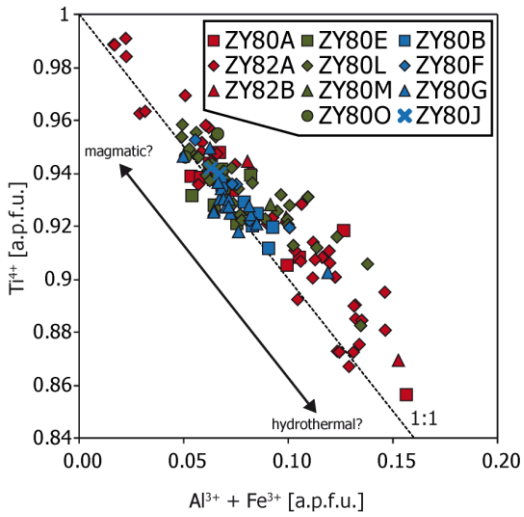

Figure 35: Binary plot displaying variable amounts of Al^{3+} and Fe^{3+} being incorporated in the titanite structure. High Ti concentrations might refer to a magmatic origin whereas high Al^{3+} and Fe^{3+}reflect hydrothermal influence as described by Che et al. (2013).

Textural evidence in anorthosites is given for at least two titanite generations: titanite appears as euhedral inclusions in thomsonite (Fig. 8D) representing low-Ti high-Al and REY compositions, and anhedral – xenomorphic titanite displaying the entire compositional range (Fig. 9D). Furthermore titanite appears as replacement product of rutile. The trace element composition of such titanite corresponds to inherited rutile grains (Fig. 26A/C). Rutile replacement textures appear in all samples but trace element composition could only be determined in sample ZY80A. Titanite compositions of some grains within the allochthonous samples display an additional event. They display areas enriched in Fe and LREE (Fig. 24D/E).

Bulk Ti-concentrations of anorthosites are low (0.196 – 0.451 wt.%), straddling BSE values, and are comparable to boninites (~ 0.33 wt.%). The Ti content in the tholeiitic sequence reaches 1.53 wt.% (Fig. 34D). This observation implies that the

strong enrichment in HFSE and REY compared to the extrusive sequence has to be attributed to other, Ti-free accessory phases, probably zircon.

4.4.2.2 Zircon

Zircon in anorthosites is very sparse and appears to be the major host of Hf (Fig. 36A) and HREE (Fig. 26B and Fig. 36H). The appearance and the amount of zircon in different anorthosite samples exert a significant effect on their bulk trace element chemistry. Differences in bulk compositions among the different anorthosites groups are attributed to zircon. This gets obvious regarding Hf isotope data of different groups. From Fig. 34A it is apparent that bulk Hf of group I and II is more or less invariant (5.574 - 6.124 ppm) whereas the variability in group III is slightly larger (5.248 – 7.313). As a consequence the correlation of the $^{176}Lu/^{177}Hf$ ratio with the Lu content has to be attributed to differences in Lu (Fig. 34I). Group III exhibits the lowest $^{176}Lu/^{176}Hf$ ratios (0.0075 – 0.0281) comparable to rocks of the TOC extrusive sequence and plagiogranites (0.0287-0.1018). Group II (0.0319 - 0.0433) and group I (0.0482 - 0.0524) display increasing Lu-concentrations and $^{176}Lu/^{176}Hf$ ratios relative to group III. However, regarding the $^{176}Lu/^{177Hf}$ ratio in respect to age corrected εHf data it is apparent that the Hf isotopic signal inherited in zircon displays different behaviour for group I - II and group III.

4.4.2.3 Constraints on crystallisation temperatures

The uptake of Ti in zircon and Zr in rutile systematically changes with temperature and can be used as a thermometer. Watson et al. (2006) experimentally calibrated these temperature dependencies and present two geothermometers based on the Ti content of zircon and the Zr content of rutile. Rutile temperatures range from 650 to 930 °C in group I and range between 660 and 780 °C in group III. The Ti

content in zircon reveals temperatures around 1180 °C. Such temperatures argue for zircon to represent magmatic compositions whereas rutile rather represents hydrothermal temperatures. The results of this geothermometer match textural observations with zircon, representing inherited grains and rutile being hydrothermally altered. However it is questionable if these temperatures represent true crystallisation temperatures as they might not display equilibrium with the melt/liquid. Even though the calculated temperatures appear to display realistic results, it has to be considered that the thermometer is not calibrated for H_2O systems and it is not unequivocal to assume Zr- and Ti activities to equal one.

4.4.2.4 Constraints on HFSE and REY mobility in hydrothermal fluids

Summarising the observations on trace element distribution in accessory phases and on the bulk isotope signal, the involvement of hydrothermal fluids is emphasized.

Proceeding on observations on titanite and rutile textures and compositions, a fluid is responsible for the (i) mobilization of Ti and the replacement of rutile by titanite (ii) for tungsten enrichment, (iii) increased Nb and Ta concentrations in rutile and (iv) for fractionated Nb/Ta ratios with increased Nb compatibility and (v) for Fe and LREE enrichment in titanite of allochthonous samples.

HFSE are generally assumed to be fluid immobile, however fluid composition exerts a significant control on solubilities. Hydrothermal fluids often contain large amounts of dissolved salts being significantly dissociated at elevated pressure. According to the Lewis concept of acids and bases (Lewis, 1923) dissociated salts increase the ionic strength of the solution and thereby increase the solubility of ionic solids (Ayers and Watson, 1991).

The mobilization of Ti in hydrothermal fluids has been shown to be possible by experiments by Rapp et al. (2010). They revealed increased Ti solubilities in hydrothermal brines. In chloride brines rutile solubility is increased by a factor of 2 – 4 compared to H_2O, and fluoride brines even increase rutile solubilities 20 – 100 times. Similarly, the solubility of W in hydrothermal fluids is affected by the presence of complexing agents, König et al. (2008) proposed that the high solubility of W reflects the stability of tungstate complexes at oxidizing conditions and high Cl-contents. It appears that W can be highly mobile in hydrous regimes (Arnórsson and Óskarsson, 2007; Seiler et al., 2005). Following the observation of high Nb and Ta contents in rutile of anorthosite samples, the liquid in equilibrium with such rutile compositions can be assumed to display a high alumina activity (Horng and Hess, 2000). Furthermore the elevated Nb contents could be the consequence of enhanced Nb mobility in F- or Cl-rich complexing agents. Concluding, to dissolve HFSE in appropriate quantities, the fluid composition is considered to correspond to a fluoride or chloride rich brine with high alumina contents.

Boninites have been shown to be influenced by subduction fluids; however, such fluids are not relevant for anorthosites. As shown by König et al. (2008) the solubility of W in subduction zone fluids is slightly higher than that of Th and U as indicated by elevated ratios of W/Th and W/U found in subduction-related magmas. Slab fluids originating from subducted sediments generally display higher W/Th and W/U ratios as observed for slab fluids from subducted oceanic crust. The difference is caused by the initially higher W abundance in pelagic sediments. However for anorthositic samples the W/Th ratio is not uniform, Th, even if strongly enriched compared to TOC extrusive rocks, appears to be rather invariant

in anorthosites whereas W is highly variable. It is noteworthy that the Th content in titanite of anorthositic samples is invariant, whereas slight variations appear for rutile (Fig. 36D). Uranium and Th appear to be positively correlated in accessory minerals whereas both elements are extremely enriched in anorthosite bulk compositions slightly favoring Th over U (Fig. 36E). Uranium is known to be soluble in oxidizing saline fluids. The solubility of Th is rather low and independent of oxygen fugacity and fluid salinity (Bali et al., 2010). However Th occurs to be more compatible in titanite and rutile than U, this might explain elevated Th contents in anorthosites relative to U (Fig. 36E).

Generally the REY are not equally enriched by hydrothermal processes. The LREE tend to be more mobile than HREE as LREE complexes with fluoride and chloride ligands are more stable than analogue HREE complexes (Williams-Jones et al., 2012). Bau (1996) claimed chemical complexation to be an effective process in aqueous systems, responsible for the fractionation of REY. For moderately acidic conditions REY distribution is controlled by sorption processes whereas La is more easily mobilized than Lu due to decreasing ionic radii from La to Lu (Bau, 1991). Titanite in the allochthonous sample reveal LREE enrichment (Fig. 26A) this might be an effect of higher LREE mobility in the hydrothermal fluid.

The negative Eu-anomaly observed in diopside, titanite, zircon and rutile is also mirrored in bulk glass compositions. The different behaviour of europium compared to the other REE, which generally behave as a coherent geochemical group during most natural processes, is owed to the fact that it may stabilize as divalent cation. The divalent Eu easily enters plagioclase crystal structure substituting for Ca. As a consequence, fractionation of plagioclase results in relative Eu depletion compared to other REE (Weill and Drake, 1973).

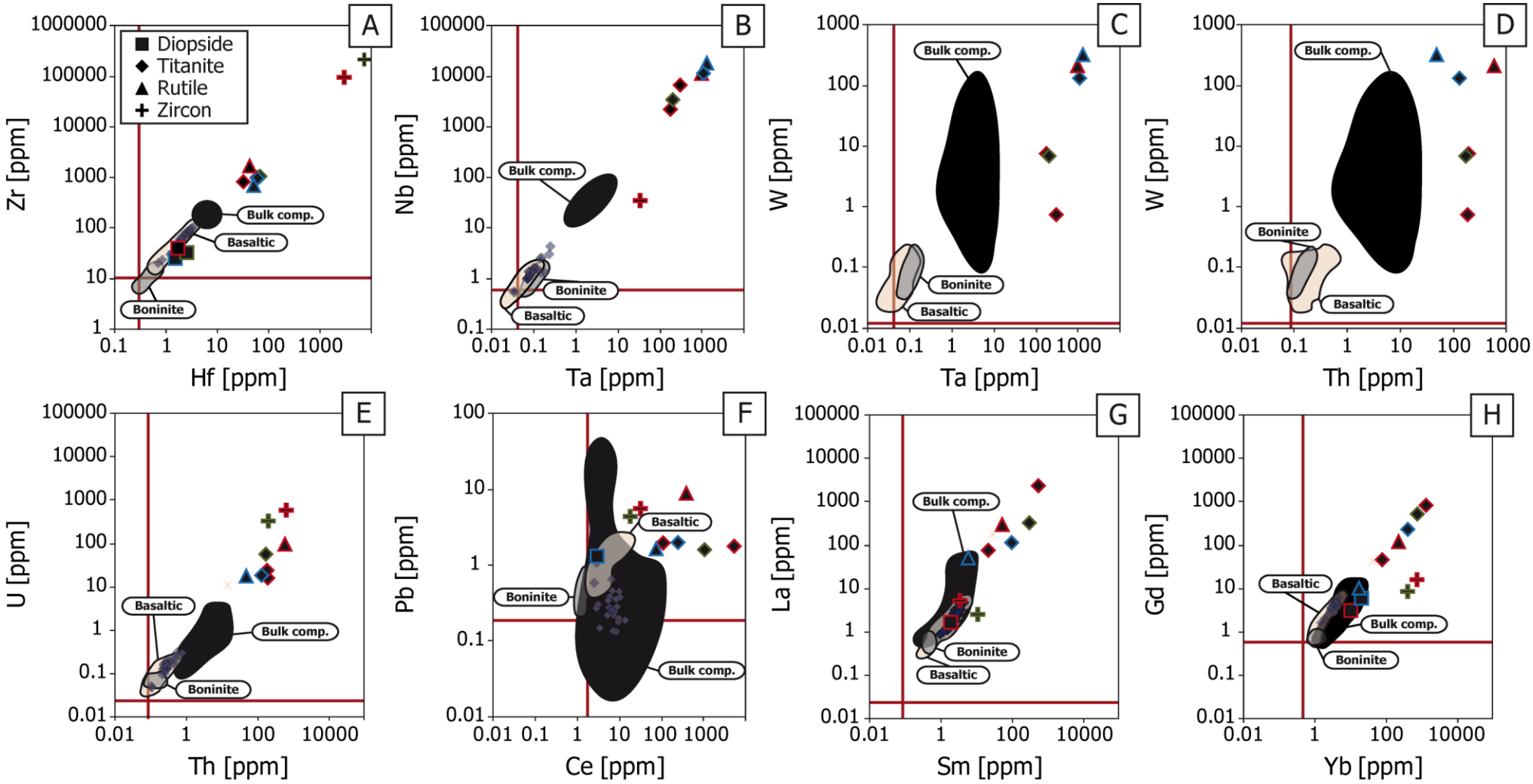
A
Diopside
Titanite
Rutile
Zircon
Zr [ppm]
Hf [ppm]
Bulk comp.
Basaltic
Boninite
B
Nb [ppm]
Ta [ppm]
Bulk comp.
Boninite
Basaltic
C
W [ppm]
Ta [ppm]
Bulk comp.
Boninite
Basaltic
D
W [ppm]
Th [ppm]
Bulk comp.
Boninite
Basaltic
E
U [ppm]
Th [ppm]
Basaltic
Bulk comp.
Boninite
F
Pb [ppm]
Ce [ppm]
Basaltic
Boninite
Bulk comp.
G
La [ppm]
Sm [ppm]
Bulk comp.
Boninite
Basaltic
H
Gd [ppm]
Yb [ppm]
Basaltic
Bulk comp.
Boninite

Figure 36: Grey shaded area corresponds to the compositional range of Cyprus boninites (König et al., 2008) and beige shaded area corresponds to the basaltic TOC sequence comprising data of: König et al. (2008), Fonseca et al. (2017) and Regelous et al. (2014). Pale dark blue diamonds correspond to plagiogranites of Cyprus (Marien, 2015). Red solid lines indicate the BSE values according to Palme et al. (2014). The black area corresponds to the averaged compositional range of anorthosites. Different symbols correspond to averaged ICP-MS analyses of minerals whereas the contour colour indicates the group (red = I, green = II and blue = III). (A) Binary plot of Hf- vs. Zr concentration. (B) Binary plot displaying Ta- vs. Nb concentrations. Nb and Ta concentrations of diopside and zircons of group II are below the detection limit. Rutile and titanite exhibit highest Nb and Ta concentrations. Note the Ta-excess in zircon. (C) Binary W vs. Ta plot indicating high variability for W but restricted range for Ta, valid for both, bulk composition and mineral separates. Note the high variability of W in titanite. (D) Binary W vs. Th plot. Note variable Th content in rutile, whereas Th content in titanite is invariant. (E) Binary U vs. Th plot. Note the strong enrichment of U in anorthosites and high U contents in accessory phases. Compatibility of Th appears to be higher for Th compared to U for titanite and rutile (F) Binary Pb vs. Ce plot, an element ratio which is known to be sensitive to fluid addition. Note the high variability of bulk Pb content of group III(G) Binary plot of La vs. Sm a ratio indicative for the LREE(H) Binary Gd vs. Yb plot indicative for the HREE. Note the offset of Yb in zircons.

The negative Eu-anomaly observed in anorthosites might be attributed to plagioclase fractionation from the anorthositic initial melt prior to diopside, zircon, titanite and rutile precipitation. However this appears unrealistic regarding the crystallisation sequence. The negative Eu-anomaly could also be reflective of an aqueous fluid in equilibrium with the melt precipitating mentioned minerals. Under most hydrothermal and metamorphic conditions, Eu in aqueous solutions is present in its divalent state (Sverjensky, 1984). As a consequence, incorporation of divalent Eu into the zircon and titanite structure differs to substitution mechanisms valid for the trivalent REE (reaction 9), probably being less efficient.

4.5 THE LATE STAGE FLUID PRECIPITATE

From field observations it is derived that the spheroidal precipitates represent in-situ pockets formed after the emplacement of the Kalavassos basalts. Thereby the spheroids represent remnants of a late magmatic fluid being trapped within the surrounding primitive basalts. The cooling rate for spheroidal late stage fluid precipitate is assumed to be short as indicated by the glassy matrix and the plagioclase quench needles. Textural- as well as field observations suggest that the

spheroids represent the solute fraction of the entrapped fluid; the remaining H_2O fraction is lost to the surrounding. For a rough estimation of the proportions of solute in the fluid, it is assumed that the voids surrounding the spheroids were initially filled with H_2O (Fig. 37 and Table 4). Derived volume proportions reveal that about 80 vol.% correspond to the solute precipitate. Such calculations represent minimum estimates of the fluid fraction. An aqueous fluid being saturated to such an extent with silicate phases might be rather described as a gel.

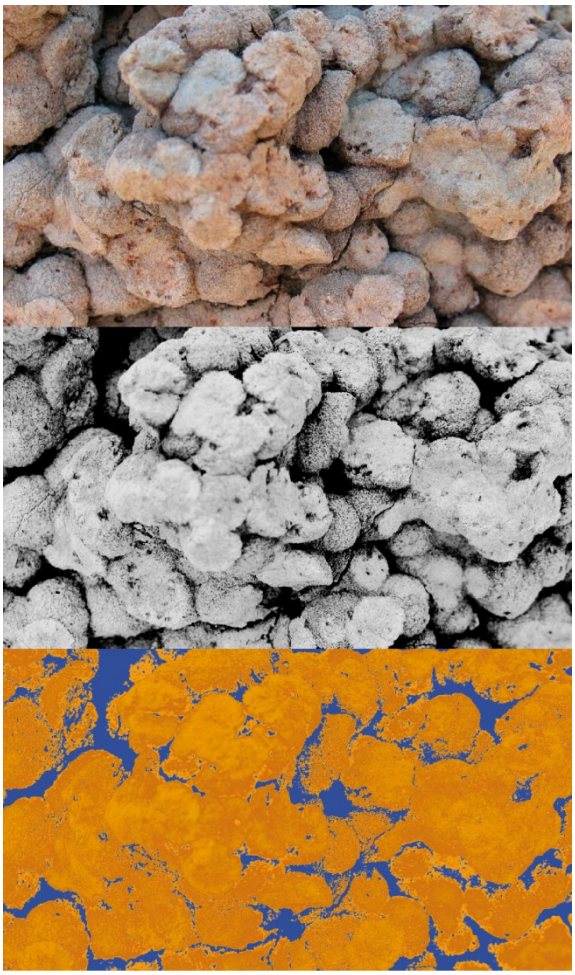

Figure 37: Example of image processing for minimum estimates of the fluid fraction. The contrast is set to maximum values and colour saturation is set to zero. By using the "select colour range function" with an appropriate tolerance value, the area covered by spherules is coloured in orange. The "inverse selection function" allows colouring the voids in blue. The relative proportions of blue and orange pixels are determined using the histogram function. The image width corresponds to ~2.5 cm.

Table 4: Relative proportions of fluid in solute calculated based on image processing. Four different photographs of the outcrop served as a basis for the calculation (Figure 37). Data reveals an extraordinary high fraction of solute. In average one fifth corresponds to the voids (escaped H_2O).

vol.% Fluid	vol.% Solute
28	72
14	86
13	87
20	80

The bulk major- and trace (Fig. 18) element composition of the late stage fluid precipitate largely corresponds to compositions of fresh UPL glass spheroids (Fonseca et al., 2017). Rubidium, U and Pb represent an exception, being slightly enriched in the fluid precipitate. Potassic feldspar (sanidine) as well as chlorite can

be assumed to represent the major Rb host in the late stage fluid precipitate (Palmer and Edmond, 1989). The enrichment of U and Pb in the spheroidal late stage fluid precipitate relative to UPL spheroids is interpreted as a result of fluid dissolution. The partition coefficient between melt and fluid ($K_D^{fluid/melt}$) is very low for U in pure aqueous systems. However, the partition behaviour is strongly dependent on the liquid compositions. Due to the formation of stable U-complexes in the fluid, $K_D^{fluid/melt}$ of U strongly increases with fluoride, chloride and CO_2 content. Chloride thereby most drastically increases the U solubility (Keppler and Wyllie, 1990). Similarly Pb has been shown to be mobile in fluids generated/relieved in subduction environments (Leeman, 1996).

Observations on similarities in bulk chemical compositions of the fluid precipitate and the spheroidal UPL tholeiites such as the location within primitive basalts confirm the generation of spheroidal fluid precipitates to be related to unmixing of a fluid or aqueous gel. The primitive basalts hosting the spheroidal precipitates initially dissolved about 4 wt.% H_2O, at temperatures around 1100 °C such a melt unmixes a fluid at crustal emplacement pressures.

Clinopyroxene exists as phenocrysts, displaying disequilibrium textures present as chemical zonation (Fig. 30). Towards the grain boundaries of pyroxene, the iron- and CaTs content increases (Fig. 38). Progressive Ca-enrichment within the cores might be the result of changing fluid composition. It has been shown that the Al-content in pyroxene is pressure sensitive (McCarthy and Patiño Douce, 1998). In this case it is rather unlikely that alumina is controlled by pressure effect as its enrichment is coupled to iron. Iron and Al are most likely substituted into the pyroxene structure as ferrous CaTs molecules representing a stable phase dissolved in the fluid.

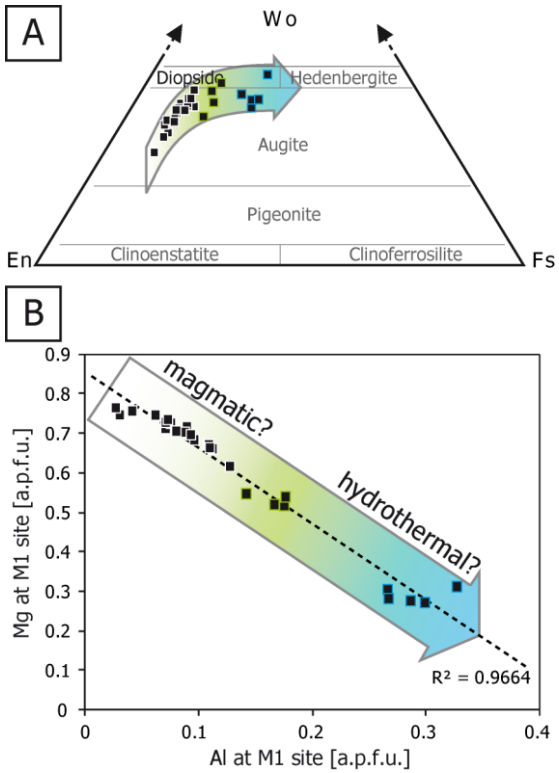

Figure 38: Pyroxene composition in the late stage fluid precipitate. (A) Pyroxene classification within the enstatite, wollastonite, ferrosilite sphere. Pyroxene compositions are generally augitic. (B) Binary plot displaying the CaTs substitution on M1 site (Si-Al exchange accordingly on T site). Al increasingly substitutes Mg, Al rich pyroxene compositions correspond to resorbed rims and might represent hydrothermal (auto-) metasomatism

5 PRELIMINARY SUMMARY AND CONCLUSIONS

Anorthositic dykes on Cyprus represent intrusive rocks precipitated from a magmatic fluid. This magmatic fluid contained a high fraction of dissolved silicate components and might be rather described as a viscous gel. The generation of such a gel is related to unmixing phenomena of a H_2O saturated melt, which, in turn is generated from a refractory mantle in a subduction related environment.

From crosscutting relations with the UPL supply channels it is inferred that anorthositic liquids were generated after the intrusion of the UPL extrusive sequence. Anorthositic dykes transect UPL supply channels in a small angle rather than squeezing in between using routing paths. Consequently it can be assumed that anorthosite dykes did not inject as an immediate succession following the UPL extrusive event. Anorthositic dyke injection is inferred as two consecutive stages,

first injecting the smaller dykes followed by the injection of larger dykes. The temperature gradient between the injected liquid (T ~ 800 °C) and the surrounding UPL supply channels is large enough to quench the remaining "melt" fraction. It is therefore concluded that mineral constituents of the primary assemblage of anorthosites (anorthite, diopside, titanite, rutile and zircon) precipitated before dyke injection. This assumption is further supported by various textures involving thomsonite, the replacement product of glass: (i) anorthosite liquid "intrudes" as an emulsion of zircon-titanite-diopside-anorthite crystals in melt, with processes comparable with "filter pressing" (Fig. 8C), and (ii) diopside and magnetite is quenched from the anorthosite residual liquid (Fig. 8A/B/D/F). Furthermore the observation of clusters of diopside and accessories could be related to the intrusion as a crystal-melt mixture. Trace element finger print of anorthosites is not unambiguous revealing a complex history of the liquid source. However, similarities to late TOC extrusives such as boninites are apparent. Not surprisingly, as they have a mutual source, the mantle, being subject of changes due to the formation of Troodos oceanic crust.

However it is evident that the source of anorthosites is affected by even more processes than the melting of a depleted refertilized mantle. The extreme enrichment in Nb, Ta, Zr and Hf cannot be solely attributed to crystal fractionation revealing further enrichment processes to be necessary. A perfect correlation of Lu with $^{176}Lu/^{176}Hf$ is observed in anorthosites but not in other effusive TOC rocks. This correlation reveals that the isotopic ratio in anorthosites is only controlled by the HREE content. This HREE controlled process has to account for the generation of the anorthosite signal. Zircon appears as the major Hf and HREE host. The hafnium isotopic system in anorthosites therefore is governed by zircon

appearances. Two different signals are inherited by zircon as apparent in age corrected εHf vs. $^{176}Lu/^{176}Hf$ data. Zircon in group III displays a signal of the melt from which the anorthosite "liquid" exsolved. Zircon probably precipitated from that highly fractionated melt, which could represent an evolved boninite composition prior to H_2O saturation. Upon unmixing, zircon is partly transferred into the liquid fraction. Due to its ascent, the unmixed fluid-zircon mixture is not able to reequilibrate with the melt fraction and continuously changes composition. As a result zircon has to equilibrate with the changing liquid composition. Zircon in group I and II displays a different trend. Probably such zircon compositions represent direct precipitates from the liquid immediately after unmixing. This assumption is further supported by the titanite mineral chemistry. Titanite within group I appears to be most influenced by a hydrothermal event but at the same time preserves the most primitive compositions. Moreover, minor differences in trace element composition occurring within different anorthosite groups are attributed to variable proportions in accessory minerals.

Alteration processes, such as albitisation and thomsonite formation are assumed to occur after emplacement of dykes in the Troodos oceanic crust and are related to fluids of ocean floor spilitization. The Sr isotopic signal indicates the influence of cretaceous seawater.

The generation of the late stage fluid precipitate is closely related to UPL lavas. Similarly as for anorthosites they represent the solute fraction of a fluid that equilibrated with the melt fraction at depth. Enrichment in Rb, U and Pb relative to UPL compositions is attributed to its genetic relation to a hydrothermal fluid. The spheroids are assumed to represent the solute charge of a highly fractionated melt.

SECTION III: EXPERIMENTAL APPROACH

1 EXPERIMENTAL AIM

The detailed investigation of anorthositic dykes revealed that they represent precipitates of a solute rich magmatic fluid. The generation of such a fluid is supposed to be related to unmixing processes from highly fractionated melts. However, field evidence and geochemistry suggest that the anorthositic compositions are somewhat associated with UPL lithologies. It is speculated that the anorthositic liquid has a mutual source with boninites. Derivative melts remaining in magma chambers that supplied boninitic extrusives reach H_2O saturation upon fractionation of diopside and forsterite, accumulating the anorthite component finally unmixing a solute rich fluid.

Experiments are performed to assess several aspects of the generation of the anorthositic liquid. The overall topic of the experimental work might be summarized as liquid-liquid immiscibility, a volatile aspect in petrology, relevant for many ore forming processes. Experiments aim to attain a better understanding of fluids coexisting and unmixing with/from a silicate melts.

Four different sets of experiments are performed: i) liquidus experiments at 500 MPa with the piston cylinder apparatus (PCA) to determine the hydrous melting temperature of the anorthositic assemblage, and to identify the liquidus phase, ii) experiments at 500 MPa and various temperatures in the pseudo-ternary H_2O saturated anorthite - diopside – forsterite system to delineate phase relations, iii) H_2O bearing decompression experiments using the piston cylinder and iv) an internally heated pressure vessel (IHPV) to test whether a hydrous mafic melt could evolve to compositions such that the unmixing solute rich fluid could generate anorthositic compositions.

2 EXPERIMENTAL TECHNIQUES

2.1 CAPSULE PREPARATION

Platinum capsules are used for all experiments. Capsules are prepared from 14 mm long rod pieces with an outer diameter of 4 mm and a wall thickness of 0.5 mm. The use of Pt capsules has the advantage of largely behaving chemically inert at high temperatures and having melting temperatures well above 1700 °C. Furthermore Pt capsules absorb most of the iron in the melt during the experiment. This might be considered as a disadvantage but can be neglected for the investigated low iron systems. To remove organic matter (oil is used for the industrial manufacturing process of the tubing) and to anneal micro fissures, the rods are cleaned with acetone and sintered for 3 h at ~ 900 °C in a batch furnace.

Experimental charges of all performed experiments contain H_2O. The success of these experiments largely relies on adequate capsule preparation. To prevent water loss upon capsule filling, about 2/3 of the sample powder is crammed into the capsule and the water is added on top using a microsyringe. The remaining sample material is added and gently compacted. The capsule is closed and welded. To minimize water loss during welding a wet tissue is tightly wrapped around the capsule and injected with a coolant spray (-30 °C).

The capsules are restored after the experiments and a 0.5 mm hole is drilled into the lower end of the capsule; if a liquid expels the experiment is considered to be successful and H_2O loss during the experiment can be vastly excluded. As double check for water loss upon welding and during the experiment, the capsule is weighed before and after the experiment. The capsule is dried at 60 °C for 3h in the

batch furnace. The entire capsule is impregnated in epoxy under vacuum, embedded into an epoxy mount and dragged and polished at the desired section.

2.2 BRISTOL TYPE PISTON CYLINDER APPARATUS

The piston cylinder apparatus (PCA) is a solid media device for generating simultaneously high pressure and temperature, allowing simulations of middle and lower crust conditions. The PCA is particularly suitable to perform experiments of this study, as it allows a sample volume which is large enough to be equilibrated with an aqueous fluid, at crustal pressure and temperature conditions.

Experiments of this study are performed with a 0.5 inch (= 1.27 cm) Bristol type pressure vessel of the facilities at the university of Bonn. The main components of the piston cylinder are labelled on the photograph in Fig. 39A/B. The temperature in the sample chamber during the experiment is monitored by a type C (WRe_{96} and WRe_{30}) thermocouple which has an accuracy of ± 1 °C. Quenching after the experiment is achieved by turning off the electrical current (operation power is set to 0), allowing a quench rate of about > 150 °C/s. The average quench rate is calculated based on observations from the temperature logging after setting the output power to zero

The assembly used for the piston experiments is illustrated in Fig. 39C. It is composed of talc as pressure transmitting media and PYREX®, a low-thermal-expansion borosilicate glass which mantles the furnace, a high resistivity graphite cylinder. To increase the slippage of talc, the assembly is warpped in Teflon-foil.

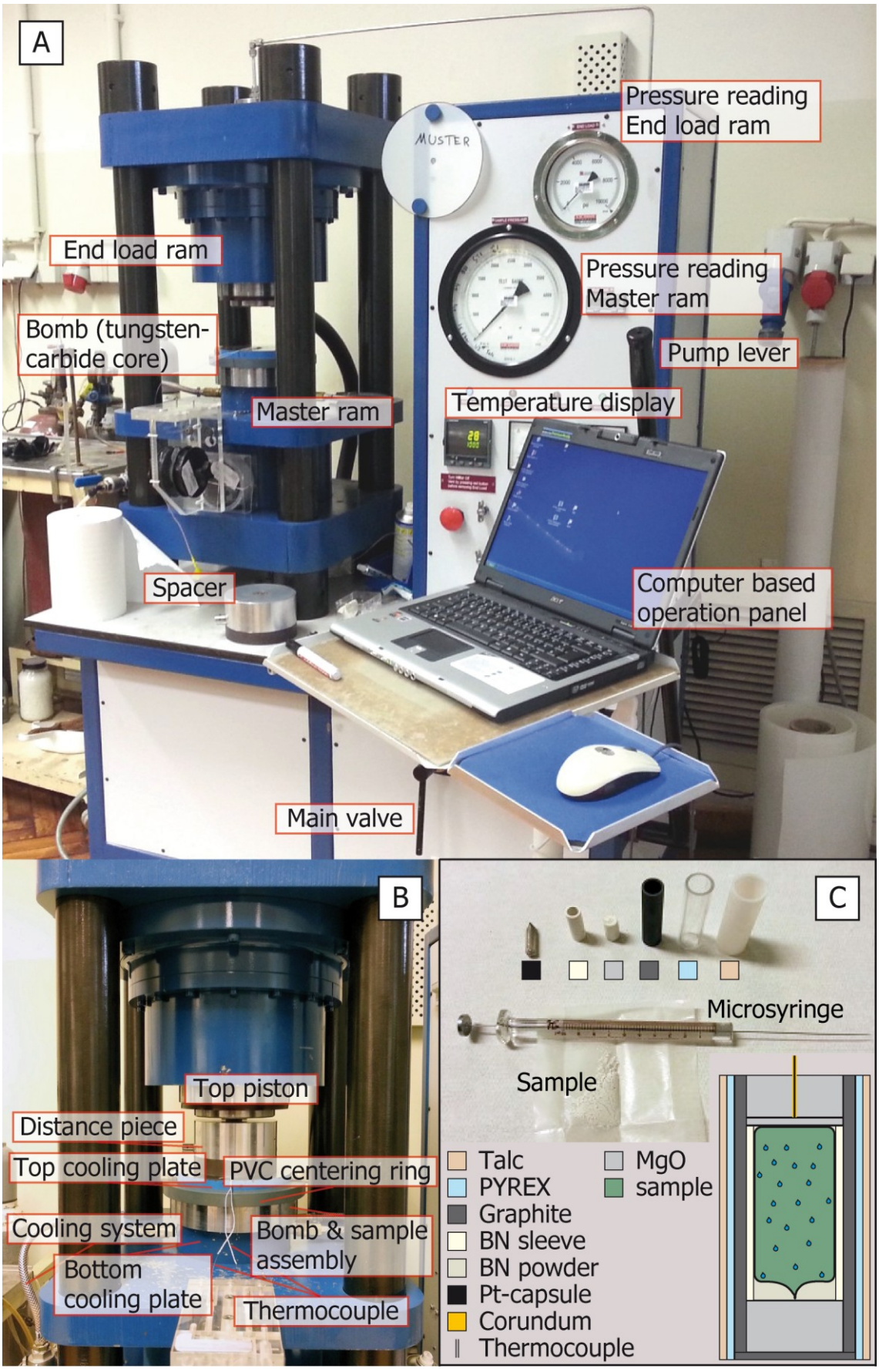

Figure 39: A/B) photographs of the Bristol type PCA at the Steinmann-Institute of the facilities at the university of Bonn; C) Photograph of the experimental assembly and sketch of the sample chamber.

2.3 INTERNALLY HEATED PRESSURE VESSEL

By definition an IHPV has a heating element, the furnace, contained inside the vessel and therefore under the same pressure as the sample (Fig. 40). An Ar-H_2 mixture is used as pressure medium and to adjust redox conditions inside the vessel. Compared to the piston, the usage of IHPV enjoys the advantages of smaller pressure and temperature uncertainties and larger sample volumes being pressurized. Furthermore these vessels are capable of holding samples of 30 cm^3 at pressure and temperature (1100 – 1500 °C) for long periods of time. The general features of a typical IHPV used for geological applications have been described by Holloway (1971).

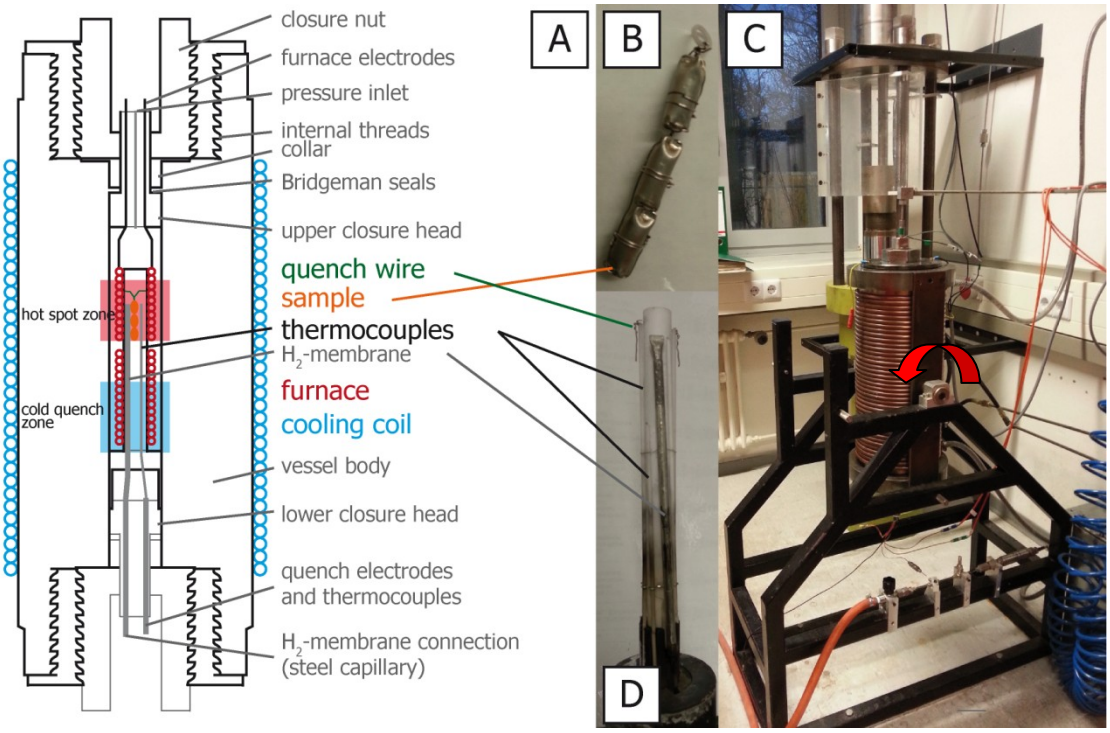

Figure 40: A) Schematic cross section of the vessel body of an IHPV equipped with rapid-quench-H_2-membrane device, redrawn after Berndt et al. (2002). B) Photograph of the sample chain which is inserted into the hot spot zone. C) Photograph of the vessel body with gas inlets cable connected to the P-generating devices and electric leads to control T. The red arrow marks the hinges along which the vessel body is turned horizontal. D) Photograph of the ceramic sample container. The sample chain is suspended onto the quench wire. The Shaw membrane and the thermocouples are fixed at the outside of the sample container. The sample container is screwed into the vessel body.

Berndt et al. (2002) presented a modified setup of IHPV comprising a hydrogen sensor membrane made of platinum (Shaw membrane) to measure f_{H2}, and therefore f_{O2}, and a rapid-quench system to avoid crystallisation of low-viscosity melts during quench. This experimental setup was successfully tested by Berndt et al. (2002) for temperatures up to 1250 °C and pressures up to 500 MPa. Basaltic melts containing up to 9.38 wt.% H_2O can be quenched as bubble-free and crystal-free glasses. A slightly modified design is used for the IHPV decompression experiments of this study, which are performed with the IHPV of the facilities of the Institute for mineralogy at the Leibniz University Hannover.

2.4 Experimental procedure Liquidus experiments

The experimental charge, containing 150 mg of previously dried (3 h at 80 °C) powder of the anorthosite sample ZY80L, and 9 µl tap water (according to 6 wt.%), is filled into a Pt capsule. The assembly is inserted in the pressure bomb (Fig. 39A/B). The entire setup is now loaded with the end load ram to 5000 psi. To ensure contact with the thermocouple, the sample pressure is set to 200 psi by pumping up the master ram. Temperature and pressure are increased simultaneously to the target values. The average heating rate is about 80 °C/min. Liquidus experiments were performed at 500 MPa corresponding to 380 psi end load and 1200 °C, 1150 °C, 1050 °C and 950 °C.

2.5 Experimental procedure simple system experiments

Thirty-one experiments at 500 MPa and temperatures ranging 1000 – 1200 °C are performed in the H_2O saturated anorthite-diopside-forsterite system to delineate the phase relations. As starting material synthetic anorthite and diopside glasses, and a mineral separate of natural forsterite (X_{Fo} = 0.92) from a refractory mantle

xenolith are used. The glasses are prepared from oxide powders (SiO_2, Al_2O_3, MgO and $CaCO_3$) mixed in the stoichiometric proportions of anorthite and diopside. Prior to weighing and mixing, the MgO and SiO_2 powder are dehydrated (according the reaction of brucite to MgO) for 3 h at 1000 °C in a batch furnace. The stoichiometric mixtures of SiO_2, Al_2O_3 and $CaCO_3$ for anorthite, and SiO_2, MgO and $CaCO_3$ for diopside respectively are decarbonated for 12 h at 950 °C. Five gram of each powder are fused in a 40 ml $Pt_{90}Rh_{10}$ crucible with a lid in a NABERTHERM® chamber furnace equipped with KANTHAL® $MoSi_2$ heating elements (facilities GZG University of Göttingen). The anorthite glass is fused in two steps; the crucible is inserted into the furnace at about 1400 °C and heated at 1600 °C for about 270 min, the furnace is cooled to 1500 °C (cooling rate of 1 °C/s) and the crucible is subsequently water-quenched, the glass is grinded and fused again for an hour at 1600 °C. The procedure for fusing diopside glass is slightly different; the crucible is inserted into the furnace already at 1200 °C and three fusing steps are necessary to obtain homogeneous glasses. A RETSCH® mortar grinder is used to grind the glasses into powder. The mineral-powders are mixed in different proportions of anorthite, diopside and forsterite for the different experiments. Starting material is always dehydrated in the batch furnace at 900 °C for several hours before being weighed and filled into the capsules. In total 140 mg of the powder mixes and 8.4 µl tap water (according to 6 wt.%) are filled in the capsules. Runtime of simple system experiments is 4 – 5 h ensuring equilibration of different phases. Equilibration can be assumed to occur after several minutes at 1000 °C and 500 MPa due to the high H_2O content. Performed experiments and run conditions are listed together with major element composition of experimental run products in table IX in the appendix.

2.6 EXPERIMENTAL PROCEDURE PCA DECOMPRESSION EXPERIMENTS

Three decompression experiments were performed with the piston cylinder. Additionally, one experiment was performed without decompression and used as a reference. As starting composition drill cores of a fresh spheroidal basaltic glass sample from Kalavassos (UPL) are used. The nature and composition of such basaltic UPL spheroids are described by Fonseca et al. (2017). Drill cores are thoroughly grinded with an agate mortar. The rock powder is dried in the batch furnace for 2 h at 100 °C before being filled (150 mg) into the Pt capsules. Fifteen µl (according to 10 wt.%) tab water is added with a microsyringe. For the chromite bearing experiment about 1 mg colloidal chromite powder is intermixed with the rock powder. The experimental charge is equilibrated at 1000 MPa and 1150 °C for 3 h before being decompressed to ~ 250 MPa. Decompression to lower pressures is constrictive, as a minimum pressure is required to permit contact with the thermocouple. To (isothermally at 1150 °C) decompress the sample chamber, the main valve is opened and the valve for sample pressure quickly opened and closed such that the pressure relief from 1000 to 250 MPa is achieved to be stepwise within 30 min (~ 28 MPa/min). To prevent the thermocouple to burn through, the maximum output power is set to the actual value (otherwise the sudden decompression would result in a rise of output power due to a theoretically lower resistivity of the furnace). After isothermal decompression, the system is stabilized for ~ 2 h. The system is cooled (0.3 °C/min) to 650 °C for PCADecExp and PCADecExpCr. For PCADecExprep the temperature is set to 600 °C, after 2 h at 1150 °C and 250 MPa before being cooled to 200 °C. During cooling the pressure is monitored and regularly readjusted to 250 MPa. After cooling, the system is quenched. One experiment (starting composition) was performed without decompression, the powder of the UPL basaltic glass is equilibrated with

10 wt.% H_2O at 1150 °C and 1000 MPa for 5 h; the obtained glass is used as a reference.

2.7 *Experimental procedure IHPV decompression experiments*

The two IHPV decompression experiments are performed in the "white" vessel of the facilities in Hannover as this vessel is equipped with a high-pressure low-flow metering valve which allows to conduct decompression experiments with continuous decompression rates (~0.0002 to >10 MPa/s). The vessel allows a maximum heating rate of 80 °C/min and is PC-operated (using IDL's ITOOLS®) permitting to regulate the temperature path and logging of P_{total}, $P_{(H2)}$ and T.

Rock powder of the UPL basaltic spheroid is used as starting material. One experiment containing 8 wt.% and the other 5 wt.% H_2O, as labeled in the sample names; IHPVDecExp-8-3 and IHPVDecExp-5-3. One experiment of this run failed (it imploded during pressurization) and is thus not further mentioned. The capsules are ranked one above the other with a Pt-wire (Fig. 40B). A ceramic ring is fixed at the top of the sample chain and the chain is suspended into the ceramic tubing equipped with the Shaw-membrane and thermocouples (Fig. 40D). The entire assembly is screwed into the vessel body which is therefore turned horizontal (Fig. 40C). The sample vessel is turned vertical and the gas inlets and power supply cables are connected. The vessel is flushed with Ar-gas before the vacuum pump is switched on to evacuate the vessel body. The membrane pump is used to pre-pressurize the system followed by the intensifier, both using Ar as pressurizing media. The redox condition in the sample chamber is adjusted to FMQ+1 by adding H_2. Before the pressure conditions for the experiments are achieved (500 MPa), the temperature ramp (80 °C/min) is initiated via PC. Due to gas expansion, the total pressure increases, the pressure excess is relieved. Starting conditions are

500 MPa and 1150 °C and held constant for an hour (1150±10 °C). The system is near-isothermally (1100-1165 °C) decompressed within 40 min to 150 MPa. The system is reequilibrated at 150 MPa and 1150±5 °C for 80 min and subsequent isobaric cooled to 700 °C within 25 h (cooling rate of 0.3 °C/min) and quenched. To quench, the quench wire is energized, the quench rate is ~ 150 °C/s.

3 EXPERIMENTAL RESULTS AND PRELIMINARY CONCLUSIONS

3.1 LIQUIDUS EXPERIMENTS

The liquidus experiments are performed to address two major questions: What is the liquidus temperature of the bulk composition of anorthosites? Does anorthite precipitate as liquidus phase? These questions are essential to understand whether the anorthositic dykes could represent liquid compositions intruding the upper crust.

Experiments were performed at 500 MPa and 1200 °C, 1150 °C, 1050°C and 950 °C respectively. A temperature of 950 °C still corresponds to super solidus conditions in the hydrous system. The experimental charge of experiment AnL-1200 is completely molten. The quenched glass notifies H_2O saturation by the presence of small degassing bubbles. Furthermore glass globules appear in the uppermost capsule area. As a consequence the upper cavity must have been filled with fluid at time of glass formation. The interface of the main glass proportion and the cavity in the top of the capsule is dished, also indicating a former interface against a fluid (Fig. 41A).

Anorthite (~ X_{An} = 0.98) appears as a stable phase in experiment AnL-1150. Crystals are intergrown with sponge like crystallized anorthite slightly enriched in the albite component (X_{Ab} = 0.1 – 0.4) reminiscent of quench textures (Fig. 41B).

The amount of crystallized anorthite increases with decreasing run temperatures, experiment AnL-1050 is crystallized to ~ 40 % (Fig. 41C) and at 950 °C the system appears to be close to the solidus being largely crystallized (Fig. 41D). Glass compositions of experimental run products are quartz, corundum and orthopyroxene normative, indicative of a silica saturated, peraluminous, subalkaline system (Yegorov et al., 1998). Furthermore the CIPW norm reveals anorthite and albite. The H_2O content of glasses quenched from different liquidus experiments scatters around 6 wt.% (Fig. 41E). The increase of the crystallized fraction of experimental run products is reflected in the glass compositions by increasing normative silica contents (Fig. 41F and Table 5). Furthermore glass compositions of low temperature runs (AnL-1050 and AnL-950) display higher normative albite contents (Fig. 41F). Temperatures suggest the melt to be H_2O saturated at run conditions. Theoretically the H_2O content is expected to increase with decreasing temperature; at lower temperatures the relative melt fraction decreases and no hydrous phase precipitates which could additionally accommodate H_2O. Therefore a change in the capacity of the remaining melt (after plagioclase extraction) to dissolve H_2O is assumed.

Table 5: Summary of experimental run products from liquidus experiments indicating the relative proportions of glass and anorthite and the normative quartz and anorthite content.

	% glass	**$CIPW_{Qtz}$**	**$CIPW_{An}$**	**% Anorthite**
AnL-1200	100	2	60	0
AnL-1150	98	11	50	2
AnL-1050	60	20	33	40
AnL-950	10	21	31	90

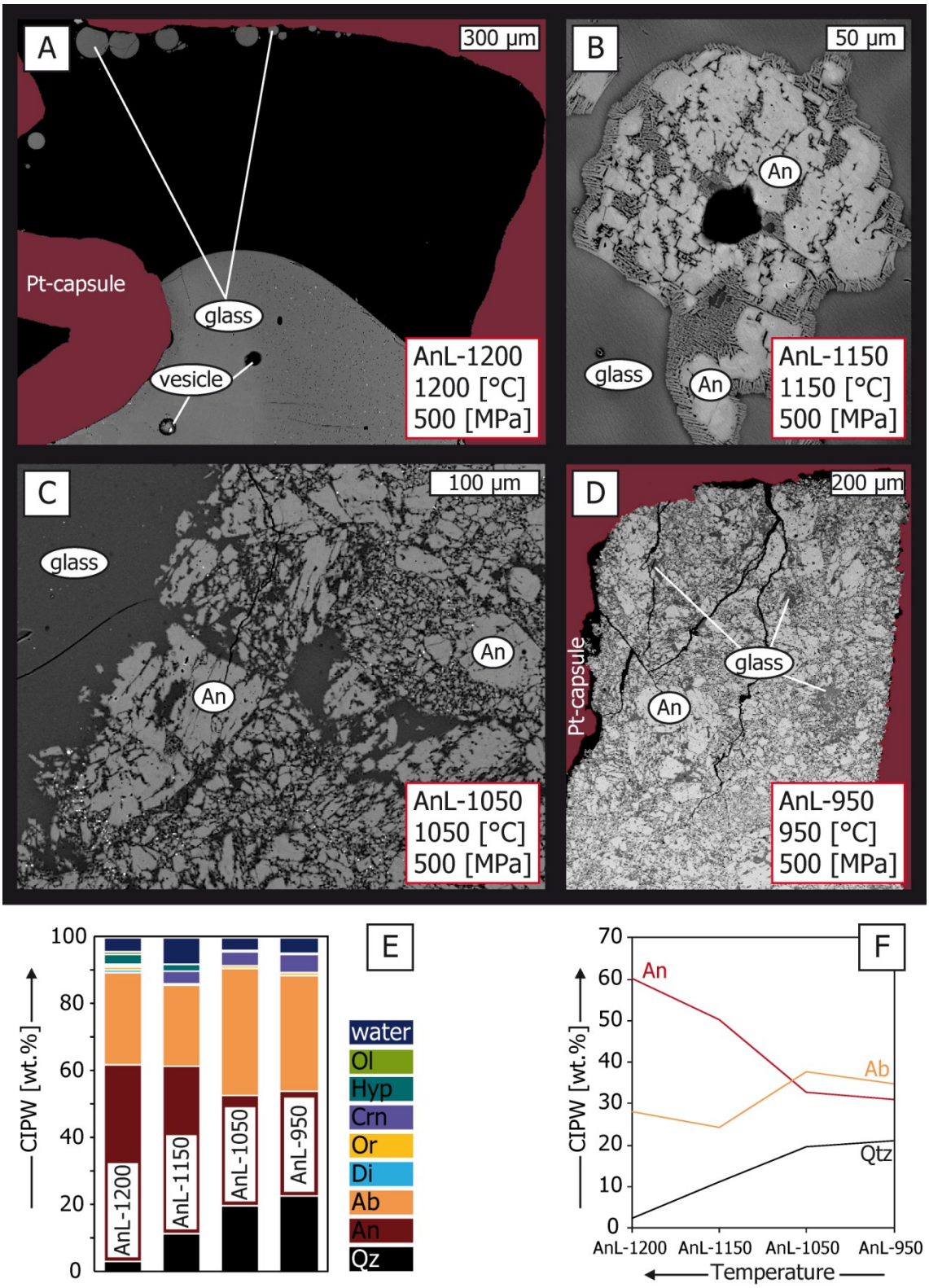

Figure 41: (A) Run product of experiment AnL-1200 showing the upper part of the Pt-capsule. The melt fraction is quenched to glass containing vesicles. Note the small glass spheroids in the top which were probably quenched within the fluid. (B) Anorthite crystal precipitated within the AnL-1150 experiment. Fibrous crystals surrounding the anorthite are enriched in albite component. Note that the texture does not reveal equilibrium anorthite crystallisation. (C) Melt pool surrounded by anorthite crystals in experiment AnL-1050. D) Largely crystallized experiment AnL-950. (E) Histogram displaying CIPW-normative composition of glasses quenched from liquidus experiments. The H_2O content is calculated by difference. (F) Binary plot displaying the relative CIPW normative content of quartz, anorthite and albite calculated in glasses of liquidus experiments.

McMillan and Holloway (1987) showed, that addition of 28 mole% diopside component or up to 67 mole% SiO_2 to anorthite melt has little effect on H_2O solubility. Similar H_2O contents of ~ 6 wt.% H_2O in glasses quenched at different

The observation that interstitial glass pods in low temperature experiment (AnL-950) are enriched in sodium component is interpreted to be the result of albite melting prior to anorthite melting. Dry melting relations of the plagioclase solid solution have long known fact (Bowen, 1913) with albite having a much lower melting temperature compared to anorthite. Hydrous melting relations in the plagioclase system at 500 MPa have been described by e.g. Yoder et al. (1957) suggesting a decrease of the melting temperature of anorthite to about 1240 °C and to ~ 750 °C for albite. The observed melting of anorthite in liquidus experiments at temperatures below 1240 °C (system entirely molten at 1200 °C in Anl-1200) might be attributed to i) the minor albite component in anorthite, or ii) the fact that the anorthositic system is more complex than the simple plagioclase-H_2O system probably effecting melting temperatures.

Major results from liquidus experiments can be summarized as follows:

- The liquidus of the hydrous anorthite assemblage is determined at temperatures between 1150 and 1200 °C
- Anorthite (X_{An} = 0.93 – 0.98) is defined as liquidus phase in the hydrous anorthositic system.
- 6 wt.% H_2O corresponds to H_2O saturation at 500 MPa in the anorthositic system.

Textures observed in anorthosite dyke rock samples suggest that the dykes were injected as a liquid that crystallized anorthite and diopside prior to intrusion. The

performed liquidus experiments confirm that assuming H_2O saturated conditions the solidus in this system is below 950 °C, a realistic temperature of intrusion. Compositions of experimental run products are listed in table VIII in the appendix.

3.2 Phase relations in the H_2O saturated Anorthite – Diopside – Forsterite System

Proceeding on the assumption that anorthositic dykes were injected as a liquid in equilibrium with anorthite and diopside it should be possible to describe the system in a phase diagram. According to the phase rule, the degree of freedom in the relevant ternary system is one – the cotectic line, where anorthite diopside and liquid coexist. However, considering the composition of the derivative melt (55 – 63 % normative anorthite assuming thomsonite corresponding to glass compositions) coexisting with anorthite and diopside, no appropriate phase diagram exists. In a simplified experimental frame, the anorthosite assemblage should be delimitable within the H_2O saturated anorthite – diopside- forsterite system. Under H_2O saturated conditions it can be expected that the stability field of the highest polymerized phase (in this case anorthite as tectosilicate) will decrease at expense of the phase with lower polymerization (forsterite as neosilicate). As a consequence the eutectic melt composition has to be enriched in the anorthite component. Simple system experiments were performed to delineate the pseudo ternary H_2O saturated anorthite – diopside – forsterite phase diagram. Furthermore it should be tested whether anorthositic dykes could represent precipitates of a solute rich fluid.

Interpretation of simple system experiments clearly displays the tendency of the system to dissolve a solute saturated fluid fraction. Within each experimental capsule it has to be distinguished between the H_2O saturated melt fraction, and the

melt saturated fluid fraction (Fig. 42). The spatial separation of these fractions is very clear in most experiments with a glassy area at the bottom of the capsule and a porous largely crystallized section at the top. The transition between the sections generally appears to be sharp, whereas a gradation in crystals, crystal size, porosity and dispersion of vesicles is visible in the area of former melt saturated fluid (Fig. 42A). However, the investigation of the phase relations within the H_2O saturated melt fraction was constructive. The unexpected set of problems of liquid-liquid immiscibility is discussed separately.

3.2.1 THE H_2O SATURATED MELT FRACTION – PHASE RELATIONS

All constraints on phase relations oppose the assumption of equilibrium between the analysed phase compositions. Phases of the H_2O saturated melt fraction include forsterite, diopside, a H_2O rich liquid and a melt. Anorthite does not crystallize in equilibrium with the fluid saturated melt but only appears in the fraction of melt saturated fluid.

Glass is quenched from the H_2O saturated melt fraction for all experiments Fig. 42B-D) confirming super-solidus conditions. The glass composition within each experimental charge, displays slight compositional variations attributed to a minor temperature gradient within the capsule. Glass compositions of experiments with identical starting composition but different run temperatures differ largely. Differences rely on the different phases crystallizing at temperatures > 1200 °C. The glass composition deviates to a greater or lesser extent from the starting composition (Fig. 43A). The residual liquid is enriched in the anorthite component with decreasing temperatures and increasing degree of crystallisation (Fig. 43B).

Forsterite (X_{Fo} = 0.93 – 0.99) is the first phase to crystallize from simple system experiments. Depending on the starting composition, precipitation starts already at T > 1200 °C. Forsterite composition is listed in table IX in the appendix. Minor differences in the fayalite component (Fig. 43C) are attributed to the temperature variability (Roeder and Emslie, 1970). Forsterite crystals, reminiscent of quench textures (Fig. 42C), display highest X_{Fo} values.

Pyroxene precipitating from the fluid saturated melt fraction is quite variable in composition (table IX appendix) especially concerning the alumina content. The CaTs component appears to correlate with the ferrosilite component for most experiments but not for those of the starting composition 60:10:30 and 65:20:15 (Fig. 43D). No temperature dependence is observed for diopside compositions. Glass compositions and experimental run conditions are listed in table IX in the appendix. Glass compositions and precipitated phases from simple system experiments can be used to delineate the stability fields of forsterite and diopside (Fig. 43E). Presnall et al. (1978) described the phase relations at 500 MPa under dry conditions as a ternary peritectic system with anorthite, diopside, forsterite, spinel and liquid as stable phases (dashed lines in Fig. 43E). Under H_2O saturated conditions it can be expected that the stability field of anorthite will decrease at expense of forsterite. Indeed, the experiments reveal that the two phase field of forsterite plus liquid expands, pushing the cotectic line with diopside towards the diopside anorthite join (Fig. 43E). The stability field of spinel disappears. The phase boundary towards anorthite could not be detected as no anorthite crystallized from the fluid saturated melt. At the top end of the cotectic line a piercing point can be speculated at temperatures < 1000 °C.

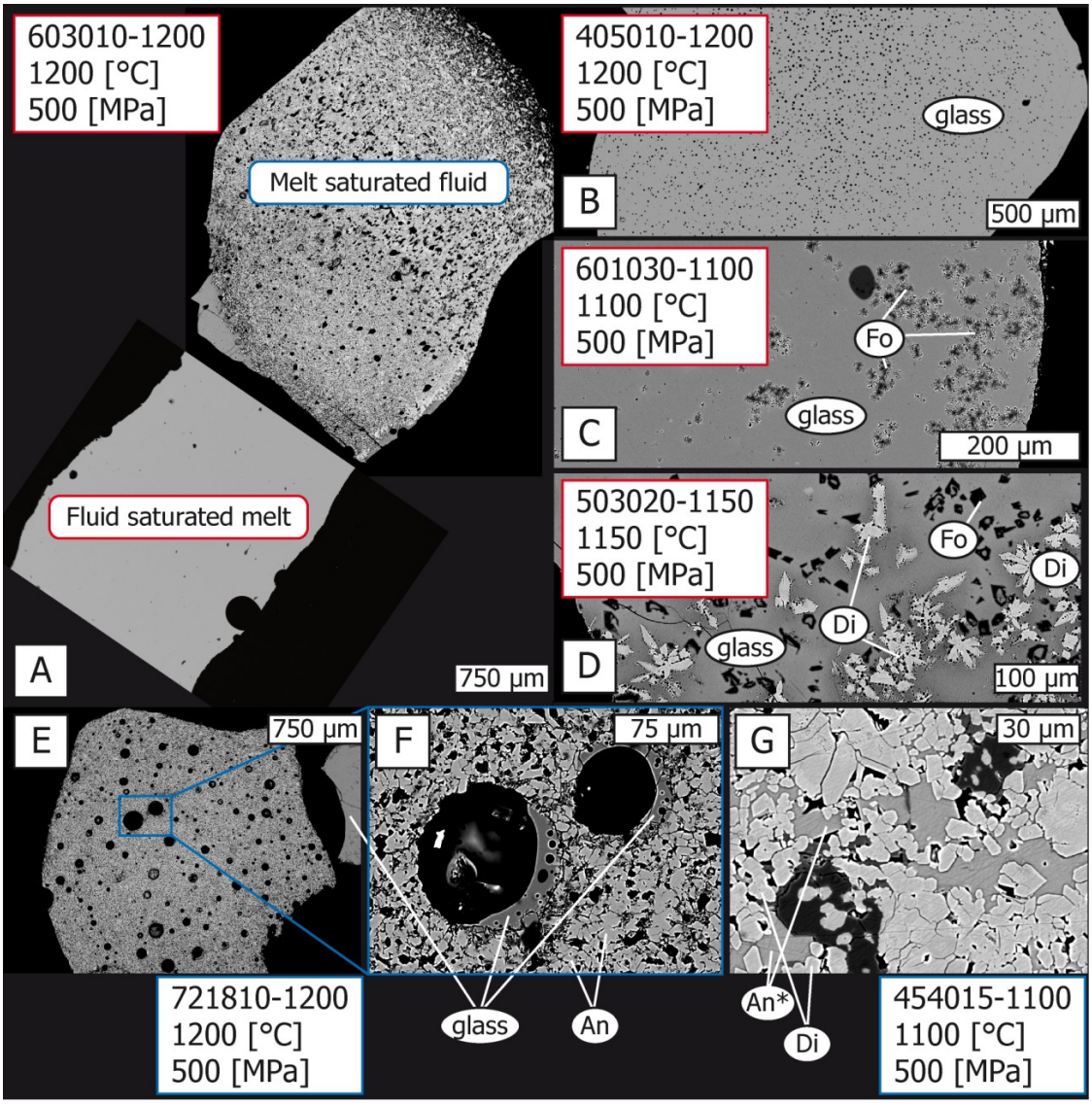

Figure 42: BSE images of experimental run products from simple system experiments: (A) Cross section through the capsule. The lower part of the capsule always displays a glassy area with numerous vesicles, the former H_2O saturated melt; such areas are used for interpretation of phase relations. (B-D) Glassy areas of fluid saturated melt in different experiments. (B) Vesicular glass. (C) Forsterite crystals and quench crystals. (D) Diopside and forsterite crystals in glassy vesicular matrix. Note increased vesicles on Cpx surfaces. (E-G) Images of the former melt saturated fluid. (E) The former melt saturated fluid. The texture is very porous and interspersed with vesicles. (F) Ten times enlarged area of the melt saturated fluid area Figure E displaying two large vesicles surrounded by little melt pods containing small vesicles. Tiny anorthite crystals form a porous matrix. (G) Area of former melt saturated fluid with diopside rich composition displaying CaTs enriched diopside crystals in a matrix of non-stoichiometric anorthite.

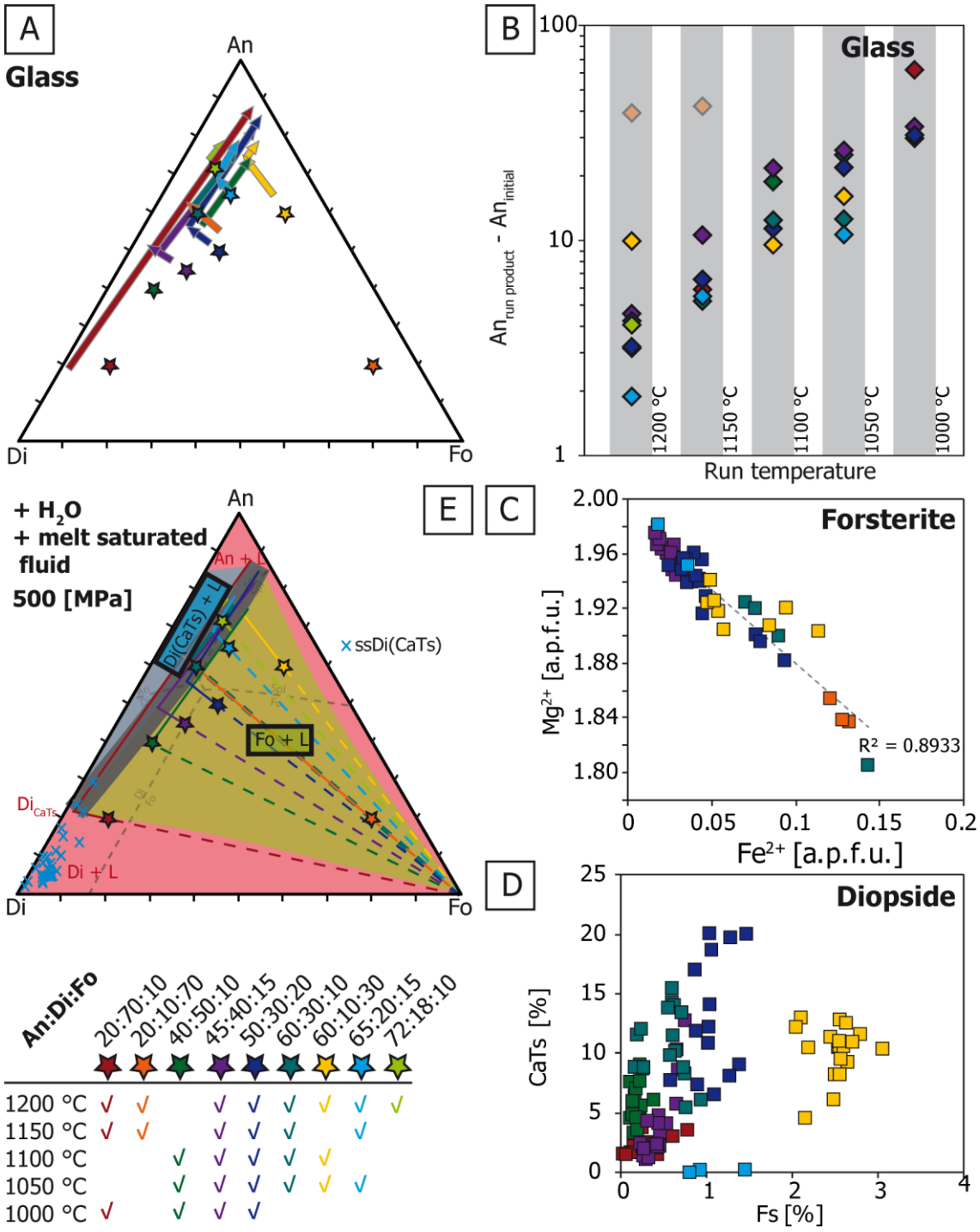

Figure 43: Different colours refer to different An - Di - Fo proportions in the starting material. (A) Ternary plot of normalised An - Di - Fo proportions (regardless quartz) calculated for different glass compositions quenched from the fluid saturated melt fraction. Bold arrows retrace the variability in glass compositions of experiments at different run temperatures. Compositions of low temperature runs plot at the tips of the arrows. (B) Absolute increase of the normative An content with decreasing run temperature in glasses quenched from the fluid saturated melt fraction. As a result of the high Fo content in the starting composition absolute normative An values of experiments 20:10:70 plot slightly off the trend (pale orange diamonds) (C) Binary plot displaying the iron content in forsterite. (D) Binary plot displaying the iron content as ferrosilite component vs. the CaTs component in diopside of crystals in equilibrium with the fluid saturated melt. A positive correlation might be speculated except for starting compositions 60:10:30 and 65:20:15. (E) Simplified isobaric ternary phase diagram of the H_2O saturated anorthite diopside forsterite system at 500 MPa. For facility of inspection the data points of individual experiments are replaced by the proposed liquid lines of descend. The proposed stability

fields phase fields of forsterite and CaTs enriched diopside (two phase fields of Fo + L and Di + L) are indicated in pale green and pale blue respectively. These two fields are separated by the proposed univariant line i.e. the equilibrium line which is derived from the glass compositions. The red fields could not be determined, thus the stability field of anorthite and pure diopside were not identified (indicated in red). A piercing point might be speculated at the top end of the univariant curve at temperatures < 1000 °C. An intermediate phase of CaTs enriched diopside can be speculated at the lower end of the univariant line. Selected compositions of CaTs enriched diopside are plotted as blue crosses indicating a solid solution between CaTs enriched diopside and pure diopside. Dashed grey lines refer to cotectic lines of the dry ternary anorthite diopside forsterite at 500 MPa, redrawn after (Presnall et al., 1978).

3.2.2 *Discourse on the peritectic reaction*

Simple system phase relation experiments give rise to numerous questions theoretically irrelevant for the anorthositic system. However, a short treatise on a possible peritectic in the H_2O saturated anorthite – diopside – forsterite system is included. The lower end of the univariant curve between forsterite and diopside appears to hit the An - Di join at about 80:20 and a peritectic can be speculated close to that join with the CaTs enriched diopside composition as intermediate phase (indicated as Di_{CaTs} on Fig. 43E). The simplified peritectic reaction would be:

$$[Ca]^{M2}[Mg]^{M1}[Si_2]^{T}O_6 + L = [Ca]^{M2}[Mg_{0.8}, Al_{0.2}]^{M1}[Si_{1.6}Al_{0.4}]^{T}O_6 \quad (10)$$

Diopside compositions crystallized from the fluid saturated melt fraction of simple system experiments appear to indicate a partial- to complete solid solution of diopside and CaTs enriched diopside or anorthite respectively. Another scenario could be that the cotectic line hits the diopside forsterite join close (~98:02) and that CaTs enrichment in diopside is the result of disequilibrium with the fluid saturated melt and reequilibration with the melt saturated fluid fraction.

Alumina entering the pyroxene structure is described as Tschermak substitution. Both, the M1 and the T sites (but not M2) are affected by this substitution. Alumina enters as well as the M1 site, substituting for manganese, and the T2 site, substituting silica. Up to 20 % of M1 and T2 sites of diopside precipitated from the fluid saturated melt fraction are occupied by alumina.

Concerning the CaTs enrichment of diopside as a result of a peritectic reaction, it has to be considered that the accumulation of a CaTs component would force the liquid composition to leave the projected anorthite diopside forsterite plane towards silica enriched compositions, as CaTs incorporates less silica than diopside (Fig. 44).

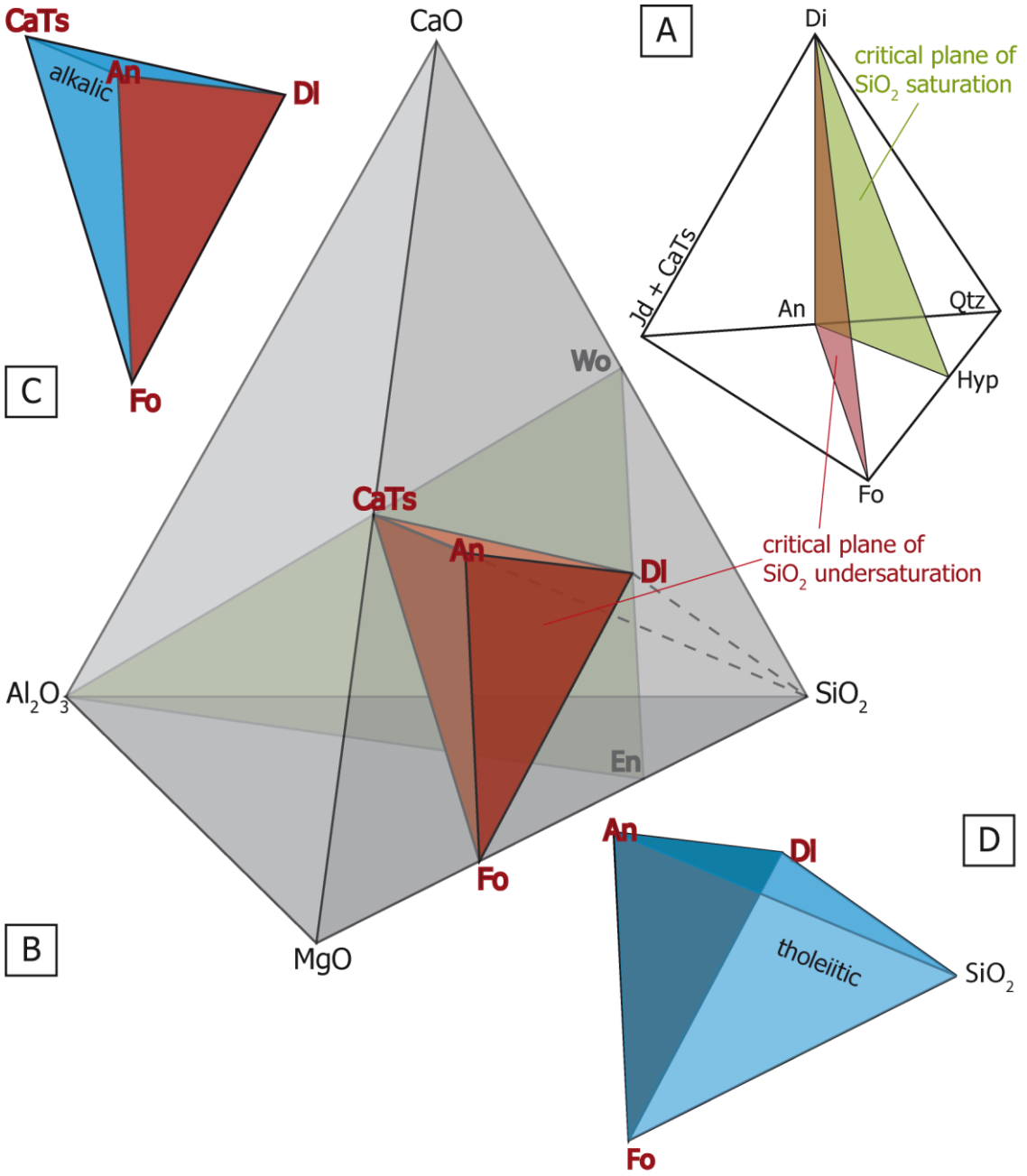

Figure 44: (A) Simplified Basalt Tetrahedron redrawn after Yoder and Tilley (1962) modified after Falloon and Green (1988) for potassium free systems, indicating the planes of silica undersaturation (red) and silica saturation (green). (B) CaO-Al_2O_3-MgO-SiO_2-Tetrahedron to display the An-Di-Fo plane which is equipollent with the critical plane of silica undersaturation. (C/D) Alkalic- and tholeiitic sub-tetrahedra to indicating that CaTs lies off the projected plane of An-Di-Fo.

The possibility to evolve the liquid (the fluid saturated melt in this case) towards more silica enriched compositions is thermodynamically not straight forward (thermal divide between olivine and quartz at the intermediate phase enstatite). This gets obvious when regarding the anorthite diopside forsterite system as part of the basalt tetrahedron (An-Di-Fo plane corresponding to the critical plane of SiO_2 undersaturation indicated as a red plane defined by Cpx, Pl and Ol in Fig. 44A). Experimental run products prove that besides the fluid saturated melt and its related crystal phases (diopside and forsterite) a melt saturated fluid exists in equilibrium. The silica access occurring due to the precipitation of CaTs enriched diopside might be accommodated by the melt saturated fluid. As a consequence the intersection of the cotectic line derived from the performed simple system experiments with the anorthite-diopside join (Fig. 43E) could be a projection artefact as melt compositions leave the projected plane towards silica.

3.2.3 THE MELT SATURATED FLUID

The melt saturated fluid fraction within the performed simple system experiments can be easily determined and discriminated from the fluid saturated melt due to differences in its texture (Fig. 41A). In contrast, determination of its composition is more complex. The fluid saturated melt fraction is well quenchable, forming a silicate glass; the melt saturated fluid fraction is not quenchable. Probably it loses its silicate charge during quenching and the leftover liquid (± pure H_2O at ambient PT conditions) is lost when the capsule is opened.

To get an approach of the composition of the melt saturated fluid fraction, several EPMA analyses were performed on different experiments. The bulk composition of the former fluid fraction should correspond to averaged compositions within a larger area of the upper part of the experimental capsule. Windows of 20 x 20 µm

were scanned with the electron beam and the averaged composition is detected by WDS. The results of this method are plotted in Fig. 45A. In some cases the compositional scatter is very large due to heterogeneities such as gradation in the melt saturated fluid fraction. Nevertheless it is evident that the compositions of fluid saturated melt overlap with compositions of the fluid saturated melt fraction (note that the crystal fraction is not included in data points for glass compositions). The best example is the melt saturated fluid composition of experiments 207010-1200 and 207010-1150. Silicate phases detected in the melt saturated fluid fraction are H_2O free (mainly anorthite and diopside). The only evidence of former H_2O presence in the melt saturated fluid fraction are the numerous vesicles contained in its texture (Fig. 41E/F).

Anorthite occurs as individual crystals (Fig. 42F) having almost stoichiometric anorthite composition in some experiments, in others it appears as interstitial fillings with non-stoichiometric composition. For non-stoichiometric compositions a good correlation ($R^2 = 0.72$) between alumina and silica (Fig. 45B) is striking, but from Raman spectra it can be proved that interstitial anorthite like areas are crystallized.

The melt saturated fluid fraction of the experimental run products of experiments with high initial anorthite content (e.g. 72:18:10 Fig. 41) texturally as well as in composition resembles anorthositic dykes. These observations confirm that dykes probably represent the precipitate of a solute rich fluid.

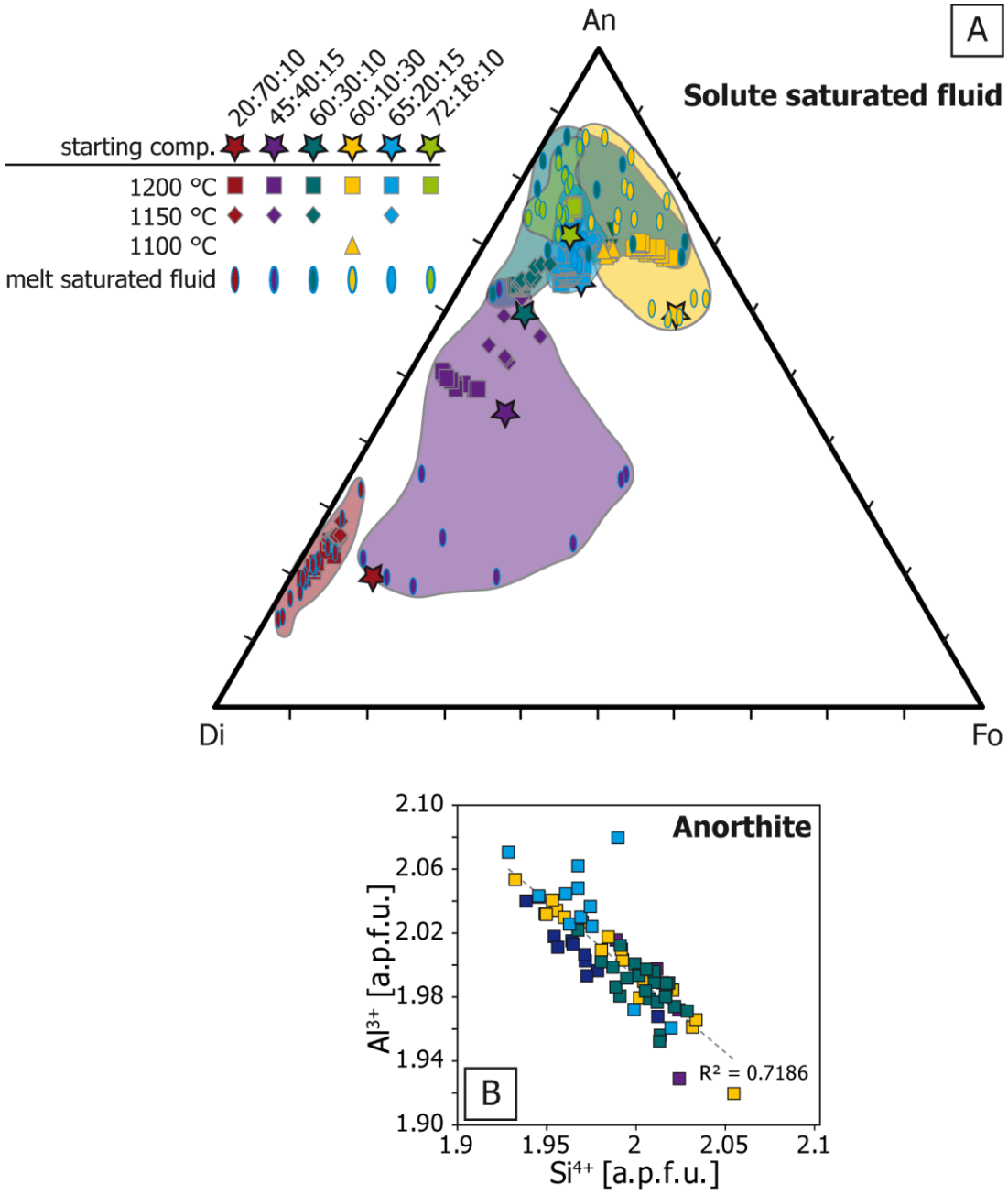

Figure 45: (A) Ternary plot indicating the compositional fields of melt saturated fluid from selected experiments. Compositions were determined as scanned areas of 50 x 50 µm using EPMA. Compositions of the melt saturated fluid coincide with glass compositions of the different experiments. (B) Binary plot displaying variation of Al and Si site occupancy in anorthite precipitated from the melt saturated fluid.

3.2.4 *Discourse on Liquid – Liquid immiscibility*

The presence of a melt saturated fluid coexisting with a fluid saturated melt in all simple system experiments, confirms H_2O oversaturated conditions at 500 MPa (not the entire amount of the 6 wt.% H_2O added can be dissolved in the melt structure). The fluid saturated melt and the melt saturated fluid are physically separated.

Theoretically a silicate melt that reaches saturation with a hydrous fluid behaves like any other system with liquid immiscibility (Philpotts, 1976; Philpotts and Ague, 2009; Roedder, 1951; Roedder, 1979). At H_2O saturation, fluid exsolution occurs because the two separate liquids (fluid and melt) have a lower bulk free energy than the homogeneous system (Cassidy and Segnit, 1955).

Liquid immiscibility, in case of simple system experiments, is manifested in the separation of the melt saturated fluid fraction and the fluid saturated melt fraction (Fig. 42A). According to Fig. 46 at given pressure the melt is saturated with H_2O. Lowering pressure reduces H_2O solubility, leading to oversaturation and liquid separation (path L to m_1 on Fig. 46). Oversaturation means that the fluid saturated melt hits the binodal (indicated as point m_1 sitting on the black dashed line representing the binodal in Fig. 46). At this stage a melt saturated fluid will exsolve (having the composition of point f_1 on Fig. 46). To attain equilibrium, the fluid saturated melt will develop towards compositions containing less dissolved fluid (according path between m_1 to s_1 on Fig. 46) and the melt saturated fluid fraction will develop to a more diluted solute (according path f_1 to f_2 on Fig. 46). But, upon cooling dry phases might precipitate from the fluid saturated melt fraction increasing relative H_2O content of the melt promoting further exsolution (f_x).

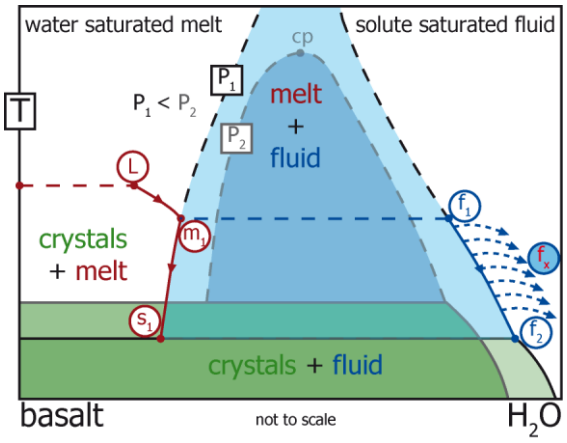

Figure 46: Schematic pseudobinary P–X diagram with melt-fluid immiscibility modified after Mysen (2014) and Ballhaus et al. (2015). Conditions illustrated for P1 correspond to an isothermal section through a hypothetical basalt-H2O diagram in P–T–X space, sectioned at a pressure below the second critical point (cp). Conditions illustrated for P2 correspond to isobaric conditions above the cp. The example indicated with red and blue arrows is described in the text below.

The process of continuous melt relief from the melt saturated fluid fraction is texturally captured in Fig. 41F. The two large vesicles can be interpreted as former pools of melt saturated fluid, upon cooling or decompression (or probably quenching in case of experiments) the fluid needs to expel some of its solute charge which is now visible as a glassy shell around the vesicle.

In theory, assuming equilibrium between melt saturated fluid and fluid saturated melt, the chemical potentials (μ_i) or the partial molar free energies of all components i (i = Al_2O_3, SiO_2, MgO and CaO in the simple system experiments) in the coexisting liquids are identical.

$$\left(\mu_{Al_2O_3}, \mu_{SiO_2}, \mu_{MgO}, \mu_{CaO}\right)^{fluid\ saturated\ melt} = \left(\mu_{Al_2O_3}, \mu_{SiO_2}, \mu_{MgO}, \mu_{CaO}\right)^{melt\ saturated\ fluid} \quad (11)$$

As a result the fluid saturated melt and the melt saturated fluid have to be saturated with the same phases at given PT conditions. Upon cooling this would imply that identical phases (An, $ssDi_{(CaTs)}$ and Fo) with identical phase compositions should crystallize from the fluid saturated melt and the melt saturated fluid. It is possible that the relative proportions of crystalline phases in both fractions differ from each other if cooled below the solidus. The differences in relative proportions of An, $ssDi_{(CaTs)}$ and Fo in the melt saturated fluid fraction and

the fluid saturated melt fraction can be explained by (i) differences in activity coefficients of components in the conjugate liquids, (ii) differences in the activation energies needed to crystallize stable nuclei of crystalline phases in the two liquids, and (iii) differential wetting properties of melt and fluid toward the surfaces of crystalline phases (see Ballhaus et al. (2015) for more theoretical background). However, it should be mentioned that differences in activation energies might have a minor impact, as H_2O rich systems are predominantly controlled by kinetic effects. Neither differences in activation coefficients nor differences in activation energies can be directly observed in the performed experiments. Concerning differences in wetting properties it is noteworthy, that in all experiments that crystallized CaTs enriched diopside from the fluid saturated melt, tiny vesicles aligned on the grain boundaries are observed (Fig. 42D) revealing a bad wetting ability. Anorthite in contrast is assumed to have a very good wetting ability. As a consequence anorthite might be bloated by the melt saturated fluid such that anorthite crystals are scavenged in the melt saturated fluid fraction.

3.2.5 MAJOR FINDINGS

- Liquid-Liquid immiscibility at run conditions (500 MPa and 1000 – 1200 °C)
- Separation of a fluid saturated melt fraction and a melt saturated fluid
- Forsterite and CaTs enriched diopside precipitate from the fluid saturated melt whereas the crystallisation of anorthite is suppressed. The remaining liquid is quenched to vesicular glass
- Phase relations deduced from the fluid saturated melt fraction reveal a decrease of the stability fields of anorthite and diopside in favor of the forsterite stability field. The stability field of spinel completely disappears.

The ternary eutectic of anorthite, diopside, forsterite and the H_2O saturated melt (projected from the melt saturated fluid fraction) is below 1000 °C

- Anorthite displays a good wetting ability and is restricted to the melt saturated fluid fraction

Cotectic precipitation of anorthite and diopside from a H_2O saturated anorthite enriched liquid is not observed in simple system experiments; anorthite crystallisation in the H_2O saturated melt is completely suppressed. Anorthite only appears within the fluid saturated melt fraction of simple system experiments. However anorthite, diopside and melt do not coexist neither within the fluid saturated melt fraction nor within the H_2O saturated melt fraction. Results of simple system experiments rather suggest anorthositic dykes to represent the melt saturated fluid fraction that dissolved from anorthite rich H_2O saturated melt compositions at depth.

The results of simple system experiments imply for the generation of late stage fluid precipitate that CaTs enrichment in diopside could be the result of precipitation from a H_2O rich liquid.

3.3 DECOMPRESSION EXPERIMENTS

From simple system experiments it is derived that anorthositic dykes could represent remnants of a solute rich fluid. This solute rich fluid had to be equilibrated with an anorthite rich melt prior to exsolution. The main question arising is whether a H_2O rich basaltic melt could evolve to high normative anorthite contents to then exsolve such a solute saturated fluid. But how to test this hypothesis if one is restricted to closed system experimental conditions? Actually it would be necessary to extract the melt saturated fluid fraction from the

H_2O saturated melt at run conditions to be able to investigate both fractions separately. However, even if one could do so, the solute charge of the melt saturated fluid fraction would separate from H_2O due to decreasing solubilities upon cooling to ambient conditions and the remaining liquid will approach pure H_2O in composition. To avoid these problems decompression recrystallisation experiments appear to be the appropriate experimental setup. Decompression in H_2O saturated systems will result in fluid exsolution. Slow cooling after decompression should theoretically promote precipitation of the solute charge which could later be used to estimate the fluid composition. However, performed decompression experiments turned out not to fit theory. The H_2O saturated melt and the melt saturated liquid could not be separated in decompression experiments. Due to the presence of H_2O, the liquidus appears to be decreased to temperatures below 650 °C such that the system is still above the liquidus after decompression. Furthermore no minerals crystallized from the solute saturated fraction upon cooling. Nonetheless experimental results of decompression experiments allow drawbacks on the generation of anorthositic dykes and the late stage fluid precipitate.

Decompression experiments were performed in two pressure regimes, decompression from 1000 MPa to 250 MPa using the piston and 500 MPa to 150 MPa using the IHPV.

3.3.1 PISTON CYLINDER DECOMPRESSION EXPERIMENTS

3.3.1.1 Textures

Three decompression experiments were performed with the piston, namely PCADecExp, PCADecExpCr and PCADecExprep. Initial pressure is high enough to allow complete miscibility between the basaltic melt and H_2O. Decompression will

lead to oversaturation and phase separation of a fluid saturated melt and a melt saturated fluid according the binodal.

Anorthite, forsterite, different pyroxenes and glass appear as major phases in experimental run products of PCA decompression experiments. The overall internal texture of experimental run products resembles in different experiments (Fig. 47A/B/C). At the bottom of the capsule a cumulate of anhedral pyroxene (predominantly diopside and hypersthene) crystals can be observed. Forsterite appears only in this bottom cumulate as inclusions in pyroxenes. The Cumulate is followed by an area with sub- to euhedral pyroxene in a glassy matrix. Numerous degassing bubbles, from several microns to hundreds of micrometer in diameter occur within the glass revealing H_2O being dissolved in the original melt (Fig. 48B). In the upper part of the capsules (hottest area during experiments) anorthite (quench) crystals appear. In the very top a cavity with a sharp boundary towards the solid phases (crystal-glass) appears.

Chromite powder was added to one of the decompression experiments to uncover the localization of former fluid. Theoretically chromite will be collected in the fluid phase due to differential wetting properties of fluid and melt against silicate and oxide surfaces (Matveev and Ballhaus, 2002). Areas of accumulated Chromite ($FeCr_2O_4$) appear very bright on BSE images (high atomic numbers of Cr and Fe) sometimes even outshining other textures (Fig. 47C). Interpretation of chromite distribution in PCADecExpCr is not straight forward from EPMA analyses. Several more or less spherical (200 – 600 µm in diameter) areas enriched in chromite appear which are distributed along the capsule – sample interface throughout the entire capsule. The true nature of these spheres remains inexplicit from microprobe analyses. Either the glass in these areas is enriched in chromite, or

large spherical voids are filled with small chromite grains. Furthermore small (~ 100 µm in diameter) chromite enriched "droplets" appear in a void at the centre of the capsule. Such textures might represent glass droplets enriched in chromite or former aggregates of chromite within the fluid. In a small scale chromite shows up as tiny crystals at the interface of glass and hollow space (Fig. 48C) or accumulated in bubbles (Fig. 48F). The latter described texture match the expectation that chromite would be collected in the fluid phase. If chromite appearances are localized within the glass it remains ambiguous why it is not evenly distributed in the glass throughout the capsule.

From image analyses of experimental run products it can be deduced that about 41 % of the initial melt fraction is crystallized (Fig. 47 and Table 6). Note that this value only refers to the relative proportions of glass and crystals and does not consider the amount of fluid (vesicles within glass and hollow space in capsule). Merged BSE images of experimental run products (Fig. 47) are used as a basis for image analyses being performed with Photoshop (ADOBE CREATIVE SUITE 2).

Table 6: relative proportions of glass and crystals in run products of PCA decompression experiments calculated on the basis of merged BSE images (Fig. 47)

[%]	**PCADecExp**	**PCADecExprep**	**PCADecExpCr**
crystals	41	37	46
glass	59	63	55

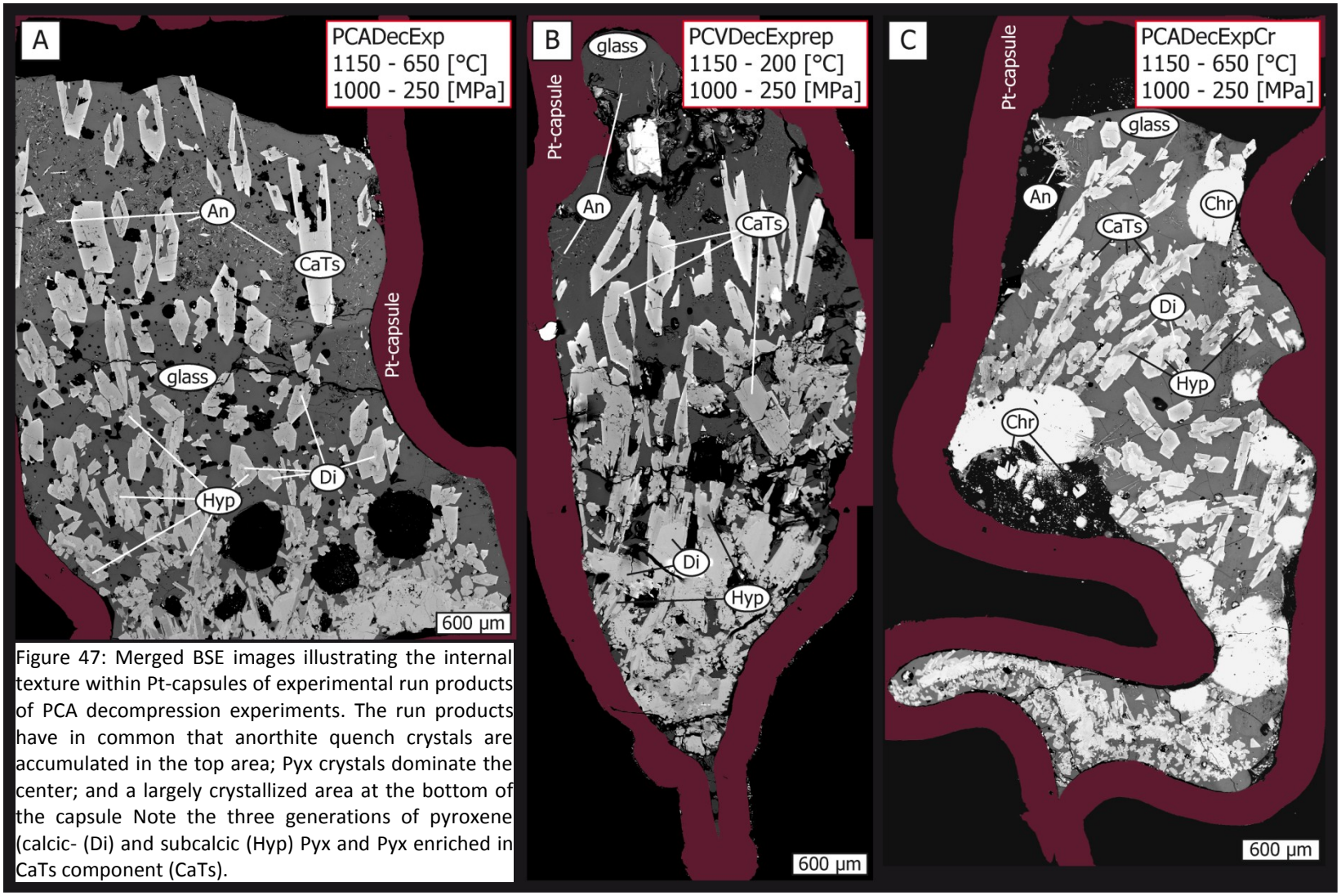

Figure 47: Merged BSE images illustrating the internal texture within Pt-capsules of experimental run products of PCA decompression experiments. The run products have in common that anorthite quench crystals are accumulated in the top area; Pyx crystals dominate the center; and a largely crystallized area at the bottom of the capsule Note the three generations of pyroxene (calcic- (Di) and subcalcic (Hyp) Pyx and Pyx enriched in CaTs component (CaTs).

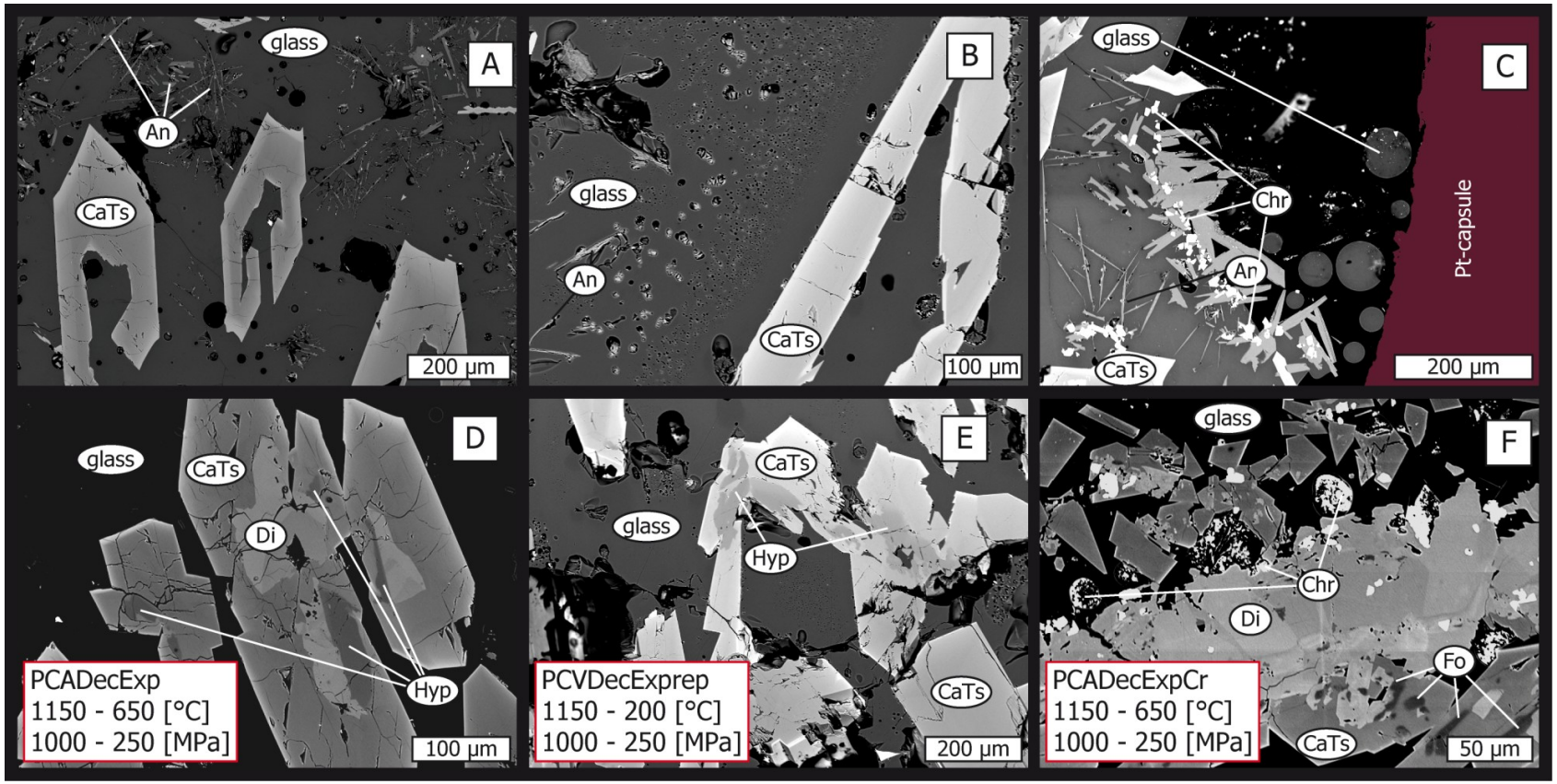

Figure 48: BSE images of different textures in experimental run products of PCA decompression experiments; left (A&D) PCADecExp, middle (B&E) PCVDecExprep and right (C&F) PCVDecExpCr. (A) Aggregates of anorthite quench crystals and skeletal CaTs enriched pyroxene in a glassy matrix. (B) Skeletal CaTs enriched pyroxene and anorthite quench needles. Note the absence of degassing bubbles along grain boundaries of pyroxene and the gradual increase in bubble diameter. Larger vesicles appear to be filled with tiny particles. (C) Anorthite crystals at the interface between glass and hollow space in the capsule. Small Cr particles appear to act as nucleation seeds for anorthite grains. Spheres of glass appear within the cavity probably representing exsolved melt from the fluid during decompression, the phase boundary might be interpreted as interface between the former fluid saturated melt and the melt saturated fluid. (D) CaTs enriched pyroxene with relicts/inclusions of diopside and hypersthene in the core. (E) Hypersthene and diopside in glassy matrix. (F) Chemically zoned (minor variations in FeO and MgO content) diopside and CaTs enriched pyroxene. Chromite is accumulated within vesicles. Note that grain boundaries of CaTs enriched pyroxene always appear to be straight

3.3.1.2 Anorthite

Plagioclase appears as needles reminiscent of quench textures ($X_{An} \sim 0.73$) in all PCA decompression experiments. Larger (10 µm) tabular anorthite crystals only appear in experiments that were slowly cooled from 1150° to 650°C (PCADecExp and PCADecExpCr). Comopsitions of larger crystals are more enriched in anorthite component ($X_{An} \sim 0.90$) compared to quench crystals. In PCADecExp, anorthite forms textures reminiscent of a kite's tail (Fig. 49A). In PCADecExp and PCADecExprep anorthite quench crystals occur in the upper part of the capsule. Anorthite is nucleated around ulvöspinel (or chromite in PCADecExpCr) wich is assumed to act as nucleation seed. In PCADecExpCr anorthite quench needles occour througout the capsule but larger tabular crystals only grow into hollow space at the top of the capsule. The hollow space had to be filled with liquid at time of quenching as it contains spherical glass droplets.

Anorthite quench needles are wetted with tiny degassing bubbles. Kite's tail textures are surrounded by larger bubbles. Upon anorthite quenching, from the H_2O bearing liquid, H_2O content around the H_2O free anorthite crystal is relatively increased. Furthermore, glass in the close vincinity of anorthite textures is depleated in plagioclase component (Maps for Si, Al and Ca on Fig. 49B). This observation strongly suggests that anorthite is precipitated from the H_2O saturated melt fraction. Textural evidence is given that the growth of tabular plagioclase enriched in anorthite happens prior to glass formation. It might be speculated that these crystals grew from the solute saturated fluid upon cooling. This is supported by the fact that such textures are absent in PCEDecExprep.

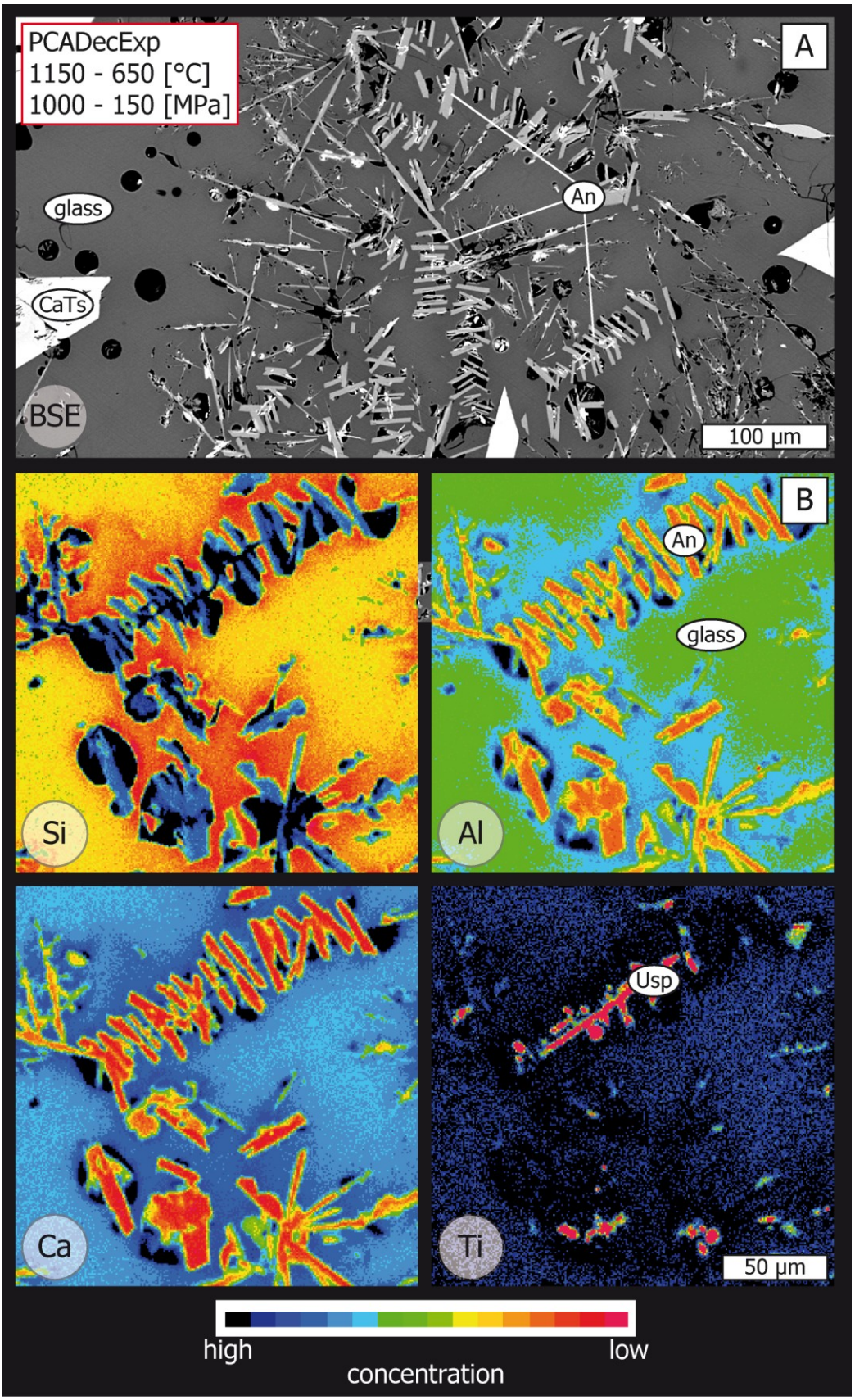

Figure 49: (A) BSE image of anorthite quench textures in a glassy matrix, displaying both, anorthite needles wetted by degassing bubbles and anorthite crystals displaying textures reminiscent of a tail of the kite. (B) Element maps for Si, Al, Ca and Ti of kite's tail anorthite textures. Note the depletion of Al and enrichment of Si and Ca in the close vicinity of crystals. Anorthite crystals are aligned i.e. nucleated around Ti rich textures (Ulvöspinel).

3.3.1.3 Pyroxenes

Three different pyroxenes appear within run products of decompression experiments; (i) an iron and CaTs enriched calcic pyroxene denoted as CaTs, (ii) a subcalcic Mg rich pyroxene denoted as hypersthene, and (iii) a calcic pyroxene denoted as diopside (compositions are listed in table X in the appendix). Textural evidence is given that the CaTs enriched pyroxene is the latest precipitated phase (Fig. 48D/E/F). The CaTs pyroxene dominates in the upper areas of capsules (Fig. 47) forming sceletal crystals with straight grain boundaries (Fig. 52A/B). Some crystals display chemical zoning, with iron and calcium enrichment at the rims. Grove and Bence (1977) showed in equilibrium experiments that the composition of equilibrium pyroxenes becomes more Ca and Fe- enriched at lower temperatures. Thereby the partitioning of Ca, Mg and Fe between pyroxene and melt is not dependent on the cooling rate but rather an effect of fractional crystallisation occurring with cooling.

Gradual enrichment of the CaTs component in diopside has previously been discussed for the simple system experiments. The CaTs enrichment in pyroxene precipitated from simple system experiments is related to the increase in alumina in the melt due to suppressed plagioclase crystallisation. Gnerally CaTs pyroxene forms a solid solution with diopside ($CaMgSi_2O_6$ – $CaAl_2SiO_6$) whereas the mole fraction of CaTs molecule in diopside increases with increasing pressure (Wood, 1976). At equilibrium the activity of $CaAl_2SiO_6$ component in the pyroxene solid solution is fixed by the reaction:

$$CaAl_2Si_2O_8 \leftrightarrow CaAl_2SiO_6 + SiO_2 \quad (12)$$

CaTs enriched pyroxenes of decompression experiments could either be the product of exchange reactions between the plagioclase saturated liquid and a

previously precipitated diopside. Or CaTs enriched pyroxenes directly precipitate from the H_2O rich evolving melt fraction. Both, the process of CaTs enrichment in diopside at the expense of anorthite component or direct precipitation of the melt, will drive the liquid to more silicic compositions (Fig. 44).

In the close vicinity of CaTs degassing bubbles are absent gradually reappearing at distance (Fig. 52B/E). This observation is in good agreement with the previously described assumption that pyroxenes reside in the melt due to their poor wetting ability. Furthermore this observation suggests the direct precipitation of CaTs pyroxene from the H_2O rich melt. Pseudomorphic replacement of previously precipitated diopside by CaTs rather appears unrealistic, as such a reaction would require the removal of manganese from the pyroxene structure.

In the central capsule area, inclusions of hypersthene and diopside appear within CaTs pyroxenes (Fig. 48D/E). Commonly both, hypersthene and diopside appear side by side within one CaTs crystal. In the lowermost capsule area large diffuse zoned diopside crystals apprar associated with CaTs, sometimes containing hypersthene inclusions (Fig. 48E). Zonation in diopside is manifested in variable iron-, manganese- and alumina conents (Fig. 50).

Textures of diopside and hypersthene inclusions in CaTs might be interpreted as disequilibrium textures, with CaTs replacing diopside and hypersthene due to changes in melt composition. However, it is evident that diopside and hypersthene precipitate at an earlier stage compared to CaTs. The coexistance of diopside and hypersthene might be explained by the diopside-enstatite miscibility gap at high pressure.

Davis and Boyd (1966) described the phase relations along the $Mg_2Si_2O_6$ - $CaMgSi_2O_6$ join at 3 GPa. They observed a metastable miscibility gap between clinoenstatite and diopside solid solutions in peridotite nodules of kimberlites. The presence of a hydrous phase might change the phase relations such that a metastable solvus appears at lower pressures relevant for experimetal conditions. The incongruent melting behaviour of enstatite (En = Fo + L) at low pressures and under dry conditions has been a known fact for a long time (Bowen and Andersen, 1914), but the peritectic disappears at elevated pressure (Boyd et al., 1964). This is not the case under hydrous conditions where the peritectic persists to at least 3000 MPa H_2O pressure (Kushiro et al., 1968b). Under hydrous conditions within the simple $MgSiO_3$ – H_2O system enstatite starts melting at about 1360 °C and 1000 MPa. In a hydrous basaltic system, enstatite obviously decomposes at lower temperatures, as observed in the decompression experiments. The decreased stability of enstatite relative to forsterite fits the premise that H_2O tends to stabilize the less polymerized phase. The presence of forsterite inclusions in diopside and CaTs within the lowermost capsule area might be relicts of the enstatite forming reaction.

Diopside compositions are variable in CaO, MgO, FeO and Al_2O_3 contents, whereas a correlation between CaO and MgO (Fig. 50A) and FeO and Al_2O_3 (Fig. 50D) is observed. Hypersthene is less variable in composition. Calcium values are all-over low and do not correlate with iron or magnesium (Fig. 50B/C). Variable amounts of manganese at the M site is exchanged by iron, whereas low FeO is correlated with low Al_2O_3 contents (Fig. 50D/E). Variability in FeO and MgO is probably related to temperature effects, displaying the restricted diopside -enstatite solid solution at the enstatite rich limb. CaTs displays uniform CaO contents (11 wt.%)

but variable contents in FeO, MgO and Al_2O_3. (Fig. 50B/C/D/E) Similarly as for hypersthene, FeO and MgO covariate. Variations might be attributed to primary processes, such as changes in melt composition during growth, or secondary processes related to autometasomatic overprinting.

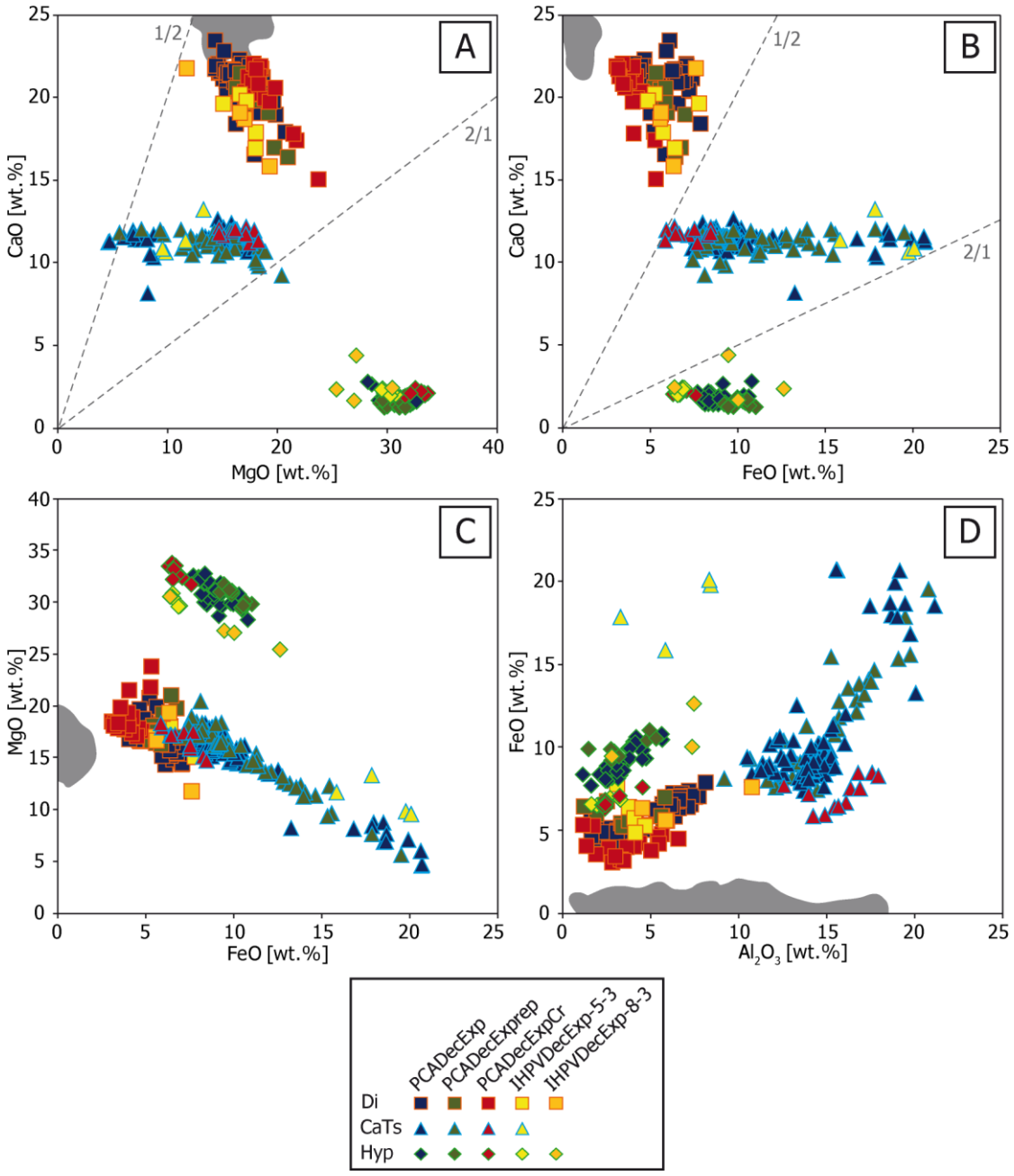

Figure 50: (A) MgO vs. CaO wt.%, the dashed lines correspond to element proportions of manganese relative to calcium. Note the trend for diopside displaying a decrease in CaO content with increasing MgO. (B) FeO vs. CaO wt.%, the dashed lines correspond to element proportions of iron relative calcium. Note the large variability in iron contents of CaTs pyroxene. (C) FeO vs. MgO wt.%, both, hypersthene and CaTs display exchange of iron and manganese. (D) Al_2O_3 vs. FeO wt.%. Note the offset of alumina data of CaTs and hypersthene for the IHPV experiment. Grey shaded areas correspond to pyroxene compositions of simple system experiments.

3.3.1.4 Glass

Glass occurs as a homogeneous matrix with degassing bubbles of various sizes in all decompression experiments (Fig. 47A/B/C). Furthermore glass droplets within hollow spaces appear in the lowermost, pinched area of the capsules (Fig. 47B) or in PCADecExpCr in larger voids (Fig. 47C/D). Glass droplets prove the existence of a fluid at the time of glass formation. In terms of its composition the glass quenched from melts of PCA decompression experiments is quartz (24 – 55 %) and corundum (0.5 – 5 %) normative displaying minor compositional variations (Fig. 51). Variation in normative plagioclase component exceeds 20 % (Table 7) and is related to anorthite quench textures. This is also reflected by the negative correlation of Al_2O_3 and CaO with silica (Fig. 51A/B/C).

Table 7: Variability, minimum and maximum values of CIPW normative anorthite content of glass quenched from decompression experiments.

	PCADecExp	PCADecExprep	PCADecExpCr
CIPW An Min [wt.%]	28	20	23
CIPW An Max [wt.%]	42	41	41
Δ CIPW An [wt.%]	14	21	18

Normative pyroxene and corundum contents (Fig. 51D/F) are not correlated with normative quartz. Averaged glass compositions are listed in table X in the appendix and illustrated in Fig. 51.

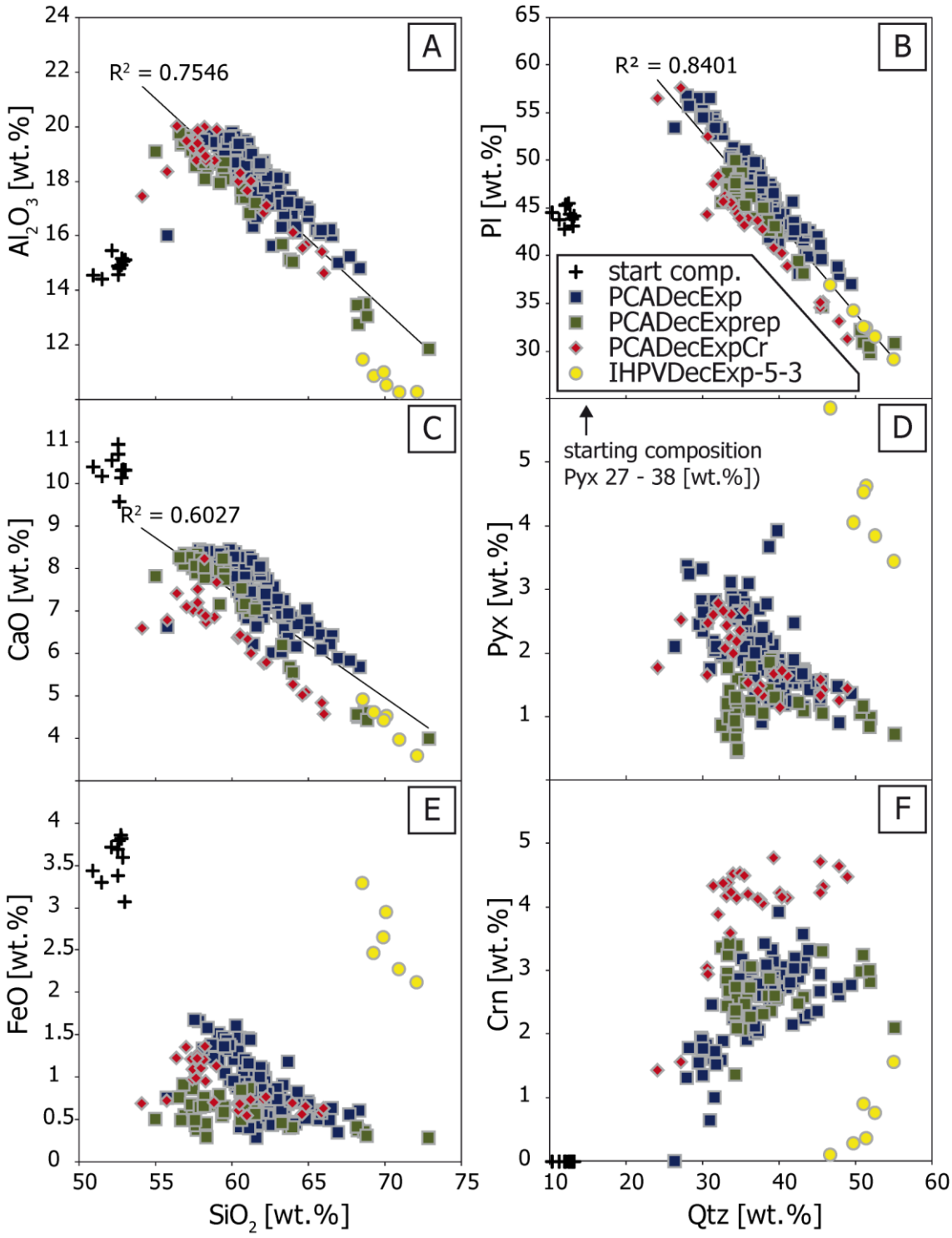

Figure 51: Glass compositions of PCA and IHPV decompression experiments. (B/D/F) CIPW normative mineral proportions. Trend lines and coefficients of determination are given for the negative correlation of Al_2O_3 (A) and CaO (B) with SiO_2 and for the CIPW normative plagioclase content with quartz. The correlation is calculated based on glass compositions of experimental run products from decompression experiments, excluding data of the starting composition.

3.3.2 *IHPV DECOMPRESSION EXPERIMENTS*

The different initial H_2O content in the performed decompression experiments corresponds to conditions above the second critical point (IHPVDecExp-5-3) and below the second critical point (IHPVDecExp-8-3). Chemical compositions of experimental run products of IHPV decompression experiments are listed together with PCA experiments in table X in the appendix.

3.3.2.1 Textures

Experimental run products of IHPV decompression experiments particularly protrude by their textures; pyroxene appears as radially arranged zoned crystals. The crystals are chemically zoned with subcalcic pyroxene in the core and calcic pyroxene at the rims (Fig. 52). Glass is only present in experiment IHPVDecExp-5-3 (Fig. 52A), whereas clinozoisite forms a matrix in experiment IHPVDecExp-8-3 (Fig. 52B).

3.3.2.2 IHPVDecExp-5-3: initially above cp

At starting conditions it can be assumed for IHPVDecExp-5-3 that the entire amount of H_2O is dissolved in the melt. At some stage upon decompression the system will reach saturation and start to exsolve a fluid.

Great similarities concerning the precipitating phases are observed to PCA decompression experiments. From image analyses it can be deduced that about 50 % is crystallized, 10 % more than for PCA decompression experiments. The higher degree in crystallisation can be attributed to the lower initial H_2O content.

Tabular plagioclase ($X_{An} \sim 0.73$) crystallized from the melt. Nests of amorphous SiO_2 are typically associated with plagioclase crystals (Fig. 52C).

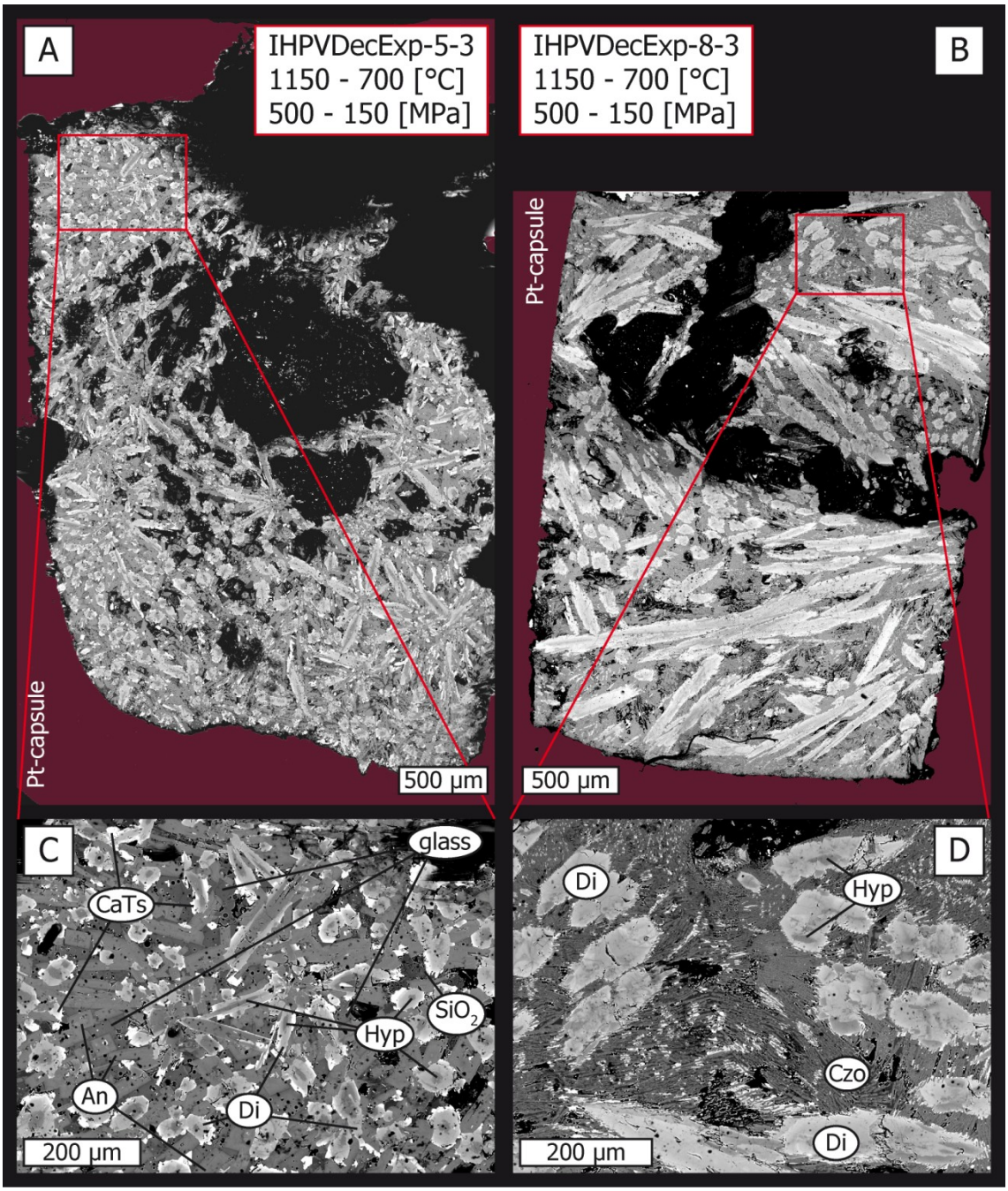

Figure 52: BSE images of run products of IHPV decompression experiments. A/B) Merged overview images of IHPVDecExp-5-3 and IHPVDecExp-8-3 experiment respectively displaying radially arranged pyroxene aggregates. C) BSE image of IHPVDecExp-5-3. Note the zonation of pyroxene (darker areas correspond to less calcic, hypersthene like compositions in the cores and increasingly brighter areas to calcic and Mg rich Cpx to CaTs enriched (also Fe, Ti and Na enriched) Cpx. D) BSE image of IHPVDecExp-8-3 displaying chemically zoned pyroxene with diffuse grain boundaries and the clinozoisite like matrix.

Three different pyroxenes appear (Hyp, Di and CaTs) similar as in PCA decompression experiments. Hypersthene and diopside compositions resemble those of the PCA decompression experiments, whereas trends within iron,

magnesium and alumina contents are less distinctive (Fig. 50). Texturally there appear considerable differences to PCA experiments. Diopside appears to resorb hypersthene and CaTs seems to overgrow some of the diopside crystals (Fig. 52C). In terms of its composition, CaTs differs from those in PCA decompression experiments by lower alumina contents (Fig. 50E), less of the CaTs component is dissolved in pyroxene ($X_{CaTs}^{Pyx} \sim 18$ in PCA and $X_{CaTs}^{Pyx} \sim 10$ in IHPVDecExp-5-3,). The compositional change from subcalcic manganese rich cores (hypersthene) towards calcic diopside, and CaTs enrichment at the rim rather suggests continuous changes during growth than diopside – enstatite exsolution along the miscibility gap as described for PCA experiments. Such continuous changes are attributed to changes in melt composition.

Glass compositions (~10 wt.% dissolved H_2O) from IHPVDecExp-5-3 resemble those of PCA experiments but generally appear to be more evolved as indicated by high silica (Fig. 51A/C/E). Alumina and CaO (Fig. 51A/C) content is lower as reflected by low normative plagioclase contents (Fig. 51B). Normative pyroxene content is relatively high (Fig. 51D).

3.3.2.3 IHPVDecExp-8-3: initially below cp

At starting conditions (1150 °C and 500 MPa) it is unequivocal if all H_2O is dissolved in the melt structure. Benne and Behrens (2003) report H_2O solubilities at 1200 °C and 500 MPa ranging from 8 to 9.5 wt.% H_2O in basalts (Fig. 53). Neglecting the temperature effect of ΔT = 50 °C (1150 °C at experimental conditions) on H_2O solubility it is possible that such a melt (containing 8 wt.% H_2O as the experimental charge) is oversaturated in H_2O under mentioned conditions. As a result, a (supercritical) fluid in equilibrium with the basaltic melt should coexist. Upon decompression to 150 MPa this fluid is further diluted with the

continuously dissolving H_2O. The amount of degassed H_2O theoretically reaches up to 6 wt.% in this scenario (Fig. 53).

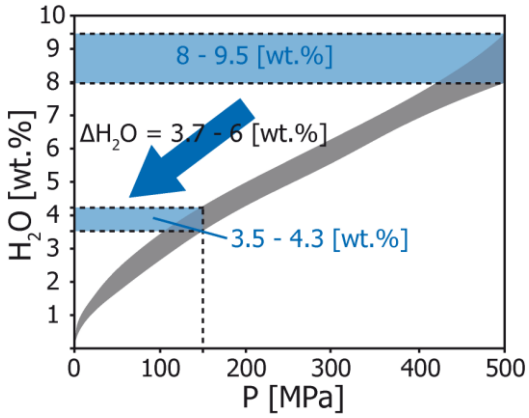

Figure 53: Pressure dependence of H_2O solubility in basalts at 1200 °C, redrawn after Benne and Behrens (2003). The dark shaded area generously covers the H_2O content of natural basalts published by Berndt et al. (2002); Dixon et al. (1995); and Hamilton et al. (1964). The blue shaded area highlights the dissolved H_2O contents at 150 and 500 MPa. Isothermal decompression from 500 to 150 MPa theoretically results in degassing of 3.1 – 5.5 wt.% H_2O.

Pyroxenes appear with diffuse crystal boundaries forming curious textures with intergrowth of hypersthene and diopside (Fig. 52D). No CaTs is present.

IHPVDecExp-8-3 differs to the less H_2O bearing experiment as no glass is preserved and no plagioclase or CaTs crystallized. Instead, fibrous textures of clinozoisite like compositions occur (Fig. 52D). The clinozoisite texture resembles anorthite needles in the spheroidal late stage fluid precipitate sample Zy92 (Fig. 13). The nests of amorphous SiO_2 appear within the clinozoisite matrix.

The initially high proportion of dissolved H_2O in the melt might be the reason why no plagioclase crystallized. Furthermore the high H_2O content might hinder a glass to be quenched from the melt, rather precipitating clinozoisite. Another possible scenario is the recrystallisation of glass (devitrification), pyroxene and feldspar to clinozoisite due to autometasomatism upon cooling. Autometasomatism is a process also involved for the generation of the late stage fluid precipitate and might explain their textural similarities. It is questionable why no clinozoisite is present in other decompression experiments pointing to the first scenario to be more realistic.

3.3.3 TEXTURAL DIFFERENCES BETWEEN PCA AND IHPV DECOMPRESSION EXPERIMENTS

Great differences appear between the internal texture of decompression experiments from IHPV runs and those of the PCA. Capsules of IHPV-runs do not display any textural zonation such as for PCA experiments. This might be explained by a temperature gradient within the capsule of PCA experiments. The temperature gradient for IHPV experiments should be negligible; it was monitored between loop1 and loop2 and did not exceed 12 °C. For PCA experiments a temperature gradient exists owed to the furnace geometry. Furthermore the IHPV-configuration allows approximately confining pressure, whereas a solid pressure medium such as used for the PCA rather results in directed pressure. Both, anisotropy in pressure and temperature gradient might be the reason for the zonal texture of PCA experiments. For PCADecExp and PCADecExprep the cumulate zone may be perceived as a result of density contrasts between melt and fractionated pyroxene crystals. Inferring the chromite bearing experiments it looks somewhat different, arguing for a different scenario. The distribution of the fluid phase in the capsule (which itself is dependent on temperature) during precipitation of pyroxene, probably, results in differences in nucleation energies throughout the capsule and thus inhomogeneous distribution of crystal sizes. Accumulation of crystals in the lower area might be the result of gravitational crystal settling. The less dense melt saturated fluid will probably favour the hot upper capsule area. But at experimental pressure and temperature conditions it is questionable, due to high kinetics, that the (supercritical) fluid is somehow distributed. The presence of glass orbicules in the lowermost pinched capsule area confirms the presence of a liquid in this area at glass formation.

3.3.4 SUMMARY DECOMPRESSION EXPERIMENTS

Generally the performed decompression experiments display two different trends: Piston cylinder experiments and IHPVDecExp-5-3 have in common, that at starting conditions the entire amount of H_2O is dissolved int the melt. In contrast, the low pressure, H_2O rich experiment IHPVDecExp-8-3 starts at slightly H_2O oversaturated conditions.

For an improved intelligibility the different scenarios attempted by different experiments are displayed in different scenarios in the pseudobinary basalt – H_2O phase diagram in Fig. 54. Decompression in all experiments happens at isothermal conditions. The influence of melt differentiation due to crystallisation is neglected on Fig. 54.

Analogue to PCA decompression experiments (P_3 = 1000 MPa, $P_2 \sim$ 600 MPa, P_1 = 250 MPa) according to Fig. 54. The red star corresponds to T = 1150 °C. Complete miscibility is observed between H_2O and the basaltic melt at 1150 °C and 1000 MPa. Upon isothermal decompression the system is saturated in H_2O at P_2. Upon further decompression the melt and the fluid will develop according the binodal: the melt will expel H_2O and the fluid will continuously discharge its solute load. The change in pressure will also affect the phase relations and phase compositions of solid phases. Generally H_2O is more compressible than melt; as a consequence a decrease in pressure will raise the solidi. Crystallizing phases have to compete with increasing liquidus temperatures and changing melt compositions. However, to initiate crystal growth, the system has to overcome nucleation energy. It is noteworthy that nucleation energy within the fluid might largely differ to that of the melt. The relative H_2O content of the fractionating melt will increase and thus promote the process of fluid exsolution. According to

isobaric cooling, the H_2O saturated melt develops according to the left side of the binodal (triangles), continuously discharging H_2O. Theoretically, in the mean time, the melt saturated fluid will develop according to the right side (hexagons) of the binodal. But, the simultaneously unmixing H_2O of the co-evolving melt will mix with the fluid and thus instantaneously dilute the composition of the fluid fraction to more H_2O rich compositions. Similar processes appear in experiment IHPVDecExp-5-3. According to a lower initial pressure, less H_2O is dissolved in the melt of IHPVDecExp-5-3 at starting conditions. However the system is slightly above the critical point at starting conditions. The red star corresponds to 1150 °C at P_3 = 500 MPa, P_2 = 200 MPa and P_1 = 150 MPa according to Fig. 54. Initially H_2O saturated experiments display similarities in precipitating phases. Hypersthene, diopside and CaTs appear in similar relations and glass is quenched from the remaining H_2O saturated melt. Forsterite is not stable in the low pressure IHPV experiment whereas remnants of an exsolved SiO_2 melt are present. Anorthite precipitating from the H_2O saturated melt fraction at lower pressures ($X_{An} \sim 0.73$) perfectly matches anorthite quenched from the melt fraction of PCA experiments ($X_{An} \sim 0.74$).

Things are different for experiment IHPVDecExp-8-3 with starting conditions at, or slightly below the second critical point (according to orange star at P_3 = 500 MPa). After a short while at run conditions a H_2O saturated melt coexists with a melt saturated fluid. The orange triangle corresponds to the composition of the H_2O saturated basaltic melt and the orange hexagon corresponds to the composition of the solute saturated fluid. Decompression results in continuous exsolution of a fluid from the melt fraction which is mixing with the coexisting solute saturated fluid. The H_2O saturated melt and solute saturated fluid evolve according the

binodal. Upon cooling hypersthene and later diopside precipitates according to the melt composition. No glass is quenched but the "melt fraction" reacts with the fluid forming clinozoisite. Different pressure and temperature conditions in the course of the PCA and IHPV decompression experiments are illustrated in Fig. 55. Processes taking place at different stages during the (initially H_2O saturated) experiments are summarised in Table 8 according to the numbers on the graph.

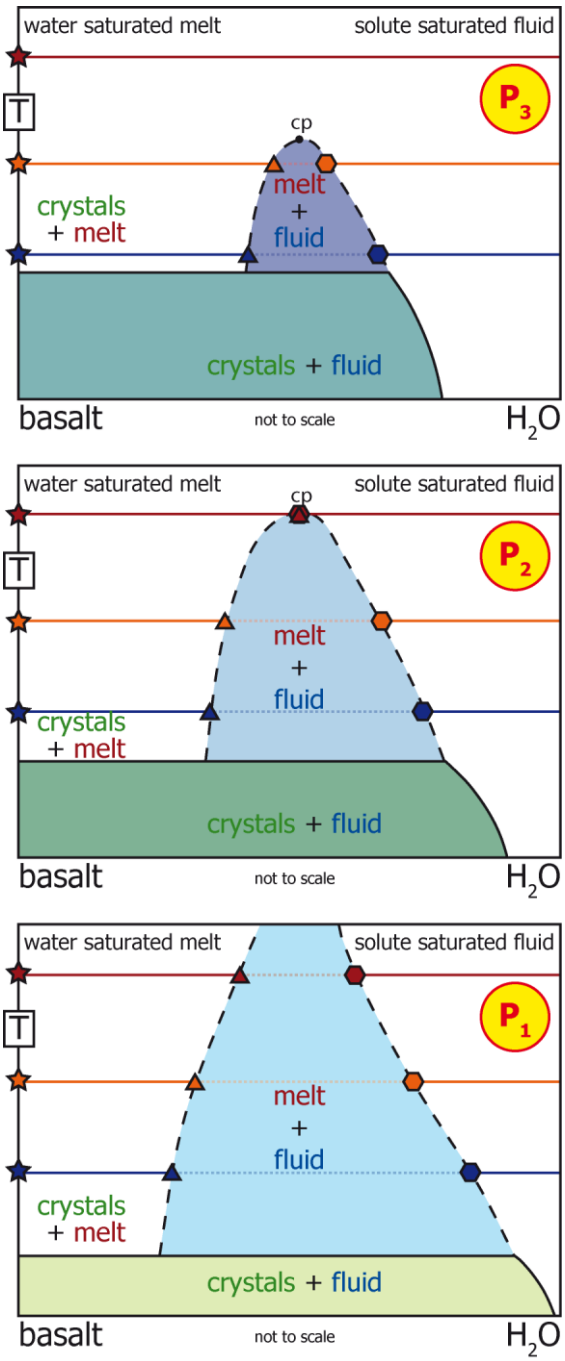

Figure 54: The effect of pressure illustrated in three schematic pseudobinary P–X diagram with melt-fluid immiscibility modified after Mysen (2014) and Ballhaus et al. (2015). Three different pressure conditions are illustrated, whereas $P_1 < P_2 < P_3$. Different coloured stars indicate three different temperatures accordingly at three different pressure conditions. Triangles and hexagons refer to the composition of the fluid saturated melt and the melt saturated fluid at temperatures according to the symbol colour. Note that to simplify the plot, the two phase field of crystals and melt is not defined. With decreasing pressure the H_2O-fraction of the fluid saturated melt (hexagons) will increase, but increase in the melt (triangles) fraction - the binodal is widened and the second critical point moves to higher temperatures. The "cp" refers to the second critical endpoint.

PCA decompression experiments:
starting: P_3 = 1000 MPa (red star = 1150 °C)
P_2 = 600 MPa
P_1 = 250 MPa

IHPVDecExp-5-3:
starting: P_3 = 500 MPa (red star = 1150 °C)
P_2 = 200 MPa
P_1 = 150 MPa

IHPVDecExp-8-3:
starting: P_3 = 500 MPa (orange star = 1150 °C)
P_2 = 200 MPa
P_1 = 150 MPa

Piston cylinder decompression experiments confirm the observation of simple system experiments that anorthite (X_{An} = 0.88 – 0.92) precipitates from the fluid fraction. The accumulation of anorthite component in the H_2O saturated basalt is restricted due to the precipitation of CaTs upon cooling. However, prior to CaTs precipitation the basaltic liquid can be assumed to be highly enriched in anorthite component.

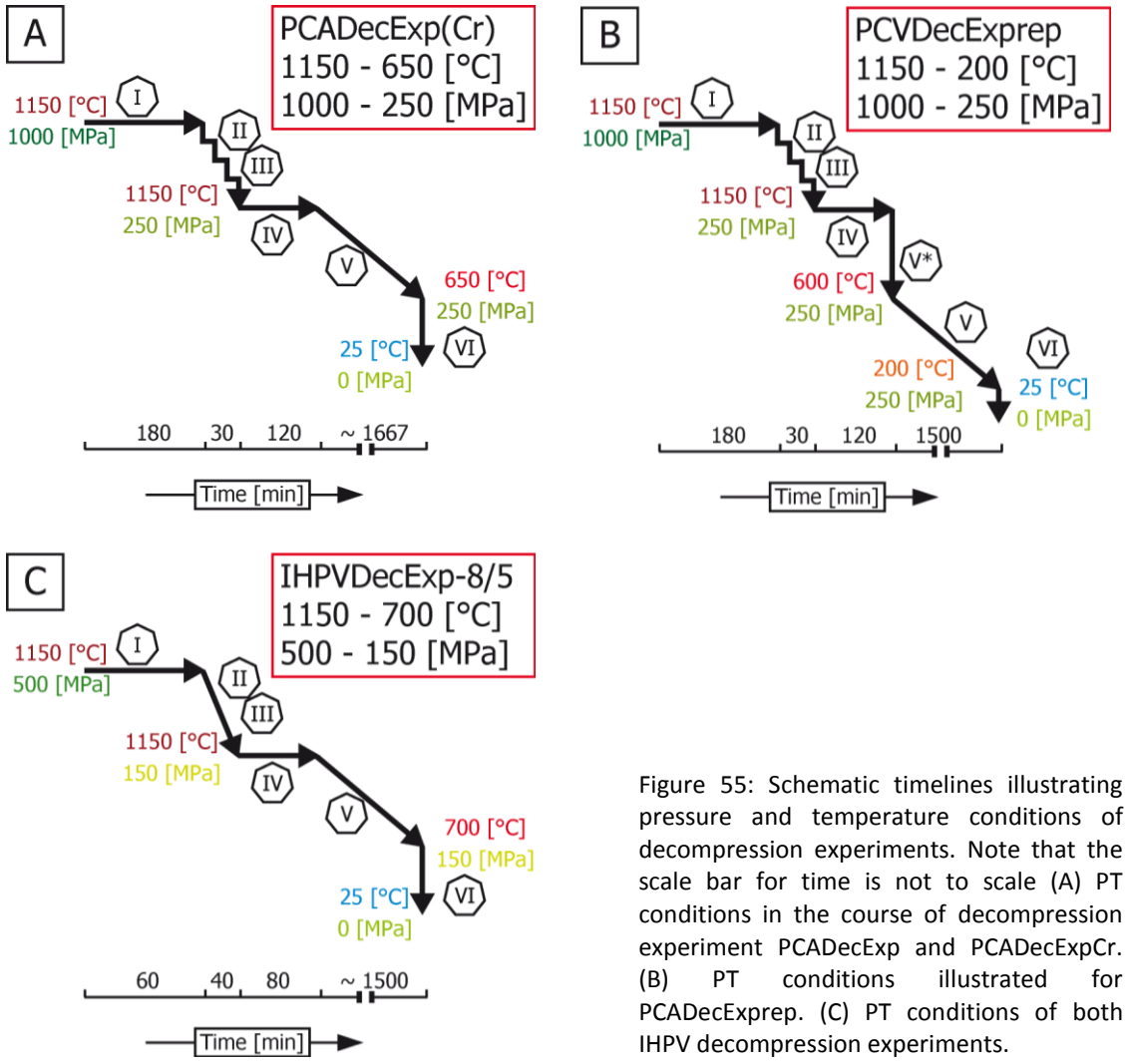

Figure 55: Schematic timelines illustrating pressure and temperature conditions of decompression experiments. Note that the scale bar for time is not to scale (A) PT conditions in the course of decompression experiment PCADecExp and PCADecExpCr. (B) PT conditions illustrated for PCADecExprep. (C) PT conditions of both IHPV decompression experiments.

Table 8: Summary of processes talking place at different stages of decompression experiments being initially H_2O saturated. Numbers refer to Figure 55.

	PCADecExp	**IHPVDecExp-5-3**
I	Equilibrium is attained after a short while at pressure and temperature, and a **basaltic- H_2O saturated melt** is stabilized. The entire amount of H_2O (10 wt.%) is dissolved in the melt structure.	After a short while at run conditions (1150 °C and 500 MPa) a **H_2O saturated basaltic melt** forms.
II	Exsolution of a melt saturated fluid from the H_2O saturated melt will start off the point of **H_2O saturation** probably around 600 MPa. Forsterite precipitates from the melt fraction whereas nucleation energy is not attained within the fluid fraction. Precipitation of forsterite drives up the H_2O content in the melt as the melt fraction decreases at the expense of forsterite. Melt and fluid will always be saturated in the same phases.	Hypersthene starts to precipitate leading to a continuous change in melt composition. The relative proportion of dissolved H_2O in the melt increases.
III	According the peritectic reaction hypersthene forms at the expense of forsterite and melt. Hypersthene starts to exsolve diopside according to the diopside – enstatite miscibility gap. Fractionation of Al-free phases drives up alumina in the melt fraction. **CaTs** ousts the precipitation of diopside and hypersthene.	At ~ 200 MPa the melt reaches **H_2O saturation** and starts to exsolve a melt saturated fluid. Due to changes in melt composition precipitation of diopside ousts hypersthene. Ongoing fractionation increases the alumina content of the melt. Increasing H_2O exsolution allows **anorthite** to crystallize. Finally **CaTs** precipitation initiates and increases the silica content of the melt and a silicic melt exsolves.
IV	The system attempts to reequilibrate by adjusting the pyroxene composition.	Subsolidus conditions are reached and fluid reacts with the crystal/**glass** assemblage initiating autometasomatism.
V*	The melt fraction of PCADecExprep is quenched to a **glass**. A small fraction of the fluid is expelled from the melt upon the transition to a glass forming degassing bubbles. **Anorthite** is quenched from the H_2O saturated melt. The fluid composition now approaches pure H_2O.	
V	Upon cooling, autometasomatic processes continue for experiment PCADecExp and PCADecExpCr and initiate for PCADecExprep. The fluid fraction of PCADecExp and PCADecExpCr starts to precipitate **anorthite**. At time of cooling the system, the fluid fraction had already lost most of its solute charge.	Autometasomatism continues. Compositions of pyroxenes are altered.
VI	The melt fraction of experiment PCADecExp and PCADecExpCr is quenched to **glass** and **anorthite** quench crystals form. Upon glass transition some of the dissolved H_2O is expelled forming small degassing bubbles. The fluid fraction which is not dissolved in the glass fraction is lost when the capsule is opened.	The fluid approaches pure H_2O and escapes when the capsule is opened.

Major findings of decompression experiments can be summarized as follows:

- Decompression results in significant changes in melt compositions related to H_2O exsolution and fractional crystallisation
- 10 wt.% H_2O is dissolved in the basaltic melt at 1150 °C and 1000 MPa
- H_2O saturation of 8 wt.% H_2O at ~ 200 MPa and 1150°C
- Super-liquidus conditions for the hydrous basaltic system at 1150 °C and 1000 MPa
- $T_l \geq 600 < 650$ °C for the H_2O saturated basaltic system at 250 MPa
- $T_l \leq 700$°C the H_2O saturated basaltic system at 150 MPa
- No hydrous phases such as amphibole precipitate

Experimental results of decompression experiments imply for the generation of anorthosites that dykes might represent the crystallized and quenched solute fraction of a fluid that exsolved at depth from evolved H_2O saturated basaltic melt.

4 SUMMARY AND CONCLUSIONS CONCERNING THE EXPERIMENTS

The performed experiments aim to simulate processes responsible for the generation of anorthositic liquids but are restricted due to the experimental procedure to closed system phenomena. Hence experimental products cannot completely duplicate the phenomena taking place in nature. However, the three different experimental approaches contribute to the general understanding of mechanisms involved for anorthositic liquid formation. Liquidus experiments, simple system experiments and decompression experiments elucidate different

aspects of the role of a fluid during magmatic processes. The different types of experiments, run conditions and their central messages are listed in Table 9.

Results of liquidus experiments reveal conditions allowing a hydrous anorthositic melt to be stable. Furthermore liquidus experiments concede anorthite (X_{An} = 0.9 – 1) as liquidus phase. A completely molten anorthositic liquid would be stable at upper mantle conditions (500 MPa corresponding to ~ 19.6 km assuming ρ = 2.6 g/cm^3) and 1150 – 1200 °C. However, from textural observations it is derived that diopside and anorthite precipitated prior to intrusion. Furthermore, from crosscutting relations with the sheeted dyke complex, the emplacement pressure is estimated to be much lower (150 - 200 MPa). Lowering the pressure would probably reduce the melting temperature. However, the decrease in H_2O solubility is a mutual reaction on lower PT conditions and counteracts melting. After all it has to be considered that today's bulk anorthosite composition does not reflect the liquid composition at time of intrusion. Probably the sodium in the system is added upon secondary hydrothermal alteration in crustal levels. Consequently anorthosite dykes do not represent precipitates from a magmatic melt.

Assuming thomsonite compositions of natural anorthosite samples to approach the composition of the anorthositic liquid after anorthite and diopside extraction ($CIPW_{An}$ = 46 - 66), the precursor liquid must have been even more enriched in anorthite component than glass compositions of liquidus experiments ($CIPW_{An}$ = 60 in AnL-1200).

Simple system experiments confirm that the precipitation of anorthite from a melt is largely suppressed at H_2O saturated conditions. As a consequence, fractionation of a hydrous basaltic melt would produce residual melts enriched in anorthite

component. The olivine stability field expands such that basaltic compositions would always plot within the two phase field of olivine plus liquid. As a consequence, basaltic liquids would always start to evolve from within the olivine stability field. Following this precondition, assuming anorthositic liquids to represent derivative basaltic melts, olivine (and diopside) has to be extracted from the melt to evolve the residual liquid towards anorthite rich compositions. Precipitation of diopside is thereby dependent on the initial Ca/Si ratio of the basaltic liquid. Liquid compositions derived from fractional crystallisation would approach eutectic composition which can be speculated to contain a relative proportion of anorthite ranging 85 – 90 %, according to glasses generated from simple system experiments. As derived from simple system experiments fluid immiscibility might be another possible scenario to generate compositions similar to anorthositic dyke rocks. The melt saturated fluid fractions of the performed phase relation experiments somehow resemble anorthosites (Fig. 42E/F/G). Whereas the precipitation of plagioclase is suppressed in the H_2O saturated melt fraction, anorthite appears within the fluid fraction. Anorthite crystals are accumulated in the fluid fraction due to its better wetting ability. In contrast to the melt fraction where changes in melt composition related to fractional crystallisation can be traced by differences in glass compositions, the evolution of the fluid remains concealed. Only the mineral load of the fluid fraction is captured, but as the fluid is not quenchable it escapes when the capsule is opened. Within the fluid fraction of some compositional series of phase relation experiments (652015, 601030, 603010, 405010 and 207010) CaTs enriched pyroxene appears within a matrix of anorthite (Fig. 42G). No appropriate explanation for these textures can be given.

The performed decompression experiments demonstrate very clearly that plagioclase crystallisation in a fluid saturated basaltic melt is largely suppressed at crustal conditions (as shown for upper mantle conditions by the simple system experiments). To accommodate the alumina content, pyroxene enriched in CaTs component precipitates as Al-host and anorthite quench textures appear. The phase separation of the melt saturated fluid and a fluid saturated melt upon decompression and cooling could not be traced unambiguously. The composition of the melt saturated fluid fraction was not trapped as no hydrous phases precipitated. However, anorthite precipitates from the solute saturated fluid fraction, the left over H_2O rich fluid probably escapes when the capsule is opened.

Concluding, it can be assumed that anorthositic dykes represent the precipitate of a solute saturated fluid that equilibrated with an highly evolved liquid at depth.

Table 9: Summary of performed experiments

Experiment	facility	#	starting composition	initial water content [wt.%]	P [MPa]	T [°C]	comment	central message
Liquidus experiments	PCA	4	anorthositic rock powder (ZY80L)	6	500	950 - 1200	Melting of albite rims already at T < 950 °C	- liquid immiscibility - anorthite appears as liquidus phase - $T_m \geq 1150 < 1200$ °C at 500 MPa - compositional-/temperature independent H_2O saturation at ~ 6 wt.% H_2O
Simple system experiments	PCA	31	different proportions of synthetic anorthite and diopside glasses and xenolithic forsterite mineral powder	6	500	1000 - 1200	nine compositional series (An/Di/Fo): 20/70/10, 20/10/70, 40/50/10, 45/40/15, 50/30/20, 60/30/10, 60/10/30, 65/20/15 and 72/18/10	- liquid immiscibility - anorthite stability field drastically downsizes - diopside stability field shrinks - spinel stability field disappears - forsterite stability field expands - ternary eutectic/ piercing point at T ≤ 1000 °C - CaTs as intermediate phase
Decompression experiments	PCA	3	rock powder of basaltic spheroid from Kalavassos (UPL)	10	1000 - 250	1150 - 200	PCADecExp = cooled to 650 °C, PCADecExpCr = intermixed with chromite powder to retrace fluid distribution, PCADecExprep = to evaluate autometasomatic processes, quenched at 600 °C and cooled to 200 °C	- complete miscibility of H_2O and basalt at 1150 °C and 1000 MPa - super-liquidus conditions at 1150 °C and 1000 MPa - anorthite precipitation largely suppressed - CaTs as major Al-bearing phase - anorthite discharged from the solute saturated fluid fraction
	IHPV	2		8 & 5	500 - 150	1150 - 700	IHPVDecExp-5-3 containing 5 wt.% H_2O and IHPVDecExp-8-3 containing 8 wt.% H_2O	- 5 wt.% H_2O can be dissolved in the melt at 1150 °C and 500 MPa whereas 8 wt.% H_2O exceeds solubility - fluid immiscibility - no hydrous phases precipitate

SECTION IV: GENETIC MODEL

1 INTRODUCTION

The following chapter aims to compile the information obtained from petrologic investigation (mineralogy and geochemistry) of natural anorthosite rocks (and related late stages spheroidal sample) and the results of the performed experiments to develop a genetic model.

Anorthosite in all its kinds of manifestation, have been matter of research since the early 19th century, and especially caught attention in the 1970s when anorthositic rocks were discovered in rock samples of the moon surface collected by the APOLLO 11 mission.

Anorthosites are rocks of igneous origin, dominated (> 90 %) by plagioclase (X_{An} = 0.2 - 1) whereas the term anorthosite refers to triclinic (anorthose) feldspar, the plagioclase. Anorthositic rocks have formed since the Archean and their appearance is quite diverse. Ashwal (1993b) categorized their occurrences based on temporal relationships and geological setting in six basic types: (1) Archean (calcic) anorthosites, (2) Proterozoic (massif-type) anorthosites, (3) Anorthosites in layered mafic complexes, (4) Anorthosites of oceanic settings, (5) Anorthosite inclusions in other igneous rocks and (6) Extraterrestrial anorthosites. Generation mechanisms of different types are still not fully understood and matter of debate. Ashwal (1993b) floats the idea to generally consider the following questions for the description of anorthosites. (i) What was the composition of the parental magma? (ii) In what manner did the magma crystallize, and how was plagioclase concentrated? (iii) Where and how was the magma generated? (iv) Where, when, and why were these magmas emplaced?

The generation of anorthositic dykes on Cyprus is considered to be somehow related to an oceanic setting - the Troodos ophiolite, and may be confined to group four after the classification of Ashwal. Generally anorthosites of oceanic settings are believed to constitute a minor fraction of the oceanic crust and are thought to represent cumulates formed from the crystallisation of basaltic magma (Ashwal, 1993a). From the outcrop of Troodos anorthositic dykes it is evident that they do not represent a cumulate and thus their classification according to Ahwal is not straight forward.

Dyke compositions had to be liquid at time of intrusion and a mechanism for the generation of such melts is the pivotal aspect of this work. The mechanism for generating plagioclase-supersaturated basic magma is also crucial to the understanding of the origin and evolution of massif anorthosites (Type 2). Flower (1984) proposed an open system polybaric (1000 MPa – 1 atm) model, invoking iterative plagioclase accumulation, magma mixing, and phenocryst resorption to produce plagioclase-supersaturated parent liquids. Applicability of Flowers model for the generation of Troodos anorthositic liquids is difficult but an analogy probably exist in the fact that liquid generation cannot be related to one single event, and rather has to be considered as a multi-phase, polybaric open system process. Massive-type anorthosites are widely believed to have crystallized from relatively anhydrous magmas (e.g. Morse, 1982). Longhi et al. (1999) presents experimental data on phase relations relevant for Type 2 anorthosites also excluding the presence of H_2O as a relevant factor for the generation of anorthosite (massif-type) parental liquids.

2 CONSTRAINTS ON FIELD OBSERVATIONS RELATED TO EXPERIMENTAL RESULTS

Both, observations concerning the petrology and geochemistry of anorthosites, and conclusions on the performed experiments are considered to reveal the generation mechanism of anorthositic dykes.

2.1 WHERE AND HOW WAS THE MAGMA GENERATED?

To answer this question it has to be considered that magma is not the direct source of anorthosites; H_2O rich magma generated at depth unmixes a fluid, that later precipitates the anorthositic assemblage. Consequently the question does not consider magma but rather a solute rich magmatic fluid.

Considering the host magma of anorthosite liquid to be highly saturated in anorthite, the unmixing fluid is assumed to be similarly rich in anorthite component. As derived from phase relation- and decompression experiments, H_2O saturated conditions are crucial to enrich the plagioclase component in the melt fraction. Theoretically a fluid phase coexisting with a H_2O saturated silicate melt is saturated in phases being also stable in the melt fraction. To assess the question of an anorthite rich melt unmixing an anorthite rich fluid, the pure anorthite- H_2O system envisaged. Complete miscibility between an anorthite melt and H_2O is developed, if both, the solubility of H_2O in the anorthite melt, and anorthite solubility in the fluid converge and consolidate in a critical point. The critical curve of the albite- H_2O system has been described by Shen and Keppler (1997). A critical point slightly above 50 wt.% H_2O is determined at 1220 MPa and 650 °C and at 1450 MPa and 763 °C (Shen and Keppler, 1997). At elevated pressure, the solubility of H_2O in silicate melts is known to significantly decrease from albite

towards anorthite compositions (Benne and Behrens, 2003). Generally Ca-silicates are assumed to be less soluble in H_2O than alkali silicates. Compared to the albite-H_2O system, both processes would argue for the critical curve of the anorthite-H_2O system to be shifted to higher temperatures and pressures. However, at upper mantle conditions complete miscibility appears to be realistic.

According to the present mineral phases and their chemical composition, the anorthosite liquid is considered to: (i) be highly saturated in anorthite component, (ii) contain high amounts of HFSE and REY being present as chloride complexes, as a consequence the fluid is considered to (iii) display moderately saline to hydrosaline aqueous compositions. Proceeding on these observations, a chloride component in the anorthosite liquid appears to exert significant control on solubilities of anorthite, HFSE and REY. Magmatic fluids unmixing from silicate melts recorded in melt inclusions have been shown to be Ca rich (Kamenetsky, 2006; Kamenetsky and Kamenetsky, 2010). Experimental work of Roselle and Baumgartner (1995) on anorthite solubilities in supercritical chloride solutions predicted high Ca solubility in saline fluids. Exsolution of hydrosaline liquids have been described in felsic to mafic magmas (Webster, 2004). Exsolution of a magmatic fluid with a high charge in anorthite solute from a highly evolved liquid appears to be a realistic assumption.

2.2 WHAT WAS THE COMPOSITION OF THE PARENTAL MAGMA?

Similarities in trace element distribution and in isotopic signal with boninites reveal coherence in generation mechanisms. The composition of the parental magma that exsolves the anorthositic liquid might be described as highly fractionated H_2O saturated “boninitic” melt. According to Crawford et al. (1989) boninite generation occurs at relatively shallow melting depths of 30 – 50 km

(850 - 1400 MPa assuming averaged crust-mantle densities of 2.9 g/cm^3). Temperatures of 1350 °C or even higher (Beccaluva and Serri, 1988; Falloon and Danyushevsky, 2000; Sun and Nesbitt, 1978) can be assumed at depths relevant for melt generation. Melting of the mantle is initiated by subduction fluids, a process referred as dehydration melting. Boninites can be considered as an "end-member" magmatic suite of supra-subduction zones. They have high H_2O contents and require the most refractory mantle sources (Falloon and Danyushevsky, 2000). Troodos boninites originate from re-melting of the highly depleted mantle wedge beneath the spreading centre left after extraction of tholeiitic melts (König et al., 2010). Trace element and isotope compositions reveal processes such as refertilization of the refractory mantle due to slab fluids and a minor influence of slab melts (fractional melting of the subducted, serpentinized oceanic crust and melts of overlaying sediments are considered to have mixed in).

The anorthositic parental magma, the boninite, is drastically modified by subsequent fractionation prior to the exsolution of the anorthositic liquid. Precipitation of plagioclase from the parental melt is largely suppressed by the presence of H_2O; hence the anorthite component is accumulated both, in the melt and in the fluid fraction. Fractional crystallisation of olivine and pyroxene further differentiates the hydrous parental melt. Crystallisation of anhydrous phases promotes H_2O saturation in the remaining melt, finally unmixing the anorthosite liquid. The unmixing fluid is spatially separated from the melt fraction upon uplift, inhibiting re-equilibration with the melt.

2.3 In what manner did the magma crystallize and how was plagioclase concentrated?

Textural evidence is given for simultaneous precipitation of anorthite and diopside. As illustrated in Fig. 56, minute changes in pressure and temperature will evoke changes in partial H_2O pressure (P_{H2O}) and result in modified stability relations. Theoretically, co-precipitation of forsterite and diopside (according the cotectic line identified by simple system experiments) appears before exsolution of the fluid. Changes in P_{H2O} are related to uplift, forcing to change the stability relations and resulting in co-precipitation of anorthite and diopside (Fig. 56). Phase relations were determined based on changes in glass compositions from the H_2O saturated melt fraction, and not for the melt saturated fluid. However, stability relations might be similar in the fluid.

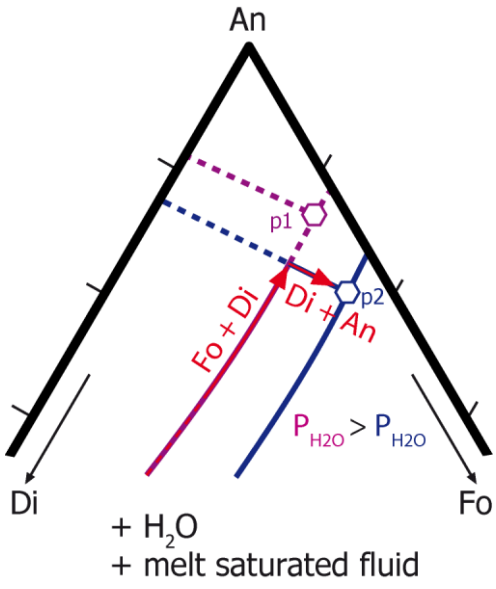

Figure 56: Excerpt of a theoretical phase diagram in the H_2O saturated basaltic An-Di-Fo system projected from H_2O and the melt saturated fluid, redrawn after Figure 43E. Purple and blue lines correspond to cotectic lines at different P_{H2O}. A decrease in partial H_2O pressure will push cotectic lines towards less polymerized phases, inflating the stability field of anorthite. The melt fractionates forsterite and diopside under H_2O saturated conditions (purple cotectic line), increasingly saturating the melt composition in anorthite. A slight decrease in partial H_2O pressure in the melt (related to lower temperatures or lower pressure) changes the phase relations and the melt composition hits the diopside – anorthite cotectic resulting in co-precipitation of diopside and anorthite (blue cotectic lines). The system is quenched shortly before reaching the piercing point p2 (~ 1000 °C according to simple system experiments).

Plagioclase accumulation is inferred as the result of H_2O saturation, the presence of the fluid largely suppresses plagioclase crystallisation forcing the system to accumulate the anorthite component. At lower crustal conditions the composition hits the liquidus, starting to precipitate anorthite.

However, the composition of the accumulated anorthite has to be considered. The performed liquidus experiments revealed that precipitation of pure anorthite is possible from hydrous anorthositic bulk compositions. But, it is evident that the liquid precipitating anorthite had a different composition. Danyushevsky et al. (1997) reported the crystallisation of Ca-rich plagioclase to be possible in a large variability of melt compositions. However, precipitation of pure anorthite is restricted to extremely refractory melts. Generally the melt composition (Al/Si and Ca/Na), especially the H_2O content, affects the plagioclase composition stable at the liquidus (Housh and Luhr, 1991). An increase in any of these compositional parameters results in crystallisation of more calcic plagioclase (Panjasawatwong et al., 1995). Precipitation of hydrothermal anorthite-rich plagioclase (X_{An} up to 0.95) has been described in the deep sheeted dykes of ODP Hole 504B in Costa Rica Rift related to saline brines (Vanko and Laverne, 1998). Accordingly it appears realistic to assume anorthite precipitation from an aqueous Cl-bearing solute rich fluid.

2.4 WHERE, WHEN AND WHY WERE THESE MAGMAS EMPLACED?

The crystal-gel mixture intrudes the UPL supply channels whereas the liquid is quenched to a glass. From crosscutting relations with the host rock, the timing of emplacement is restricted to a late magmatic period; giving the UPL supply channels enough time to cool, solidify and slightly tilt, but early enough to be able to generate mantle melts from subduction related fluids.

The emplacement mechanism is assumed to be related with sudden decompression and fluid exsolution. As described for simple system experiments, due to sudden fluid relief, anorthite-diopside-melt mixture might be flushed upwards intruding the crust. Anorthite has a better wetting ability compared to

diopside as observed in phase relation- and decompression experiments. Diopside in anorthositic samples is observed to appear as clusters (Fig. 7E). At time of the intrusion of anorthositic crystal-liquid mix, anorthite and diopside are sorted according to their wetting ability, whereas transportation of anorthite in the fluid is more efficient than for diopside, leaving behind areas "enriched" in diopside. The transition of pyroxene rich areas in sample ZY80E2 towards more anorthite rich assemblages (Fig. 6B) could be also related to such fluid based sorting.

2.5 A SHORT GENERATION HISTORY OF ANORTHOSITES AND THE LATE STAGE FLUID PRECIPITATE

A H_2O rich melt is generated from the refractory refertilized mantle, the boninite magma. Boninite intrudes as part of the UPL extrusive sequence. Upon intrusion of the boninitic melt, H_2O saturation is reached and a CO_2-fluid, saturated in silicates, unmixes precipitating as in-situ pockets. The left over magma at depth, further differentiates, accumulating anorthite component. However, plagioclase precipitated from the host magma prior to unmixing of the anorthosite fluid as indicated by the negative Eu-anomaly. Furthermore, zircon is precipitated prior to the point of H_2O saturation. Titanium in zircon temperature (~ 1180 °C) confirms magmatic conditions. A solute saturated anorthite, HFSE, REY and chloride rich fluid unmixes scavenging (some of) the zircon from the melt fraction. The melt and the fluid fraction are spatially separated inhibiting further re-equilibration. Zircon reacts with the fluid fraction, adopting composition. Upon fluid ascent diopside and anorthite such as Ti- bearing accessory minerals precipitate. Zirconium in rutile thermometry reveals hydrothermal temperatures (650 – 930 °C). The fluid composition continuously differentiates probably continuously unmixing some of its H_2O content. The anorthosite dykes intrude as a crystal-"melt" mixture. Quench

textures of diopside and hematite form upon glass transition. The compositions of anorthosite dykes are altered by hydrothermal fluids (cretaceous seawater), responsible for albite and thomsonite forming reactions. The allochthonous sample further displays green-schist metamorphic overprinting with chlorite and epidote formation.

APPENDIX

I. LITERATURE

Anfilogov, V.N., 1975. Liquidation in magmas and petrographic criteria for its recognition. Geokhimiya, 7(in Russian; translated in Geochemistry International Vol. 12, 4, 54-61): 1035-1042.

Arnórsson, S., Óskarsson, N., 2007. Molybdenum and tungsten in volcanic rocks and in surface and <100 °C ground waters in Iceland. Geochimica et Cosmochimica Acta, 71(2): 284-304.

Ashwal, L.D., 1993a. Anorthosites of Oceanic Settings, Anorthosites. Springer Berlin Heidelberg, Berlin, Heidelberg, pp. 262-280.

Ashwal, L.D., 1993b. Introduction, Anorthosites. Springer Berlin Heidelberg, Berlin, Heidelberg, pp. 1-4.

Auer, S., Bindeman, I., Wallace, P., Ponomareva, V., Portnyagin, M., 2009. The origin of hydrous, high-δ18O voluminous volcanism: diverse oxygen isotope values and high magmatic water contents within the volcanic record of Klyuchevskoy volcano, Kamchatka, Russia. Contributions to Mineralogy and Petrology, 157(2): 209-230.

Ayers, J.C., Watson, E.B., 1991. Solubility of Apatite, Monazite, Zircon, and Rutile in Supercritical Aqueous Fluids with Implications for Subduction Zone Geochemistry. Philosophical Transactions of the Royal Society of London. Series A: Physical and Engineering Sciences, 335(1638): 365-375.

Baker, D.R., Alletti, M., 2012. Fluid saturation and volatile partitioning between melts and hydrous fluids in crustal magmatic systems: The contribution of experimental measurements and solubility models. Earth-Science Reviews, 114(3–4): 298-324.

Bali, E., Audétat, A., Keppler, H., 2010. The mobility of U and Th in subduction zone fluids: an indicator of oxygen fugacity and fluid salinity. Contributions to Mineralogy and Petrology, 161(4): 597-613.

Ballhaus, C., Fonseca, R.O.C., Münker, C., Kirchenbaur, M., Zirner, A., 2015. Spheroidal textures in igneous rocks – Textural consequences of H2O saturation in basaltic melts. Geochimica et Cosmochimica Acta, 167: 241-252.

Barrer, R.M., Denny, P.J., 1961. 202. Hydrothermal chemistry of the silicates. Part X. A partial study of the field CaO-Al2O3-SiO2-H2O. Journal of the Chemical Society (Resumed)(0): 983-1000.

Barth-Wirsching, U., Holler, H., 1989. Experimental studies on zeolite formation conditions. European Journal of Mineralogy: 489-506.

Bau, M., 1991. Rare-earth element mobility during hydrothermal and metamorphic fluid-rock interaction and the significance of the oxidation state of europium. Chemical Geology, 93(3): 219-230.

Bau, M., 1996. Controls on the fractionation of isovalent trace elements in magmatic and aqueous systems: evidence from Y/Ho, Zr/Hf, and lanthanide tetrad effect. Contributions to Mineralogy and Petrology, 123(3): 323-333.

Beccaluva, L., Serri, G., 1988. Boninitic and low-Ti subduction-related lavas from intraoceanic arc-backarc systems and low-Ti ophiolites: a reappraisal of their petrogenesis and original tectonic setting. Tectonophysics, 146(1): 291-315.

Behrens, H. et al., 2009. Solubility of H2O and CO2 in ultrapotassic melts at 1200 and 1250 °C and pressure from 50 to 500 MPa. American Mineralogist, 94(1): 105-120.

Behrens, H., Ohlhorst, S., Holtz, F., Champenois, M., 2004. CO2 solubility in dacitic melts equilibrated with H2O-CO2 fluids: Implications for modeling the solubility of CO2 in silicic melts. Geochimica et Cosmochimica Acta, 68(22): 4687-4703.

Benne, D., Behrens, H., 2003. Water solubility in haplobasaltic melts. European Journal of Mineralogy, 15(5): 803-814.

Berger, G., Schott, J., Guy, C., 1988. Behavior of Li, Rb and Cs during basalt glass and olivine dissolution and chlorite, smectite and zeolite precipitation from seawater: Experimental investigations and modelization between 50° and 300°C. Chemical Geology, 71(4): 297-312.

Berndt, J., Koepke, J., Holtz, F., 2004. An Experimental Investigation of the Influence of Water and Oxygen Fugacity on Differentiation of MORB at 200 MPa. Journal of Petrology, 46(1): 135-167.

Berndt, J. et al., 2002. A combined rapid-quench and H2-membrane setup for internally heated pressure vessels: Description and application for water solubility in basaltic melts, American Mineralogist, pp. 1717.

Blank, J.G., Brooker, R.A., 1994. Experimental Studies of Carbon Dioxide in Silicate Melts: Solubility, Speciation, and Stable Carbon Isotope Behavior. In: Carroll,

M.R., Holloway, J.R. (Eds.), Volatiles in Magmas. Mineralogical Society of America, pp. 157 - 186.

Blank, J.G., Stolper, E.M., Carroll, M.R., 1993. Solubilities of carbon dioxide and water in rhyolitic melt at 850°C and 750 bars. Earth and Planetary Science Letters, 119(1–2): 27-36.

Blundy, J.D., Robinson, J.A.C., Wood, B.J., 1998. Heavy REE are compatible in clinopyroxene on the spinel lherzolite solidus. Earth and Planetary Science Letters, 160(3–4): 493-504.

Boettcher, A.L., Wyllie, P.J., 1969. Phase relationships in the system NaAlSiO4 -SiO2 -H2O to 35 kilobars pressure. American Journal of Science, 267(8): 875-909.

Boles, J.R., 1982. Active albitization of plagioclase, gulf coast Tertiary. American Journal of Science, 282(2): 165-180.

Botcharnikov, R., Freise, M., Holtz, F., Behrens, H., 2005. Solubility of C-O-H mixturesin natural melts: new experimental data and application range of recent models. Annals of Geophysics.

Botcharnikov, R.E., Behrens, H., Holtz, F., 2006. Solubility and speciation of C–O–H fluids in andesitic melt at T = 1100–1300 °C and P = 200 and 500 MPa. Chemical Geology, 229(1–3): 125-143.

Bowen, N.L., 1913. The melting phenomena of the plagioclase feldspars. American Journal of Science, 35(4): 577-599.

Bowen, N.L., Andersen, O., 1914. The binary system MgO-SiO2. American Journal of Science, Series 4 Vol. 37(222): 487-500.

Boyd, F.R., England, J.L., Davis, B.T.C., 1964. Effects of pressure on the melting and polymorphism of enstatite, MgSiO3. Journal of Geophysical Research, 69(10): 2101-2109.

Bressan, D., 2010. History of Geology The Granite Controversy: Neptunism vs. Plutonism.

Brooker, R.A., Kohn, S.C., Holloway, J.R., McMillan, P.F., 2001. Structural controls on the solubility of CO2 in silicate melts: Part II: IR characteristics of carbonate groups in silicate glasses. Chemical Geology, 174(1–3): 241-254.

Bryan, W.B., 1972. Morphology of quench crystals in submarine basalts. Journal of Geophysical Research, 77(29): 5812-5819.

Burke, W.H. et al., 1982. Variation of seawater 87Sr/86Sr throughout Phanerozoic time. Geology, 10(10): 516-519.

Burnham, C.W., 1975. Water and magmas; a mixing model. Geochimica et Cosmochimica Acta, 39(8): 1077-1084.

Burnham, C.W., 1981. The nature of multicomponent aluminosilicate melts. Physics and Chemistry of the Earth, 13: 197-229.

Cameron, E.W., Nisbet, E.G., Dietrich, V.J., 1979. Petrographic dissimilarities between ophiolite and ocean floor basalts. In: Panayiotou, A. (Editor), Ophiolites: proceedings, International Ophiolite Symposium, Cyprus, 1979. Republic of Cyprus, Ministry of Agriculture and Natural Resources, Geological Survey Dept., Nicosia, Cyprus, pp. 182-192.

Cameron, W.E., 1985. Petrology and origin of primitive lavas from the Troodos ophiolite, Cyprus. Contributions to Mineralogy and Petrology, 89(2-3): 239-255.

Carroll, M.R., Holloway, J.R., 1994. Volatiles in Magmas, 30. Mineralogical Society of America.

Cassidy, W.A., Segnit, E.R., 1955. Liquid immiscibility in a silicate melt. Nature, 176(4476): 305-305.

Cempírek, J., Houzar, S., Novák, M., 2008. Complexly zoned niobian titanite from hedenbergite skarn at Písek, Czech Republic, constrained by substitutions Al(Nb,Ta)Ti-2, Al(F,OH)(TiO)-1 and SnTi-1. Mineralogical Magazine, 72(6): 1293-1305.

Che, X.D., Linnen, R.L., Wang, R.C., Groat, L.A., Brand, A.A., 2013. Distribution of trace and rare earth elements in titanite from tungsten and molybdenum depositis in Yukon and British Columbia, Canada. The Canadian Mineralogist, 51(3): 415-438.

Coleman, R.G., 2014. The ophiolite concept evolves. Elements, 10(2): 82-84.

Constantinou, G., 1980. Metallogenesis associated with Troodos Ophiolite, Cyprus Geological Survey Department, Nicosia.

Crawford, A.J., Falloon, T.J., Green, D.H., 1989. Classification, petrogenesis and tectonic setting of boninites. Boninites and related rocks: 1-49.

Cundy, C.S., Cox, P.A., 2003. The Hydrothermal Synthesis of Zeolites: History and Development from the Earliest Days to the Present Time. Chemical Reviews, 103(3): 663-702.

Danyushevsky, L.V., Caroll, M.R., Falloon, T.J., 1997. Origin of high-An plagioclase in Tongan high-Ca Boninites: Implications for plagioclase-melt equilibria at low p(H2O). Canadian Mineralogist, 35: 313– 326.

Davis, B.T.C., Boyd, F.R., 1966. The join Mg2Si2O6-CaMgSi2O6 at 30 kilobars pressure and its application to pyroxenes from kimberlites. Journal of Geophysical Research, 71(14): 3567-3576.

De'Gennaro, M., Langella, A., Cappelletti, P., Colella, C., 1999. Hydrothermal conversion of trachytic glass to zeolite. 3. Monocationic model glasses. Clays and clay minerals, 47: 348-357.

Di Matteo, V., Carroll, M.R., Behrens, H., Vetere, F., Brooker, R.A., 2004. Water solubility in trachytic melts. Chemical Geology, 213(1–3): 187-196.

Dilek, Y., Furnes, H., 2009. Structure and geochemistry of Tethyan ophiolites and their petrogenesis in subduction rollback systems. Lithos, 113(1–2): 1-20.

Dilek, Y., Furnes, H., 2014. Ophiolites and Their Origins. Elements, 10(2): 93-100.

Dixon, J., Eaby, 1997. Degassing of alkalic basalts, American Mineralogist, pp. 368.

Dixon, J., Eaby, Pan, V., 1995. Determination of the molar absorptivity of dissolved carbonate in basanitic glass, American Mineralogist, pp. 1339.

Dixon, J.E., Stolper, E.M., 1995. An Experimental Study of Water and Carbon Dioxide Solubilities in Mid-Ocean Ridge Basaltic Liquids. Part II: Applications to Degassing. Journal of Petrology, 36(6): 1633-1646.

Dixon, J.E., Stolper, E.M., Holloway, J.R., 1995. An Experimental Study of Water and Carbon Dioxide Solubilities in Mid-Ocean Ridge Basaltic Liquids. Part I: Calibration and Solubility Models. Journal of Petrology, 36(6): 1607-1631.

Duncan, R.A., Green, D.H., 1987. The genesis of refractory melts in the formation of oceanic crust. Contributions to Mineralogy and Petrology, 96(3): 326-342.

Edwards, S., Hudson Edwards, K., Cann, J., Malpas, J., Xenophontos, C., 2010. Cyprus. Classic Geology in Europe 7. Terra Publishing, Harpenden, UK.

Ellis, L., 2000. Edward Luby: Reverse Stratigraphy, Archaeological Method and Theory: An Encyclopedia. Garland Publishing, Inc., New York, pp. 1102.

Falloon, T.J., Danyushevsky, L.V., 2000. Melting of Refractory Mantle at 1·5, 2 and 2·5 GPa under Anhydrous and H2O-undersaturated Conditions: Implications for the Petrogenesis of High-Ca Boninites and the Influence of

Subduction Components on Mantle Melting. Journal of Petrology, 41(2): 257-283.

Falloon, T.J., Green, D.H., 1988. Anhydrous Partial Melting of Peridotite from 8 to 35 kb and the Petrogenesis of MORB. Journal of Petrology, Special_Volume(1): 379-414.

Flower, M.F.J., 1984. Anorthosite genesis: The mid-ocean ridge analogue. Geology, 12(11): 651-654.

Flower, M.F.J., Levine, H.M., 1987. Petrogenesis of a tholeiite-boninite sequence from Ayios Mamas, Troodos ophiolite: evidence for splitting of a volcanic arc? Contributions to Mineralogy and Petrology, 97(4): 509-524.

Foley, S., Tiepolo, M., Vannucci, R., 2002. Growth of early continental crust controlled by melting of amphibolite in subduction zones. Nature, 417(6891): 837-840.

Foley, S.F., Barth, M.G., Jenner, G.A., 2000. Rutile/melt partition coefficients for trace elements and an assessment of the influence of rutile on the trace element characteristics of subduction zone magmas. Geochimica et Cosmochimica Acta, 64(5): 933-938.

Fonseca, R.O.C. et al., 2017. Fingerprinting fluid sources in Troodos ophiolite complex orbicular glasses using high spatial resolution isotope and trace element geochemistry. Geochimica et Cosmochimica Acta.

Freund, S., Haase, K.M., Keith, M., Beier, C., Garbe-Schönberg, D., 2014. Constraints on the formation of geochemically variable plagiogranite intrusions in the Troodos Ophiolite, Cyprus. Contributions to Mineralogy and Petrology, 167(2): 1-22.

Gass, I.G., Smewing, J.D., 1973. Intrusion, Extrusion and Metamorphism at Constructive Margins: Evidence from the Troodos Massif, Cyprus. Nature, 242(5392): 26-29.

Ghiorso, M.S., Sack, R.O., 1995. Chemical mass transfer in magmatic processes IV. A revised and internally consistent thermodynamic model for the interpolation and extrapolation of liquid-solid equilibria in magmatic systems at elevated temperatures and pressures. Contributions to Mineralogy and Petrology, 119(2-3): 197-212.

Gillespie, G., Engel, M., Dieterle, B., 2008. Romantic Prose Fiction A Comparative History of of Literatures in European Languages. John Benjamins Publishing Company, Amsterdam/Philadelphia.

Goranson, R.W., 1931. Solubility of water in granite magmas. Eos, Transactions American Geophysical Union, 12(1): 183-183.

Green, T.H., Pearson, N.J., 1987. An experimental study of Nb and Ta partitioning between Ti-rich minerals and silicate liquids at high pressure and temperature. Geochimica et Cosmochimica Acta, 51(1): 55-62.

Grove, T.L., Bence, A.E., 1977. Experimental study of pyroxene-liquid interaction in quartz-normative basalt 15597, Lunar Science Conference. Pergamon Press, Houston, Texas, pp. 1549-1579.

Hamilton, D.L., Burnham, C.W., Osborn, E.F., 1964. The Solubility of Water and Effects of Oxygen Fugacity and Water Content on Crystallization in Mafic Magmas. Journal of Petrology, 5(1): 21-39.

Hawkins, D.B., 1981. Kinetics of glass dissolution and zeolite formation under hydrothermal conditions. Clays and Clay Minerals, 29(5): 331-340.

Hay, R.L., 1986. Geologic occurrence of zeolites and some associated minerals, Pure and Applied Chemistry, pp. 1339.

Hess, P.C., 1971. Polymer model of silicate melts. Geochimica et Cosmochimica Acta, 35(3): 289-306.

Hoffmann, J.E. et al., 2010. Highly depleted Hadean mantle reservoirs in the sources of early Archean arc-like rocks, Isua supracrustal belt, southern West Greenland. Geochimica et Cosmochimica Acta, 74(24): 7236-7260.

Hofmann, A.W., 1975. Diffusion of Ca and Sr in a basalt melt. Carnegie Inst. Washington Yearb. 74: 183.

Holloway, J.R., 1971. Internally Heated Pressure Vessels. In: Ulmer, G.C. (Ed.), Research Techniques for High Pressure and High Temperature. Springer Berlin Heidelberg, Berlin, Heidelberg, pp. 217-258.

Holloway, J.R., Blank, J.G., 1994. Application of experimental results to C-O-H species in natural melts. Reviews in mineralogy, 30: 187-187.

Horng, W.-S., Hess, P.C., 2000. Partition coefficients of Nb and Ta between rutile and anhydrous haplogranite melts. Contributions to Mineralogy and Petrology, 138(2): 176-185.

Housh, T.B., Luhr, J.F., 1991. Plagioclase-melt equilibria in hydrous systems. American Mineralogist, 76(3-4): 477-492.

Hövelmann, J., Putnis, A., Geisler, T., Schmidt, B.C., Golla-Schindler, U., 2009. The replacement of plagioclase feldspars by albite: observations from hydrothermal experiments. Contributions to Mineralogy and Petrology, 159(1): 43-59.

Hume-Rothery, W., Anderson, E., 1960. Eutectic compositions and liquid immiscibility in certain binary alloys. Philosophical Magazine, 5(52): 383-405.

Hunt, J.D., Manning, C.E., 2012. A thermodynamic model for the system near the upper critical end point based on quartz solubility experiments at 500–1100 °C and 5–20 kbar. Geochimica et Cosmochimica Acta, 86: 196-213.

Iacovino, K., Moore, G., Roggensack, K., Oppenheimer, C., Kyle, P., 2013. H2O–CO2 solubility in mafic alkaline magma: applications to volatile sources and degassing behavior at Erebus volcano, Antarctica. Contributions to Mineralogy and Petrology, 166(3): 845-860.

Jakobsson, S., 1997. Solubility of water and carbon dioxide in an icelandite at 1400 °C and 10 kilobars. Contributions to Mineralogy and Petrology, 127(1): 129-135.

Jochum, K.P. et al., 2011. Determination of Reference Values for NIST SRM 610–617 Glasses Following ISO Guidelines. Geostandards and Geoanalytical Research, 35(4): 397-429.

Johannes, W., 1978. Melting of plagioclase in the system Ab-An-H2O and Qz–Ab–An–H2O at P (H2O) = 5 kbars, an Equilibrium Problem Contributions to Mineralogy and Petrology, 66(3): 295-303.

Juan, V.C., Lo, H.J., 1968. Phase relations in the system NaAlSi3O8-CaAl2Si2O8-H2O. Proceedings of the Geological Society of China, 12: 22-29.

Kamenetsky, V.S., 2006. Melt inclusion record of magmatic immiscibility in crustal and mantle magmas. Melt inclusions in plutonic rocks: 81-98.

Kamenetsky, V.S., Kamenetsky, M.B., 2010. Magmatic fluids immiscible with silicate melts: examples from inclusions in phenocrysts and glasses, and implications for magma evolution and metal transport. Geofluids, 10(1-2): 293-311.

Kent, A.J.R., 2008. Melt Inclusions in Basaltic and Related Volcanic Rocks. Reviews in Mineralogy and Geochemistry, 69(1): 273-331.

Keppler, H., Wyllie, P.J., 1990. Role of fluids in transport and fractionation of uranium and thorium in magmatic processes. Nature, 348(6301): 531-533.

King, P.L., Holloway, J.R., 2002. CO2 solubility and speciation in intermediate (andesitic) melts: the role of H2O and composition. Geochimica et Cosmochimica Acta, 66(9): 1627-1640.

King, P.L. et al., 2002. Analytical techniques for volatiles: A case study using intermediate (andesitic) glasses, American Mineralogist, pp. 1077.

Klemme, S., Prowatke, S., Hametner, K., Günther, D., 2005. Partitioning of trace elements between rutile and silicate melts: Implications for subduction zones. Geochimica et Cosmochimica Acta, 69(9): 2361-2371.

König, S., Münker, C., Schuth, S., Garbe-Schönberg, D., 2008. Mobility of tungsten in subduction zones. Earth and Planetary Science Letters, 274(1–2): 82-92.

König, S. et al., 2010. Boninites as windows into trace element mobility in subduction zones. Geochimica et Cosmochimica Acta, 74(2): 684-704.

Kudo, A.M., Weill, D.F., 1970. An igneous plagioclase thermometer. Contributions to Mineralogy and Petrology, 25(1): 52-65.

Kushiro, I., Syono, Y., Akimoto, S.-i., 1968a. Melting of a peridotite nodule at high pressures and high water pressures. Journal of Geophysical Research, 73(18): 6023-6029.

Kushiro, I., Yoder, H.S., Nishikawa, M., 1968b. Effect of Water on the Melting of Enstatite. Geological Society of America Bulletin, 79(12): 1685-1692.

Lafuente, B., Downs, R.T., Yang, H., Stone, N., 2015. The power of databases: the RRUFF project. Highlights in Mineralogical Crystallography. De Gruyter W., Berlin, Germany, 1-30 pp.

Leeman, W.P., 1996. Boron and Other Fluid-mobile Elements in Volcanic Arc Lavas: Implications for Subduction Processes, Subduction Top to Bottom. American Geophysical Union, pp. 269-276.

Lewis, G.N., 1923. Valence and the Structure of Atoms and Molecules. Chemical Catalog Com.; New York.

Loewinson-Lessing, V., Franz, 1884. Die Variolite von Jalguba im Gouvernement Olonez. Petrogr. Mitt, 6: 281-300.

Longerich, H.P., Jackson, S.E., Günther, D., 1996. Inter-laboratory note. Laser ablation inductively coupled plasma mass spectrometric transient signal data acquisition and analyte concentration calculation. Journal of Analytical Atomic Spectrometry, 11(9): 899-904.

Longhi, J., Auwera, J.V., Fram, M.S., Duchesne, J.-C., 1999. Some Phase Equilibrium Constraints on the Origin of Proterozoic (Massif) Anorthosites and Related Rocks. Journal of Petrology, 40(2): 339-362.

Manning, C.E., 2004. The chemistry of subduction-zone fluids. Earth and Planetary Science Letters, 223(1–2): 1-16.

Marien, C., 2012. Isotopen- und Spurenelementuntersuchungen an Plagiograniten, Universität zu Köln, Köln, 80 pp.

Marien, C., 2015. The pertogenesis of oceanic plagiogranites from Cyprus. Institut für Geologie und Mineralogie Universität zu Köln, Cologne, pp. 77.

Mariner, R.H., Surdam, R.C., 1970. Alkalinity and Formation of Zeolites in Saline Alkaline Lakes. Science, 170(3961): 977-980.

Mathez, E.A., 1973. Refinement of the Kudo-Weill plagioclase thermometer and its application to basaltic rocks. Contributions to Mineralogy and Petrology, 41(1): 61-72.

Matveev, S., Ballhaus, C., 2002. Role of water in the origin of podiform chromitite deposits. Earth and Planetary Science Letters, 203(1): 235-243.

McBriney, A., R., 1993. Igneous petrology, 2nd. CBS Publishers & Distributors Pvt, Boston, USA, 503 pp.

McCarthy, T.C., Patiño Douce, A.E., 1998. Empirical calibration of the silica–Ca-tschermak's–anorthite (SCAn) geobarometer. Journal of Metamorphic Geology, 16(5): 675-686.

McConnell, H.M., Vrljic, M., 2003. Liquid-Liquid Immiscibility in Membranes. Annual Review of Biophysics and Biomolecular Structure, 32(1): 469-492.

McConnell, J.D.C., 1974. Analyses ot time-temperature-transormation behavior of the plagioclase feldspars. In: MacKenzie, W.S., Zussman, J. (Eds.), The Feldspars. Manchester University Press, Manchester, pp. 460-477.

McDade, P., Blundy, J.D., Wood, B.J., 2003. Trace element partitioning on the Tinaquillo Lherzolite solidus at 1.5 GPa. Physics of the Earth and Planetary Interiors, 139(1–2): 129-147.

McMillan, P., Holloway, J., 1987. Water solubility in aluminosilicate melts. Contributions to Mineralogy and Petrology, 97(3): 320-332.

Miyashiro, A., 1973. The Troodos ophiolitic complex was probably formed in an island arc. Earth and Planetary Science Letters, 19(2): 218-224.

Moores, E.M., 1975. Discussion of "origin of troodos and other ophiolites: A reply to hynes", by akiho miyashiro. Earth and Planetary Science Letters, 25(2): 223-226.

Moores, E.M., Robinson, P.T., Malpas, J., Xenophonotos, C., 1984. Model for the origin of the Troodos massif, Cyprus, and other mideast ophiolites. Geology, 12(8): 500-503.

Moores, E.M., Vine, F.J., 1971. The Troodos Massif, Cyprus and other Ophiolites as Oceanic Crust: Evaluation and Implications. Philosophical Transactions of the Royal Society of London A: Mathematical, Physical and Engineering Sciences, 268(1192): 443-467.

Morimoto, N., 1988. Nomenclature of Pyroxenes. Mineralogy and Petrology, 39(1): 55-76.

Morizet, Y., Brooker, R.A., Kohn, S.C., 2002. CO2 in haplo-phonolite melt: solubility, speciation and carbonate complexation. Geochimica et Cosmochimica Acta, 66(10): 1809-1820.

Morizet, Y., Paris, M., Gaillard, F., Scaillet, B., 2010. C–O–H fluid solubility in haplobasalt under reducing conditions: An experimental study. Chemical Geology, 279(1–2): 1-16.

Morse, S.A., 1982. A partisan review of Proterozoic anorthosites. American Mineralogist, 67(11-12): 1087-1100.

Moulson, A.J., Roberts, J.P., 1961. Water in silica glass. Transactions of the Faraday Society, 57(0): 1208-1216.

Muenow, D.W., Garciat, M.O., Aggrey, K.E., Bednarz, U., Schmincke, H.U., 1990. Volatiles in submarine glasses as a discriminant of tectonic origin: application to the Troodos ophiolite. Nature, 343(6254): 159-161.

Mukasa, S.B., Ludden, J.N., 1987. Uranium-lead isotopic ages of plagiogranites from the Troodos ophiolite, Cyprus, and their tectonic significance. Geology, 15(9): 825-828.

Münker, C., Weyer, S., Scherer, E., Mezger, K., 2001. Separation of high field strength elements (Nb, Ta, Zr, Hf) and Lu from rock samples for MC-ICPMS measurements. Geochemistry, Geophysics, Geosystems, 2(12): n/a-n/a.

Münker, C., Wörner, G., Yogodzinski, G., Churikova, T., 2004. Behaviour of high field strength elements in subduction zones: constraints from Kamchatka–Aleutian arc lavas. Earth and Planetary Science Letters, 224(3–4): 275-293.

Mysen, B.O., 1977. The solubility of H2O and CO2 under predicted magma genesis conditions and some petrological and geophysical implications. Reviews of Geophysics, 15(3): 351–361

Mysen, B.O., 2014. Water-melt interaction in hydrous magmatic systems at high temperature and pressure. Progress in Earth and Planetary Science, 1(1): 4.

Mysen, B.O., Cody, G.D., Smith, A., 2004. Solubility mechanisms of fluorine in peralkaline and meta-aluminous silicate glasses and in melts to magmatic temperatures1. Geochimica et Cosmochimica Acta, 68(12): 2745-2769.

Newman, S., Lowenstern, J.B., 2002. VolatileCalc: a silicate melt–H2O–CO2 solution model written in Visual Basic for excel. Computers & Geosciences, 28(5): 597-604.

Osozawa, S. et al., 2012. Geochemistry and geochronology of the Troodos ophiolite: An SSZ ophiolite generated by subduction initiation and an extended episode of ridge subduction? Lithosphere, 4(6): 497-510.

Paillat, O., Elphick, S., Brown, W., 1992. The solubility of water in NaAlSi3O8 melts: a re-examination of Ab–H2O phase relationships and critical behaviour at high pressures. Contributions to Mineralogy and Petrology, 112(4): 490-500.

Palme, H., Lodders, K., Jones, A., 2014. Solar system abundances of the elements. Planets, Asteriods, Comets and The Solar System, 1: 15-36.

Palmer, M.R., Edmond, J.M., 1989. Cesium and rubidium in submarine hydrothermal fluids: Evidence for recycling of alkali elements. Earth and Planetary Science Letters, 95(1): 8-14.

Panjasawatwong, Y., Danyushevsky, L., Crawford, A., Harris, K., 1995. An experimental study of the effects of melt composition on plagioclase-melt equilibria at 5 and 10 kbar: implications for the origin of magmatic high-An plagioclase. Contributions to Mineralogy and Petrology, 118(4): 420-432.

Pearce, J.A., 1975. Basalt geochemistry used to investigate past tectonic environments on Cyprus. Tectonophysics, 25(1–2): 41-67.

Pearce, T.H., Kolisnik, A.M., 1990. Observations of plagioclase zoning using interference imaging. Earth-Science Reviews, 29(1): 9-26.

Philpotts, A.R., 1976. Silicate liquid immiscibility; its probable extent and petrogenetic significance. American Journal of Science, 276(9): 1147-1177.

Philpotts, A.R., Ague, J., 2009. Principles of igneous and metamorphic petrology. Cambridge University Press.

Plank, T., Kelley, K.A., Zimmer, M.M., Hauri, E.H., Wallace, P.J., 2013. Why do mafic arc magmas contain ~4 wt% water on average? Earth and Planetary Science Letters, 364(0): 168-179.

Portnyagin, M.V., Danyushevsky, L.V., Kamenetsky, V.S., 1997. Coexistence of two distinct mantle sources during formation of ophiolites: a case study of primitive pillow-lavas from the lowest part of the volcanic section of the Troodos Ophiolite, Cyprus. Contributions to Mineralogy and Petrology, 128(2): 287-301.

Presnall, D.C. et al., 1978. Liquidus phase relations on the join diopside-forsterite-anorthite from 1 atm to 20 kbar: Their bearing on the generation and crystallization of basaltic magma. Contributions to Mineralogy and Petrology, 66(2): 203-220.

Prowatke, S., Klemme, S., 2005. Effect of melt composition on the partitioning of trace elements between titanite and silicate melt. Geochimica et Cosmochimica Acta, 69(3): 695-709.

Putnis, A., 2002. Mineral replacement reactions: from macroscopic observations to microscopic mechanisms. Mineralogical Magazine, 66(5): 689-708.

Putnis, A., Putnis, C.V., 2007. The mechanism of reequilibration of solids in the presence of a fluid phase. Journal of Solid State Chemistry, 180(5): 1783-1786.

Rapp, J.F., Klemme, S., Butler, I.B., Harley, S.L., 2010. Extremely high solubility of rutile in chloride and fluoride-bearing metamorphic fluids: An experimental investigation. Geology, 38(4): 323-326.

Rautenschlein, M. et al., 1985. Isotopic and trace element composition of volcanic glasses from the Akaki Canyon, Cyprus: implications for the origin of the Troodos ophiolite. Earth and Planetary Science Letters, 75(4): 369-383.

Read, H.H., 1957. The granite controversy. Thomas murby.

Regelous, M. et al., 2014. Formation of the Troodos Ophiolite at a triple junction: Evidence from trace elements in volcanic glass. Chemical Geology, 386: 66-79.

Republic of Cyprus, Ministry of Agriculture, Rural Development and Environment, Geological Survey Department, 2005-2016. Geology of Cyprus. In: Geological Survey Department (Editor),

http://www.moa.gov.cy/moa/gsd/gsd.nsf/dmlTroodos_en/dmlTroodos_en?OpenDocument#.

Richet, P., Lejeune, A.-M., Holtz, F., Roux, J., 1996. Water and the viscosity of andesite melts. Chemical Geology, 128(1–4): 185-197.

Robertson, A.H.F., Woodcock, N.H., 1979. Mamonia Complex, southwest Cyprus: Evolution and emplacement of a Mesozoic continental margin. Geological Society of America Bulletin, 90(7): 651-665.

Robinson, P.T., Melson, W.G., O'Hearn, T., Schmincke, H.-U., 1983. Volcanic glass compositions of the Troodos ophiolite, Cyprus. Geology, 11(7): 400-404.

Roedder, E., 1951. Low temperature liquid immiscibility in the system K2O-FeO-Al2O3-SiO2. American Mineralogist, 36: 282-286.

Roedder, E., 1979. Silicate Liquid Immiscibility in magmas, Evolution of the Igneous Rocks: Fiftieth Anniversary Perspectives. Princeton University Press, pp. 15-58.

Roedder, E., 2003. Significance of melt inclusions. In: Benedetto De, V., Robert, J.B. (Eds.), Developments in Volcanology. Elsevier, pp. xv-xvi.

Roedder, E., Weiblen, P.W., 1970. Silicate Liquid Immiscibility in Lunar Magmas, Evidenced by Melt Inclusions in Lunar Rocks. Science, 167(3918): 641-644.

Roedder, E., Weiblen, P.W., 1971. Petrology of silicate melt inclusions, Apollo 11 and Apollo 12 and terrestrial equivalents, Lunar and Planetary Science Conference Proceedings, pp. 507.

Roeder, P.L., Emslie, R.F., 1970. Olivine-liquid equilibrium. Contributions to Mineralogy and Petrology, 29(4): 275-289.

Roselle, G.T., Baumgartner, L.P., 1995. Experimental determination of anorthite solubility and calcium speciation in supercritical chloride solutions at 2 kb from 400 to 600°C. Geochimica et Cosmochimica Acta, 59(8): 1539-1549.

Sand, L.B., 1980. Zeolite synthesis and crystallization. Pure and Applied Chemistry, 52(9): 2105-2113.

Schmincke, H.-U., Rautenschlein, M., Robinson, P.T., Mehegan, J.M., 1983. Troodos extrusive series of Cyprus: A comparison with oceanic crust. Geology, 11(7): 405-409.

Schreyer, W., 1976. Hochdruckforschung in der modernen Gesteinskunde, Anwendung der organischen Geochemie für die Erdölexploration.

Hochdruckforschung in der modernen Gesteinskunde: 240. Sitzung am 4. Februar 1976 in Düsseldorf. VS Verlag für Sozialwissenschaften, Wiesbaden, pp. 41-83.

Seiler, R.L., Stollenwerk, K.G., Garbarino, J.R., 2005. Factors controlling tungsten concentrations in ground water, Carson Desert, Nevada. Applied Geochemistry, 20(2): 423-441.

Shannon, R., 1976. Revised effective ionic radii and systematic studies of interatomic distances in halides and chalcogenides. Acta Crystallographica Section A, 32(5): 751-767.

Shen, A.H., Keppler, H., 1997. Direct observation of complete miscibility in the albite-H2O system. Nature, 385(6618): 710-712.

Shishkina, T.A., Botcharnikov, R.E., Holtz, F., Almeev, R.R., Portnyagin, M.V., 2010. Solubility of H2O- and CO2-bearing fluids in tholeiitic basalts at pressures up to 500 MPa. Chemical Geology, 277(1–2): 115-125.

Simonian, K.O., Gass, I.G., 1978. Arakapas fault belt, Cyprus: A fossil transform fault. Geological Society of America Bulletin, 89(8): 1220-1230.

Sobolev, A.V., 1996. Melt inclusions in minerals as a source of principle petrological information. Petrology, 4(3): 209-220.

Sobolev, A.V. et al., 1993. Petrology of ultramafic lavas and associated rocks of the Troodos Massif, Cyprus. Petrology, 1: 331-361.

Stalder, R., Ulmer, P., Thompson Alan, B., Günther, D., 2000. Experimental approach to constrain second critical end points in fluid/silicate systems: Near-solidus fluids and melts in the system albite-H2O, American Mineralogist, pp. 68.

Stolper, E.M., 1982. The speciation of water in silicate melts. Geochimica et Cosmochimica Acta, 46(12): 2609-2620.

Stracke, A., Scherer, E., Reynolds, B., 2014. 15.4 Application of isotope dilution in geochemistry. Treatise on Geochemistry (Second Edition). Elsevier, Oxford: 71-86.

Sun, S.-S., Nesbitt, R.W., 1978. Geochemical regularities and genetic significance of ophiolitic basalts. Geology, 6(11): 689-693.

Sverjensky, D.A., 1984. Europium redox equilibria in aqueous solution. Earth and Planetary Science Letters, 67(1): 70-78.

Tamic, N., Behrens, H., Holtz, F., 2001. The solubility of H2O and CO2 in rhyolitic melts in equilibrium with a mixed CO2–H2O fluid phase. Chemical Geology, 174(1–3): 333-347.

Thy, P., Schiffman, P., Moores, E., 1989. Igneous mineral stratigraphy and chemistry of the Cyprus Crustal Study Project drill core in the plutonic sequences of the Troodos ophiolite. Cyprus Crustal Study Project, Hole CY-4: Geological Survey of Canada, Paper: 88-9.

Vanko, D.A., Laverne, C., 1998. Hydrothermal anorthitization of plagioclase within the magmatic/hydrothermal transition at mid-ocean ridges: examples from deep sheeted dikes (Hole 504B, Costa Rica Rift) and a sheeted dike root zone (Oman ophiolite). Earth and Planetary Science Letters, 162(1–4): 27-43.

Veatch, S.L., Keller, S.L., 2003. Separation of Liquid Phases in Giant Vesicles of Ternary Mixtures of Phospholipids and Cholesterol. Biophysical Journal, 85(5): 3074-3083.

Vetere, F., Botcharnikov, R.E., Holtz, F., Behrens, H., De Rosa, R., 2011. Solubility of H2O and CO2 in shoshonitic melts at 1250 °C and pressures from 50 to 400 MPa: Implications for Campi Flegrei magmatic systems. Journal of Volcanology and Geothermal Research, 202(3–4): 251-261.

Wasserburg, G.J., 1957. The Effects of H2O in Silicate Systems. The Journal of Geology, 65(1): 15-23.

Watson, E.B., Wark, D.A., Thomas, J.B., 2006. Crystallization thermometers for zircon and rutile. Contributions to Mineralogy and Petrology, 151(4): 413-433.

Webster, J.D., 2004. The exsolution of magmatic hydrosaline chloride liquids. Chemical Geology, 210(1): 33-48.

Weill, D.F., Drake, M.J., 1973. Europium Anomaly in Plagioclase Feldspar: Experimental Results and Semiquantitative Model. Science, 180(4090): 1059-1060.

Weyer, S., Münker, C., Rehkämper, M., Mezger, K., 2002. Determination of ultra-low Nb, Ta, Zr and Hf concentrations and the chondritic Zr/Hf and Nb/Ta ratios by isotope dilution analyses with multiple collector ICP-MS. Chemical Geology, 187(3–4): 295-313.

Whitney, D.L., Evans, B.W., 2010. Abbreviations for names of rock-forming minerals. American mineralogist, 95(1): 185.

Williams-Jones, A.E., Migdisov, A.A., Samson, I.M., 2012. Hydrothermal Mobilisation of the Rare Earth Elements – a Tale of "Ceria" and "Yttria". Elements, 8(5): 355-360.

Witham, F. et al., 2012. SolEx: A model for mixed COHSCl-volatile solubilities and exsolved gas compositions in basalt. Computers & Geosciences, 45: 87-97.

Wood, B.J., 1976. Mixing properties of tschermakitic clinopyroxenes. Am Mineral, 61: 599-602.

Yegorov, D.G., Korobeinikov, A.N., Dubrovskii, M.I., 1998. chempet—Calculation for the chemical systematics of igneous rocks based on the CIPW norm. Computers & Geosciences, 24(1): 1-5.

Yoder, H.S., 1995. J. Frank Schairer, Biographical Memoirs pp. 288-320.

Yoder, H.S., Stewart, D.B., Smith, J.R., 1957. Ternary feldspars. Carnegie Institution of Washington Year Book, Washington.

Yoder, H.S., Tilley, C.E., 1962. Origin of Basalt Magmas: An Experimental Study of Natural and Synthetic Rock Systems. Journal of Petrology, 3(3): 342-532.

Ziewiec, K. et al., 2016. Microstructure and phase transformations in a liquid immiscible Fe60Cu20P10Si5B5 alloy. Intermetallics, 69: 47-53.

Zimmer, M.M. et al., 2010. The Role of Water in Generating the Calc-alkaline Trend: New Volatile Data for Aleutian Magmas and a New Tholeiitic Index. Journal of Petrology, 51(12): 2411-2444.

Zitter, T.A.C., Huguen, C., ten Veen, J., Woodside, J.M., 2006. Tectonic control on mud volcanoes and fluid seeps in the Anaximander Mountains, eastern Mediterranean Sea. Geological Society of America Special Papers, 409: 615-631.

Zotov, N., Keppler, H., 1998. The influence of water on the structure of hydrous sodium tetrasilicate glasses. American Mineralogist, 83(7): 823-834.

II. MINERAL -ABBREVIATIONS AND –FORMULAE

Mineral abbreviations according to Whitney and Evans (2010)

Ab	Albite	$NaAlSi_3O_8$
Acm	Acmite	$NaFe^{(III)}Si_2O_6$
An	Anorthite	$CaAl_2Si_2O_8$
Ap	Apatite (hydroxyl-)	$Ca_5(PO_4)_3(OH)$
Brc	Brucite	$Mg(OH)_2$
Cal	Calcite	$CaCO_3$
Chl	Chlorite group	
	Clinochlore	$Mg_5Al(AlSi_3O_{10})(OH)_8$
	Chamosite	$(Fe^{(II)},Mg,Al,Fe^{(III)})_6(Si,Al)_4O_{10}(OH,O)_8$
Chr	Chromite	$FeCr_2O_4$
Crn	Corundum	Al_2O_3
Czo	Clinozoisite	$\{Ca_2\}\{Al_3\}(Si_2O_7)(SiO_4)O(OH)$
Di	Diopside	$CaMgSi_2O_6$
Ep	Epidote	$A_2M_3(Si_2O_7)(SiO_4)O(OH)$
Fs	Ferrosilite	$Fe^{II}{}_2Si_2O_6$
Gth	Goethite	$FeO(OH)$
Hbl	Hornblende	$Ca_2[Mg_4(Al,Fe^{III})]Si_7AlO_{22}(OH)_2$
Hem	Hematite	Fe_2O_3
Hyp	Hypersthene	$(Mg, Fe)_2Si_2O_6$
Ilm	Ilmenite	$FeTiO_3$
K sil.	Potassium silicate	K_2SiO_3
Lrn	Larnite	Ca_2SiO_4
Mag	Magnetite	$Fe^{II}Fe^{III}{}_2O_4$
Mc	Microcline	$KAlSi_3O_8$
Mnt	Montmorillonite	$(Na,Ca)_{0.3}(Al,Mg)_2Si_4O_{10}(OH)_2 \cdot$
Mrbk	Magnesioriebeckite	$Na_2(Mg_3Fe^{III}{}_2)Si_8O_{22}(OH)_2$
Na sil.	Sodium silicate	$NaSiO_3$
Nph	Nepheline	$NaAlSiO_4$
Ol	Olivine (Foersterite-Fayalite)	Mg_2SiO_4 - $Fe^{II}{}_2SiO_4$
Or	Orthoclase	$KAlSi_3O_8$
Phl	Phlogopite	$KMg_3(Si_3Al)O_{10}(OH)_2$
Pl	Plagioclase (Albite-Anorthite)	$NaAlSi_3O_8$ - $CaAl_2Si_2O_8$
Prh	Prehnite	$Ca_2Al(Si_3Al)O_{10}(OH)_2$
Prv	Perovskite	$CaTiO_3$
Pyx	Pyroxene comprising clinopyroxene and orthopyroxene	
Qz	Quartz	SiO_2
Rt	Rutile	TiO_2
Thm	Thomsonite	$NaCa_2[Al_5Si_5O_{20}] \cdot 6H_2O$
Ttn	Titanite (Sphene)	$CaTiSiO_5$
Usp	Ulvöspinel	Fe_2TiO_4
Vrm	Vermiculite	$Mg_{0.7}(Mg,Fe^{III},Al)_6(Si,Al)_8O_{20}(OH)_4 \cdot$
Wo	Wollastonite	$CaSiO_3$
Zeo	Zeolite	e.g. $Na_2Al_2Si_3O_{10} \cdot 2H_2O$
Zrn	Zircon	$ZrSiO_4$

III. ABBREVIATIONS

AM	Amorphous Material
amu	Atomic mass unit
BSE	Bulk silicate Earth
BSE	Back Scattered Electron
ca.	approximately (Latin = circa)
CaTs	Calcium tschermaks molecule $CaAl_2SiO_6$
CIPW	Cross', Iddings', Pirsson's and Washington's way of calculating the normative mineralogical composition of a melt/glass.
cf.	compare with (Latin = confer)
CLS	Classical Least Squares
cm	Centimeter is a SI derived unit for length. SI base unit corresponding to 1 cm= 10^{-2} m
Cpx	Clinopyroxene
CryM	Crystallized Material
EDS	Energy Dispersive Spectroscopy
EPMA	Electron Probe Micro Analyser
e.g.	for example (Latin = exempli gratia)
EMCCD	Electron Multiplying Charge-Coupled Device
EPMA	Electron Probe Micro Analyser
et al.	and co-workers (Latin = et alii)
FTIR	Fourier Transform Infrared
g	gram is a derived unit for mass. Si base unit corresponding to 1 g = 10^{-3} kg
h	hour a SI derived unit of time. 1 h = 3600 s
HFSE	High Field Strength Elements in the proper meaning of the word include Nb, Ta, Ti, Zr and Hf. HFSE are usually extended to W and Mo and sometimes include Th and U
HREY	Heavy Rare Earth Elements and Yttrium (Y, Tb, Dy, Ho, Er, Tm, Yb and Lu)
Hz	hertz, a SI derived unit of frequency, defined as one cycle per second and named after Heinrich Rudolf Hertz. (In SI base units Hz = s^{-1})

i.a.	among other things (Latin = inter alia)
i.e.	more precisely (Latin = id est)
J	Joule is a SI derived unit of energy, it is equal to the energy transferred to an object when a force of 1 N acts on that object in the direction of its motion through a distance of 1 m. (In SI base units 1 J = kg x m^2 x s^{-2}) It is named after the English physicist James Prescott Joule
IC	Ion Chromatography
ID	Isotope Dilution
IHPV	Internally Heated Pressure Vessel
IUGS	International Union of Geological Sciences
K	SI unit for temperature based upon an absolute scale. It is defined such that the triple point of H_2O is exactly at 273.16 K. Absolute zero corresponds to the temperature at which all thermal motion ceases in the classical description of thermodynamics. The Kelvin scale is named after the engineer and physicist William Lord Kelvin. 1 K = + 273.15 °C
kV	kilovolt 1 kV = 1000 V with V being the derived unit for electric potential, electric potential difference (voltage), and electromotive force in the text used for voltage. In Si base notion V = kg x m^2 x s^{-3} x A^{-1}. Named after the Italian physicist Alessandro Volta
kW	kilowatt 1 kW = 1000 W with W being the derived unit of power. In SI base notion W = kg x m^2 x s^{-3}. Named after the Scottish engineer James Watt.
LFC	Limassol Forest Complex (Sr, Ba, K, Rb and Cs)
LILE	Large Ion Lithophile Elements
L.O.I.	Loss on Ignition
LPL	Lower Pillow Lava
LREE	Light Rare Earth Elements (La, Ce, Pr, Nd, Sm, Eu and Gd)
M	Molarity giving the concentration of a solution calculated by taking the moles of solute and dividing by the liters of solution
Ma	Megaannus is a unit of time equal to one million (1000000) years. In the text it is used as million years ago. In SI base units 1 Ma = 3.1536 x 10^{13} s
ml	Milliliter SI derived unit for Volume. The Si base unit l is equal to 1 cubic decimeter dm^3. 1 ml = 10^{-3} l

Moho	Mohorovičić discontinuity synonymously used in the text as crust-mantle boundary. The Mohorovičić discontinuity is 5 to 10 km below the ocean floor and 20 to 90 km, with an average of 35 km, beneath typical continental crusts.
mole	Mole, SI unit for amount of substance
N	normality or equivalent concentration is a unit for the concentration of a solution and is defined as the molar concentration divided by an equivalence factor
NBO/T	Ratio of non-bridging oxygens per tetrahedral network-forming cation
Nd:YAG	Neodymium-doped yttrium aluminium garnet ($Nd:Y_3Al_5O_{12}$)
N	Newton, the SI unit of force named after Isaac Newton (In SI base units: $N = kg \times m/s^2$)
nA	Nanoampere 1 nA = 10^{-9} A with A being the SI unit of electric current. Named after the French mathematician and physicist André-Marie Ampère.
mA	Milliampere 1 Ma = 10^{-3} A
mm	millimeter is a unit of length. (in SI base units 1 mm = 10^{-3} m)
µm	micrometer is a unit of length. (in SI base units 1 µm = 10^{-6} m)
OIB	Ocean Island Basalt
P	Acronym for pressure, SI unit = Pa
Pa	SI derived unit of pressure named after the French polymath Blaise Pascal. In SI base units 1 Pa = $kg \times m^{-1} \times s^{-2}$
PCA	Piston Cylinder Apparatus
ppm	parts-per-million, 10^{-6}
psi	pound per square inch, i.e. pound-force per square inch. The pressure resulting from a force of one pound-force applied to an area of one square inch. (1 psi = 6894.757 $N \times m^{-2}$)
PVC	Polyvinyl Chloride
QAPF	Quartz, Alkali feldspar, Plagioclase, Feldspathoid classification diagram of igneous rocks also called Streckeisen-diagram
REY	Rare Earth Elements of the lanthanides and Yttrium, a transition metal.
s	Second SI unit for time
SI	The International System of Units

Spl	Sample
SSZ	Supra Subduction Zone
T	Acronym for temperature, SI unit T K note 0 K = -273.15 °C
T_g	Glass transition temperature
T_l	Liquidus temperature
T_m	Temperature of melting
TOC	Troodos Ophiolite Complex
UPL	Upper Pillow Lava
vs.	against (Latin = versus)
WDS	Wavelength Dispersive Spectroscopy
WD-XRF	Wavelength Dispersive X-ray Fluorescence
WR	Whole Rock
wt.	weight
wt.%	Abbreviation for weight percent, a unit indicating the mass fraction, i.e. the ratio of one substance relative to the mass of the total mixture. Multiplying the mass fraction by 100 gives the mass percentage wt.%
XRD	X-ray Diffraction (spectroscopy)
XRF	X-ray Fluorescence (spectroscopy) the prefix WD-XRF refers to a wavelength dispersive detector
yrs	years
ρ	Greek symbol Rho as acronym for density (SI unit ρ = kg x m^{-3})
λ	Greek symbol Lambda as acronym for the decay constant
°C	SI derived unit for temperature. Celsius, also known as centigrade is based on 0 °C for the freezing point of water and 100 °C for the boiling point of water. It is named after the Swedish astronomer Anders Celsius. 1 °C = − 273.15 K
Ø	Symbol for diameter

IV. DATA

Table I: Bulk chemistry of anorthosites measured in glasses fused from rock powder

EPMA	Group I	Group I	Group I	Group I	Group I	Group I	Group I	Group I
Sample	ZY80A(1)	ZY80A(1)	ZY80A(2)	ZY80A(2)	ZY82A	ZY82A	ZY82B	ZY82B
#	13	13	10	10	5	5	5	5
	Ø	S.D.	Ø	S.D.	Ø	S.D.	Ø	S.D.
EPMA [wt.%]								
SiO_2	52.9	0.30	60.0	0.44	51.5	0.24	51.4	0.16
TiO_2	0.29	0.07	0.23	0.06	0.38	0.05	0.32	0.02
Al_2O_3	28.2	0.18	23.9	0.17	24.6	0.12	27.2	0.23
FeO	0.77	0.05	0.73	0.08	1.10	0.06	0.86	0.07
MgO	0.67	0.02	0.66	0.03	3.18	0.04	2.00	0.02
MnO	0.02	0.02	0.02	0.02	0.06	0.05	0.03	0.03
CaO	13.7	0.13	11.7	0.12	17.3	0.15	15.8	0.03
Na_2O	4.00	0.08	3.49	0.09	2.71	0.07	3.15	0.05
K_2O	0.05	0.01	0.04	0.01	0.08	0.01	0.05	0.01
Total	100.7	0.31	100.9	0.39	101.0	0.3	100.9	0.4
CIPW [wt.%]								
Qz	0.7		14.9		-		-	
An	58.7		49.5		54.8		60.0	
Ab	33.8		29.5		22.2		25.6	
Or	0.3		0.2		0.5		0.3	
ne	-		-		0.4		0.6	
Di	5.4		5.4		19.9		12.8	
Hyp	-		-		-		-	
Wo	1.1		0.8		2.4		0.9	
Ol	-		-		-		-	
Ilm	0.6		0.4		0.7		0.6	
Ttn	-		-		-		-	
∑	100.6		100.8		100.9		100.9	
XRD	Group I		Group I		Group I		Group I	
Sample	ZY80A(1)		ZY80A(2)		ZY82A		ZY82B	
#	1		1		1		1	
XRD [%]								
Qz	2.43		20.2		-		-	
An	34.2		27.4		30.6		49.5	
Ab	39.6		33.3		24.3		25.5	
Di	7.28		8.43		11.1		10.0	
Thm	16.5		10.7		12.7		15.0	
Mrbk	-		-		7.08		-	
Prh	-		-		14.3		-	
Crystallized	94.4		82.7		100.0		97.6	
Amorphous	5.62		17.3		-		2.37	
∑	100.0		100.0		100.0		100.0	

Table I (continued): Bulk chemistry of anorthosites measured in glasses fused from rock powder

EPMA	Group II	Group II	Group II	Group II	Group II	Group II	Group II	Group II
Sample	ZY80E(2)	ZY80E(2)	ZY80L	ZY80L	ZY80M(1)	ZY80M(1)	ZY80M(2)	ZY80M(2)
#	5	5	5	5	5	5	5	5
	Ø	S.D.	Ø	S.D.	Ø	S.D.	Ø	S.D.
EPMA [wt.%]								
SiO_2	53.8	0.17	50.9	0.21	53.3	0.34	50.9	0.25
TiO_2	0.28	0.04	0.30	0.04	0.27	0.05	0.23	0.02
Al_2O_3	15.0	0.10	31.2	0.09	28.9	0.14	28.5	0.07
FeO	1.92	0.09	0.08	0.02	0.48	0.05	0.55	0.05
MgO	8.66	0.08	0.10	0.02	0.38	0.03	1.69	0.05
MnO	0.02	0.02	0.01	0.03	0.01	0.02	0.03	0.02
CaO	17.9	0.13	14.6	0.09	13.0	0.09	15.9	0.07
Na_2O	2.95	0.08	3.30	0.08	4.42	0.07	3.01	0.08
K_2O	0.02	0.01	0.04	0.02	0.05	0.02	0.02	0.01
Total	100.6	0.41	100.6	0.28	100.9	0.52	100.9	0.22
CIPW [wt.%]								
Qz	-		0.6		-		-	
An	27.7		70.3		58.9		64.2	
Ab	19.6		27.9		37.3		24.6	
Or	0.1		0.2		0.3		0.1	
ne	2.9		-		0.1		0.5	
Di	48.4		0.5		2.9		10.4	
Hyp	-		-		-		-	
Wo	-		0.3		0.9		0.7	
Ol	1.3		-		-		-	
Ilm	0.5		0.2		0.5		0.4	
Ttn	-		0.5		-		-	
∑	100.6		100.6		100.9		100.9	

XRD		Group II			Group II	
Sample		ZY80L			ZY80M(2)	
#		1			1	
XRD [%]						
Qz		-			-	
An		48.8			45.2	
Ab		32.2			26.6	
Di		2.58			9.54	
Thm		16.4			18.7	
Mrbk		-			-	
Prh		-			-	
Crystallized		94.6			100.0	
Amorphous		5.40			0.01	
∑		100.0			100.0	

Table I (continued): Bulk chemistry of anorthosites measured in glasses fused from rock powder

EPMA	Group II	Group II	Group II	Group II	Group III	Group III	Group III	Group III
Sample	ZY80O(1)	ZY80O(1)	ZY80O(2)	ZY80O(2)	ZY80B(1)	ZY80B(1)	ZY80B(2)	ZY80B(2)
#	5	5	5	5	15	15	10	10
	Ø	S.D.	Ø	S.D.	Ø	S.D.	Ø	S.D.
EPMA [wt.%]								
SiO_2	51.3	0.11	51.1	0.15	52.8	0.24	53.7	0.20
TiO_2	0.33	0.03	0.29	0.05	0.44	0.04	0.45	0.04
Al_2O_3	30.9	0.09	30.6	0.18	27.3	0.17	26.2	0.20
FeO	0.09	0.04	0.16	0.07	0.48	0.08	0.55	0.05
MgO	0.22	0.01	0.39	0.02	1.52	0.03	1.89	0.05
MnO	0.02	0.02	0.03	0.02	0.02	0.03	0.01	0.02
CaO	14.2	0.08	14.5	0.13	14.4	0.08	14.4	0.09
Na_2O	3.60	0.11	3.53	0.07	3.60	0.07	3.57	0.12
K_2O	0.03	0.01	0.03	0.01	0.03	0.01	0.02	0.01
Total	100.8	0.30	100.7	0.48	100.7	0.28	100.8	0.27
CIPW [wt.%]								
Qz	0.0		-		1.4		2.5	
An	68.1		67.6		58.3		55.3	
Ab	30.5		29.5		30.5		30.2	
Or	0.2		0.2		0.2		0.1	
ne	-		0.2		-		-	
Di	1.2		2.1		8.5		10.7	
Hyp	-		-		-		-	
Wo	0.1		0.6		0.9		1.1	
Ol	-		-		-		-	
Ilm	0.2		0.4		0.8		0.9	
Ttn	0.5		-		-		-	
∑	100.7		100.6		100.6		100.7	

XRD	Group II	Group II	Group III	Group III
Sample	ZY80O(1)	ZY80O(2)	ZY80B(1)	ZY80B(2)
#	1	1	1	1
XRD [%]				
Qz	-	-	4.22	4.13
An	48.7	46.1	39.2	36.0
Ab	30.1	30.0	28.8	32.7
Di	3.13	3.97	12.4	14.2
Thm	18.0	19.9	15.3	13.1
Mrbk	-	-	-	-
Prh	-	-	-	-
Crystallized	100.0	100.0	90.5	92.6
Amorphous	-	-	9.50	7.43
∑	100.0	100.0	100.0	100.0

Table I (continued): Bulk chemistry of anorthosites measured in glasses fused from rock powder

EPMA	Group III	Group III	Group III	Group III	Group III	Group III
Sample	ZY80F	ZY80F	ZY80G	ZY80G	ZY80J(1)	ZY80J(1)
#	5	5	5	5	10	10
	Ø	S.D.	Ø	S.D.	Ø	S.D.
EPMA [wt.%]						
SiO_2	54.2	0.22	54.2	0.20	53.3	0.31
TiO_2	0.43	0.06	0.45	0.05	0.44	0.03
Al_2O_3	26.7	0.15	28.5	0.21	29.1	0.31
FeO	0.43	0.05	0.21	0.06	0.24	0.04
MgO	1.52	0.02	0.66	0.03	0.70	0.12
MnO	0.04	0.01	0.01	0.02	0.02	0.03
CaO	13.0	0.10	12.5	0.10	13.2	0.12
Na_2O	4.54	0.19	4.63	0.07	4.33	0.08
K_2O	0.04	0.01	0.04	0.01	0.04	0.01
Total	101.0	0.32	101.3	0.42	101.4	0.52
CIPW [wt.%]						
Qz	0.1		0.4		-	
An	52.4		56.9		59.7	
Ab	38.4		39.2		36.6	
Or	0.2		0.2		0.2	
ne	-		-		-	
Di	8.5		3.5		3.8	
Hyp	-		0.1		-	
Wo	0.5		-		0.1	
Ol	-		-		-	
Ilm	0.8		0.5		0.6	
Ttn	-		0.5		0.1	
∑	100.9		101.2		101.3	
XRD	Group III		Group III		Group III	
Sample	ZY80F		ZY80G		ZY80J(1)	
#	1		1		1	
XRD [%]						
Qz	-		-		-	
An	35.1		41.5		41.7	
Ab	37.4		38.9		37.8	
Di	7.91		3.27		4.70	
Thm	19.5		16.3		15.8	
Mrbk	-		-		-	
Prh	-		-		-	
Crystallized	100.0		100.0		100.0	
Amorphous	-		-		-	
∑	100.0		100.0		100.0	

Table I (continued): Bulk chemistry of anorthosites measured in glasses fused from rock powder

EPMA	Group III	Group III	Group III	Group III	**XRF**	Group I	Group III
Sample	ZY80J(2)	ZY80J(2)	ZY80K	ZY80K	Sample	ZY80A(1)	ZY80B(1)
#	5	5	5	5	#	1	1
	Ø	S.D.	Ø	S.D.			
EPMA [wt.%]					XRF [wt.%]		
SiO_2	54.0	0.28	53.4	0.24	SiO_2	51.7	53.6
TiO_2	0.40	0.02	0.20	0.04	TiO_2	0.30	0.45
Al_2O_3	26.3	0.12	29.0	0.24	Al_2O_3	25.9	23.5
FeO	1.04	0.07	0.22	0.03	Fe_2O_3	1.02	0.71
MgO	2.67	0.01	0.66	0.03	MgO	0.87	2.30
MnO	0.03	0.02	0.00	0.00	MnO	0.02	0.01
CaO	12.4	0.08	13.0	0.08	CaO	12.2	13.2
Na_2O	4.16	0.16	4.40	0.07	Na_2O	4.02	3.16
K_2O	0.03	0.00	0.03	0.01	K_2O	0.04	0.03
Total	101.0	0.56	100.9	0.37	L.O.I.	2.85	2.25
					Total	99.2	99.5
CIPW [wt.%]					CIPW [wt.%]		
Qz	0.4		-		Qz	2.5	6.8
An	52.9		59.3		An	52.5	49.9
Ab	35.2		37.2		Ab	34.0	26.7
Or	0.2		0.2		Or	0.2	0.2
ne	-		0.0		Di	4.7	11.0
Di	6.9		3.7		Hyp	-	0.7
Hyp	4.7		-		Wo	0.5	-
Wo	-		0.2		Ilm	0.0	0.0
Ol	-		-		Hem	1.0	0.7
Ilm	0.8		0.4		Ttn	0.7	1.1
Ttn	-		-		∑	96.1	97.0
∑	101.0		100.9				

XRD	Group III	Group III
Sample	ZY80J(2)	ZY80K
#	1	1
XRD [%]		
Qz	0.00	0.00
An	39.3	37.6
Ab	32.4	36.7
Di	0.00	3.95
Thm	16.4	21.8
Mrbk	11.9	0.00
Prh	0.00	0.00
Crystallized	100.0	100.0
Amorphous	0.00	0.00
∑	100.0	100.0

Table I (continued): Bulk chemistry of anorthosites measured in glasses fused from rock powder

ICP-MS	Group I	Group I	Group I	Group I	Group I	Group I	Group I	Group I
Sample	ZY80A(1)	ZY80A(1)	ZY80A(2)	ZY80A(2)	ZY82A	ZY82A	ZY82B	ZY82B
#	15	15	15	15	10	10	10	10
	Ø	S.D.	Ø	S.D.	Ø	S.D.	Ø	S.D.
Sc	26.2	0.3	34.8	0.4	20.0	0.3	35.0	0.6
Ti	1173.9	16.5	1189.3	30.7	1525.9	21.4	2403.0	68.7
V	28.8	0.8	30.9	0.7	50.7	1.5	41.9	0.8
Cr	10.0	1.1	8.3	0.8	73.5	5.1	22.2	1.4
No	17.0	0.5	21.8	0.7	60.6	2.0	45.3	3.1
Cu	5.6	0.5	12.0	0.7	4.6	0.3	6.0	0.5
Zn	4.6	0.3	10.6	0.3	2.7	0.2	1.6	0.2
Rb	n.a.	-	n.a.	-	0.2	0.0	0.2	0.0
Sr	n.a.	-	n.a.	-	197.2	3.7	292.4	9.6
Y	95.7	1.2	102.1	1.4	49.1	0.5	70.6	1.1
Zr	164.5	4.5	163.8	3.3	101.6	2.2	153.5	2.8
Nb	62.0	0.6	59.9	0.7	44.3	0.6	65.4	1.2
Mo	6.0	3.4	3.4	4.3	0.6	0.1	0.6	0.1
Cs	n.a.	-	n.a.	-	0.1	0.0	0.1	0.0
Ba	4.1	0.1	4.2	0.1	6.8	0.1	6.5	0.1
La	36.4	0.3	36.5	0.4	29.4	0.2	32.8	0.5
Ce	56.7	1.0	55.0	0.9	49.0	0.8	63.1	1.4
Pr	5.0	0.1	5.1	0.1	4.3	0.1	5.5	0.1
Nd	17.5	0.2	18.4	0.3	15.2	0.2	19.1	0.4
Eu	1.0	0.0	1.0	0.0	0.9	0.0	0.7	0.0
Gd	9.2	0.2	9.7	0.2	6.1	0.1	8.0	0.2
Tb	1.8	0.0	1.9	0.0	1.0	0.0	1.4	0.0
Dy	14.3	0.2	15.1	0.2	7.6	0.1	11.3	0.2
Ho	3.5	0.1	3.7	0.1	1.7	0.0	2.6	0.0
Er	11.3	0.2	11.9	0.2	5.6	0.1	8.4	0.2
Tm	1.8	0.0	1.8	0.0	0.9	0.0	1.4	0.0
Yb	13.1	0.1	13.8	0.2	7.4	0.2	10.8	0.3
Sm	5.2	0.1	5.5	0.2	3.8	0.1	5.1	0.2
Lu	2.0	0.0	2.1	0.0	1.2	0.0	1.6	0.0
Hf	5.5	0.2	5.7	0.2	3.0	0.1	4.5	0.2
Ta	4.1	0.1	4.3	0.1	3.0	0.0	4.6	0.1
W	14.4	3.3	0.6	0.0	0.4	0.0	2.0	0.1
Pb	0.3	0.1	0.8	0.1	0.5	0.1	0.3	0.0
Th	7.7	0.2	7.9	0.2	6.6	0.1	8.5	0.2
U	2.1	0.1	2.1	0.1	0.9	0.0	1.3	0.0
Eu*	13.6		14.5		9.6		12.6	

Table I (continued): Bulk chemistry of anorthosites measured in glasses fused from rock powder

ICP-MS	Group II	Group II	Group II	Group II	Group II	Group II	Group II	Group II
Sample	ZY80E(2)	ZY80E(2)	ZY80L	ZY80L	ZY80M(1)	ZY80M(1)	ZY80M(2)	ZY80M(2)
#	10	10	10	10	10	10	10	10
	Ø	S.D.	Ø	S.D.	Ø	S.D.	Ø	S.D.
Sc	73.7	0.8	7.24	0.433	16.19	0.346	47.55	1.17
Ti	1621.9	217.7	2151	19.0	2068	52.8	1659	19.2
V	141.2	1.7	8.88	0.456	23.01	0.751	37.83	1.80
Cr	434.0	14.9	7.54	1.89	27.5	1.91	16.4	1.79
No	171.8	4.6	3.79	0.410	17.9	0.874	33.4	1.13
Cu	5.0	0.4	5.41	0.515	6.07	0.334	4.56	0.39
Zn	2.9	0.2	1.03	0.201	1.11	0.212	0.890	0.140
Rb	0.1	0.0	0.154	0.037	0.197	0.033	0.108	0.021
Sr	246.8	4.8	243	3.01	267	2.40	226	6.59
Y	86.0	1.5	66.4	1.99	62.2	0.65	55.0	1.58
Zr	15.7	0.7	140	4.38	140	4.50	134	4.47
Nb	16.0	0.3	67.1	2.25	64.2	0.675	48.1	0.619
Mo	2.0	0.3	0.56	0.10	0.69	0.095	2.62	0.198
Cs	0.0	0.0	0.033	0.013	0.020	0.006	0.076	0.013
Ba	1.3	0.0	3.84	0.062	3.58	0.068	3.13	0.050
La	4.9	0.1	2.71	0.080	3.68	0.038	2.21	0.055
Ce	9.8	0.2	10.3	0.200	11.1	0.111	8.59	0.096
Pr	1.1	0.0	1.50	0.024	1.46	0.019	1.26	0.028
Nd	4.7	0.1	7.13	0.080	6.81	0.104	5.99	0.1462
Eu	0.1	0.0	0.253	0.017	0.375	0.021	0.174	0.040
Gd	5.7	0.1	5.48	0.220	5.12	0.094	4.51	0.184
Tb	1.4	0.0	1.20	0.045	1.09	0.018	0.984	0.031
Dy	12.2	0.3	10.0	0.400	9.42	0.210	8.37	0.334
Ho	3.0	0.1	2.39	0.065	2.21	0.048	1.96	0.085
Er	9.8	0.3	7.59	0.306	7.24	0.138	6.29	0.247
Tm	1.6	0.0	1.21	0.032	1.16	0.023	1.02	0.035
Yb	13.0	0.5	9.12	0.278	8.95	0.262	7.77	0.297
Sm	2.3	0.1	2.96	0.088	2.81	0.154	2.57	0.170
Lu	2.0	0.0	1.22	0.029	1.22	0.025	1.11	0.052
Hf	0.6	0.0	4.68	0.143	4.52	0.087	4.73	0.127
Ta	1.0	0.0	4.69	0.105	4.52	0.060	3.59	0.106
W	1.3	0.2	1.16	0.427	1.22	0.041	91.6	3.96
Pb	0.2	0.0	0.271	0.062	0.334	0.032	0.276	0.036
Th	0.8	0.0	7.35	0.132	8.28	0.181	8.42	0.217
U	0.1	0.0	0.978	0.059	1.06	0.031	0.827	0.055
Eu*	7.2		8.0		7.5		6.8	

Table I (continued): Bulk chemistry of anorthosites measured in glasses fused from rock powder

ICP-MS	Group II	Group II	Group II	Group II	Group III	Group III	Group III	Group III
Sample	ZY80O(1)	ZY80O(1)	ZY80O(2)	ZY80O(2)	ZY80B(1)	ZY80B(1)	ZY80B(2)	ZY80B(2)
#	10	10	10	10	15	15	15	15
	Ø	S.D.	Ø	S.D.	Ø	S.D.	Ø	S.D.
Sc	18.82	0.841	17.28	0.338	22.59	0.393	21.37	1.31
Ti	2277	79.5	2470	197	1761	26.9	2012	1.2
V	11.96	0.577	15.23	0.542	24.60	0.851	28.04	2.41
Cr	12.2	0.94	19.4	2.07	17.4	2.95	20.3	9.41
No	6.47	1.15	17.0	2.03	34.8	2.09	42.9	3.65
Cu	4.72	0.50	4.71	0.30	12.6	1.03	3.59	7.70
Zn	0.669	0.136	0.721	0.167	8.96	0.432	1.83	14.7
Rb	0.292	0.059	0.141	0.025	n.a.	-	n.a.	-
Sr	244	2.06	250	3.45	n.a.	-	n.a.	-
Y	71.0	1.05	76.1	7.49	26.6	0.43	34.2	1.62
Zr	138	4.18	144	3.53	142	5.61	125	2.23
Nb	71.6	0.745	72.2	1.83	43.0	0.435	44.0	1.23
Mo	0.751	0.382	1.24	0.755	3.10	2.41	4.62	63.0
Cs	0.088	0.010	0.033	0.006	n.a.	-	n.a.	-
Ba	4.43	0.122	3.62	0.203	3.49	0.138	2.95	4.65
La	2.85	0.061	3.53	0.123	1.24	0.038	1.10	2.75
Ce	11.6	0.225	13.5	0.992	2.80	0.066	2.60	1.63
Pr	1.67	0.042	1.93	0.083	0.353	0.010	0.359	2.29
Nd	7.84	0.182	9.07	0.300	1.53	0.060	1.72	3.32
Eu	0.291	0.017	0.272	0.011	0.079	0.006	0.085	7.50
Gd	6.01	0.185	6.62	0.396	1.65	0.065	2.16	4.01
Tb	1.30	0.041	1.38	0.072	0.412	0.011	0.549	3.42
Dy	11.0	0.345	11.8	0.891	3.52	0.080	4.61	1.65
Ho	2.59	0.066	2.75	0.240	0.884	0.020	1.14	3.05
Er	8.35	0.243	8.90	0.803	2.97	0.071	3.74	2.33
Tm	1.32	0.040	1.41	0.122	0.465	0.015	0.575	2.86
Yb	9.97	0.414	10.9	0.677	3.50	0.092	4.07	2.00
Sm	3.34	0.094	3.68	0.209	0.725	0.042	0.927	4.79
Lu	1.33	0.040	1.50	0.112	0.551	0.014	0.611	2.92
Hf	4.41	0.110	4.55	0.136	4.37	0.210	3.89	3.38
Ta	4.60	0.081	4.34	0.116	3.33	0.097	3.34	1.72
W	9.66	0.976	1.32	0.288	0.703	0.030	0.952	38.3
Pb	0.275	0.049	0.182	0.035	0.716	0.160	0.147	23.1
Th	9.88	0.223	9.47	0.375	7.75	0.245	7.22	1.82
U	1.12	0.050	1.13	0.045	0.72	0.033	0.731	5.16
Eu*	8.9		9.8		2.2		2.8	

Table I (continued): Bulk chemistry of anorthosites measured in glasses fused from rock powder

ICP-MS	Group III	Group III	Group III	Group III	Group III	Group III	Group III	Group III
Sample	ZY80F	ZY80F	ZY80G	ZY80G	ZY80J(1)-A	ZY80J(1)-A	ZY80J(1)-B	ZY80J(1)-B
#	10	10	10	10	10	10	10	10
	Ø	S.D.	Ø	S.D.	Ø	S.D.	Ø	S.D.
Sc	43.95	0.435	18.14	0.324	33.60	0.298	29.61	0.469
Ti	2590	227	2788	36.9	3074	49.5	2999	35.9
V	23.62	0.760	14.38	0.523	18.33	0.765	16.72	0.420
Cr	61.2	3.84	17.8	2.33	34.8	2.11	34.0	2.15
No	26.0	1.75	14.2	0.920	19.9	1.11	34.0	2.26
Cu	5.68	0.408	7.48	0.687	5.92	0.248	6.49	0.550
Zn	1.56	0.211	1.12	0.219	0.686	0.152	3.53	0.250
Rb	0.236	0.034	0.199	0.050	0.169	0.042	0.284	0.045
Sr	257	4.87	255	3.07	252	4.00	264	7.84
Y	34.1	0.709	18.4	0.350	27.2	0.739	20.5	0.357
Zr	193	3.10	177	3.48	171	3.51	174	5.09
Nb	50.5	0.508	64.22	0.98	60.44	1.12	67.68	0.93
Mo	0.495	0.035	2.49	0.657	0.488	0.096	0.510	0.097
Cs	0.088	0.007	0.023	0.016	0.010	0.005	0.025	0.004
Ba	3.65	0.098	3.23	0.049	3.37	0.115	56.1	1.06
La	1.18	0.035	0.800	0.036	0.809	0.050	0.917	0.026
Ce	3.43	0.115	1.87	0.051	1.80	0.064	3.84	0.100
Pr	0.411	0.018	0.177	0.010	0.228	0.012	0.244	0.013
Nd	1.81	0.070	0.842	0.055	1.18	0.085	1.04	0.050
Eu	0.083	0.007	0.050	0.008	0.060	0.008	0.058	0.008
Gd	1.99	0.065	0.983	0.088	1.49	0.068	1.13	0.062
Tb	0.492	0.020	0.250	0.011	0.389	0.017	0.285	0.017
Dy	4.56	0.141	2.34	0.073	3.55	0.103	2.57	0.07
Ho	1.14	0.036	0.596	0.013	0.891	0.022	0.641	0.011
Er	3.88	0.143	1.99	0.059	2.95	0.100	2.18	0.071
Tm	0.651	0.029	0.341	0.016	0.483	0.018	0.365	0.013
Yb	5.08	0.184	2.68	0.104	3.58	0.136	2.76	0.119
Sm	0.894	0.082	0.439	0.111	0.622	0.123	0.495	0.066
Lu	0.753	0.021	0.411	0.019	0.511	0.019	0.397	0.016
Hf	5.78	0.153	4.85	0.107	4.70	0.105	4.74	0.115
Ta	5.02	0.076	4.86	0.058	4.38	0.090	4.77	0.112
W	1.74	0.099	2.39	0.245	0.951	0.742	1.74	0.911
Pb	29.6	1.29	0.224	0.034	0.253	0.028	2.97	0.093
Th	9.97	0.169	8.77	0.140	5.02	0.185	6.28	0.155
U	1.15	0.044	0.686	0.039	0.554	0.019	0.825	0.030
Eu*	2.6		1.3		1.9		1.5	

Table I (continued): Bulk chemistry of anorthosites measured in glasses fused from rock powder

ICP-MS	Group III	Group III	Group III	Group III
Sample	ZY80J(2)	ZY80J(2)	ZY80K	ZY80K
#	10	10	10	10
	Ø	S.D.	Ø	S.D.
Sc	38.49	0.774	10.97	0.509
Ti	2702	76.6	1487	20.2
V	42.40	1.78	11.08	0.592
Cr	24.6	3.96	26.3	1.60
No	84.2	2.43	17.0	0.434
Cu	4.18	0.433	7.96	0.616
Zn	2.33	0.222	1.40	0.137
Rb	0.121	0.022	0.131	0.030
Sr	249	2.32	287	2.99
Y	34.5	0.419	11.3	0.163
Zr	152	4.12	176	3.40
Nb	51.58	0.49	25.36	0.28
Mo	0.913	0.517	0.726	0.093
Cs	0.032	0.006	0.014	0.004
Ba	2.90	0.059	3.43	0.063
La	1.69	0.038	0.685	0.025
Ce	4.06	0.077	1.71	0.051
Pr	0.510	0.018	0.183	0.008
Nd	2.44	0.080	0.779	0.059
Eu	0.180	0.011	0.048	0.006
Gd	2.34	0.054	0.679	0.043
Tb	0.533	0.019	0.160	0.011
Dy	4.68	0.105	1.44	0.04
Ho	1.17	0.022	0.368	0.020
Er	3.97	0.082	1.26	0.064
Tm	0.661	0.017	0.218	0.007
Yb	5.42	0.151	1.69	0.052
Sm	1.14	0.054	0.3156	0.064
Lu	0.894	0.015	0.260	0.008
Hf	4.32	0.119	4.75	0.096
Ta	4.26	0.095	2.83	0.050
W	10.1	1.55	0.988	0.060
Pb	0.151	0.048	0.175	0.026
Th	5.81	0.143	1.63	0.022
U	0.443	0.037	0.364	0.017
Eu*	3.2		0.9	

Table II: Plagioclase composition of anorthosites

EPMA [wt. %]	Albite Group I Max Ab	Albite Group I Min Ab	Albite Group I Median Ab	Albite Group I Mean Ab	Albite Group I S.D. (n=17)
SiO_2	67.0	57.2	63.7	64.0	3.0
Al_2O_3	21.5	27.3	23.3	23.3	1.6
CaO	1.52	8.50	4.15	4.11	1.67
Na_2O	10.6	6.90	9.79	9.48	0.95
K_2O	0.04	0.02	0.05	0.05	0.02
∑	100.7	99.9	101.1	101.2	1.30
cations per 8 oxygens normalised to 5					
Si	2.9	2.6	2.8	2.8	0.1
Al	1.1	1.4	1.2	1.2	0.1
Ca	0.1	0.4	0.2	0.2	0.1
Na	0.9	0.6	0.8	0.8	0.1
K	0.0	0.0	0.0	0.0	0.0
∑	5.0	5.0	5.0	5.0	0.0
An	8.7	42.5	19.9	19.7	8.6
Ab	90.3	58.1	80.8	79.7	8.0
Or	0.2	0.1	0.3	0.3	0.1

EPMA [wt. %]	Anorthite Group I Max An	Anorthite Group I Min Am	Anorthite Group I Median An	Anorthite Group I Mean An	Anorthite Group I S.D. (n=37)
SiO_2	43.3	46.3	43.6	44.4	0.85
Al_2O_3	37.3	34.5	24.6	34.6	4.08
CaO	20.2	17.4	26.8	20.1	2.43
Na_2O	0.37	1.58	0.13	0.64	0.38
K_2O	0.01	0.01	0.01	0.01	0.01
∑	101.2	99.9	95.3	99.9	2.22
cations per 8 oxygens normalised to 5					
Si	2.0	2.1	2.1	2.1	0.1
Al	2.0	1.9	1.4	1.9	0.2
Ca	1.0	0.9	1.4	1.0	0.2
Na	0.0	0.1	0.0	0.1	0.0
K	0.0	0.0	0.0	0.0	0.0
∑	5.0	5.0	5.0	5.0	0.0
An	100.1	86.3	94.6	94.6	3.3
Ab	0.9	13.6	9.8	6.0	3.5
Or	0.1	0.0	0.1	0.1	0.1

Table II (continued): Plagioclase composition of anorthosites

EPMA [wt. %]	Albite Group II Max Ab	Albite Group II Min Ab	Albite Group II Median Ab	Albite Group II Mean Ab	Albite Group II S.D. (n=55)
SiO_2	66.1	60.6	65.0	65.1	1.7
Al_2O_3	21.5	25.1	22.4	22.5	0.8
CaO	0.64	6.27	2.85	2.68	1.17
Na_2O	12.0	8.31	10.1	10.1	0.70
K_2O	0.02	0.02	0.04	0.03	0.02
∑	100.4	100.4	100.5	100.5	1.15
cations per 8 oxygens normalised to 5					
Si	2.9	2.7	2.8	2.9	0.1
Al	1.1	1.3	1.2	1.2	0.0
Ca	0.0	0.3	0.1	0.1	0.1
Na	1.0	0.7	0.9	0.9	0.1
K	0.0	0.0	0.0	0.0	0.0
∑	5.0	5.0	5.0	5.0	0.0
An	7.0	30.6	14.6	14.3	4.9
Ab	95.7	70.0	85.3	85.3	4.8
Or	0.1	0.1	0.2	0.2	0.1

EPMA [wt. %]	Anorthite Group II Max An	Anorthite Group II Min An	Anorthite Group II Median An	Anorthite Group II Mean An	Anorthite Group II S.D. (n=83)
SiO_2	43.0	44.4	43.8	43.9	0.71
Al_2O_3	37.1	35.3	36.5	36.3	0.71
CaO	20.2	8.84	19.4	19.0	1.84
Na_2O	0.33	0.87	0.47	0.57	0.29
K_2O	0.01	0.00	0.00	0.01	0.01
∑	100.7	89.6	100.2	100.0	2.02
cations per 8 oxygens normalised to 5					
Si	2.0	2.3	2.0	2.0	0.1
Al	2.0	2.1	2.0	2.0	0.1
Ca	1.0	0.5	1.0	0.9	0.1
Na	0.0	0.1	0.0	0.1	0.0
K	0.0	0.0	0.0	0.0	0.0
∑	5.0	5.0	5.0	5.0	0.0
An	100.6	76.5	97.1	96.0	4.1
Ab	0.5	14.0	3.1	4.1	2.9
Or	0.0	0.0	0.0	0.0	0.1

Table II (continued): Plagioclase composition of anorthosites

EPMA [wt. %]	Albite Group III Max Ab	Albite Group III Min Ab	Albite Group III Median Ab	Albite Group III Mean Ab	Albite Group III S.D. (n=26)
SiO_2	67.5	63.4	66.1	65.2	1.5
Al_2O_3	21.3	24.2	22.2	22.4	0.7
CaO	1.49	5.21	2.57	2.78	0.80
Na_2O	11.2	9.17	10.4	10.2	0.55
K_2O	0.04	0.01	0.04	0.03	0.01
∑	101.4	102.0	101.4	100.6	1.39
cations per 8 oxygens normalised to 5					
Si	2.9	2.7	2.9	2.8	0.0
Al	1.1	1.2	1.1	1.2	0.0
Ca	0.1	0.2	0.1	0.1	0.0
Na	0.9	0.8	0.9	0.9	0.0
K	0.0	0.0	0.0	0.0	0.0
∑	5.0	5.0	5.0	5.0	0.0
An	7.7	24.2	12.8	14.4	3.8
Ab	92.5	76.3	87.2	85.5	3.8
Or	0.2	0.1	0.2	0.2	0.1

EPMA [wt. %]	Anorthite Group III Max An	Anorthite Group III Min An	Anorthite Group III Median An	Anorthite Group III Mean An	Anorthite Group III S.D. (n=62)
SiO_2	43.2	45.9	44.1	44.0	0.59
Al_2O_3	37.3	35.0	36.9	36.4	0.76
CaO	20.2	17.6	19.3	19.4	0.62
Na_2O	0.20	1.61	0.64	0.55	0.28
K_2O	0.00	0.00	0.01	0.01	0.02
∑	101.0	100.2	101.0	100.4	1.07
cations per 8 oxygens normalised to 5					
Si	2.0	2.1	2.0	2.0	0.0
Al	2.0	1.9	2.0	2.0	0.0
Ca	1.0	0.9	0.9	1.0	0.0
Na	0.0	0.1	0.1	0.0	0.0
K	0.0	0.0	0.0	0.0	0.0
∑	5.0	5.0	5.0	5.0	0.0
An	100.7	88.2	96.8	96.7	2.6
Ab	0.1	12.6	3.7	3.7	2.5
Or	0.0	0.0	0.0	0.1	0.1

Table III: Pyroxene compositions of anorthosites and late stage fluid precipitate

EPMA [wt.%]	Group I Max En ZY80A	Group I Min En ZY80A	Group I Median En ZY80A	Ø Group I	S.D. n=27	Group II Max En ZY80L	Group II Min En ZY80L	Group II Median En ZY80L	Ø Group II	S.D. n=71
SiO_2	54.6	52.7	52.7	53.7	0.85	54.8	52.3	53.6	53.1	1.43
TiO_2	0.02	0.02	0.08	0.05	0.05	0.03	0.00	0.52	0.23	0.22
Al_2O_3	0.41	0.76	2.01	0.65	0.55	0.81	0.56	2.37	1.64	0.97
FeO	1.12	11.6	5.90	5.69	2.96	1.08	9.36	2.86	3.55	1.68
MnO	b.d.l.	0.24	0.28	b.d.l.	0.10	b.d.l.	0.06	b.d.l.	b.d.l.	b.d.l.
MgO	18.1	11.3	15.0	15.1	1.81	17.3	12.2	15.6	15.5	1.15
CaO	26.3	23.6	24.0	25.2	0.90	25.7	25.0	24.9	25.2	0.66
Na_2O	0.06	0.21	0.37	0.11	0.11	0.00	0.12	0.46	0.31	0.18
∑	100.6	100.5	100.4	100.5	0.97	99.8	99.6	100.3	99.6	2.20
cations per 6 oxygens										
Si (T)	2.0	2.0	1.9	2.0	0.0	2.0	2.0	1.9	2.0	0.0
Al (T)	0.0	0.0	0.1	0.0	0.0	0.0	0.0	0.1	0.0	0.0
Al (M1)	0.0	0.0	0.0	0.0	0.0	0.0	0.0	0.1	0.0	0.0
Fe (M1)	0.0	0.4	0.2	0.2	0.1	0.0	0.3	0.1	0.1	0.1
Mg (M1)	1.0	0.6	0.8	0.8	0.1	0.9	0.7	0.8	0.9	0.1
Ti (M1)	0.0	0.0	0.0	0.0	0.0	0.0	0.0	0.0	0.0	0.0
Fe (M2)	0.0	0.0	0.0	0.0	0.0	0.0	0.0	0.0	0.0	0.0
Mn (M2)	0.0	0.0	0.0	0.0	0.0	0.0	0.0	0.0	0.0	0.0
Mg (M2)	0.0	0.0	0.0	0.0	0.0	0.0	0.0	0.0	0.0	0.0
Ca (M2)	1.0	1.0	0.9	1.0	0.0	1.0	1.0	1.0	1.0	0.0
Na (M2)	0.0	0.0	0.0	0.0	0.0	0.0	0.0	0.0	0.0	0.0
CaTs	1.4	0.6	2.8	1.2	0.8	0.6	1.0	2.5	2.2	1.1
Wo	50.2	48.8	48.5	49.8	0.7	50.8	50.8	51.1	50.8	0.6
En	48.1	32.4	42.2	41.4	4.3	47.5	34.4	44.4	43.6	2.7
Fs	1.7	18.7	9.3	8.9	4.8	1.7	14.8	4.6	5.6	2.6

Table III (continued): Pyroxene compositions of anorthosites and late stage fluid precipitate

EPMA [wt.%]	Group III Max En ZY80F	Group III Min En ZY80J	Group III Median En ZY80J	Ø Group III	S.D. n=19
SiO_2	55.1	53.1	53.6	54.2	0.69
TiO_2	0.03	0.03	0.11	0.18	0.23
Al_2O_3	0.45	0.52	1.43	1.11	0.90
FeO	2.21	9.23	3.17	3.41	1.61
MnO	b.d.l.	b.d.l.	b.d.l.	b.d.l.	b.d.l.
MgO	17.2	12.5	15.6	15.9	1.11
CaO	25.6	24.9	25.0	25.4	0.48
Na_2O	0.00	0.00	0.00	0.11	0.18
∑	100.5	100.3	99.1	100.4	1.05
cations per 6 oxygens					
Si (T)	2.0	2.0	2.0	2.0	0.0
Al (T)	0.0	0.0	0.0	0.0	0.0
Al (M1)	0.0	0.0	0.0	0.0	0.0
Fe (M1)	0.1	0.3	0.1	0.1	0.1
Mg (M1)	0.9	0.7	0.9	0.9	0.1
Ti (M1)	0.0	0.0	0.0	0.0	0.0
Fe (M2)	0.0	0.0	0.0	0.0	0.0
Mn (M2)	0.0	0.0	0.0	0.0	0.0
Mg (M2)	0.0	0.0	0.0	0.0	0.0
Ca (M2)	1.0	1.0	1.0	1.0	0.0
Na (M2)	0.0	0.0	0.0	0.0	0.0
CaTs	0.4	0.6	1.2	1.2	1.0
Wo	49.9	50.2	50.9	50.6	0.5
En	46.8	35.2	44.1	44.1	2.5
Fs	3.4	14.5	5.0	5.3	2.5

EPMA [wt.%]	Max En ZY92	Min En ZY92	Median En ZY92	Ø	S.D. n=27
SiO_2	53.7	39.0	50.4	49.4	3.55
TiO_2	0.18	1.05	0.44	0.51	0.27
Al_2O_3	2.22	15.1	5.66	7.20	4.00
FeO	6.65	12.1	6.84	8.02	2.50
MnO	b.d.l.	b.d.l.	0.12	b.d.l.	b.d.l.
MgO	22.3	8.17	16.9	16.16	3.64
CaO	14.0	18.8	19.3	18.2	1.52
Na_2O	0.11	0.34	0.20	0.16	0.07
∑	99.8	94.6	99.8	99.8	1.22
cations per 6 oxygens					
Si (T)	1.9	1.6	1.9	1.8	0.1
Al (T)	0.1	0.4	0.1	0.2	0.1
Al (M1)	0.0	0.3	0.1	0.1	0.1
Fe (M1)	0.2	0.4	0.2	0.2	0.1
Mg (M1)	0.7	0.3	0.7	0.6	0.2
Ti (M1)	0.0	0.0	0.0	0.0	0.0
Fe (M2)	0.0	0.0	0.0	0.0	0.0
Mn (M2)	0.0	0.0	0.0	0.0	0.0
Mg (M2)	0.5	0.2	0.2	0.3	0.1
Ca (M2)	0.5	0.8	0.8	0.7	0.1
Na (M2)	0.0	0.0	0.0	0.0	0.0
CaTs	3.2	21.6	7.5	9.2	4.9
Wo	27.9	47.4	40.1	39.0	4.2
En	61.8	28.7	48.8	47.4	8.2
Fs	10.3	23.8	11.1	13.6	5.3

Table III (continued): Pyroxene compositions of anorthosites and late stage fluid precipitate

Q-ICP-MS [ppm]	Group I		Group II		Group III	
	Ø n=11	S.D.	Ø n=2	S.D.	Ø n=9	S.D.
Sc	232	133	1003	126	501	342
Ti	592	455	364	70.5	708	442
V	259	239	224	157	151	72
Cr	59.8	60.0	349	38.8	391	214
No	311	164	225	2.23	304	76.9
Cu	b.d.l.	-	b.d.l.	-	14.2	-
Zn	8.61	1.84	b.d.l.	-	7.56	2.31
Rb	b.d.l.	-	b.d.l.	-	b.d.l.	-
Sr	97.7	197	67.5	8.35	186	239
Y	46.3	66.7	18.0	11.2	125	88.6
Zr	39.5	49.4	32.5	5.21	25.1	17.0
Nb	6.15	6.61	b.d.l.	-	1.99	0.911
Mo	b.d.l.	-	b.d.l.	-	b.d.l.	-
Cs	b.d.l.	-	0.040	-	b.d.l.	-
Ba	1.76	2.30	1.02	0.533	2.46	3.15
La	1.64	1.67	b.d.l.	-	b.d.l.	-
Ce	5.95	7.39	b.d.l.	-	2.56	1.73
Pr	b.d.l.	-	b.d.l.	-	b.d.l.	-
Nd	2.75	2.12	0.886	0.265	2.99	1.77
Eu	b.d.l.	-	b.d.l.	-	b.d.l.	-
Gd	3.10	4.16	b.d.l.	-	5.92	4.05
Tb	b.d.l.	-	b.d.l.	-	1.61	1.08
Dy	5.93	8.63	2.19	1.38	14.3	10.1
Ho	1.52	2.20	b.d.l.	-	3.89	2.70
Er	5.15	6.68	2.13	1.62	13.3	9.67
Tm	0.990	1.11	b.d.l.	-	2.29	1.63
Yb	10.3	9.98	5.26	3.33	20.7	14.9
Sm	1.89	1.65	b.d.l.	-	2.01	0.916
Lu	2.49	2.07	b.d.l.	-	3.70	2.60
Hf	1.72	1.93	2.56	0.240	1.53	0.978
Ta	b.d.l.	-	b.d.l.	-	b.d.l.	-
W	b.d.l.	-	b.d.l.	-	b.d.l.	-
Pb	b.d.l.	-	b.d.l.	-	1.31	1.66
Th	1.35	1.76	b.d.l.	-	1.48	0.905
U	b.d.l.	-	b.d.l.	-	b.d.l.	-
Eu*	3.60	5.03	1.14	0.628	7.11	4.65

Table IV: Thomsonite compositions of anorthosites

	Thomsonite Group I	Thomsonite Group I	Thomsonite Group II	Thomsonite Group II	Thomsonite Group III	Thomsonite Group III
#	39	39	109	109	46	46
EPMA [wt.%]	Ø	S.D.	Ø	S.D.	Ø	S.D.
SiO_2	40.7	1.51	40.1	1.12	39.9	0.94
Al_2O_3	30.0	0.41	30.3	0.48	30.0	0.34
CaO	12.2	0.72	12.3	0.59	12.2	0.43
Na_2O	4.30	0.33	3.86	0.42	4.02	0.31
∑	87.2	0.89	86.6	0.75	86.2	0.74
cations per 80 oxygens						
Si	21.5	0.5	21.3	0.4	21.3	0.3
Al	18.6	0.5	19.0	0.4	18.9	0.3
Ca	6.9	0.5	7.0	0.4	7.0	0.3
Na	4.4	0.3	4.0	0.4	4.2	0.3
∑	51.4	0.3	51.2	0.4	51.4	0.2

Table V: Compositions of accessory minerals in anorthosites

EPMA	Titanite Group I				Titanite Group II		Titanite Group III	
#	56				42		31	
[wt.%]	Ø	S.D.			Ø	S.D.	Ø	S.D.
SiO_2	30.0	0.47			29.9	0.54	30.2	0.39
TiO_2	36.2	2.26			37.0	1.08	37.1	0.81
ZrO_3	0.26	0.32			0.04	0.06	0.03	0.04
Al_2O_3	1.12	0.36			1.54	0.52	1.48	0.26
FeO	1.74	1.09			0.68	0.29	0.66	0.12
CaO	27.6	0.92			28.2	0.95	28.7	0.61
∑	96.7	2.45			97.4	1.86	98.1	1.40
cations based on 5 Oxygens								
Si	1.0	0.0			1.0	0.0	1.0	0.0
Ti	0.9	0.0			0.9	0.0	0.9	0.0
Zr	0.0	0.0			0.0	0.0	0.0	0.0
Al	0.0	0.0			0.1	0.0	0.1	0.0
Fe	0.0	0.0			0.0	0.0	0.0	0.0
Ca	1.0	0.0			1.0	0.0	1.0	0.0
∑	3.0	0.0			3.0	0.0	3.0	0.0
ICP-MS	ZY80A Group I		ZY82B Group I		Group II		Group III	
#	8		2		14		3	
[ppm]	Ø	S.D.	Ø	S.D.	Ø	S.D.	Ø	S.D.
Sc	80.2	22.3	175.2	22.9	98.2	52.5	479.9	376.5
Ti	184313	28993	179747	37342	193316	38380	384272	272300
V	743	146	159	17.5	745	477	1497	1020
Cr	306	73.7	b.d.l.	-	528	343	1655	1222
Cu	27.3	9.8	b.d.l.	-	26.2	14.1	50.0	24.3
Zn	17.0	4.8	10.7	-	12.7	3.9	33.2	18.5
Sr	85.4	97.3	105	107	46.3	50.2	15.7	5.75
Y	727	472	9428	1349	6027	2061	4172	3077
Zr	816	584	992	90.8	1051	1959	957	186
Nb	2220	1233	6723	2815	3447	1893	11413	13391
Mo	9.21	4.24	b.d.l.	-	15.8	7.54	7.09	5.80
La	76.3	61.1	2359.80	626.21	327.76	174.39	115.03	11.0
Ce	109	98.0	5222	1939	1047	491	246	82.4
Pr	10.1	7.21	543	223	152	65.1	32.6	19.0
Nd	45.9	25.7	2097	711	742	285	171	119
Eu	3.01	1.78	12.7	6.99	26.6	13.7	5.02	2.98
Gd	46.1	24.7	831	19.2	523	167	232	176
Tb	11.6	6.1	179	15.1	117	38.5	66.0	49.6
Dy	95.5	50.2	1409	237	896	297	555	409
Ho	23.7	13.4	348	58.9	214	73.0	141	103
Er	69.5	41.7	1108	178	649	223	425	304
Tm	11.0	7.2	174	19.0	102	36.1	63.7	45.9
Yb	78.1	55.2	1330.1	51.6	758.0	269.1	407.4	294.0
Sm	21.6	10.0	545	116	305	102	97.6	74.1
Lu	10.3	9.1	188	10.4	101	36.6	38.8	26.0
Hf	32.4	15.6	60.5	20.5	68.2	104	60.9	15.7
Ta	176	76.5	301	99.8	202	118	1069	1305
W	7.56	5.84	0.742	0.245	6.88	9.22	133	170
Pb	1.96	0.641	1.78	0.099	1.59	0.790	1.99	0.811
Th	194	60.7	185	44.0	171	85.0	130	38.7
U	16.0	7.54	24.0	1.60	56.6	45.9	18.4	9.17
Eu*	64.2	32.4	1336	150	797	256	311	235

Table V (continued): Compositions of accessory minerals in anorthosites

	Rutile Group I		Rutile Group II		Rutile Group III	
#	4		11		12	
	Ø	S.D.	Ø	S.D.	Ø	S.D.
SiO_2	0.08	0.02	0.08	0.07	0.02	0.01
TiO_2	98.1	0.85	96.3	2.40	95.2	2.43
ZrO_3	0.08	0.06	0.24	0.15	0.07	0.05
Al_2O_3	0.01	0.02	0.08	0.04	0.11	0.05
FeO	1.34	0.35	1.27	0.42	1.67	0.80
CaO	0.69	0.28	0.67	0.33	0.39	0.22
∑	100	1.08	98.5	2.26	97.5	1.81
cations based on 2 Oxygens						
Si	0.0	0.0	0.0	0.0	0.0	0.0
Ti	1.0	0.0	1.0	0.0	1.0	0.0
Zr	0.0	0.0	0.0	0.0	0.0	0.0
Al	0.0	0.0	0.0	0.0	0.0	0.0
Fe	0.0	0.0	0.0	0.0	0.0	0.0
Ca	0.0	0.0	0.0	0.0	0.0	0.0
∑	1.0	0.0	1.0	0.0	1.0	0.0
ICP-MS	Group I				Group III	
#	2				3	
[ppm]	Ø	S.D.			Ø	S.D.
Sc	218	-			201	62.0
Ti	589557	623			572739	14627
V	2110	391			2076	378
Cr	822	213			2081	925
Cu	359	-			51.9	10.6
Zn	52.0	4.48			38.6	9.07
Sr	34.4	0.413			5.78	3.51
Y	1925	1533			151	151
Zr	1680	1627			694	105
Nb	11399	3563			18318	5340
Mo	33.3	-			9.80	4.35
La	299	349			50.9	32.8
Ce	385	367			74.3	51.0
Pr	34.4	30.6			5.14	3.42
Nd	149	120			16.3	11.6
Eu	5.58	6.02			0.653	0.423
Gd	120	100			10.1	8.18
Tb	28.5	23.4			2.75	2.73
Dy	231	191			21.2	20.5
Ho	62.1	48.0			5.29	5.37
Er	187	141			16.1	15.6
Tm	31.2	24.4			2.67	2.56
Yb	225	190			17.6	17.8
Sm	52.7	44.9			5.93	5.14
Lu	28.7	27.6			2.29	1.93
Hf	43.1	19.8			51.7	7.39
Ta	959	239			1282	592
W	212	206			324	75.7
Pb	8.90	3.56			1.64	1.07
Th	588	671			48.3	32.8
U	96.7	111			17.7	10.0
Eu*	163	137			15.5	12.9

Table V (continued): Compositions of accessory minerals in anorthosites

	Zircon Group I		Zircon Group II		Zircon Group III	
#	2		7		3	
	Ø	S.D.	Ø	S.D.	Ø	S.D.
SiO_2	32.0	0.53	32.4	0.48	33.0	0.34
TiO_2	0.21	0.29	0.38	0.27	0.02	0.03
ZrO_3	62.4	1.08	63.5	1.08	63.7	0.91
Al_2O_3	0.02	0.03	0.10	0.26	0.03	0.02
FeO	0.02	0.00	0.29	0.18	0.09	0.10
CaO	0.24	0.01	0.26	0.17	0.15	0.10
∑	94.9	1.36	96.9	1.35	97.0	0.97
cations based 4 Oxygens						
Si	1.0	0.0	1.0	0.0	1.0	0.0
Ti	0.0	0.0	0.0	0.0	0.0	0.0
Zr	1.0	0.0	1.0	0.0	1.0	0.0
Al	0.0	0.0	0.0	0.0	0.0	0.0
Fe	0.0	0.0	0.0	0.0	0.0	0.0
Ca	0.0	0.0	0.0	0.0	0.0	0.0
∑	2.0	0.0	2.0	0.0	2.0	0.0
ICP-MS	Group I		Group II			
#	1		1			
[ppm]						
Sc	84.5		169			
Ti	162		560			
V	10.4		b.d.l.			
Cr	b.d.l.		b.d.l.			
Cu	b.d.l.		b.d.l.			
Zn	b.d.l.		122			
Sr	234		113			
Y	1591		766.7			
Zr	97804		220918			
Nb	35.6		10.2			
Mo	b.d.l.		b.d.l.			
La	5.34		2.59			
Ce	30.9		17.6			
Pr	2.01		6.77			
Nd	5.58		7.57			
Eu	b.d.l.		b.d.l.			
Gd	16.4		8.74			
Tb	8.42		7.03			
Dy	106		65.3			
Ho	48.4		23.9			
Er	258		123			
Tm	63.7		32.4			
Yb	712		391			
Sm	3.36		10.6			
Lu	139		80.0			
Hf	2915		7190			
Ta	32.9		b.d.l.			
W	b.d.l.		b.d.l.			
Pb	5.7		4.4			
Th	618		194			
U	602		341			
Eu*	17.8		19.6			

Table VI: Wet chemistry

	Group I	Group I	Group I	Group II	Group II	Group II	Group II	Group II	Group III	Group III	Group III	Group III
	ZY82A*	ZY82A	ZY82B	ZY80L	ZY80M(1)	ZY80M(2)	ZY80O(1)	ZY80O(2)	ZY80F	ZY80J(1)	ZY80J(2)	ZY80K
Zr [ppm]	177.5	179.0	176.1	167.6	151.8	156.0	154.0	164.9	218.3	189.0	169.5	196.9
Lu [ppm]	2.094	2.082	1.960	1.378	1.389	1.339	1.613	1.699	0.837	0.587	1.037	0.315
Hf [ppm]	5.676	5.715	5.766	6.124	5.639	5.750	5.643	5.574	7.313	5.854	5.248	5.936
$^{176}Lu/^{177}Hf$	0.0524	0.0517	0.0482	0.0319	0.0350	0.0330	0.0406	0.0433	0.0162	0.0142	0.0281	0.0075
$^{176}Hf/^{177}Hf$	0.2831	0.2831	0.2831	0.2831	0.2831	0.2831	0.2831	0.2831	0.2830	0.2830	0.2830	0.2830
± 2σ in 6th digit	8.1638	5.7874	7.7588	7.1069	6.5171	6.1072	6.0120	7.4945	9.6019	7.4774	9.6959	7.8487
εHf(90 Ma)	9.2023	9.4280	9.3399	10.3586	10.7385	10.4659	10.5175	10.0470	9.8490	9.1349	9.3508	9.2989
Rb [ppm]	0.3549	0.2238	0.1843	0.2136	2.7268	0.4275	0.6313	0.2795	0.7444	0.8626	0.1445	0.3965
Sr [ppm]	280.1	282.2	281.7	224.8	242.0	222.1	223.6	235.1	241.9	243.2	250.5	272.3
$^{87}Rb/^{86}Sr$	0.0037	0.0023	0.0019	0.0027	0.0326	0.0056	0.0082	0.0034	0.0089	0.0103	0.0017	0.0042
$^{87}Sr/^{86}Sr$	0.7065	0.7065	0.7063	0.7062	0.7069	0.7069	0.7062	0.7063	0.7062	0.7065	0.7065	0.7063
± 2σ in 6th digit	8.4972	8.2642	8.9594	9.7836	14.6056	15.0675	9.2860	10.5249	10.0106	11.4624	6.3112	11.5546
$^{87}Sr/^{86}Sr$ (90 Ma)	0.7065	0.7065	0.7063	0.7062	0.7068	0.7068	0.7062	0.7063	0.7062	0.7065	0.7065	0.7063

* the procedure of ion chromatography was performed twice with sample ZY82A

Table VII: Bulk chemistry late stage fluid precipitate

EPMA					**ICP-MS**				
Sample	ZY92(A)	ZY92(A)	ZY92(B)	ZY92(B)	Sample	ZY92A	ZY92A	ZY92B	ZY92B
#	60	60	60	60	#	29	29	30	30
	Ø	S.D.	Ø	S.D.		Ø	S.D.	Ø	S.D.
EPMA [wt.%]					Sc	41.38	1.16	41.43	1.45
CaO	51.5	0.48	53.9	0.28	Ti	2331	44.8	2297	53.2
Al_2O_3	15.8	0.12	15.8	0.11	V	224	6.66	197	6.24
FeO	8.13	0.21	7.56	0.22	Cr	456	19.8	407	19.4
MgO	7.15	0.09	9.89	0.07	No	161	8.21	127	6.11
CaO	13.6	0.10	10.7	0.08	Cu	28.3	2.33	24.9	1.81
Na_2O	1.13	0.06	1.14	0.06	Zn	81.5	4.43	56.0	1.97
K_2O	1.99	0.03	0.77	0.02	Rb	25.1	0.875	17.9	0.629
Total	99.2	0.77	99.8	0.47	Sr	78.6	1.40	75.2	1.77
					Y	8.99	0.319	5.57	0.178
CIPW [wt.%]					Zr	18.9	1.08	21.4	1.19
Qz	-		4.0		Nb	0.93	0.06	0.86	0.06
An	32.1		35.8		Mo	4.08	1.68	10.0	4.59
Ab	9.6		9.6		Cs	0.244	0.013	0.346	0.020
Or	11.8		4.6		Ba	14.6	0.467	20.0	0.582
Di	28.9		14.2		La	1.43	0.053	0.900	0.039
Hyp	12.4		31.6		Ce	3.19	0.082	2.25	0.060
Ol	4.5		-		Pr	0.426	0.017	0.266	0.011
∑	99.2		99.8		Nd	2.34	0.116	1.50	0.087
					Eu	0.361	0.023	0.301	0.018
XRD					Gd	1.11	0.069	0.760	0.048
Sample	ZY92				Tb	0.208	0.010	0.143	0.011
#	1				Dy	1.52	0.07	1.05	0.051
					Ho	0.329	0.016	0.226	0.012
XRD [%]					Er	0.96	0.053	0.66	0.040
An	35.5				Tm	0.136	0.009	0.096	0.008
Or	6.66				Yb	1.07	0.061	0.748	0.040
Di	22.1				Sm	0.840	0.058	0.568	0.042
Mnt	23.0				Lu	0.147	0.010	0.1030	0.009
Hbl	5.06				Hf	0.552	0.032	0.524	0.030
Cal	7.71				Ta	0.057	0.005	0.052	0.004
∑	100				W	0.968	0.049	1.49	0.222
					Pb	1.05	0.096	3.98	0.544
					Th	0.145	0.010	0.138	0.009
					U	0.104	0.021	0.051	0.004
					Eu*	1.9		1.3	

TABLE VIII: Compositions of experimental run products of liquidus experiments. *The H_2O content is calculated by difference

Experiment #	Glass AnL-1200 n=10		Glass AnL-1150 n=10		Glass AnL-1050 n=4		Glass AnL-950 n=5	
EPMA [wt.%]	Ø	S.D.	Ø	S.D.	Ø	S.D.	Ø	S.D.
SiO_2	50.2	1.88	50.9	1.49	60.1	0.48	59.1	1.31
TiO_2	0.36	0.11	0.41	0.05	0.61	0.09	0.56	0.10
Al_2O_3	27.6	1.42	26.4	0.75	23.8	0.29	23.7	0.33
FeO	0.01	0.02	0.02	0.03	0.00	0.01	0.00	0.00
MgO	1.09	0.35	0.82	0.05	0.18	0.01	0.21	0.02
MnO	0.01	0.02	0.01	0.01	0.01	0.01	0.03	0.04
CaO	12.5	0.90	10.1	0.80	6.59	0.10	6.27	0.55
Na_2O	3.31	0.21	2.85	0.44	4.46	0.29	4.10	0.22
K_2O	0.12	0.07	0.07	0.01	0.07	0.01	0.10	0.03
H_2O*	4.62	1.08	8.28	0.42	4.02	0.13	5.82	1.82
∑	95.4	1.08	91.7	0.42	96.0	0.13	94.2	1.82
CIPW [wt.%]								
Qz	2.5		11.1		19.5		21.1	
An	60.2		50.3		32.7		31.1	
Ab	28.0		24.1		37.7		34.7	
Or	0.7		0.4		0.4		0.6	
Crn	-		3.2		4.4		5.5	
Di	0.6		-		-		-	
Hyp	2.4		2.0		0.5		0.5	
Rt	-		0.4		0.6		0.5	
Ilm	0.0		0.1		0.0		0.1	
Ttn	0.8		-		-		-	
∑	95.3		91.6		95.9		94.1	

Experiment	Anorthite X_{An} max AnL-1150	Anorthite X_{An} min AnL-1050	Quench X_{An} max AnL-1050	Quench X_{An} min AnL-950
EPMA [wt.%]				
SiO_2	44.8	45.5	46.8	53.1
Al_2O_3	37.0	35.4	35.2	26.8
MgO	b.d.l.	b.d.l.	b.d.l.	0.78
CaO	20.2	19.0	18.0	9.09
Na_2O	0.20	0.91	1.38	3.22
∑	102	101	102	93.5
Cations per 8 Oxygens normalised to 5				
Si	2.0	2.1	2.1	2.6
Al	2.0	1.9	1.9	1.5
Mg	-	-	-	0.1
Ca	1.0	0.9	0.9	0.5
Na	0.0	0.1	0.1	0.3
∑	5.0	5.0	5.0	5.0
An	1.0	0.9	0.9	0.5
Ab	0.0	0.1	0.1	0.4
Or	0.0	0.0	0.0	0.0

TABLE IX: Compositions of experimental run products from simple system experiments * H_2O content by difference. †Mineral proportions normalised to 100 % regardless Qz

	Glass	Glass	Glass	Glass	Glass	Glass	Glass	Glass
Experiment	207010-1200	207010-1200	201070-1150	201070-1150	201070-1000	201070-1000	201070-1200	201070-1200
initial An:Di:Fo	20:70:10	20:70:10	20:70:10	20:70:10	20:70:10	20:70:10	20:10:70	20:10:70
T [°C]	1200	1200	1150	1150	1000	1000	1200	1200
P [Mpa]	500	500	500	500	500	500	500	500
coexisting phases	L+Fo	L+Fo	L+Fo+Di	L+Fo+Di	L+Fo+Di	L+Fo+Di	L+Fo	L+Fo
#	12	12	31	31	10	10	7	7
Glass EPMA [wt.%]	Ø	S.D.	Ø	S.D.	Ø	S.D.	Ø	S.D.
SiO_2	49.4	1.41	49.0	0.58	50.8	1.39	43.7	0.21
Al_2O_3	7.82	0.73	8.73	0.18	21.5	0.77	18.8	0.28
FeO	0.17	0.06	0.15	0.04	0.21	0.05	5.23	0.21
MgO	13.7	0.51	13.3	0.20	4.45	0.68	8.36	0.62
CaO	22.2	0.60	21.9	0.15	13.6	0.79	16.3	0.35
∑	93.3	2.49	93.2	0.61	90.6	0.48	92.3	0.28
H_2O*	6.69	2.49	6.83	0.61	9.38	0.48	7.71	0.28
An [%]†	23.2	2.1	25.9	0.5	82.4	3.8	59.3	0.8
Di [%]†	75.2	2.4	72.0	0.6	9.6	3.8	26.4	1.1
Fo [%]†	1.6	0.3	2.1	0.4	8.0	0.8	14.2	1.5
	Glass	Glass	Glass	Glass	Glass	Glass	Glass	Glass
Experiment	201070-1150	201070-1150	405010-1100	405010-1100	405010-1050	405010-1050	405010-1000	405010-1000
initial An:Di:Fo	20:10:70	20:10:70	40:50:10	40:50:10	40:50:10	40:50:10	40:50:10	40:50:10
T [°C]	1150	1150	1100	1100	1050	1050	1000	1000
P [Mpa]	500	500	500	500	500	500	500	500
coexisting phases	L+Fo	L+Fo	L+Fo+Di	L+Fo+Di	L+Fo+Di	L+Fo+Di	L+Fo+Di	L+Fo+Di
#	12	12	19	19	15	15	4	4
Glass EPMA [wt.%]	Ø	S.D.	Ø	S.D.	Ø	S.D.	Ø	S.D.
SiO_2	43.8	0.16	43.8	0.29	42.4	0.56	42.2	0.68
Al_2O_3	19.7	0.42	19.6	0.16	21.7	0.41	22.7	0.49
FeO	5.05	0.17	0.22	0.03	0.25	0.03	0.24	0.07
MgO	6.40	0.78	10.6	0.09	10.1	0.37	9.92	0.58
CaO	17.1	0.37	17.9	0.09	17.2	0.41	15.9	0.50
∑	92.1	0.46	92.1	0.39	91.6	0.98	91.0	0.66
H_2O*	7.90	0.46	7.88	0.39	8.41	0.98	8.98	0.66
An [%]†	62.3	1.3	58.8	0.4	65.1	1.5	70.0	1.9
Di [%]†	28.2	1.1	30.3	0.4	22.6	2.1	15.1	3.1
Fo [%]†	9.5	1.9	10.8	0.2	12.3	1.0	14.9	1.5

TABLE IX (continued): Compositions of experimental run products from simple system experiments * H_2O content by difference. †Mineral proportions normalised to 100 % regardless Qz

	Glass	Glass	Glass	Glass	Glass	Glass	Glass	Glass
Experiment	454015-1200	454015-1200	454015-1150	454015-1150	454015-1100	454015-1100	454015-1050	454015-1050
initial An:Di:Fo	45:40:15	45:40:15	45:40:15	45:40:15	45:40:15	45:40:15	45:40:15	45:40:15
T [°C]	1200	1200	1150	1150	1100	1100	1050	1050
P [Mpa]	500	500	500	500	500	500	500	500
coexisting phases	L+Fo	L+Fo	L+Fo+Di	L+Fo+Di	L+Fo+Di	L+Fo+Di	L+Fo+Di	L+Fo+Di
#	10	10	6	6	10	10	9	9
Glass EPMA [wt.%]	Ø	S.D.	Ø	S.D.	Ø	S.D.	Ø	S.D.
SiO_2	43.5	0.92	43.4	0.71	41.4	2.12	42.6	1.94
Al_2O_3	16.2	0.09	18.2	1.03	20.9	0.63	22.1	0.44
FeO	0.41	0.05	0.44	0.09	0.50	0.13	0.44	0.10
MgO	12.1	0.18	11.0	1.11	8.88	0.62	8.41	0.30
CaO	19.1	0.15	17.9	0.48	16.4	0.32	15.7	0.54
∑	91.2	0.88	90.9	1.03	88.0	2.77	89.2	2.62
H_2O*	8.77	0.88	9.11	1.03	11.95	2.77	10.8	2.62
An [%]†	49.6	1.0	55.6	3.7	66.8	2.3	71.4	1.6
Di [%]†	43.9	1.4	33.9	3.5	21.9	2.5	16.0	2.3
Fo [%]†	6.6	2.2	10.5	2.2	11.3	1.3	12.7	0.8
	Glass	Glass	Glass	Glass	Glass	Glass	Glass	Glass
Experiment	454015-1000	454015-1000	503020-1200	503020-1200	503020-1150	503020-1150	503020-1100	503020-1100
initial An:Di:Fo	45:40:15	45:40:15	50:30:20	50:30:20	50:30:20	50:30:20	50:30:20	50:30:20
T [°C]	1000	1000	1200	1200	1150	1150	1100	1100
P [Mpa]	500	500	500	500	500	500	500	500
coexisting phases	L+Fo+Di	L+Fo+Di	L+Fo	L+Fo	L+Fo+Di	L+Fo+Di	L+Fo+Di	L+Fo+Di
#	11	11	7	7	25	25	26	26
Glass EPMA [wt.%]	Ø	S.D.	Ø	S.D.	Ø	S.D.	Ø	S.D.
SiO_2	44.1	0.69	44.1	0.52	43.6	0.58	43.2	0.62
Al_2O_3	23.3	0.34	17.5	0.27	19.0	0.25	20.2	0.48
FeO	0.54	0.06	1.11	0.13	0.79	0.11	1.36	0.11
MgO	7.03	0.41	11.7	0.80	12.1	0.73	9.41	1.12
CaO	14.4	0.60	17.6	0.45	17.3	0.43	17.7	0.41
∑	89.3	0.68	92.0	0.32	92.7	1.02	91.8	1.17
H_2O*	10.7	0.68	7.99	0.32	7.30	1.02	8.15	1.17
An [%]†	79.0	1.0	53.2	0.9	56.6	0.5	61.4	1.6
Di [%]†	7.6	2.2	34.0	1.7	28.8	1.5	28.0	0.9
Fo [%]†	13.5	1.6	12.8	2.0	14.5	1.8	10.6	2.1

TABLE IX (continued): Compositions of experimental run products from simple system experiments * H_2O content by difference. †Mineral proportions normalised to 100 % regardless Qz

	Glass	Glass	Glass	Glass	Glass	Glass	Glass	Glass
Experiment	503020-1050	503020-1050	503020-1000	503020-1000	603010-1200	603010-1200	603010-1150	603010-1150
initial An:Di:Fo	50:30:20	50:30:20	50:30:20	50:30:20	60:30:10	60:30:10	60:30:10	60:30:10
T [°C]	1050	1050	1000	1000	1200	1200	1150	1150
P [Mpa]	500	500	500	500	500	500	500	500
coexisting phases	L+Fo+Di	L+Fo+Di	L+Fo+Di	L+Fo+Di	L	L	L+Fo+Di	L+Fo+Di
#	13	13	9	9	15	15	33	33
Glass EPMA [wt.%]	Ø	S.D.	Ø	S.D.	Ø	S.D.	Ø	S.D.
SiO_2	40.7	3.46	43.6	0.51	44.1	0.20	44.0	0.28
Al_2O_3	22.0	0.62	24.0	0.50	21.1	0.08	21.4	0.18
FeO	1.36	0.24	1.22	0.07	0.29	0.04	0.30	0.04
MgO	7.68	0.29	5.70	0.65	8.26	0.09	8.26	0.21
CaO	15.7	0.48	14.8	0.59	18.3	0.11	18.0	0.31
∑	87.5	4.32	89.3	0.83	92.1	0.29	92.0	0.52
H_2O*	12.5	4.32	10.7	0.83	7.95	0.29	8.00	0.52
An [%]†	71.9	1.3	81.1	2.5	64.2	0.1	65.2	0.9
Di [%]†	16.8	1.3	7.6	2.8	28.7	0.3	27.1	1.4
Fo [%]†	11.3	1.5	11.3	1.4	7.1	0.3	7.6	0.6
	Glass	Glass	Glass	Glass	Glass	Glass	Glass	Glass
Experiment	603010-1100	603010-1100	603010-1050	603010-1050	601030-1200	601030-1200	601030-1100	601030-1100
initial An:Di:Fo	60:30:10	60:30:10	60:30:10	60:30:10	60:10:30	60:10:30	60:10:30	60:10:30
T [°C]	1100	1100	1050	1050	1200	1200	1100	1100
P [Mpa]	500	500	500	500	500	500	500	500
coexisting phases	L+Fo+Di	L+Fo+Di	L+Fo+Di	L+Fo+Di	L+Fo	L+Fo	L+Fo	L+Fo
#	6	6	10	10	17	17	10	10
Glass EPMA [wt.%]	Ø	S.D.	Ø	S.D.	Ø	S.D.	Ø	S.D.
SiO_2	44.8	0.89	43.3	0.49	41.5	0.45	42.5	0.36
Al_2O_3	22.6	0.72	22.0	0.12	21.4	0.13	21.5	0.19
FeO	0.46	0.15	0.18	0.03	1.33	0.07	1.54	0.03
MgO	7.97	0.61	8.59	0.10	10.8	0.75	9.26	0.14
CaO	15.9	0.49	15.0	0.18	13.7	0.25	14.9	0.07
∑	91.8	0.54	89.1	0.81	88.7	0.84	89.7	0.52
H_2O*	8.24	0.54	10.9	0.81	11.3	0.84	10.3	0.52
An [%]†	72.5	2.0	72.6	0.4	70.0	0.7	69.6	0.3
Di [%]†	15.8	2.3	13.3	0.6	8.8	1.2	14.0	0.5
Fo [%]†	11.8	1.5	14.0	0.3	21.3	1.8	16.4	0.3

TABLE IX (continued): Compositions of experimental run products from simple system experiments * H_2O content by difference. †Mineral proportions normalised to 100 % regardless Qz

	Glass	Glass	Glass	Glass	Glass	Glass	Glass	Glass
Experiment	601030-1050	601030-1050	652015-1200	652015-1200	652015-1150	652015-1150	652015-1050	652015-1050
initial An:Di:Fo	60:10:30	60:10:30	65:20:15	65:20:15	65:20:15	65:20:15	65:20:15	65:20:15
T [°C]	1050	1050	1200	1200	1150	1150	1050	1050
P [Mpa]	500	500	500	500	500	500	500	500
coexisting phases	L+Fo+Di	L+Fo+Di	L	L	L+Fo	L+Fo	L+Fo+Di	L+Fo+Di
#	4	4	41	41	28	28	7	7
Glass EPMA [wt.%]	Ø	S.D.	Ø	S.D.	Ø	S.D.	Ø	S.D.
SiO_2	40.3	0.38	43.5	0.71	42.7	0.94	43.0	0.70
Al_2O_3	23.4	0.42	22.3	0.53	23.6	0.46	25.9	0.63
FeO	1.48	0.11	0.51	0.10	0.61	0.10	0.63	0.13
MgO	7.74	0.29	9.59	0.40	8.98	0.50	6.85	0.26
CaO	14.8	0.26	17.2	0.30	17.2	0.36	18.2	0.18
∑	87.7	0.27	93.0	0.65	93.0	1.34	94.6	1.25
H_2O*	12.3	0.27	7.04	0.65	6.97	1.34	5.41	1.25
An [%]†	76.1	1.4	66.9	1.2	70.5	0.9	75.7	1.3
Di [%]†	8.9	2.0	20.9	1.2	17.6	1.3	16.1	1.3
Fo [%]†	14.9	1.0	12.2	0.9	11.9	1.4	8.2	0.5

	Glass	Glass
Experiment	721810-1200	721810-1200
initial An:Di:Fo	72:18:10	72:18:10
T [°C]	1200	1200
P [Mpa]	500	500
coexisting phases	L	L
#	10	10
Glass EPMA [wt.%]	Ø	S.D.
SiO_2	42.7	0.25
Al_2O_3	25.6	0.16
FeO	0.13	0.03
MgO	6.96	0.11
CaO	17.8	0.17
∑	93.3	0.51
H_2O*	6.75	0.51
An [%]†	76.1	0.5
Di [%]†	15.7	0.7
Fo [%]†	8.3	0.3

TABLE IX (continued): Compositions of experimental run products from simple system experiments

	Anorthite 454015	Anorthite 454015	Anorthite 503020	Anorthite 503020	Anorthite 601030	Anorthite 601030	Anorthite 603010	Anorthite 603010	Anorthite 652015	Anorthite 652015
EPMA [wt. %]	Ø	S.D.	Ø	S.D.	Ø	S.D.	Ø	S.D.	Ø	S.D.
SiO_2	43.8	0.27	43.2	0.45	42.4	1.04	43.2	0.69	42.9	0.48
Al_2O_3	36.6	0.52	37.4	0.38	36.4	0.83	36.3	0.50	37.5	0.86
FeO	0.03	0.01	0.09	0.04	0.20	0.14	0.03	0.03	0.10	0.08
MgO	0.26	0.25	0.19	0.09	0.27	0.15	0.23	0.15	0.31	0.20
CaO	20.0	0.11	20.7	0.15	19.6	0.42	19.9	0.33	19.7	0.36
∑	101	0.30	102	0.34	98.9	1.64	99.7	1.36	100	0.89
cations per 8 oxygens normalised to 5										
Si	2.01	0.01	1.97	0.02	1.99	0.03	2.00	0.01	1.97	0.02
Al	1.98	0.03	2.01	0.02	2.01	0.03	1.99	0.02	2.03	0.04
Fe	0.00	0.00	0.00	0.00	0.01	0.01	0.00	0.00	0.00	0.00
Mg	0.02	0.02	0.01	0.01	0.02	0.01	0.02	0.01	0.02	0.01
Ca	0.99	0.00	1.01	0.01	0.98	0.01	0.99	0.01	0.97	0.02
∑	5.00	0.00	5.00	0.00	5.00	0.00	5.00	0.00	5.00	0.00
An	98.4	1.26	101	1.39	99.6	2.62	99.0	1.02	100	1.51
Ab	0.53	0.60	-1.23	0.84	-0.57	1.52	0.24	0.61	-1.27	1.06
Or	0.00	0.00	0.00	0.00	0.00	0.00	0.00	0.00	0.00	0.00

TABLE IX (continued): Compositions of experimental run products from simple system experiments

EPMA [wt. %]	Forsterite 503020 Fe Median	Forsterite 454015 Fe Min	Forsterite 603010 Fe Max
SiO_2	41.8	42.3	41.3
Al_2O_3	0.05	0.03	0.21
FeO	2.02	0.84	6.92
MgO	54.1	55.8	49.0
CaO	0.30	0.45	0.67
∑	98.2	99.4	98.2
cations per 4 oxygens			
Si	1.0	1.0	1.0
Al	0.0	0.0	0.0
Fe	0.0	0.0	0.1
Mg	1.9	2.0	1.8
Ca	0.0	0.0	0.0
∑	3.0	3.0	3.0
Fo	97.9	99.2	92.7
Fa	2.1	0.8	7.3

[wt. %]	Pyroxene 503020 Max Wo = Max CaTs	Pyroxene 454015 Max En	Pyroxene 601030 Max Fs	Pyroxene 652015 Min CaTs
SiO_2	44.4	54.7	49.1	55.2
Al_2O_3	18.1	1.78	9.83	2.31
FeO	0.56	0.24	1.78	0.47
MgO	12.8	19.4	14.6	15.8
CaO	24.6	24.2	23.8	23.8
∑	100	100	99.2	97.5
cations per 6 oxygens				
Si (T)	1.6	2.0	1.8	2.0
Al (T)	0.4	0.0	0.2	0.0
Al (M)	0.4	0.0	0.2	0.1
Fe (M)	0.0	0.0	0.1	0.0
Mg (M)	0.7	1.0	0.8	0.9
Ca (M)	0.9	0.9	0.9	0.9
∑	4.0	4.0	4.0	3.9
CaTs	20.1	2.1	10.4	0.0
Wo	57.3	47.2	52.3	51.7
En	41.6	52.5	44.7	47.5
Fs	1.0	0.4	3.0	0.8

TABLE X: Compositions of experimental run products of decompression experiments

Sample	starting composition		PCADecExp		PCADecExprep		PCADecExpCr		IHPVDecExp-5-3	
#	10		100		36		29		6	
EPMA [wt.%]	Ø	S.D.	Ø	S.D.	Ø	S.D.	Ø	S.D.	Ø	S.D.
SiO_2	52.3	0.67	61.7	2.25	60.5	4.19	59.7	3.11	70.1	1.25
TiO_2	0.37	0.04	0.09	0.08	0.10	0.08	0.13	0.07	0.43	0.10
Al_2O_3	14.9	0.32	18.1	1.23	17.5	2.19	18.2	1.53	10.7	0.47
FeO (Fe_2O_3)*	3.57	0.26	0.92	0.35	0.57	0.17	0.90	0.27	2.63	0.44
MgO	8.07	0.40	0.18	0.08	0.11	0.05	0.17	0.05	0.11	0.03
MnO	n.a.	-	0.05	0.03	n.a.	-	0.04	0.02	n.a.	-
CaO	10.4	0.36	7.43	0.74	7.21	1.33	6.53	0.91	4.35	0.48
Na_2O	1.03	0.14	1.21	0.29	0.91	0.12	1.31	0.33	1.33	0.11
K_2O	0.18	0.04	0.16	0.02	0.20	0.05	0.17	0.02	n.a.	-
H_2O*	9.15	1.11	10.4	1.30	12.9	1.09	12.8	1.60	10.3	0.46
∑	90.8	1.11	89.6	1.30	87.1	1.09	87.2	1.60	89.7	0.46
CIPW [wt.%]										
Qz	12.14		37.2		38.4		36.5		51.1	
An	35.6		36.9		35.8		32.4		21.6	
Ab	8.7		10.2		7.7		11.1		11.2	
Or	1.1		1.0		1.2		1.0			
Crn	-		2.4		2.7		4.0		0.7	
Di	12.6		-		-		-		-	
Hyp	20.0		2.0		1.2		1.9		4.4	
Ilm	0.7		0.2		0.2		0.3		0.8	
∑	90.9		89.8		87.1		87.1		89.7	

TABLE X (continued): Compositions of experimental run products of decompression experiments

	Anorthite PCADecExp 9		Anorthite PCADecExprep 5		Anorthite PCADecExpCr 5		Anorthite IHPVDecExp-5-3 2	
EPMA [wt.%]	Ø	S.D.	Ø	S.D.	Ø	S.D.	Ø	S.D.
SiO_2	46.4	0.44	46.8	1.56	46.0	0.36	48.9	0.18
Al_2O_3	35.4	0.66	33.1	2.32	35.4	0.23	30.7	0.20
FeO	0.42	0.09	0.52	0.47	0.16	0.05	0.72	0.19
CaO	18.7	0.18	16.7	1.63	18.4	0.19	15.4	0.27
Na_2O	1.07	0.10	1.52	0.19	1.44	0.16	2.54	0.22
K_2O	n.a.	-	0.04	0.02	0.01	0.01	n.a.	-
∑	102	0.90	98.9	2.10	101	0.43	98.6	0.02
Cations per 8 Oxygens								
Si	2.1	0.0	2.2	0.1	2.1	0.0	2.3	0.0
Al	1.9	0.0	1.8	0.1	1.9	0.0	1.7	0.0
Fe	0.0	0.0	0.0	0.0	0.0	0.0	0.0	0.0
Ca	0.9	0.0	0.8	0.1	0.9	0.0	0.8	0.0
Na	0.1	0.0	0.1	0.0	0.1	0.0	0.2	0.0
K	-	-	0.0	0.0	0.0	0.0	-	-
∑	5.0	0.0	5.0	0.0	5.0	0.0	5.0	0.0
An	90	1	82	9	90	1	73	1
Ab	10	1	15	5	11	1	25	1
Or	0	0	0	0	0	0	0	0

TABLE X (continued): Compositions of experimental run products of decompression experiments

	CaTs PCADecExp		CaTs PCADecExprep		CaTs PCADecExpCr		CaTs IHPVDecExp-5-3	
#	75		41		12		4	
EPMA [wt.%]	Ø	S.D.	Ø	S.D.	Ø	S.D.	Ø	S.D.
SiO_2	44.7	2.20	44.0	2.41	44.3	1.19	45.1	3.68
TiO_2	0.92	0.30	0.84	0.26	1.21	0.22	2.15	1.20
Al_2O_3	14.6	2.24	14.8	2.56	15.7	1.58	6.46	2.43
FeO	10.7	3.64	11.2	2.96	7.19	0.94	18.4	1.96
MnO	0.14	0.03	n.a.	-	0.10	0.02	n.a.	-
MgO	14.7	3.48	14.8	3.26	16.6	1.25	11.1	1.75
CaO	11.4	0.57	11.2	0.63	11.8	0.30	11.5	1.18
Na_2O	1.46	0.26	1.41	0.21	1.72	0.15	1.15	0.65
∑	98.4	1.23	98.2	0.36	98.7	0.37	95.9	1.34
Cations per 6 Oxygens								
Si(T)	1.7	0.1	1.6	0.1	1.6	0.0	1.8	0.1
Al(T)	0.3	0.1	0.4	0.1	0.4	0.0	0.2	0.1
∑(T)	2.0	0.1	2.0	0.0	2.0	0.0	2.0	0.0
Al(M1)	0.3	0.1	0.3	0.1	0.3	0.0	0.1	0.1
Fe(M1)	0.3	0.1	0.4	0.1	0.2	0.0	0.6	0.1
Mg(M1)	0.3	0.2	0.3	0.1	0.4	0.1	0.2	0.1
Ti(M1)	0.0	0.0	0.0	0.0	0.0	0.0	0.1	0.0
∑(M1)	1.0	0.0	1.0	0.0	1.0	0.0	1.0	0.0
Fe(M2)	0.0	0.0	0.0	0.0	0.0	0.0	0.0	0.0
Mn(M2)	0.0	0.0	-	-	0.0	0.0	-	-
Mg(M2)	0.5	0.0	0.5	0.0	0.5	0.0	0.4	0.0
Ca(M2)	0.5	0.0	0.4	0.0	0.5	0.0	0.5	0.0
Na(M2)	0.1	0.0	0.1	0.0	0.1	0.0	0.1	0.1
∑(M2)	1.0	0.0	1.1	0.0	1.1	0.0	1.0	0.0
∑ (M)	2.0	0.0	2.1	0.0	2.1	0.0	2.0	0.0
CaTs	17.0	0.0	18.0	0.0	19.0	0.0	10.0	0.1
Wo	28	2	28	3	29	1	28	1
En	50	10	50	9	57	3	37	4
Fs	21	9	22	7	14	2	35	5

TABLE X (continued): Compositions of experimental run products of decompression experiments

	Diopside PCADecExp		Diopside PCADecExprep		Diopside PCADecExpCr		Diopside IHPVDecExp-5-3		Diopside IHPVDecExp-8-3	
#	75		12		18		5		4	
EPMA [wt.%]	Ø	S.D.	Ø	S.D.	Ø	S.D.	Ø	S.D.	Ø	S.D.
SiO_2	51.9	1.67	52.0	1.01	52.5	1.19	50.8	0.48	49.2	2.61
TiO_2	0.38	0.29	0.27	0.12	0.34	0.24	0.30	0.08	0.46	0.26
Al_2O_3	4.65	1.93	3.92	1.51	3.59	1.53	3.94	0.58	6.75	2.74
FeO	5.67	1.05	5.85	0.56	4.03	0.65	6.00	1.15	6.28	0.95
MnO	0.14	0.03	n.a.	-	0.12	0.03	n.a.	-	n.a.	-
MgO	16.9	1.55	17.9	1.39	18.9	1.72	17.0	1.23	16.2	3.19
CaO	20.9	1.18	19.6	1.47	20.3	1.79	18.9	1.41	18.8	2.43
Na_2O	0.18	0.07	0.18	0.06	0.20	0.08	0.19	0.15	0.14	0.03
∑	101	1.21	99.9	0.42	100	0.59	97.1	0.85	97.8	0.34
Cations per 6 Oxygens										
Si (T)	1.9	0.1	1.9	0.0	1.9	0.0	1.9	0.0	1.8	0.1
Al (T)	0.1	0.1	0.1	0.0	0.1	0.0	0.1	0.0	0.2	0.1
∑ (T)	2.0	0.0	2.0	0.0	2.0	0.0	2.0	0.0	2.0	0.0
Al (M1)	0.1	0.0	0.1	0.0	0.1	0.0	0.1	0.0	0.1	0.0
Fe (M1)	0.2	0.0	0.2	0.0	0.1	0.0	0.2	0.0	0.2	0.0
Mg (M1)	0.7	0.1	0.7	0.0	0.8	0.0	0.7	0.0	0.7	0.1
Ti (M1)	0.0	0.0	0.0	0.0	0.0	0.0	0.0	0.0	0.0	0.0
∑ (M1)	1.0	0.0	1.0	0.0	1.0	0.0	1.0	0.0	1.0	0.0
Fe (M2)	0.0	0.0	0.0	0.0	0.0	0.0	0.0	0.0	0.0	0.0
Mn (M2)	0.0	0.0	-	-	0.0	0.0	-	-	-	-
Mg (M2)	0.2	0.0	0.2	0.1	0.2	0.1	0.2	0.1	0.2	0.1
Ca (M2)	0.8	0.0	0.8	0.1	0.8	0.1	0.8	0.1	0.8	0.1
Na (M2)	0.0	0.0	0.0	0.0	0.0	0.0	0.0	0.0	0.0	0.0
∑ (M2)	1.0	0.0	1.0	0.0	1.0	0.0	1.0	0.0	1.0	0.0
∑ (M)	2.0	0.0	2.0	0.0	2.0	0.0	2.0	0.0	2.0	0.0
CaTs	6.0	0.0	5.0	0.0	5.0	0.0	5.0	0.0	8.0	0.0
Wo	43	3	40	3	41	4	40	3	41	7
En	48	4	51	3	53	4	50	3	48	8
Fs	9	2	9	1	6	1	10	2	11	2

TABLE X (continued): Compositions of experimental run products of decompression experiments

	Hypersthene PCADecExp		Hypersthene PCADecExprep		Hypersthene PCADecExpCr		Hypersthene IHPVDecExp-5-3		Hypersthene IHPVDecExp-8-3	
#	38		9		9		5		4	
EPMA	Ø	S.D.	Ø	S.D.	Ø	S.D.	Ø	S.D.	Ø	S.D.
SiO_2	55.7	0.90	54.2	1.14	55.6	0.58	54.3	0.82	52.4	2.08
TiO_2	0.10	0.05	0.09	0.04	0.13	0.03	0.09	0.04	0.17	0.08
Al_2O_3	3.22	1.00	3.67	1.36	2.70	0.70	2.30	0.66	4.99	2.80
FeO	9.00	0.82	10.09	0.60	6.74	0.37	6.68	0.21	9.63	2.57
MnO	0.20	0.04	n.a.	-	0.15	0.02	n.a.	-	n.a.	-
MgO	30.9	1.10	30.5	0.79	32.9	0.68	30.2	0.56	27.6	2.14
CaO	1.74	0.31	1.43	0.19	2.13	0.14	2.17	0.18	2.71	1.17
Na_2O	0.02	0.02	0.01	0.01	0.07	0.05	0.06	0.05	0.04	0.01
∑	101	1.24	100	0.66	100	0.59	95.8	0.79	97.5	0.98
Cations per 6 Oxygens										
Si (T)	1.9	0.0	1.9	0.0	1.9	0.0	2.0	0.0	1.9	0.1
Al (T)	0.1	0.0	0.1	0.0	0.1	0.0	0.0	0.0	0.1	0.1
∑ (T)	2.0	0.0	2.0	0.0	2.0	0.0	2.0	0.0	2.0	0.0
Al (M1)	0.1	0.0	0.0	0.0	0.0	0.0	0.1	0.0	0.1	0.1
Fe (M1)	0.3	0.0	0.2	0.0	0.2	0.0	0.2	0.0	0.3	0.1
Mg (M1)	0.7	0.0	0.8	0.0	0.8	0.0	0.7	0.0	0.6	0.1
Ti (M1)	0.0	0.0	0.0	0.0	0.0	0.0	0.0	0.0	0.0	0.0
∑ (M1)	1.0	0.0	1.0	0.0	1.0	0.0	1.0	0.0	1.0	0.0
Fe (M2)	0.0	0.0	0.0	0.0	0.0	0.0	0.0	0.0	0.0	0.0
Mn (M2)	0.0	0.0	0.0	0.0	0.0	0.0	-	-	-	-
Mg (M2)	0.9	0.0	0.9	0.0	0.9	0.0	0.9	0.0	0.9	0.0
Ca (M2)	0.1	0.0	0.1	0.0	0.1	0.0	0.1	0.0	0.1	0.0
Na (M2)	0.0	0.0	0.0	0.0	0.0	0.0	0.0	0.0	0.0	0.0
∑ (M2)	1.0	0.0	1.0	0.0	1.0	0.0	1.0	0.0	1.0	0.0
∑ (M)	2.0	0.0	2.0	0.0	2.0	0.0	2.0	0.0	2.0	0.0
CaTs	3.0	0.0	0.0	0.0	4.0	0.0	2.0	0.0	5.0	0.0
Wo	3	1	4	0	4	0	4	0	6	2
En	83	2	86	1	86	1	85	1	79	5
Fs	14	1	10	1	10	1	11	0	16	4

TABLE X (continued): Compositions of experimental run products of decompression experiments

	Clinozoisite IHPVDecExp-8-3 7 dark areas		Clinozoisite IHPVDecExp-8-3 5 bright areas			SiO_2 IHPVDecExp-5-3 3		SiO_2 IHPVDecExp-8-3 18	
EPMA [wt.%]	Ø	S.D.	Ø	S.D.	EPMA [wt.%]	Ø	S.D.	Ø	S.D.
SiO_2	52.3	2.34	57.9	4.64	SiO_2	94.6	1.39	95.2	4.36
TiO_2	0.04	0.03	0.22	0.14	TiO_2	0.10	0.04	0.11	0.08
Al_2O_3	28.6	1.64	24.2	2.42	Al_2O_3	0.79	0.66	1.85	2.88
FeO	0.66	0.17	1.14	0.67	FeO	0.35	0.19	0.24	0.19
MgO	0.11	0.03	0.23	0.23	CaO	0.12	0.05	0.58	1.05
CaO	13.7	0.93	11.3	1.10	Na_2O	0.16	0.03	0.31	0.52
Na_2O	2.90	0.41	2.88	0.49	∑	96.1	0.73	98.3	1.51
∑	98.3	0.99	97.9	0.79					
Cations per 13 Oxygens					Cations per 2 Oxygens				
Si	3.9	0.2	4.3	0.3	Si	1.0	0.0	1.0	0.0
Ti	0.0	0.0	0.0	0.0	Ti	0.0	0.0	0.0	0.0
Al	2.5	0.2	2.1	0.2	Al	0.0	0.0	0.0	0.0
Fe	0.0	0.0	0.1	0.0	Fe	0.0	0.0	0.0	0.0
Mg	0.0	0.0	0.0	0.0	Ca	0.0	0.0	0.0	0.0
Ca	1.1	0.1	0.9	0.1	Na	0.0	0.0	0.0	0.0
Na	0.4	0.1	0.4	0.1	∑	1.0	0.0	1.0	0.0
∑	8.0	0.1	7.8	0.2					

V. FIGURES

Title Section I:
Front piece of “The granite controversy” By (Read, 1957), Drawn by D. A. Walton

Title Section II:
Photograph of anorthositic dyke crosscutting microgabbro

Title Section III:
Photograph of the Piston Cylinder Apparatus of the Steinmann-Institute facilities in Bonn

Title Section IV:
Charlie in the engine; Photograph of Charlie Chaplin in the movie Modern times (http://www.follow-me-now.de/assets/images/Moderne_Zeiten-Charlie_in_der_Maschine.jpg)

V. ACKNOWLEDGEMENTS

I would like to express my sincere gratitude to my supervisor **Prof. Dr. Christian G. Ballhaus** for providing confidence in me and for offering me the opportunity to work on such an exciting topic. It was a gratifying experience to mutually collect observations in the field, to illuminate the complexity of processes, and finally to develop the content of reasonable questions to be asked during the following research. The sometimes unconventional way of facing petrological problems is definitely something that enhanced my understanding of science and was an invaluable experience. I always felt encouraged in following up on my pragmatic handling of scientific questions. And I am deeply grateful for the way he handled the circumstances of my pregnancy.

I am furthermore feeling highly grateful to **PD Dr. Raúl O. C. Fonseca** for accepting to be my second supervisor. I want to express my gratitude for introducing me to the art of handling a piston cylinder apparatus and his support in MC-ICP-MS analyses.

My special thanks go to **Prof. Dr. Thorsten Geisler-Wierwille** His personality and political understanding is something that I appreciate very much. His help concerning Raman-Spectroscopic investigation of samples and his comments on the interpretation of textures allowed drawing important conclusions.

I want to thank **Prof. Dr. Carsten Münker** for helpful discussions on aspects concerning geochemistry.

Thank you to **Dr. Roman Botcharnikov** for the support with IHPV experiments, and for giving me insights to the enormous spectrum of possibilities in experimental work in petrology. I had a very interesting time in Hannover.

Furthermore I want to thank **Prof. Dr. Hans Keppler** at the BGI Bayreuth, for sharing his ideas on the behaviour of complete miscibility in the anorthite H_2O system.

A special thanks to **Dr. Burkhard Schmidt** for investing his time to fuse my samples in the Nabertherm batch furnace at the facilities in Göttingen.

I feel grateful for the help of **Christian Marien** doing the high precision element and isotope chemistry with me.

My thanks also go to **Thomas Schulz** for his support in the high pressure lab, especially during the time my left hand was out of order.

I would also like to thank **Dieter Lülsdorf** for the technical support and for always helping me to find a smart solution for missing parts in the high pressure lab. I apologize for always putting pressure on him when asking to generate new assemblies.

I feel very grateful to **Nils Jung** for sample preparation. Thank you also for letting me work with the stone saw.

I should like to extend warm thanks particularly to **PD Dr. Thorsten Nagel** for introducing me to the application of the Electron Microprobe.

Furthermore I want to thank **Hans Henning Friedrich** for the generation of XRD data.

My gratitude goes to **Dr. Georg Nover** and to **Dr. Jutta von der Gönna** for spreading friendly atmosphere in the high pressure lab. They were always willing to help me with any kind of problem arising during experimental work.

I would also like to thank **Dr. Renate Schumacher** for the inspiring discussion of the Huttenlocher-Exsolution and for providing books.

Thank you to **Kerstin Stange** for the help generating the Raman spectra.

Furthermore I want to thank **Christoph Lenting** for cross-reading the analytical section and his comments on Raman relevant data.

I also thank **Dorothee Pahsmann** for her refreshing and honest character and for her help with the batch furnace.

I would particularly like to honor and thank **Dagmar Hambach** and **Daniela Bungartz**. Thank you for their constant willingness to help and for their patience. I doubt that I will ever fill out a form without a mistake.

I am particularly grateful to **Dr. Lisa Baldwin**, my fellow PhD student; I am looking forward to finally publishing our journal on spectacular BSE images. It was good to experience the joyfulness of science.

Thanks to **Dr. Christopher Giehl**, **Katharina Sanders** and **Martin Mangler** for commenting on this work and to correct my “Aurenglish”.

Thank you **Vicktoria Zippman**, you know what I would like to say!

Bonn, 2017

Aurelia Lucretia Katharina Zirner